



University  
of Glasgow

Basith, Mohammed Abdul (2011) *A TEM investigation of patterned ferromagnetic nanostructures by lithographic techniques*.  
PhD thesis.

<http://theses.gla.ac.uk/2962/>

Copyright and moral rights for this thesis are retained by the author

A copy can be downloaded for personal non-commercial research or study, without prior permission or charge

This thesis cannot be reproduced or quoted extensively from without first obtaining permission in writing from the Author

The content must not be changed in any way or sold commercially in any format or medium without the formal permission of the Author

When referring to this work, full bibliographic details including the author, title, awarding institution and date of the thesis must be given

# A TEM INVESTIGATION OF PATTERNED FERROMAGNETIC NANOSTRUCTURES BY LITHOGRAPHIC TECHNIQUES

Mohammed Abdul Basith, M.Phil.



*Submitted in fulfilment of the requirements for  
the Degree of Doctor of Philosophy*

*School of Physics and Astronomy  
College of Science and Engineering  
University of Glasgow*

*To Zahin and her ma moni*

## Abstract

This PhD research project encompasses an investigation into the controlled behaviour of magnetic domain walls in patterned ferromagnetic nanostructures using advanced nanofabrication techniques and characterised by the techniques of transmission electron microscopy. By fabricating Permalloy (Py) nanowires using electron beam lithography (EBL) and focused ion beam (FIB) milling a comparative study has been made in which key differences in the magnetic behaviour have been identified. Nominally identical Py nanowires, with widths down to 150 nm, were fabricated onto a single electron transparent  $\text{Si}_3\text{N}_4$  membrane. Transmission electron microscopy (TEM) experiments were performed to compare the nanostructures produced by these two techniques in what we believe is the first direct comparison of fabrication techniques for nominally identical nanowires. Both EBL and FIB methods produced high quality structures with edge roughness being of the order of the mean grain size 5 -10 nm observed in the continuous films. However, significant grain growth was observed along the edges of the FIB patterned nanowires. Lorentz TEM *in situ* imaging was carried out to compare the magnetic behavior of the domain walls (DWs) in the patterned nanowires with anti-notches present to pin DWs. The overall process of DW pinning and depinning at the anti-notches showed consistent behaviour between nanowires fabricated by the two methods with the FIB structures having slightly lower characteristic fields compared to the EBL wires. However, a significant difference was observed in the formation of a vortex structure inside the anti-notches of the EBL nanowires after depinning of the domain walls. No vortex structure was seen inside the anti-notches of the FIB patterned nanowires. Whilst the two fabrication methods show that well defined structures can be produced for the dimensions considered here, the differences in the magnetic behavior for nominally identical structures may be an issue if such structures are to be used as conduits for domain walls in potential memory and logic applications.

In this project, investigations were also carried out on ion irradiation of nanowires in which DW pinning sites arise from a controlled local modification of the magnetic properties of the nanowire. The nanowires comprised a multilayer thin film of Cr(3



nm)/Py(10 nm)/Cr(5 nm) in which the local magnetic properties were varied by irradiation with *Ga* ions in a focused ion beam microscope. Alloying Py with Cr is known to significantly change its magnetic properties. The nanowires were patterned and irradiated in the FIB, a single irradiation line was used to create a pinning site at an angle of 45 degrees to the wire length. Observation of the magnetic state of the nanowires was made using Lorentz microscopy. A transverse DW (TDW) was created at the end of a 500 nm wide nanowire and then a field applied to move it towards the pinning site. This TDW was pinned at the irradiated line for low doses. For lines with increased dose the TDW was often seen to transform into a vortex DW. The change of micromagnetic wall structure and the dependence of the subsequent depinning field on the dose and wall type were investigated together with initial simulation results modeling these features. In addition to the control of the DWs, our findings indicate potential for engineering and filtering DWs of certain types as they pass irradiated features at predefined locations in nanowires, dependent on the dose associated with these features in magnetic nanowires sandwiched between metallic layers.

On a continuous  $16.9 \pm 0.8$  nm thick Py film, magnetically softer and harder stripes, which are in direct lateral contact by means of exchange coupling, were fabricated by focused *Ga*<sup>+</sup> irradiation. The irradiation dose was  $6.24 \times 10^{15}$  ions/cm<sup>2</sup> and the width of the alternate exposed and unexposed stripes were varied from 1000 nm to 200 nm. Low angle electron diffraction experiment confirmed that due to this amount of ion dose, saturation magnetic induction of the irradiated stripe is reduced to  $72.0 \pm 0.7\%$  of the unirradiated stripe, assuming a thickness reduction of  $2.9 \pm 0.7$  nm determined from TEM cross-sectional image. Magnetisation reversal experiments were carried out using high resolution Lorentz microscopy. Starting from a stripe width of 1000 nm a pronounced two step reversal with nearly anti-parallel orientated magnetisation in neighboring stripes is observed. Differential phase contrast (DPC) images demonstrate a transition from the discrete switching of the wider nanostripes to the tendency of collective switching of the narrower stripes of width 200 nm. This transition is associated with vanishing ability of hosting neighboring high angle domain walls between adjacent stripes.

# Contents

<b>1</b>	<b>Patterned ferromagnetic thin films</b>	<b>1</b>
1.1	Introduction . . . . .	1
1.1.1	Outline of this thesis . . . . .	1
1.2	Basic concept of ferromagnetism . . . . .	2
1.3	Micromagnetic energy terms . . . . .	4
1.3.1	Exchange energy . . . . .	4
1.3.2	Magnetostatic energy . . . . .	6
1.3.3	Anisotropy energy . . . . .	7
1.3.4	Zeeman energy . . . . .	9
1.3.5	Total energy . . . . .	9
1.4	Magnetic domains and domain walls . . . . .	10
1.4.1	Magnetic domains . . . . .	10
1.4.2	Magnetic domain walls . . . . .	11
1.4.3	Domain walls width . . . . .	13
1.4.4	Domain wall spin structures in nanowires . . . . .	14
1.5	Micromagnetic simulation . . . . .	16
1.6	Magnetisation reversal . . . . .	19
1.6.1	Hysteresis . . . . .	19
1.6.2	Reversal processes in a rectangular thin film element . . . . .	21
1.7	Motivation of this PhD project . . . . .	22
1.7.1	Nanofabrication using alternative techniques . . . . .	23
1.7.2	Ion induced pinning sites for DWs trapping . . . . .	24
1.7.3	Magnetisation reversal processes in hybrid nanostructures . . . . .	26

<b>2</b>	<b>Materials deposition and nanofabrication techniques</b>	<b>34</b>
2.1	Introduction . . . . .	34
2.2	Substrate for deposition . . . . .	36
2.3	Materials deposition . . . . .	37
2.3.1	Thermal evaporation . . . . .	38
2.3.2	Molecular beam epitaxy . . . . .	39
2.3.3	Magnetron sputter deposition . . . . .	41
2.4	Nanofabrication . . . . .	42
2.4.1	Electron beam lithography . . . . .	42
2.5	Focused ion beam technique . . . . .	48
2.5.1	Focused ion beam systems . . . . .	48
2.5.2	Dual beam system . . . . .	50
2.5.3	Ion-solid interactions . . . . .	50
2.5.4	FIB milling . . . . .	53
2.5.5	FIB irradiation . . . . .	56
2.5.6	TEM sample preparation using FIB technique . . . . .	58
2.6	TRIDYN simulation . . . . .	63
<b>3</b>	<b>Instrumentation and characterisation techniques</b>	<b>71</b>
3.1	Introduction . . . . .	71
3.2	Transmission electron microscopy . . . . .	71
3.3	The electron gun . . . . .	73
3.4	The microscope column . . . . .	74
3.5	Structural characterisation . . . . .	77
3.6	Bright field and dark field imaging . . . . .	80
3.7	Magnetic imaging in TEM . . . . .	81
3.7.1	Lorentz microscopy . . . . .	82
3.7.2	Fresnel imaging . . . . .	86
3.7.3	Differential phase contrast imaging . . . . .	88
3.8	Lorentz image calculation . . . . .	92
3.9	<i>In situ</i> Magnetising experiments . . . . .	96
3.10	Low angle electron diffraction (in CM 20) . . . . .	97

<b>4 Nanostructures patterned by EBL and FIB milling: a direct comparison</b>	<b>102</b>
4.1 Objective and motivation . . . . .	102
4.2 Material deposition and nanofabrication . . . . .	103
4.3 Structural characterisation . . . . .	105
4.3.1 Plan-view TEM images . . . . .	105
4.3.2 Cross-sectional TEM images . . . . .	107
4.3.3 Double cut vs single cut approaches for pattern generation . . .	110
4.4 Magnetic characterisation . . . . .	112
4.4.1 Formation of domain walls . . . . .	112
4.4.2 Propagation of domain walls . . . . .	115
4.4.3 Micromagnetic simulation . . . . .	119
4.5 Summary . . . . .	124
<b>5 Controlling of domain walls in planar nanowires by ion irradiated features</b>	<b>129</b>
5.1 Objective and motivation . . . . .	129
5.2 Property modification by ion irradiation . . . . .	130
5.3 Optimisation of materials thickness using TRIDYN simulation . . . . .	131
5.4 Materials deposition . . . . .	134
5.5 FIB irradiation . . . . .	135
5.6 Modification of the material system: low angle electron diffraction experiments . . . . .	138
5.7 Patterning of nanowires and pinning features . . . . .	146
5.8 <i>In situ</i> magnetizing experiments . . . . .	149
5.8.1 Patterns generation on isotropic film . . . . .	149
5.8.2 Patterns generation on anisotropic film . . . . .	154
5.9 Micromagnetic simulation . . . . .	163
5.10 Summary . . . . .	166
<b>6 Magnetisation reversal processes in ion irradiated magnetic stripes</b>	<b>172</b>
6.1 Objective and motivation . . . . .	172
6.2 Material deposition and sample preparation . . . . .	173

6.3	Characterisation technique . . . . .	175
6.4	Reduction of integrated magnetic induction due to irradiation . . . . .	176
6.5	Magnetic characterisation . . . . .	178
6.5.1	Fresnel imaging . . . . .	178
6.5.2	DPC imaging . . . . .	185
6.5.3	Micromagnetic simulation on stripe patterns . . . . .	188
6.6	Domain wall width in the unconstrained and constrained film . . . . .	192
6.7	Summary . . . . .	199
<b>7</b>	<b>Conclusions and Future Work</b>	<b>202</b>
7.1	Introduction . . . . .	202
7.2	Conclusions . . . . .	203
7.3	Future work . . . . .	208

# List of Figures

1.1	Schematic diagram of the alignment of magnetic moment's in (a) paramagnetic, (b) ferromagnetic, (c) ferrimagnetic and (d) antiferromagnetic specimens. . . . .	3
1.2	Schematically temperature dependence of the saturation magnetisation of the ferromagnetic materials. . . . .	3
1.3	Schematically the demagnetising field that arises depending on whether the ellipsoid is magnetised along the (a) long or (b) short axis. (a) has lower demagnetising field than (b) and was indicated by the relative sizes of the red arrow sign. . . . .	8
1.4	Illustration of the magnetostatic field generated in (a) the single domain state, (b), (c) multidomain states and quenching of the magnetostatic field by the formation of (d) a flux-closure state. (e) a single domain state induced by shape anisotropy. . . . .	10
1.5	Plan view schematic illustrations of (a) Bloch-type wall, (b) Néel-type wall and (c) cross-tie wall. . . . .	12
1.6	Example of an arctangent and hyperbolic tangent functions. . . . .	14
1.7	A phase diagram of domain wall spin structures for straight nanowires of a given width and thickness. Adapted from reference [14]. . . . .	14
1.8	Schematic illustration of (a,b) clockwise and counterclockwise vortex DWs, respectively; (c,d) transverse DW with central spin up and down, respectively; and (e-h) asymmetric transverse domain walls. . . . .	15
1.9	Precession of the magnetisation vector $\mathbf{M}$ around the effective field : (a) precessional motion without damping, (b) gyro-precessional motion with damping. . . . .	17
1.10	Schematically a typical hysteresis loop for a ferromagnetic specimen. . .	20

1.11	Schematic illustration of reversal processes in a rectangular thin film element during field application. . . . .	22
2.1	Schematic illustration of the processing steps of two alternative lithographic techniques. The processing steps for writing patterns using (a) EBL technique and (b) FIB milling technique. The latter technique is faster and a new addition to the range of nanofabrication techniques. .	35
2.2	A schematic of the substrates used to fabricate thin film elements. (a) A $2 \times 2$ membrane set containing etched markers is used for electron beam lithography, (b)Front, (c) back and (d) cross-sectional schematics of single $\text{Si}_3\text{N}_4$ membrane. . . . .	37
2.3	Schematic of the thermal evaporator used to deposit thin films. . . . .	39
2.4	A schematic of the MBE system used for the multilayer thin films Cr/Py/Cr on $\text{Si}_3\text{N}_4$ membrane. . . . .	40
2.5	Schematically parallel plate DC magnetron sputtering system for thin film deposition. . . . .	42
2.6	Schematic diagram of the VB6 beam writer used to pattern part of the structures in <b>chapter 4</b> . . . . .	44
2.7	Schematic illustration of the resist profile of (a) positive and (b) negative single component resist. The positive resist is weakened by chain scission to produce organic molecules of a lower molecular weight. On the other hand, the negative resist is strengthened during exposure by random cross-linkage of main and side polymer chains and become less soluble in the developer. . . . .	45
2.8	Schematic illustration of the resist and deposited metal profile with (a) a single resist layer and (b) a bilayer of electron sensitive resist. The later one facilitates the subsequent lift-off process of the resist, forming a suitable undercut profile. . . . .	46
2.9	TEM image shows both the nanowires and rectangles written by using EBL technique in a single piece of membrane. Later on inside these rectangles, patterns were written using FIB milling. . . . .	47
2.10	Schematic illustration of an ion column. . . . .	49

2.11	Schematic of the dual beam system, in which both electron and ion beams are co-focused at the eucentric point of the sample surface. . . .	51
2.12	Schematic illustration of a dual-beam FIB-SEM instrument. Expanded view shows the electron and ion beam sample interaction. Figure adapted from reference [7]. . . . .	52
2.13	Schematic illustration of a collision cascade generated by a 30 keV $Ga^+$ incident on a crystal lattice, showing the projected range $R_p$ and lateral range $R_i$ of the implanted ion. Figure adapted from reference [7]. . . .	53
2.14	Schematic illustration of ion irradiation with 0% overlap, where $d$ and $s$ are equal and are the pixel size and pixel spacing, respectively. $A$ is the area in $\mu m^2$ . . . . .	54
2.15	Scanning procedures with arrows indicating scanning direction: (a) raster scan (b) serpentine scan and (c) using a stream file generated by the 'edgestream' program. . . . .	55
2.16	TEM bright field images show (a) the creation of holes at the interface of two milling cuts, (b) pattern written by a single cut approach. . . .	56
2.17	SEM images show (a) patterned nanowires written by FIB milling. The rectangular region show the area of interest for x-sectioning and (b) E-beam deposited Pt layer. . . . .	59
2.18	SEM image show (a) ion beam assisted Pt protective layer and (b) using 6000 pA beam current rough undercut. . . . .	60
2.19	SEM image show (a) bulk trench cuts using 1000 pA current, (b) Omniprobe tip and the specimen was welded by depositing Pt. . . . .	61
2.20	SEM images of (a) Pt attach lift-out of the sample with the Omniprobe needle and (b) TEM grid was mounted. . . . .	61
2.21	SEM images show (a) specimen was attached with the TEM grid and (b) the Omniprobe tip was released from the sample. . . . .	62
2.22	SEM images show that (a) thinning was performed at different tilt angles (1.2 degree) using 300 pA currents and 30 keV energy and (b)polishing using cleaning cross-section ( beam current 100 pA and energy 30 keV and tilt angle 1 degree). . . . .	62



2.23	(a) Fine thinning of the sample using 5 keV beam energy and 16 pA beam current. (b) X-sectional sample for TEM imaging. . . . .	63
2.24	Tridyn simulation of Cr concentration profiles with varying dose. . . . .	65
2.25	TRIDYN simulations of the relative concentrations of the individual elements as a function of sample depth before implantation (a), and for implantation doses of (b) $2 \times 10^{14} \text{ ions/cm}^2$ , (c) $6 \times 10^{14} \text{ ions/cm}^2$ , and (d) $10 \times 10^{14} \text{ ions/cm}^2$ . . . . .	66
3.1	Schematic ray diagram of a typical CTEM column illustrating the positions of the various lenses and apertures used to form an image. . . . .	75
3.2	Schematically electron diffraction on crystal lattice: (a) two incident waves reflecting on ( <i>hkl</i> ) planes are in-phase when their path difference is equal to an integer number of wavelengths, and (b) principle of electron diffraction in the TEM. . . . .	78
3.3	(a) An example diffraction pattern obtained in a CTEM (b) Plan view TEM bright field image of a permalloy nanowire patterned by FIB milling showing the grain structure. . . . .	79
3.4	Principle of bright-field and dark-field imaging: (a) bright-field image, (b) dark-field image and (c) centred dark-field image. . . . .	80
3.5	An example of (a) bright field (BF) and (b) dark field (DF) plan-view images of the centre region of the nanowire patterned by FIB milling . . . . .	81
3.6	Schematically deflection of the electrons due to Lorentz force when passing through a thin magnetic specimen. . . . .	83
3.7	(a) Schematic illustration of the principle of Fresnel imaging mode. The main imaging lens is defocused a distance $\Delta$ above or below the specimen plane to observe contrast at the positions of domain walls and at the edges of the element. Fresnel images (b-g) demonstrate a vortex domain wall at different values of $\Delta$ in nanowires patterned by electron beam lithography (b-d) and focused ion beam milling (e-g). . . . .	87

3.8	(a) Schematically the principle of DPC mode of Lorentz microscopy. The emergent beam is deflected by angle $\beta_L$ due to the Lorentz force. The difference signals measured from opposite quadrants on the detector provides information on the magnetic induction in the sample. (b) Fresnel image shows a black contrast domain wall along the irradiated stripe 'A'. (c and d) show the orthogonal components obtained from the red marked region in Fresnel image (b). Red arrows indicate the direction of magnetic induction each image is sensitive to. (e) shows the intensity profile obtained from the marked region of (c). . . . .	89
3.9	(a) Schematic illustration of the low magnification scanning (LMS) in which the upper Lorentz lens is switched off to form a larger probe at the specimen. (b) Schematically high magnification scanning (HMS) mode in which the Upper Lorentz lens is switched on to achieve a smaller probe at the specimen. . . . .	90
3.10	Schematically the phase change incurred by the electrons on passing through (a) a magnetic and (b) a non-magnetic specimen. The schematic of derivative of the phase and the Laplacian, for a small defocus value, are given below accordingly. . . . .	93
3.11	Experimental Fresnel image of a vortex domain wall in a 20 nm thick permalloy nanowire containing an anti-notch is compared with simulated Lorentz images. (a) Magnetisation as calculated from OOMMF simulation. (b) and (c) are the x and y components of the magnetisation. From this the (d) magnetic and (e) electrostatic phase are calculated. (f) and (g) are the orthogonal components of the magnetic induction where arrows are indicating the sensitivity direction. (h) Fresnel image contrast from purely magnetic phase and including electrostatic and amplitude effect (i). (j) is an experimental image for comparison . The out of plane component of magnetisation curl (k) is in good agreement with the Fresnel contrast. . . . .	95
3.12	Generating a magnetic field parallel to the specimen plane by tilting the specimen. . . . .	97

3.13	(a) Schematic representation of the split central diffraction spot containing $180^\circ$ domain walls. (b) Fresnel image show a $180^\circ$ domain wall in a continuous thin film. (c) Two diffraction spots recorded by illuminating the area in image (b). . . . .	98
4.1	Schematic of the nanowire geometry. The distance between the anti-notches has been reduced for this schematic indicated by vertical bars.	103
4.2	(a) Patterns were written onto one half of the membrane using EBL/lift off techniques. Four large size rectangles were also written using EBL technique onto the other half of the membrane. Later on identical patterns were written into these rectangles using FIB milling. (b) TEM image shows the patterns written by EBL and FIB techniques onto a single membrane on which the Py film of the same thickness and quality was deposited. . . . .	104
4.3	Schematically different processing steps of EBL/lift off technique as was described in <b>chapter 2</b> . . . . .	105
4.4	TEM bright field images of the plan view of 320 nm wide nanowires patterned by EBL (a) and FIB (b). Higher magnification TEM bright field images of the plan view of 320 nm wide nanowires patterned by EBL (a) and FIB (b). Circle marked regions indicate grain growth along FIB patterned nanowire edge (b). . . . .	106
4.5	X-sectional TEM bright field images showing the wire edges of the 320 nm wide nanowires patterned by EBL (a,b). The individual layers are labeled in (a). X-sectional TEM bright field images showing the wire edges of the 320 nm wide nanowires patterned by FIB (c,d). Figure (e) is showing schematically the individual layers of image (c). X-sectional image (f) is showing the one edge of a 150 nm wide FIB patterned nanowire. . . . .	108
4.6	TEM bright field images showing the nanowires patterned by a (a) two cut approach, (b) SEM image showing the extreme damage due to the milling of the film and (c) TEM image demonstrating the single cut approach. . . . .	110

4.7	Left edges of the nanowires written by a multiple cut approach (a) and single cut approach (b) along with milling areas. The individual layers in the milling areas in images (a) and (b) are shown schematically in the schematic (c). . . . .	111
4.8	A TEM x-sectional image shows an overview of a nanowire patterned by EBL technique. The individual layers in the either edges of the nanowire are shown schematically in (b). . . . .	112
4.9	Domain wall structure phase diagram proposed by Y. Nakatani et al [28]. The red circles indicate the location within the domain wall structure phase diagram of the wire geometries considered for the investigation in <b>chapter 4</b> . . . . .	113
4.10	Formation of the asymmetric transverse DW (a), ccw VDW (c) and cw VDW (e) at the zero field in 320 nm wide EBL patterned nanowires. DWs of different chiralities were formed by applying a magnetic field at different angles counter clockwise from the hard axis and relaxing to zero. For the formation of a ccw VDW, a magnetic field was applied at an angle of 2-4 degrees whereas for a cw VDW formation, the angle of the applied magnetic field was increased to 10-12 degrees. (b, d and f) are the corresponding schematics of (a, c and e). 'A' and 'B' indicate the black thick fringe at the upper edge of the diamond shaped pad and lower edge of the straight wire, respectively. 'C' denotes the vortex core. . . . .	114
4.11	Fresnel images of a ccw VDW at zero field in 320 nm wide nanowires patterned by EBL (a) and FIB (b). (d and e) are showing ccw VDW is pinned prior to the anti-notches. State after DW depinning is showing (g and h). Completion of reversal in EBL wire is showing (k). Schematic interpretation of (a and b) is (c), (d and e) is (f) and (g and h) are (i and j), respectively. . . . .	116

4.12	Fresnel images (a) and (b) are showing a cw VDW at zero field in 320 nm wide nanowires fabricated by EBL and FIB, respectively. (d and e) are showing part of the cw VDW merged inside the anti-notches. (g and h) are showing state after DW depinning. (k) is showing completion of reversal in EBL wire. (c) is the schematic of (a and b), (f) is the (d and e) and (i and j) are the schematics of (g and h), respectively. . . . .	117
4.13	Simulations were carried out by varying the edge profiles. Schematic cross-section of the ideal nanowires with rectangular edge (a) and sloped edge (b). (c and d) The edge profile of the nanowires based on the x-sectional TEM images 4.5 (a and c). (e) $M_s$ were reduced up to a distance of 40 nm along the wire edge in the nanowire (b). The width of the nanowires has been reduced for this schematic indicated by vertical bars. . . . .	121
4.14	Simulated Fresnel images (a-d) show the magnetisation reversal process in 320 nm wide nanowire (sloped edge) with uniform $M_s$ throughout the wire. A DW has moved through the anti-notch and a vortex structure is formed inside the anti-notch, as shown in (c). Simulated Fresnel images (e-g) are showing the reversal process of the nanowire of same geometry but with $M_s$ of 50% along the wire edge. The DW has moved through the anti-notch without the presence of the vortex structure, as shown in (g). . . . .	122
4.15	DW depinning field and vortex annihilation fields as a function of $M_s$ along the wire edge. The simulations were carried out for a ccw VDW in a 320 nm wide and 20 nm thick wire as shown in the schematic cross-section 4.13(e) . . . . .	124
5.1	Reduction of saturation magnetisation $M_s$ due to doping Cr in Py as a function of Cr concentration. Data was adapted from reference [31]. . . . .	132
5.2	The amount of Cr concentration at the centre of the Py film as a function of dose for different combinations of Cr/Py/Cr/substrate thin films. Cr concentration at the centre of the Py is higher for a combination of Cr(3 nm)/Py(10 nm)/Cr(5 nm) (red colour). . . . .	133

5.3	(a) Schematically multi-layer thin film system considered for the present investigation. (b) The Cr concentration as a function of sample depth for different ion doses obtained from TRIDYN simulation. (c-f) Histograms show the amount of Cr concentration in the Py layer for different ion doses. . . . .	134
5.4	MOKE easy (EA) and hard axis (HA) hysteresis loops for the as-deposited film with field induced anisotropy. . . . .	135
5.5	Schematic illustration of micro-alloying due to a combined effect of the focused $Ga^+$ irradiation and interfacial atomic mixing. . . . .	136
5.6	Schematically alternate unirradiated and irradiated stripe patterns written on thin continuous film using focused ion beam. . . . .	137
5.7	TEM bright field images of the (a) unirradiated continuous film and (b) alternate unirradiated irradiated stripe patterns. The average grain size in the irradiated stripe is larger than that of the unirradiated stripe. . .	137
5.8	(a) Fresnel image show the formation of a DW perpendicular to the stripes. Diffraction patterns were taken against $180^\circ$ DW from (b) unirradiated continuous film, (c and d) irradiated regions. Irradiation doses were $4 \times 10^{14} \text{ ions/cm}^2$ (c) and $8 \times 10^{14} \text{ ions/cm}^2$ (d). . . . .	139
5.9	(a) A schematic of magnetisation direction of the unirradiated and irradiated regions against an $180^\circ$ DW. Two pairs of diffraction spots were expected from such an anti-parallel alignment of unirradiated and irradiated magnetisation regions. (b) Schematic illustration of stray magnetic fields originated from the surface charges in the uniformly magnetised and reduced magnetised regions. Pairs of diffraction spots were observed experimentally due to the influence of oppositely oriented stray magnetic fields in the unirradiated and irradiated regions. . . . .	140
5.10	The schematic diagrams show stray magnetic fields when DW is formed (a) perpendicular to the long stripe and (b) parallel to the same stripe. The influence of stray magnetic fields in the integrated magnetic induction is significant when DW is formed perpendicular to the long stripe (a) and is negligible when DW is formed parallel to the long stripe (b). . . . .	140

5.11	(a) Using image processing software package DM, alternate uniformly magnetised and reduced magnetised (50 %) stripes were created including an 180° DW. (b) is a profile of the magnetisation in the upper region.	142
5.12	$\int \mathbf{B}dz$ % as a function of the magnetisation of the irradiated stripe. The vertical axis is a normalised value of integrated induction scaled to $B_s t$ of the unirradiated film. The magnetisation of the unirradiated stripe is 100 %.	142
5.13	$\int \mathbf{B}dz$ and deduced $\mu_0 M_s t$ as a function of the irradiation ion doses.	144
5.14	(a) Fresnel image showing black contrast domain wall along alternative unirradiated and ion irradiated stripe patterns. Diffraction patterns from (b) unirradiated continuous film region and (c) alternative unirradiated and irradiated region. The irradiation dose was $16 \times 10^{14} \text{ ions/cm}^2$	144
5.15	Fresnel image showing white contrast domain wall along alternate unirradiated and ion irradiated large size rectangles. The irradiation dose was $d \times 10^{14} \text{ ions/cm}^2$ ( $d = 4, 8, 12$ and $16$ ) in the rectangles b to e, respectively	145
5.16	Diffraction pattern taken from unirradiated film region (a) and patterned regions (b-e), respectively as a function of doses	146
5.17	(a, b and c) Schematics of the nanowire geometry. The length of the wire axis has been reduced for this schematic, indicated by vertical bars. Ion irradiated pinning sites were indicated by the two lines oriented at $\pm 45^\circ$ and marked as pinning sites 1 and 2 in each nanowire.	147
5.18	(a) TEM image shows the nanostructures written by FIB milling along with a schematic of the direction of the irradiated site 1 (cyan). Red circles are indicating the position of the marker spots. (b) TEM image at the centre of the nanowire along which irradiation line was written. The location of the line is between the red dots on the image. (c) TEM BF image shows the bend corner of an L-shaped nanowire.	148
5.19	Pinning and depinning of DWs as a function of applied magnetic fields at irradiation sites 1 and 2. The irradiation dose is $12 \times 10^{15} \text{ ions/cm}^2$ . The corresponding schematics of (a-d) are (e-h), respectively.	150

5.20	Pinning and depinning of DWs as a function of applied magnetic fields at irradiation sites 1 and 2. The irradiation dose is $16 \times 10^{15} \text{ ions/cm}^2$ . Reversal of the nanowire was started also from the other end of the wire and consequently a tail to tail VDW is pinned at site 2 as shown in image (c). Figures (e-h) are the corresponding schematics showing the magnetisation distribution deduced from the image (a-d). . . . .	151
5.21	Pinning and depinning of DWs as a function of applied magnetic fields at site 1 which were irradiated with an ion doses of $20 \times 10^{15} \text{ ions/cm}^2$ . The schematic diagrams of (a, b and c) are (d, e and f), respectively. .	152
5.22	Patterned nanowire showing the presence of strong ripple contrast which ultimately influenced the reversal process including pinning and depinning of DWs at irradiation sites. The irradiation dose was same of wire Fig. 5.21 i.e. $20 \times 10^{15} \text{ ions/cm}^2$ . . . . .	153
5.23	Fresnel image (a) showing the structure of an asymmetric TDW (magnetisation points up) in a wire with a schematic of the magnetisation shown in Fig. (e). DW is initially pinned at site 1 without changing it's structure and later on pin again at site 2 after depin from 1. The ion irradiation dose is $4 \times 10^{15} \text{ ions/cm}^2$ . Schematic interpretation of (b, c and d) are (f, g and h), respectively. Fresnel image (d) shows the completion of the reversal process. . . . .	155
5.24	(a)Initially formed asymmetric TDW with magnetisation points up at the centre of the wall. (b) DW is pinned at site 1 by changing the magnetisation direction points from up to down. The ion irradiation dose is $8 \times 10^{15} \text{ ions/cm}^2$ . Fresnel image (c) shows that DW remains stable at this position. Schematic diagrams (d, e and f) demonstrate the magnetisation distribution in Fresnel images (a, b and c), respectively.	157
5.25	Initially formed asymmetric TDW (a) is pinned with transforming wall structure to a cw VDW (b). The irradiation dose at sites 1 and 2 were $8 \times 10^{15} \text{ ions/cm}^2$ . Fresnel image (c) shows that cw VDW remains stable at pinning site 1. Schematic interpretation of images (a, b and c) are (d, e and f) respectively. . . . .	158



5.26	(a)Initially formed asymmetric TDW with magnetisation points down at the centre of the wall in the bend corner of an L-shaped nanowire. (b) DW is pinned at site 1 without changing the magnetisation direction. The ion irradiation line dose is $4 \times 10^{15} \text{ ions/cm}^2$ . Schematic diagrams (c and d) demonstrate the magnetisation distribution in Fresnel images (a and b), respectively. . . . .	159
5.27	Fresnel image (a) showing the structure of an asymmetric TDW (magnetisation points down) in the bend corner of an L shape wire. DW is initially pinned at site 1 by changing it's structure and later on pin again at site 2 after depin from 1. The ion irradiation dose is $4 \times 10^{15} \text{ ions/cm}^2$ . Schematic interpretation of (a, b and c) are (d, e and f), respectively. .	160
5.28	(Fresnel image shows that initially formed asymmetric TDW (a) is pinned and transform to a cw VDW (b) under the application of magnetic fields. The irradiation line dose is $16 \times 10^{15} \text{ ions/cm}^2$ . Magnetisation distribution in Fresnel images (a and b) are shown schematically in (c and d), respectively. . . . .	161
5.29	(a) Schematic diagram shows that the ferromagnetic (FM1) properties of the nanowire is unmodified at either side of the pinning site. At the pinning site the magnetic property is modified and denoted by FM2. (b) Schematic diagram illustrates that the pinning site behave as an attractive potential well for DW and the well gets deeper for higher irradiation doses. The vertical axis is a measure of potential. Notably, higher irradiation dose allows DW to change structure. . . . .	162

- 5.30 (a) Schematic of initial configuration before relaxation. This is an asymmetric TDW along with the modelled pinning site in a 300 nm wide and 10 nm thick nanowire. The length of the wire axis has been reduced for this schematic indicated by vertical bars. (b) Schematically part of the 8 (horizontal) x 4 (vertical) cells modelled pinning site. (c) Calculated Fresnel image shows pinning of an asymmetric TDW at the pinning site in which  $M_s$  is 70% of its original value and exchange constant was changed accordingly. (d) Calculated Fresnel image demonstrates the transformation of initial asymmetric TDW into a VDW at the pinning site in which  $M_s$  is 30% of its original value and the exchange constant was changed accordingly. . . . . 164
- 6.1 (a) Schematic diagram of unirradiated and irradiated stripe patterns in a thin continuous Py film. (b) Plan-view TEM bright field (BF) image demonstrates irradiated stripes by the increased grain size surrounded by the unirradiated stripe. Higher magnification TEM BF images show (c) the grain size distribution in the unirradiated stripe and (d) the grain growth inside the irradiated stripe due to the effects of irradiation . . . 174
- 6.2 (a) Fresnel image showing the oppositely magnetised magnetic region of the unirradiated and irradiated stripes by forming a  $180^\circ$  domain wall along the stripe pattern. (b) Electron diffracted spots were obtained by illuminating the area, marked by red circle in image (a), from low angle diffraction experiments using Lorentz TEM. The two outer spots (green mark) arise from the unirradiated regions whereas two inner spots (blue mark) are from the irradiated regions. (c) cross-sectional TEM image of a non changed area between two FIB irradiated stripes (this cross-section was prepared in Dresden). (d) A schematic of the TEM cross-section (c). 177

6.3	(a) Schematic diagram illustrates that saturation magnetisation of the unirradiated stripe ( $M_{su}$ ) is higher than that of the irradiated stripe ( $M_{si}$ ). Film thickness $t_i$ of the irradiated stripe is lower than that of the unirradiated stripe $t_u$ . Electron deflection from the unirradiated stripe is larger compared to that of the irradiated stripe, and (b) Resulting intensity distribution due to the deflections of the electron beams. . . .	179
6.4	Fresnel image sequences (a-d) for magnetisation reversal of the 1000 nm wide stripe patterns. Magnetisation reversal inside the stripe panel is driven by domain walls in the surrounding film. Reversal completed with an intermediate anti-parallel orientation of magnetisation in neighboring stripes. . . . .	180
6.5	(a) Fresnel image showing strong black and white wall contrast as an example within the blue marked region. (b) Schematically magnetisation directions in the unirradiated and irradiated stripes followed by blue rectangular region of Fresnel image (a). Cross-section of the stripe patterns showing schematically (c) magnetisation directions of the unirradiated and irradiated stripes in the region 'A' of schematic (b), where w and b indicate white and black contrast, respectively; (d) reversal of the irradiated stripes take place in region 'B' and white and black contrast became stronger as indicated by <b>W</b> and <b>B</b> , respectively. . . .	181
6.6	Fresnel image sequences (a-c,e,f) for magnetisation reversal of the 500 nm wide stripe patterns. Magnetisation reversal inside the stripe panel is driven by domain walls in the surrounding film. (d) is a schematic of blue marked region of Fresnel image (c). . . . .	183
6.7	Fresnel image sequences (a-d, f) for magnetisation reversal of the 200 nm wide stripe patterns. (e) is the schematic within the blue marked region of Fresnel image (d) and showing the magnetisation directions. . . . .	184
6.8	Domain state of a separate reversal experiment in 1000 nm wide stripe pattern. The induction component parallel and perpendicular to the stripes are shown in (a) and (b). Induction components in (a) and (b) are shown schematically in (c). . . . .	186

6.9	DPC images of stripe array with stripe width of 200 nm. The two sensitivities are shown in the upper and lower row. Images b and c (f and g) are showing the magnification of the square marked regions of image a (e). (d) is the schematic of the marked region in Fresnel image (c). . . . .	188
6.10	(a) Schematic cross-section of the initial magnetisation configuration of the stripe patterns where $M_s$ is 100% for one stripe and 60% for the other. The exchange stiffness constants of the unirradiated and irradiated regions are indicated as $A_{11}$ and $A_{22}$ , respectively. The coupling term between these two regions are indicated as $A_{12}$ . (b) Initial magnetisation states with anti-parallel orientation of magnetisation of the unirradiated and irradiated stripes. . . . .	189
6.11	Magnetisation reversal process as a function of applied field from an initial anti-parallel orientation of magnetisation states of the stripe patterns. Magnetisation of the unirradiated and irradiated stripes are 100% and 60%, respectively in (a-h). Magnetisation is 100% in the two stripes in (i-l). Magnetic field was applied away from the interface at (a-d) and towards the interface at (e-l). . . . .	190
6.12	(a) Initial state of the magnetisation configurations in which an anti-parallel orientation of the magnetisation was settled in the unirradiated stripe. (b) The relax state of the initial configuration, DW is formed in the region of the irradiated stripe where $M_s$ is 60%. . . . .	191
6.13	Example of an arctangent and hyperbolic tangent functions. . . . .	192
6.14	(a) Fresnel image showing a $125^\circ$ DW in the continuous film, marked by red rectangle. DPC images of (b) longitudinal and (c) transverse induction component (in respect to wall) of the unconstrained wall in the continuous film as shown in Fresnel image (a). (d) Experimental induction profile, fitted profile and derivative of the fitted profile marked by black, red and blue circles, respectively. In Figs. (b,c) red arrows indicate the direction of the integrated induction components. . . . .	194

6.15	(a) Fresnel image showing a $90^\circ$ DW in the constrained unirradiated stripe, marked by green rectangle and green arrow. Longitudinal (b) and transverse (c) induction components (in respect to wall) of the magnetisation in the constrained wall. (d) Experimental induction profile, tanh fitted profile and derivative of the fitted profile marked by black, red and blue circles, respectively. In Figs.(b,c) red arrows indicate the direction of the integrated induction components. . . . .	195
6.16	Gray scale images of the magnetisation components of a 20 nm thick Py element with in-plane dimensions $2\ \mu m \times 500nm$ as calculated from OOOMMF simulation package. The three components of magnetisation are (a) $M_x$ , (b) $M_y$ and (c) $M_z$ . Double headed red arrows indicate the direction of sensitivity of magnetisation components.(d) Schematically the four domain structure. . . . .	196
6.17	Magnetisation components parallel to the wall were fitted to (a-d) arctan function and (e-h) tanh function. The corresponding positions of the line traces were shown in (i-l). Red arrows in simulated images (i-l) indicate the sensitivity direction of the magnetisation components. . . . .	197
6.18	The parallel component of magnetisation values around the edges of the different elements. . . . .	198
7.1	(a) Schematic of the nanowires geometry. The length of the wire axis has been reduced for this schematic indicated by vertical bars. Ion irradiated pinning sites were indicated by the two lines oriented at $\pm 45^\circ$ and marked as pinning sites 1 and 2 in each nanowire. This structure was used in <b>chapter 5</b> for magnetising experiments. (b) The orientation of the pinning sites has been changed. . . . .	209

# List of Tables

4.1	Domain wall depinning field dependency on the fabrication technique and chiralities of the DWs in 320 and 150 nm wide nanowires. Each experimentally measured field is an average from 4 identical nanowires each of which were measured from separate magnetising cycles. Field values are the mean values of the repeated experiments and error bars represent their standard deviation. The vortex annihilation fields are also inserted inside the table 4.1. Domain wall depinning fields for rectangular (rec.) and sloped (slop.) edge profiles of the nanowires obtained from micromagnetic simulations are also included inside the bottom part of the table 4.1. . . . .	118
5.1	Type of the micromagnetic wall structure on arriving at the pinning site irradiated with different ion doses under the application of magnetic fields. DW depinning fields as a function of irradiation doses for two different types of initial wall structures. Error bars depict the standard deviation for 30+30=60 observations for both initial TDW structure with magnetisation points up and down involving six nanowires irradiated with same line dose. . . . .	156
6.1	Structures and ion irradiation parameters. . . . .	174
6.2	Domain wall widths for two different wall angles. Experimental wall widths were compared to theory [23] for 20 nm thick continuous film. .	194
6.3	Domain wall width of an 180° domain wall measured from magnetisation components in different elements of varying width. In each element the position of the profiles were kept same. . . . .	198

# Acknowledgements

First and foremost, I would like to express my sincere gratitude to my supervisors Dr. Stephen McVitie, Professor John Chapman and Dr. Damien McGrouther for their excellent guidance, support and encouragement. It has been an honor and life-changing experience working with scientists like them. I would like to mention my first supervisor Stephen's contribution to my development not only as a research student but as a person in general. In terms of research, his innovative ideas, on one hand, provided the foundation of this research and, on the other hand, his inspiration, meticulousness, pursuit for perfection greatly enhanced its quality. To me Stephen is more than a supervisor and I am extremely grateful to him. John was busy for administration duties as Dean of Faculty; even then he was so kind to spend time to discuss my results and to provide innovative suggestions. Prior to start my PhD, I did not hear the name of focused ion beam microscopy but prior to leave Glasgow, I was addicted to work with this microscope. This is Damien who has supported me for writing high quality patterns using ion beam microscope. Thanks a lot John and Damien.

Like all other students, I am grateful to Sam who works hard for regularly ensuring all microscopes including CM 20 were kept up and running. Beside this, I was really delighted to discover Sam as a cricket fan of our national team. Long live Sam!!!

Special thanks to Dr. Donald MacLaren who has been a philosopher and mentor from my first year at Glasgow. I am grateful to you Donald, for your care and endless help during all the ups and downs. In the last year of my PhD, I have enjoyed to discuss my results with Professor Robert Stamps. His continued interest in my research progress inspired me a lot. Thanks Bob for coming here in Glasgow from the University of Western Australia.

My special thanks are due to Professors Alan Craven, Dr. Ian MacLaren and Professor Joachim Loos for their time to time inspiration. I would like to express my grateful-

ness to Colin How, Billy Smith and Brian Miller for their technical assistance with microscopes and sample preparation. I am really thankful to Lucy for arranging my flights to attend in conferences and meetings inside and outside UK. Thanks must also go to Dr. Stephen Thoms and the staff at the JWNC who provided assistance with nanofabrication.

I also would like to thank Mr. Strache Thomas HZDR, Institute of Ion Beam Physics and Materials Research, Dresden, Germany for being a nice partner for hunting exchange spring structure behaviour. Special thanks to Professor Jürgen Fassbender, Dr. Jeffrey McCord from Dresden for their collaborative work, comprehensive discussion and hospitality during my stay in Dresden, Germany. Thanks due to Dr. Maciej Oskar Liedke from Dresden and Mr. R. Mattheis from IPTH Jena, Germany for their invaluable help for magnetic film deposition.

Working in the SSP group of the University of Glasgow was the most remarkable and enjoyable chapters of my life. This was possible for all SSP group members past and present who have made my PhD experience thoroughly enjoyable. I really enjoyed the company and all the exciting discussions I had at coffee break with folk like Nils, Paul, Paolo, Omar, Susan, Ricardo, Eleonora, Quang, Maria, Rhet, LiQiu, Julia, Marco and everyone else in the Group I am forgetting to name! For often helping in the Lorentz TEM, computing and nanofabrication Dr. Kerry O'Shea was superb. For all matters related to LaTeXing or entertaining my friend Dr. Duc-The Ngo was always beside me. My office mates Gary, Roberts, Zoe has also been outstanding company and I feel most free with to engage in conversations of any kind with them. Special thanks to Roberts in advance for printing, binding and submitting my thesis in the Graduate School. I was fortunate to have a nice Bangladeshi friend Dr. Shimul Saha. Thanks a lot Shimul vai and vabi for sharing moments of joys and disappointments.

Finally I would like to acknowledge the care, support and guidance of my family specially my mum and brother. Sincere tribute to my late father who would be very happy for my career, although without understanding what I did here in Glasgow. I can never thank my wife Chapa for always being there as my best friend and for helping me follow my dreams at the cost of her excellent job in Bangladesh. I am thankful to my daughter Zahin, just for being so wonderful!



# Declaration

This thesis is a record of the investigation carried out by myself in the Solid State Physics Group of the School of Physics and Astronomy at the University of Glasgow during the period 2007 - 2011. The work described herein is my own with the exception of the materials deposition described in **chapters 5 and 6**. Multilayer films of Cr/Py/Cr were deposited using MBE technique by Dr. Dr. Maciej Oskar Liedke, using the MBE system available in the HZDR, Institute of Ion Beam Physics and Materials Research, Dresden, Germany. Alternatively, these films were also deposited using sputter deposition technique by Mr. R. Mattheis from IPHT Jena, Germany. In **chapter 5** the MOKE investigation was carried out by Mr. Thomas Strache, HZDR, Institute of Ion Beam Physics and Materials Research, Dresden, Germany. Results presented in **chapter 6** is a joint collaboration with HZDR, Institute of Ion Beam Physics and Materials Research, Dresden, Germany. In this chapter alternative unirradiated and irradiated stripe pattern generation including Py deposition were performed by the collaborators. Some of the works in this thesis have been published at the following journal:

1. M.A. Basith, S. McVitie, D. McGrouther, J.N. Chapman, and J.M.R. Weaver, **Direct comparison of domain wall behavior in Permalloy nanowires patterned by electron beam lithography and focused ion beam milling**, J. Appl. Phys. **110** 083904 (2011).

This thesis has not previously been submitted for a higher degree.

# Chapter 1

## Patterned ferromagnetic thin films

### 1.1 Introduction

The advent of nanofabrication technology opens up unique opportunities for patterning magnetic structures with dimensions comparable to or smaller than some fundamental length scales in magnetics, such as domain wall width and exchange interaction length. Patterned magnetic structures exhibit magnetic behaviour which is different from that of a thin continuous film and have applications in the data storage industry where the scaling of bits to few nm dimensions require a detailed understanding and control of magnetic materials at the nanoscale [1]. This PhD project presents an investigation into the controlled behaviour of domain walls in patterned Permalloy nanostructures using advanced fabrication techniques and characterised by the techniques of transmission electron microscopy. A brief outline of this investigation is presented in the next section.

#### 1.1.1 Outline of this thesis

The basic concept of ferromagnetism will be discussed in section 1.2 of **chapter 1** along with a description of the various magnetic energy contributions in section 1.3. The physics of domains and domain walls (DWs) will be presented in section 1.4. Micromagnetic simulations will be carried out throughout this investigation and the theory behind this micromagnetic calculation will be explained in section 1.5. Magnetisation reversal processes will be discussed in section 1.6. Finally an overview of the experimental works will be presented in section 1.7.

Materials deposition and nanofabrication techniques used throughout the thesis will be described in **chapter 2**. In section 2.5 the focused ion beam system (FIB) and ion

## Chapter 1: Patterned ferromagnetic thin films

---

irradiation by FIBing including TEM cross-sectional (x-sectional) sample preparation by FIB milling will be presented. The dynamic simulation package TRIDYN, which will be used to optimise the materials thickness and to quantify the relative atomic concentrations, will be explained in section 2.6.

The experimental techniques used for the present investigations will be illustrated in **chapter 3**. In this chapter emphasise will be given to describe Lorentz microscopy which will be used throughout the thesis for magnetic imaging.

**Chapter 4** will present the results on direct comparison of domain walls behaviour in Py nanowires patterned by EBL and FIB milling techniques. In this chapter, TEM x-sectional images will be presented to compare the edge profile of the nanowires patterned by double cut and single cut approach of FIB milling.

**Chapter 5** will contain the results on the effects of ion irradiation on thin continuous Cr/Py/Cr films in which ion induced pinning sites will be created for trapping DWs.

**Chapter 6** will present the results on magnetisation reversal processes in saturation magnetisation modulated stripes using high resolution Lorentz microscopy.

Finally, the results will be concluded and a brief outlook to possible future experiments will be presented in **chapter 7**.

## 1.2 Basic concept of ferromagnetism

The origin of magnetism lies in the orbital and spin motions of electrons and how the electrons interact with one another. Therefore, magnetic properties of materials are mainly restricted to compounds of transition metals and lanthanides, many of which possess unpaired d or f electrons. In all other materials, electrons are paired in their orbitals with opposite spin and their magnetic effects cancel. These type of materials are known as diamagnetic materials.

The class of materials in which atoms or ions have a net magnetic moment due to unpaired electrons in partially filled orbitals is known as paramagnetic. Without an external magnetic field, magnetic moments are randomly oriented and thus they mutually cancel one another. As a result, like diamagnetism, the net magnetisation in these materials is zero (Fig. 1.1 (a)). However, when an external field is applied the individual magnetic vectors tend to turn into the field direction.

## Chapter 1: Patterned ferromagnetic thin films

Ferromagnetism is a phenomenon by which a material can exhibit a spontaneous magnetisation below a critical temperature named as Curie temperature ( $T_c$ ) and is responsible for most of the magnetic behaviour encountered in everyday life. In ferromagnetic materials, the spontaneous magnetisation varies with temperature, and has a maximum value at 0 K and is reduced to zero at the  $T_c$ . An increase in temperature progressively destroys the spontaneous alignment and eventually at  $T_c$  thermal fluctuations overcome the exchange interaction between the spins and the behaviour becomes paramagnetic. A schematic of the transition from ferromagnetic to paramagnetic is shown in Fig. 1.2.

In a particular class of ferromagnetic materials, instead of a parallel alignment of all the spins, there can be an anti-parallel alignment of unequal spins as shown in Fig. 1.1 (c).

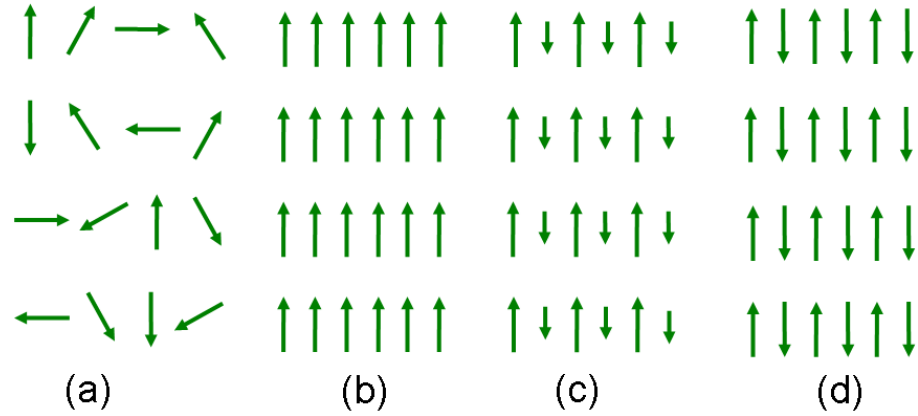


Figure 1.1: Schematic diagram of the alignment of magnetic moment's in (a) paramagnetic, (b) ferromagnetic, (c) ferrimagnetic and (d) antiferromagnetic specimens.

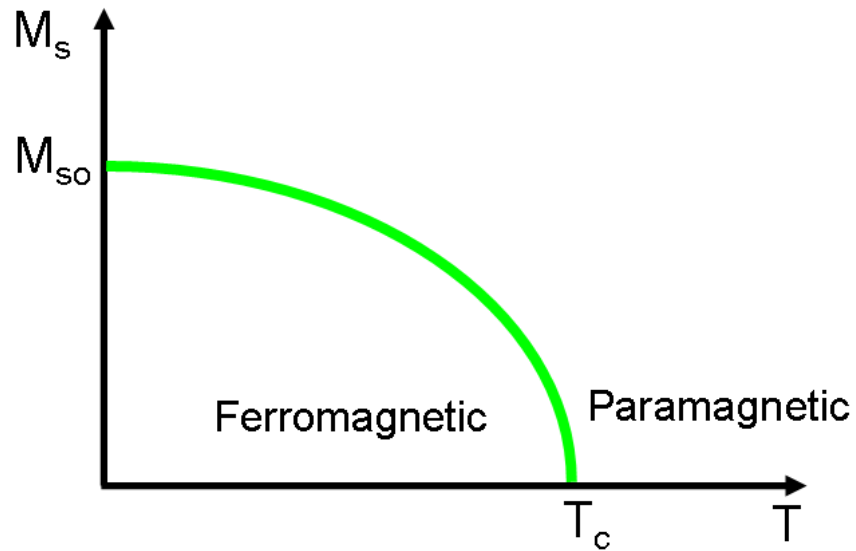


Figure 1.2: Schematically temperature dependence of the saturation magnetisation of the ferromagnetic materials.

This also results in a spontaneous magnetisation, which is known as ferrimagnetism. On the other hand, antiferromagnetic materials exhibit, just as ferromagnetics, spontaneous alignments of moments below a critical temperature. However, the responsible neighbouring atoms in antiferromagnetics are aligned in an antiparallel fashion and hence the net magnetic moment is zero, Fig.1.1 (d).

The mechanism for the appearance of spontaneous magnetisation in ferromagnetic materials was first clarified by P. Weiss in 1907 [2]. Weiss postulated that the magnetic moment of the individual electrons (or atoms) interact with each other and possess a spontaneous magnetisation in the absence of an applied magnetic field. Weiss described the origin of this interaction in the form of an internal molecular field,  $B_m$ , which is proportional to the spontaneous magnetisation.

$$\mathbf{B}_m = \lambda \mathbf{M}, \quad (1.1)$$

where  $\lambda$  is known as the molecular field coefficient. Heisenberg later explained the nature of this field in the quantum mechanical exchange effect [3], and is described by the Heisenberg exchange Hamiltonian,

$$H_{ij} = -2J \mathbf{s}_i \mathbf{s}_j \quad (1.2)$$

where the  $H_{ij}$  is the exchange energy of two interacting electron spins ( $\mathbf{s}_i$  and  $\mathbf{s}_j$ ) and  $J$  is the exchange integral, which is dependent on the material. The exchange energy is discussed in section 1.3 along with other energy terms.

## 1.3 Micromagnetic energy terms

A number of different competitive micromagnetic energy terms contribute to the total energy of a ferromagnetic specimen. A stable state is reached when the micromagnetic energy is locally minimised. These energy terms are discussed in the following sections.

### 1.3.1 Exchange energy

The exchange energy suggests a uniform magnetisation and is at the origin of ferromagnetic order. It is a consequence of the Pauli exclusion principle, which forbids electrons with the same spins from having the same spatial wavefunction. To understand ex-

change energy in terms of the Pauli exclusion principle, let us consider that two atoms with unpaired electrons approach each other. If the spins of these two electrons are antiparallel to each other, the electrons will share a common orbit. Therefore, the electrostatic Coulomb energy is increase. If, however, the spins of these two electrons are parallel, they can not share a common orbit because of the Pauli exclusion principle. They form separate orbits and thus reduce the Coulomb interaction [4]. The exchange energy between two interacting electrons is given by:

$$e_{ex} = -2J_{12}\mathbf{s}_1\mathbf{s}_2 \quad (1.3)$$

where  $J_{12}$  is the exchange integral between the two electrons, which can be negative or positive, and  $\mathbf{s}_1$ ,  $\mathbf{s}_2$  their spin vectors. The total exchange energy for a solid is found by summing the exchange over all electrons which contribute. In most cases this summation need only be carried out for nearest neighbours. Thus, the total exchange energy for the solid from all nearest neighbour spins is:

$$E_{ex} = -2JS^2 \sum_{ij} \cos \psi_{ij} \quad (1.4)$$

where  $S$  is the magnitude of the spin vector,  $\psi_{ij}$  is the angle between spins  $i$  and  $j$ .

The exchange integral for ferromagnetic materials is positive. The negative sign in the expression then implies that a minimum exchange energy results from spins aligned parallel. For antiferromagnetic coupling this exchange integral is negative, giving the result that antiparallel alignment is preferred.

Alternatively, taking into account the three dimensional nature of the crystal and integrating over a finite volume of the material (in simple cubic system), the exchange energy can be written in the form:

$$E_{ex} = A \int_V [(\nabla\alpha_1)^2 + (\nabla\alpha_2)^2 + (\nabla\alpha_3)^2] dV \quad (1.5)$$

Here  $\alpha_1$ ,  $\alpha_2$ ,  $\alpha_3$  are the direction cosines with respect to the crystal axes, and  $A$  is the exchange stiffness constant of the material, which is given by (for a cubic system):

$$A = \frac{kJS^2}{a} \quad (1.6)$$

with  $k$  a structure-dependent constant (1 for simple cubic, 2 for body centred cubic and 4 for face-centred cubic crystals) and  $a$  the lattice parameter. The exchange stiffness constant  $A$  for Permalloy, the material used for the present investigation is  $13 \times 10^{-12} \text{ J/m}$  [5].

### 1.3.2 Magnetostatic energy

Inside a magnetic specimen, the magnetic induction  $\mathbf{B}$  is expressed as

$$\mathbf{B} = \mu_0(\mathbf{H} + \mathbf{M}) \quad (1.7)$$

where  $\mu_0$  is the permeability of free space,  $\mathbf{H}$  is the magnetic field strength and  $\mathbf{M}$  is the magnetisation of the uniformly magnetised specimen. Using this relationship, the divergence of  $\mathbf{M}$  can be expressed as

$$\nabla \cdot \mathbf{M} = \frac{\nabla \cdot \mathbf{B}}{\mu_0} - \nabla \cdot \mathbf{H} \quad (1.8)$$

From Maxwell's equation,

$$\nabla \cdot \mathbf{B} = 0 \quad (1.9)$$

Therefore,

$$\nabla \cdot \mathbf{H} = -\nabla \cdot \mathbf{M} \quad (1.10)$$

This non zero divergence of magnetisation at the sample surface and also from within volume of the material give rise to field  $\mathbf{H}$  that ensures the continuity of lines of  $\mathbf{B}$ . This field is known as the demagnetising field or magnetostatic field or stray field  $\mathbf{H}_d$ . Therefore, we can write

$$\nabla \cdot \mathbf{H}_d = -\nabla \cdot \mathbf{M} \quad (1.11)$$

The energy associated with this stray field  $\mathbf{H}_d$  is given by:

$$E_d = -\frac{\mu_0}{2} \int_V \mathbf{M} \cdot \mathbf{H}_d dV. \quad (1.12)$$

$E_d$  can be minimised by reducing the amount of magnetic charge that builds up at the edges, surfaces and volume charges within the material.

### 1.3.3 Anisotropy energy

Magnetic anisotropy is related to the variations in the magnetic energy with the spatial orientation of the magnetisation. A variety of anisotropy contributions are possible such as intrinsic magnetocrystalline anisotropy, the magnetoelastic anisotropy, surface anisotropy, field induced anisotropy etc and originate microscopically from the spin-orbit coupling. From the perspective of the present thesis two main types of anisotropy: magnetocrystalline and shape anisotropy are described in the following sections.

#### Magnetocrystalline anisotropy

Weiss [2] suggested that in a demagnetised single crystal the domain magnetisations could lie in all directions. This would imply that measured magnetisation curves for the crystal would be indistinguishable whatever the direction of the applied field relative to the crystal axes. But experimental magnetisation curves revealed that much smaller applied fields are required to induce a given magnetisation in some directions of some materials, termed the easy directions, than in others. A deviation of the magnetisation from an easy axis leads to an increase in the anisotropy energy, which has its maximum along a "hard axis". In the case of cubic anisotropy, the energy,  $E_k$  can be described by a series expansion:

$$E_k = \int_V [K_1(\alpha_1^2\alpha_2^2 + \alpha_2^2\alpha_3^2 + \alpha_3^2\alpha_1^2) + K_2\alpha_3^2\alpha_1^2] dV, \quad (1.13)$$

where  $\alpha_1$ ,  $\alpha_2$ ,  $\alpha_3$  are the direction cosines of the magnetisation along 1, 2, 3, the respective crystallographic axes and  $K_1$ ,  $K_2$  are first and second magnetocrystalline anisotropic constants, respectively, for the particular material. For example, for Ni,  $K_1 = -0.45 \times 10^4 J/m^3$  so that the easy axes are along the body diagonals (111), while for Fe,  $K_1 = 4.8 \times 10^4 J/m^3$  and the easy axes are along along (100) [4]. These descriptions are only valid for single crystal materials. The material system used for the present investigation is the polycrystalline Permalloy ( $Ni_{80}Fe_{20}$ ). In the case of the polycrystalline material, there is no overall preferred axis for magnetisation (unless field induced anisotropy is created by certain treatment procedures mentioned in the next section) as the crystallites are randomly oriented with respect to each other. Instead, the anisotropy direction varies from crystallite to crystallite, resulting in local



easy axes. A consequence of this variation is the formation of the magnetisation ripple which will be observed in the Fresnel images presented in **chapters 5 and 6**. The magnetisation ripple arise due to a deviation of the magnetisation from uniformity and run perpendicular to the average direction of the magnetisation [6].

### Shape anisotropy

The magnetic shape anisotropy is particularly important to the magnetic configurations of the thin films and objects with reduced dimensions. It refers to the magnetostatic effects of the system rather than the overlap of electron orbitals. When a magnetic specimen is uniformly magnetised, the magnetic charges or *free poles* are present at the surface of the specimen. This surface charge distribution is itself a source of a magnetic field, called the demagnetising field.

Figure 1.3 illustrates the magnetostatic dipole interactions in an ellipsoid specimen magnetised along the long and short axes. It can be seen that free poles are separated by relatively long and short distances in an ellipsoid. The long and short distance correspond to the two directions of magnetisation considered in the Fig. 1.3(a) and (b). The demagnetising field will be less if the magnetisation is along the long axis rather than the short axes. This produces an easy axis of magnetisation along the long axis. A sphere, on the other hand, has no shape anisotropy.

Inside a specimen with ellipsoid shape (Fig. 1.3), the demagnetising field,  $H_d$ , is aligned oppositely to the direction of the magnetisation and the shape anisotropy energy will be given by:

$$E_k = \int_V K_{eff} \sin^2 \theta dV. \quad (1.14)$$

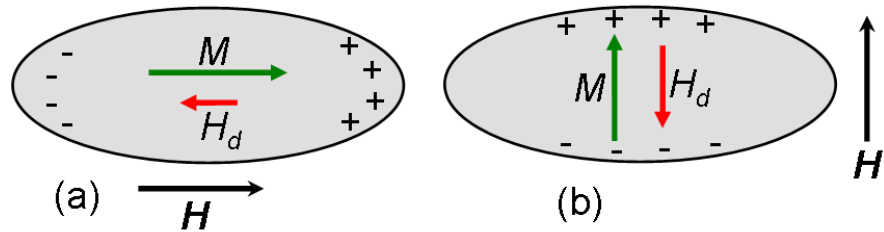


Figure 1.3: Schematically the demagnetising field that arises depending on whether the ellipsoid is magnetised along the (a) long or (b) short axis. (a) has lower demagnetising field than (b) and was indicated by the relative sizes of the red arrow sign.

Here,

$$K_{eff} = \frac{(N_b - N_a)M^2}{2}, \quad (1.15)$$

where  $\theta$  is the angle between the long axis and the magnetisation direction,  $M$  is the magnetisation, and  $N_a$ ,  $N_b$  are demagnetising factors in the long and the short axes, respectively.

Beside magnetocrystalline and shape anisotropy, induced anisotropy can be created by certain treatment procedures e.g. magnetic annealing, in which an external magnetic field is applied during the heat treatment [7]. Another form of field induced anisotropy is possible to create in thin films, particularly in Py film [8]. In this case, the Py film is deposited on a substrate by evaporation in vacuum with a magnetic field applied in the plane of the substrate. As a result, the direction of the field is subsequently found to be an easy direction for the spontaneous magnetisation. In the present investigation, such field induced anisotropy will be employed during the deposition of the Py film by sputter deposition technique and results will be presented in **chapters 5 and 6**.

### 1.3.4 Zeeman energy

When the specimen is placed in an external field, the magnetic moments within the specimen will tend to align parallel to the applied field. The Zeeman energy takes into account the orientation of the magnetisation with respect to the applied field and is given by :

$$E_z = -\mu_0 \int_V \mathbf{M} \cdot \mathbf{H} dV \quad (1.16)$$

where  $\mu_0$  is the permeability of free space.

### 1.3.5 Total energy

The total energy of a ferromagnetic specimen is the sum of the individual energy terms which were described in the previous sections

$$E_{total} = E_{ex} + E_k + E_z + E_d \quad (1.17)$$

and the magnetic configuration (domain structure discussed in the next section) is a direct consequence of its local or global minimisation.

## 1.4 Magnetic domains and domain walls

### 1.4.1 Magnetic domains

In ferromagnetic materials, the spins of unfilled d-bands spontaneously align parallel to each other below  $T_c$ , i.e. they align within small domains without the presence of an external magnetic field. Now the question is that, in the virgin state, why is the spontaneous division into many individual domains apparently preferred to one single domain? The theory behind the formation of this domain structure has been given by Landau and Lifshitz [9] who showed that the sub-division of a specimen into domains could result in a considerable reduction in the magnetostatic energy from that of the saturation condition, albeit at the cost of an increase in exchange energy. The reduction of magnetostatic energy that causes an increase in exchange energy is due to the deviation of spins from a parallel alignment. Let us assume for a moment that all electron spins in a specimen are indeed aligned in parallel, Fig. 1.4(a). As a consequence, magnetic charges (north and south poles) would be created on opposite

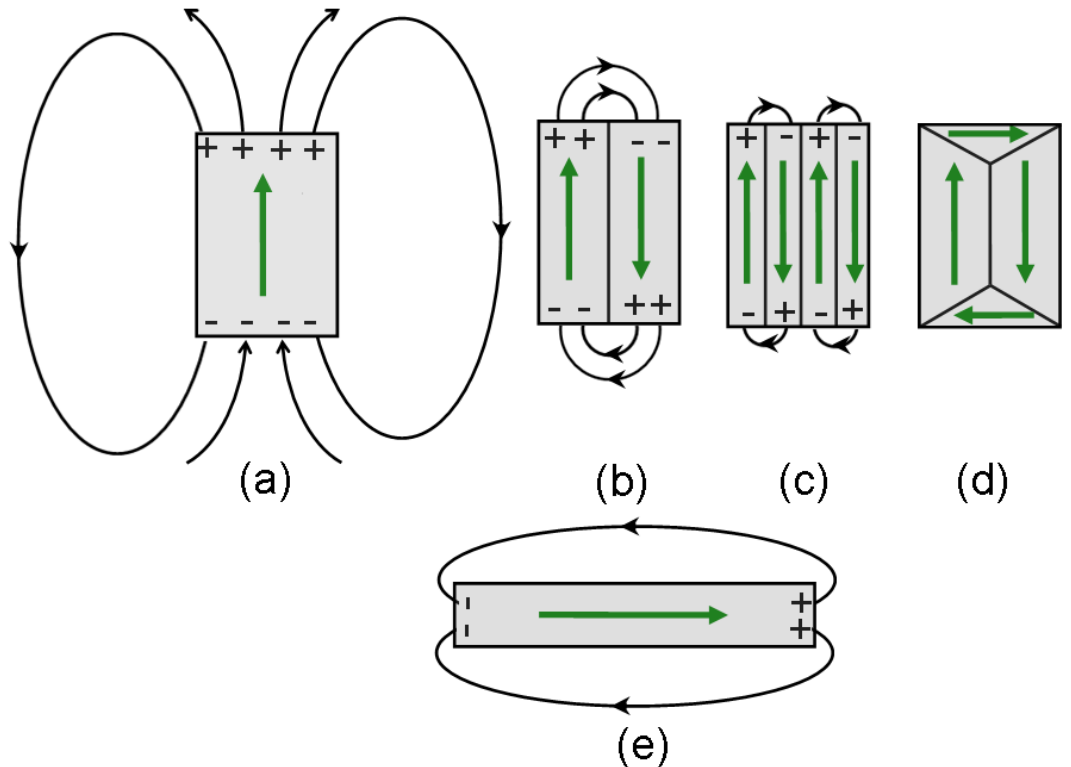


Figure 1.4: Illustration of the magnetostatic field generated in (a) the single domain state, (b), (c) multidomain states and quenching of the magnetostatic field by the formation of (d) a flux-closure state. (e) a single domain state induced by shape anisotropy.

ends of the specimen. This would be energetically unfavourable because it would be the source of a large external magnetic field (magnetostatic field). The magnetostatic energy of this field can be approximately halved if the specimen contains two domains that are magnetised in opposite directions. This way, opposite charges (north and south poles) are closer together and the external magnetic field is confined to a smaller area Fig. 1.4(b). Further divisions into still smaller and smaller domains with concomitant reductions in magnetostatic energies lead, however, eventually to an optimal domain size (Figs. 1.4(c,d)). Notably, Fig. 1.4 (a) is a possible preferred state for a material with strong uniaxial anisotropy in the vertical direction as shown. Depending on the material parameters, sub-division into smaller domains may occur, Figs. 1.4(b) and (c). Figure 1.4 (d) shows a structure for a material with cubic anisotropy or weak anisotropy. The sub-division of the material, Fig. 1.4(a) into domains causes a reduction of magnetostatic energy at the cost of an increase in exchange energy due to the deviation of spins from a parallel alignment, as shown in Fig. 1.4(d).

In Fig. 1.4(e), the shape anisotropy of the element aligns the magnetisation parallel to the long axis and is usually the lowest energy configuration for long magnetic wires in the absence of an external field. It may be noted here that, at zero applied magnetic field, this domain structure depends considerably on the material geometry and properties in addition to the sample history and temperature. When an external magnetic field is introduced, the magnetic state that changes irreversibly by domain formation and domain wall movement is responsible for the material exhibiting hysteresis, as will be discussed in section 1.6.

### 1.4.2 Magnetic domain walls

The region separating two domains in which the magnetisation direction is continuously changing is referred to as a domain wall. In ferromagnetic materials, a domain wall between two domains with opposite magnetisation directions can be a Bloch wall (named after Felix Bloch) or Néel wall (named after Louis Néel). In the Néel wall, magnetic moments gradually rotate in the plane of the film whereas in the Bloch wall, the magnetic moment rotation is out-of-plane. A Bloch wall (Fig. 1.5(a)) generates magnetic charge at the surface of the film and thus has associated stray field energy cost. Néel realised that Bloch's description of a domain wall is extremely energetically

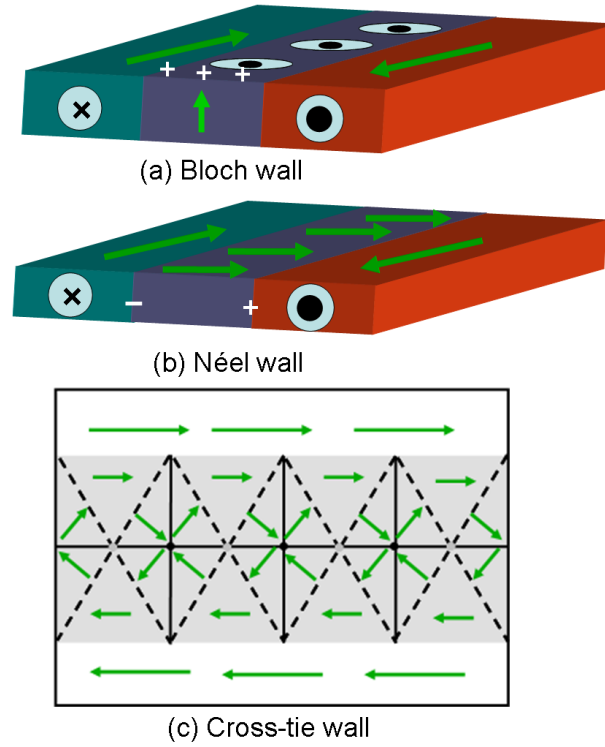


Figure 1.5: Plan view schematic illustrations of (a) Bloch-type wall, (b) Néel-type wall and (c) cross-tie wall.

costly in thin films as soon as film thickness and domain wall width are comparable. Therefore, below a critical film thickness ( $< 30$  nm [10]) Néel type walls are more favourable (Fig.1.5 (b)). Since, within Néel walls, the magnetisation rotates about a plane parallel to the plane of the film, thus the magnetic charges form at the sides of the wall. Therefore, the corresponding magnetostatic energy is due to volume charges appearing inside the film and its contribution to the domain wall energy density decreases with decreasing film thickness. Néel walls have charges from divergence of  $\mathbf{M}$  as was introduced into the magnetostatic energy section. At intermediate film thicknesses of between 30 and 90 nm for Py films, a combination of Bloch and Néel wall types can form, known as a cross-tie wall, (Fig. 1.5(c)). In this schematic, the solid and dashed black lines represent  $90^\circ$  and  $45^\circ$  Néel walls, respectively and the circles represent Bloch lines where the magnetisation is out of plane. Notably, around the circles the rotation of magnetisation is continuous. Black circles are known as cross Bloch lines (cross-ties) and white circles represent circular Bloch lines (vortex cores). In the present investigation, Py film thickness below 20 nm was investigated for which the favoured wall type is obviously Néel walls. A comprehensive overview on domain walls was given in the textbook by Hubert and Schäfer [11].

### 1.4.3 Domain walls width

In their text book 'Magnetic Domains, The Analysis of Magnetic Microstructures', Hubert and Schäfer [11] state that there cannot exist "a unique definition of a domain wall width", since "domain walls form a continuous transition between two domains" (p. 219 in [11]). Therefore, the general difficulty in measuring a domain wall width is obvious. Domain walls in Py films of the thickness studied in the present investigation are expected from theory [12, 13] to be one dimensional symmetric Néel walls. The tail of the Néel type wall is more extended in the unconstrained film than that of the constrained region. Therefore, for measuring wall width from TEM micrographs, the fitting of the magnetic induction or magnetisation profile in an arctangent function for the unconstrained region and a hyperbolic tangent function for the constrained region is a convenient and reasonable approximation [12].

For a long straight one-dimensional DW with no variation of magnetisation throughout the thickness of the thin film, the magnetisation parallel to the wall is approximated by [12, 13]

$$M_y(x) = \frac{\pi}{2} \times M_s \arctan\left(\frac{x}{A}\right) \quad (1.18)$$

$$M_y(x) = M_s \tanh\left(\frac{x}{A}\right) \quad (1.19)$$

where,  $x$  as the coordinate normal to the wall and  $y$  as the coordinate parallel to the domain wall,  $M_s$  is the saturation magnetisation and  $A$  is the domain wall parameter. The width of the domain walls is determined as the full width at half maximum (FWHM) of the first-order derivative of the fitted magnetisation profile functions discussed above. This gives a width of  $2A$  for arctan function and  $1.76A$  for tanh function [12, 13]. Figure 1.6 shows an example of an arctangent and hyperbolic tangent functions.

For Néel type of DW, the in-plane component of magnetisation  $M_x$ , perpendicular to the wall is given by,

$$M_x(y) = \sqrt{1 - M_y^2} \quad (1.20)$$

In **chapter 6** (section 6.6), the domain wall width will be measured and compared for a continuous thin film and restricted film of Py.

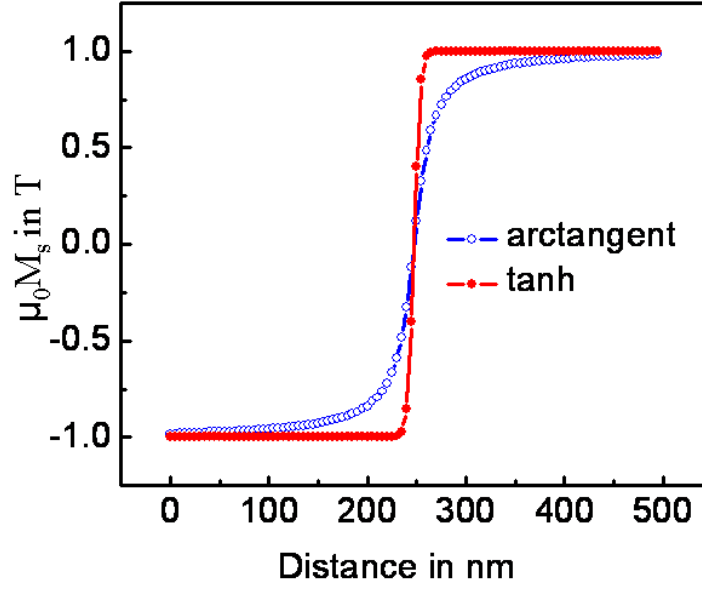


Figure 1.6: Example of an arctangent and hyperbolic tangent functions.

#### 1.4.4 Domain wall spin structures in nanowires

In a domain wall, the spins gradually change direction going from one domain to the other. In soft magnetic structures like Py nanowires or nanostripes, the spin direction is restricted parallel to the wire axis because of the large shape anisotropy. Therefore, the spin structure of domain walls in these nanowires depends on the element width and

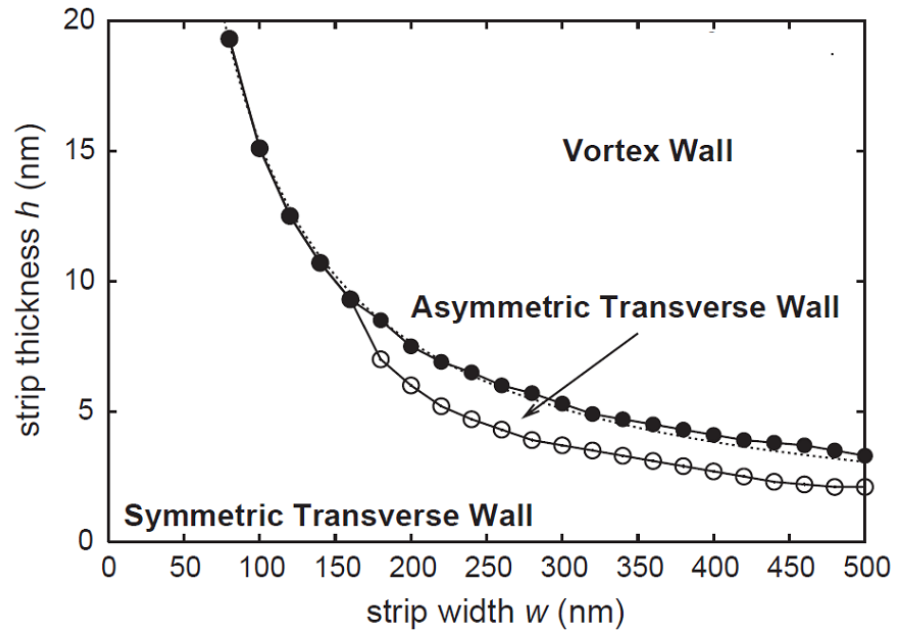


Figure 1.7: A phase diagram of domain wall spin structures for straight nanowires of a given width and thickness. Adapted from reference [14].

thickness. Nakatani et al. [14] have established a refined phase diagram by numerical calculations and found different domain wall spin configurations which are energetically favourable for certain element widths and thicknesses. Figure 1.8 illustrates the wall types introduced by the phase diagram in Fig. 1.7. These magnetic configurations are characterised by their axial magnetisation alignment, which can be either head-to-head or tail-to-tail depending on if the magnetisations are pointing towards or away from the wall, respectively. The vortex domain wall (Fig. 1.8(a,b)) consists of three distinct wall sections where the magnetisation rotates about a central vortex core, an out-of-plane magnetisation component. A vortex wall is also identified by the vortex chirality, which can be clockwise (Fig. 1.8(a)) or counter clockwise (Fig. 1.8(b)) depending on the sense of spin rotation about the vortex core. The transverse wall comprises, to a first approximation, two  $90^\circ$  walls with the spin in the central domain perpendicular (either magnetisation pointing up or down) to the wire axis, (Figs. 1.8(c,d)). Besides these two basic types, an asymmetric transverse wall (Figs. 1.8(e-h)) is energetically favourable for certain element widths and thicknesses. These wall structures will be realised using Lorentz microscopy experiments in the patterned Py nanowires and results will be presented in **chapters 4 and 5**.

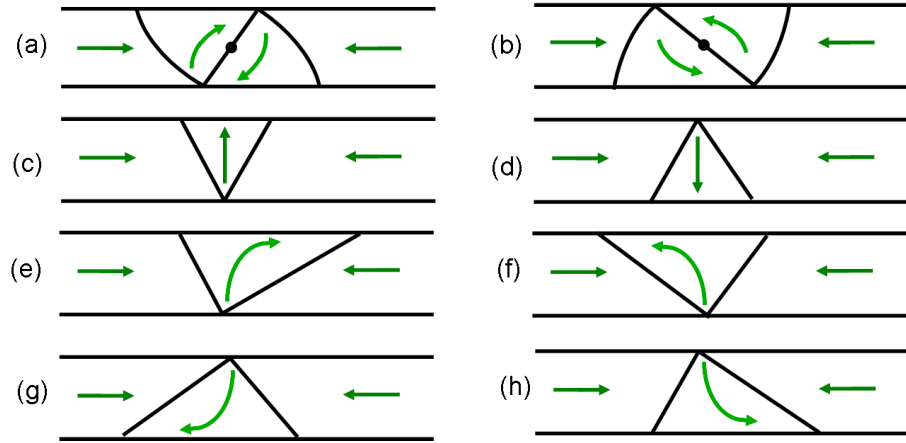


Figure 1.8: Schematic illustration of (a,b) clockwise and counterclockwise vortex DWs, respectively; (c,d) transverse DW with central spin up and down, respectively; and (e-h) asymmetric transverse domain walls.



## 1.5 Micromagnetic simulation

To assist the interpretation of experimental observations like magnetic image contrast realised in Lorentz microscopy and also to compare the experimental results, micromagnetic simulations were carried out using the freely available OOMMF package developed by National Institute of Standard and Technology (NIST), USA [15]. The field of micromagnetics started in 1935 with a paper by Landau and Lifshitz [9] on the structure of a wall between two anti-parallel domains and later on several works of Brown in 1940 [16]. Recently, micromagnetic simulations based on Landau-Lifshitz and Landau-Lifshitz-Gilbert equations of motion has become an important tool to characterise the magnetic behaviour of different materials like recording media, patterned magnetic elements and nanocrystalline permanent magnets. To determine the magnetisation distribution that minimises the total energy of the system, Landau-Lifshitz (LL) equation of motion is given by,

$$\frac{d\mathbf{M}}{dt} = -\gamma\mathbf{M} \times \mathbf{H}_{\text{eff}} - \frac{\lambda}{M_s}\mathbf{M} \times (\mathbf{M} \times \mathbf{H}_{\text{eff}}) \quad (1.21)$$

where  $dt$  is the time,  $\gamma$  is the electron gyromagnetic ratio,  $\lambda$  is a damping parameter,  $\mathbf{M}$  is the magnetisation vector,  $M_s$  is the saturation magnetisation and  $\mathbf{H}_{\text{eff}}$  is the effective field. The effective field  $\mathbf{H}_{\text{eff}}$  interacting on  $\mathbf{M}$  is obtained by differentiating the total energy with respect to the magnetisation,

$$\mathbf{H}_{\text{eff}} = -\frac{1}{\mu_0} \frac{dE_{\text{tot}}}{d\mathbf{M}} \quad (1.22)$$

which takes into account contributions from all involved energy terms  $E_{\text{tot}}$  (exchange, anisotropy, Zeeman and demagnetising energy) which was described in the previous sections.

Gilbert in 1955 derived the micromagnetic equation of motion [17] using a different approach. Gilbert proposed a different damping parameter, giving the Landau-Lifshitz-Gilbert (LLG) equation.

$$\frac{d\mathbf{M}}{dt} = -\gamma^*\mathbf{M} \times \mathbf{H}_{\text{eff}} - \frac{\alpha}{M_s}\mathbf{M} \times \frac{d\mathbf{M}}{dt} \quad (1.23)$$

where  $\alpha$  is the Gilbert damping constant;  $\gamma^*$  is described later on.

## Chapter 1: Patterned ferromagnetic thin films

The OOMMF code calculates micromagnetism by solving the LLG equation 1.23. The first term of the LLG equation describes the precession of magnetisation vector  $\mathbf{M}$  around the effective field,  $\mathbf{H}_{\text{eff}}$ . The second term relates to the damping contribution i.e. the dissipation of energy as illustrated in Fig. 1.9. The damping term leads to the convergence of the precession cone towards the effective field. The higher the value of the Gilbert damping parameter the faster the convergence of  $\mathbf{M}$  towards  $\mathbf{H}_{\text{eff}}$ .

With each spin iteration, the equation is re-evaluated until equilibrium is reached. Equilibrium may be specified either by setting a minimum value of the torque,  $\frac{d\mathbf{M}}{dt}$  (typically set to 0.01 deg/ns), or by imposing a limit on the number of iterations or simulation time. This process is repeated with each step-wise increase of the applied field.

The two equations, 1.21 and 1.23 are mathematically equivalent, if the later equation is rewritten in the following form,

$$\frac{d\mathbf{M}}{dt} = -\frac{\gamma^*}{(1 + \alpha^2)} \mathbf{M} \times \mathbf{H}_{\text{eff}} - \gamma^* \frac{\alpha}{(1 + \alpha^2) M_s} \mathbf{M} \times (\mathbf{M} \times \mathbf{H}_{\text{eff}}) \quad (1.24)$$

In fact, equations 1.21 and 1.23 are identical with the following choices of the parameters  $\gamma$  and  $\lambda$  in equation 1.21:

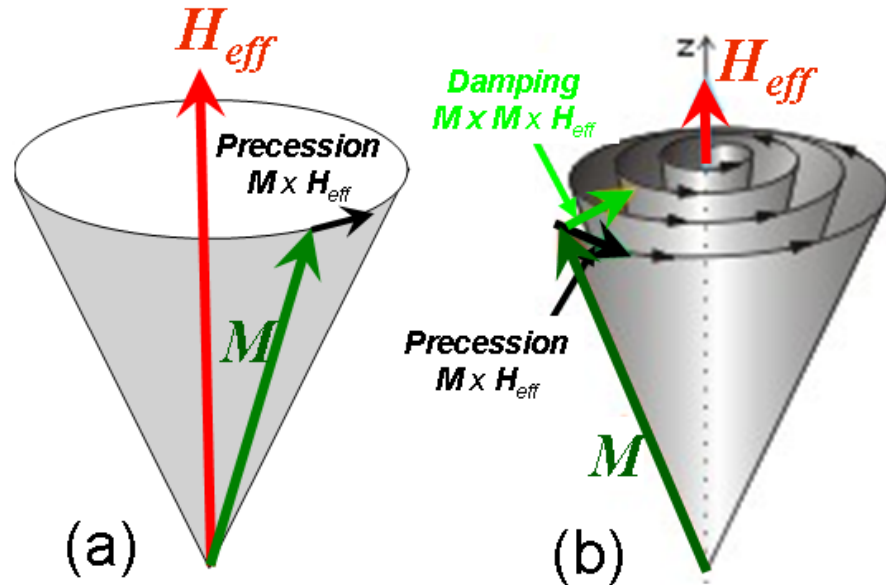


Figure 1.9: Precession of the magnetisation vector  $\mathbf{M}$  around the effective field : (a) precessional motion without damping, (b) gyro-precessional motion with damping.

$$\gamma = \frac{\gamma^*}{(1 + \alpha^2)} \quad (1.25)$$

and

$$\lambda = \frac{\gamma^* \alpha}{(1 + \alpha^2)}. \quad (1.26)$$

The question now arises concerning the physical difference between the two equations of motion, 1.21 and 1.23. For small damping, there is usually no significant difference and in the limit of zero damping ( $\lambda, \alpha \rightarrow 0$ ) the LL and LLG equations are equivalent. In other words, in the case of large damping, i.e.  $\lambda \rightarrow \infty$ , the LL equation is given by  $\frac{d\mathbf{M}}{dt} \rightarrow \infty$ . In contrast, when  $\alpha \rightarrow \infty$ , the LLG equation is given by  $\frac{d\mathbf{M}}{dt} \rightarrow 0$ . Therefore, in the case of large damping, LLG equation suggests a slow loss of energy and slow approach to the low-energy state, whereas LL equation predicts a rapid loss of energy where the system quickly reaches its low-energy state. This ultimately suggest that the Gilbert type of damping gives a physically more realistic description. However, it was reported earlier that the damping parameter is material specific [18]. The material used for the present investigation is Py and the measured damping parameter  $\alpha$  for Py estimates between 0.013 and 0.03 [19–21]. In this thesis, a damping parameter of 0.5 was used throughout to speed up the computations. In papers [22,23] for example, a value of  $\alpha = 0.5$  was also used and the simulated results were in good qualitative agreement with their experimental observations. The dynamics of domain wall motion in permalloy nanowires have been simulated [24] using LLG equation of motion. The domain wall speed was calculated by varying the Gilbert damping parameter  $\alpha$  and nanowire width. The maximum domain wall speed was found to be independent of  $\alpha$  and dependent on the wire width.

In order to bridge the gap between theoretical predictions and experimental observations, an ideal simulation of a nanomagnetic specimen would take into account every atomic moment in the specimen. Realistically, however, in spite of the rapid advances in computer capabilities in recent years, this is still not achievable due to the limitations on available computing power and time. A more realistic approach may be the dividing up of the nanomagnetic specimen into a set of discrete 3-dimensional cells of uniform magnetisation. In that case, the cell size is an important parameter in determining the outcome of the simulation and is normally of the order of the ferromagnetic exchange-

interaction length,  $L_{ex}$ , of the material in the specimen (e.g.  $L_{ex} = \sqrt{\frac{A}{2\mu_0 M_s^2}} \approx 5.3$  nm for Py using the standard value for exchange stiffness constant  $A = 13 \times 10^{-12}$  J/m and  $M_s = 860$  kA/m). In general, a cell size close to the ferromagnetic exchange-interaction length provides sensible results whilst keeping the simulation time to a convenient length. The simulations performed throughout this thesis used a cell size of 5 nm which is close to the exchange length for Py as was already mentioned.

Another issues related to simulations to be considered are that the use of the square cells to define the structure form geometrically perfect elements with straight edges which do not contain any structural roughness. In reality, element edges contain structural roughness produced by the fabrication processes and ultimately affect the magnetic properties (this will be illustrated in **chapter 4**). Such defects are difficult to simulate accurately and play a role when the outcome of the simulations is compared with experimental observations. Moreover, in reality, elements produced by the fabrication process will not have perfectly defined edges rather edges of the elements are either tapered or sloped as was observed in the present investigation (refer to **chapter 4**). Using the present version of OOMMF it is possible to design multi-layered structure and therefore, elements with non ideal edge structure were simulated and results will be presented in **chapter 4**. Simulations also neglect thermal effects as simulations are performed at 0 K whereas experiments were performed at room temperature which can vary the magnetisation distributions. Therefore, the field required to depin a domain wall from the anti-notch, as described in **chapter 4** for example is larger in a simulation than in an experiment performed at room temperature. This will be reported in **chapter 4**.

## 1.6 Magnetisation reversal

### 1.6.1 Hysteresis

The magnetisation of a ferromagnet depends not only on the external magnetic field experienced at some point in time, but also on the field history, resulting in a double-valued magnetisation vs field curves referred to as hysteresis loops [25, 26]. The important features of hysteresis curves are when specimen is taken through a cycle of magnetisation (to near -saturation in opposite directions) the changes which occur are

mixture of reversible and irreversible steps and involve a loss of energy - the hysteresis loss [27].

In order to understand the hysteresis curve, initially we consider a ferromagnetic specimen that has been deposited in the absence of an applied magnetic field. In this state, the material is likely to consist of magnetic domains arranged in such a fashion that the net magnetisation is close to zero, point 'o' in Fig. 1.10. If the external field strength is increased, then the magnetisation  $M$  rises at first slowly and then more rapidly. Finally,  $M$  levels off and reaches a constant value, called the saturation magnetisation,  $M_s$ , (Fig. 1.10 point (a)). When the applied field is reduced to zero, the magnetisation relaxes to what is known as remanence or the remanent magnetisation,  $M_r$ , point 'b' in Fig. 1.10. It is this retained magnetisation that is utilized in permanent magnets. The remanent magnetisation can be removed by reversing the magnetic field strength to a value  $H_c$ , called the coercive field, (Fig. 1.10 point (c)). Materials with low coercivity are called soft; those with high coercivity are called hard magnetic materials. In a special high stability magnet  $SmCo_5$  the coercivity is of the order of 1T. Soft material like Py has a typical coercivity of 0.04 mT [28].

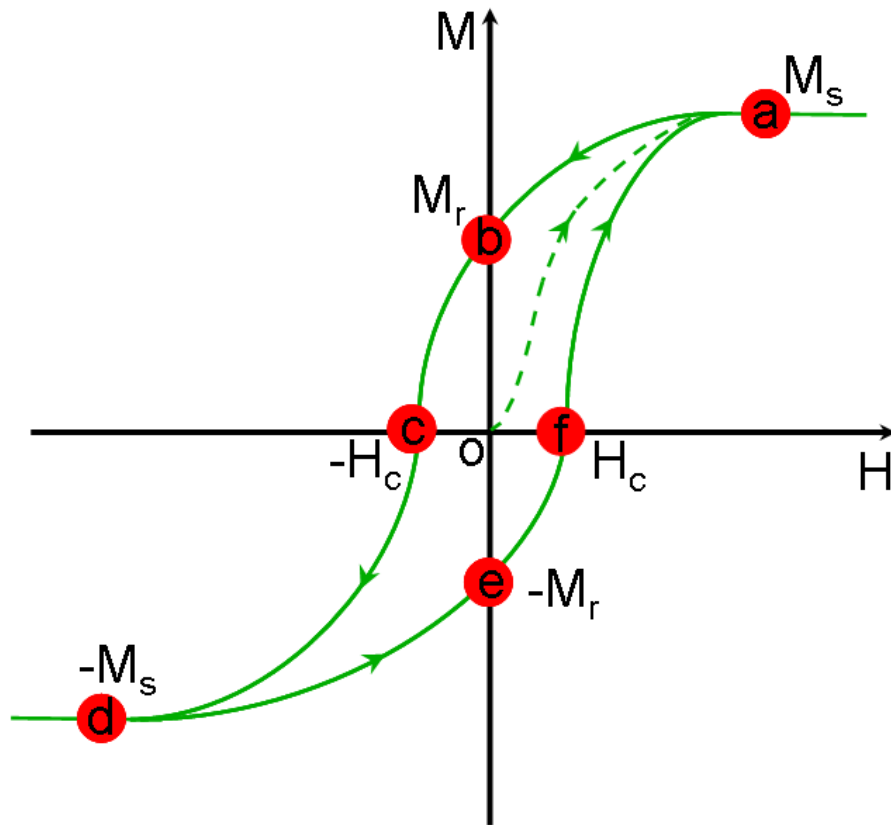


Figure 1.10: Schematically a typical hysteresis loop for a ferromagnetic specimen.

The material will saturate in the opposite direction for a further increment of this negative field, (Fig. 1.10 point (d)). By removing the field, the material will again reach remanence (point e in Fig. 1.10) before being demagnetised by the application of another positive field, (Fig. 1.10 point f). Therefore, the M-H plot produced as the field is swept in the positive and negative directions is known as a hysteresis loop.

### **1.6.2 Reversal processes in a rectangular thin film element**

The process of magnetising a specimen to saturation will evidently consist of converting it to a single domain, in which the magnetisation has a direction parallel to the applied field. This may happen in two ways: (a) domain wall movement; (b) rotation of the magnetisation within a domain. To describe the reversal mechanism, let us consider a rectangular thin film element exhibiting initial flux closure (Fig. 1.11(a)) at zero applied magnetic field. If magnetic field is applied in a direction parallel to the long axis (easy axis) of the rectangular element, domains oriented favourably with respect to the field will grow by the displacement of the DWs at the expense of those unfavourably oriented domains as shown in Fig. 1.11(b). Upon the application of small amount of magnetic field, DWs move through small distances and return to their original positions on removal of the field. These are termed reversal displacement and correspond to the initial curved part of the magnetisation curve. As the applied field is increase, however, DWs annihilation occur and the domain unfavourably aligned with the field is removed, Fig. 1.11(c). Here again it is notable that for larger applied field, the DWs are found to jump discontinuously through larger distances and do not return to their original position on removal of the field. This behaviour indicates some form of barriers to DW movement, which the DW can overcome when it has acquired sufficient magnetic energy. Therefore, in larger applied fields, the motion becomes irreversible (in example given)-the walls do not return to their original position when the field is removed. When all the unfavourable domains are eliminated, rotation of the magnetisation in the remaining domains begins. Finally, a single domain state is reached, Fig. 1.11(d), when the magnetisation reaches alignment with the applied field. If the field is aligned at  $90^\circ$  (for example) to the easy axis, however, there would be no reason for one type of domain to grow rather than another. Magnetisation would then have to proceed by rotation only, gradually coming into alignment as the field is increased. Magnetisation reversal

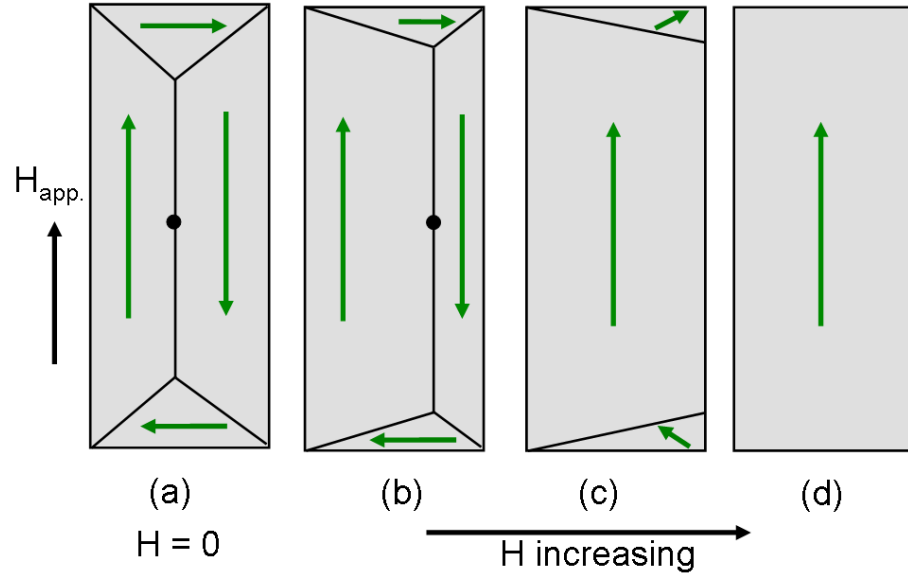


Figure 1.11: Schematic illustration of reversal processes in a rectangular thin film element during field application.

by coherent (i.e. it remains uniform even while it is rotating) rotation was first proposed by Stoner and Wohlfarth [29] and usually occurs in small single domain particles with uniaxial anisotropy where the introduction of domain walls would cost more energy than spin rotation. It may also be the preferred method of reversal in small elements without any uniaxial anisotropy but with significant shape anisotropy such as an ellipse. The present thesis deals throughout with the precise understanding and controlling of magnetisation reversal processes in the patterned ferromagnetic nanostructures in which shape anisotropy is dominating. In the next section of this chapter motivation behind this PhD project is described along with a description of the methodology of the experimental investigation.

## 1.7 Motivation of this PhD project

It is worth mentioning that recent advancement in nanofabrication technology opens fascinating opportunity for engineering innovative magnetic materials [1, 2, 30–32] and pushes the dimension of ferromagnetic structure into nanoscale. At the nanoscale, the structure of magnetic domain walls in ferromagnetic nanowires is governed by the geometry of the material in addition to the intrinsic material properties. Therefore, it is possible to appropriately engineer the geometry to tailor the domain wall spin structure and switching behaviour of the patterned nanowires, which is particularly true in the

case of soft magnetic materials like Py where the effect of magnetocrystalline anisotropy is small. Magnetic DWs in these patterned nanowires can also be manipulated using external magnetic fields [6, 22, 23, 33–38, 40–42] and spin polarised currents [43–47]. A precise understanding and control of magnetic DWs in the patterned ferromagnetic nanostructures is of recent fundamental scientific interest. They have also attracted increasing attention due to their promising applicability in future spintronic devices such as racetrack memory [48–50] and DW logic [51, 52] where the information will be conveyed with the aid of the controlled movement of DWs along the patterned nanowires. The motivation along with a brief overview of this dissertation is presented in the following sections.

### 1.7.1 Nanofabrication using alternative techniques

As a part of the upsurge in global research interest in patterned ferromagnetic nanostructures, using magnetic imaging techniques and micromagnetic simulations Glasgow researchers have contributed useful information for a greater understanding of the fundamental properties and behaviour of DWs in the patterned Permalloy ( $Ni_{80}Fe_{20}$ ) nanowires [6, 15, 22, 23, 40, 54]. Key questions of these investigations were - how can DWs in the patterned nanowires be reproducibly nucleated [6, 15, 22, 23]? How does the pinning potential of geometrical features such as notch/anti-notch [23, 40, 54] interact with DWs to identify precisely the location of the DWs? Another important consideration which was not investigated comprehensively is the influence of nanofabrication techniques on the reproducible nucleation and propagation of DWs in the fabricated nanowires. It is noteworthy that to ensure the reliable operation of the proposed ferromagnetic devices by reducing the performance variability, high quality nanofabrication is extremely important. Previous reports [55–59] indicate that the structural roughness at the edges of the nanowires produced by fabrication processes affect the magnetic properties of the nanostructures. Therefore, the initial interest of the present investigation is to reveal the differences between nominally identical ferromagnetic nanowires produced by the alternative fabrication techniques.

The multilevel fabrication technique electron beam lithography (EBL) [60, 61] is widely used for high resolution submicron scale patterning of magnetic materials. However, this technique requires a number of steps including resist spinning, pattern exposure,



metallisation, removal of resist from the sample surface and lift off of the residual materials. On the contrary, focused ion beam (FIB) [62] based fabrication is essentially a one step patterning process of a continuous film and an excellent tool for rapid device proto-typing. Nevertheless, FIB has some disadvantages [63] especially due to the heavy  $Ga^+$  ions used for the milling process, e.g. radiation induced damage, unwanted ion implantation etc. Therefore, in the present investigation, by fabricating nominally identical nanowires by electron beam and focused ion beam lithography a comparative study will be carried out in which key differences in the magnetic behaviour will be identified. The outcomes of this investigation will be presented in **chapter 4**.

Cross-sectional (x-sectional) [63] samples will be prepared using FIB milling to observe the details of the nature of the physical structure of the patterned nanowires around their edges. Transmission electron microscopy (TEM) experiments like bright field plan view and x-sectional TEM imaging will be performed to compare the nanostructures produced by these two techniques. Fresnel mode of Lorentz TEM [64] will be used to explore the magnetic behaviour of DWs in the patterned nanowires. Furthermore, to assist interpretation of images and also for comparison with experimental results, micromagnetic simulations will be carried out using simulation package Object Oriented Micromagnetic Framework (OOMMF) [15].

### 1.7.2 Ion induced pinning sites for DWs trapping

One of the most challenging aspects of the future ferromagnetic devices is the controlled movement of DWs along the patterned nanowires. In order to control the position of a DW, artificial geometric features, e.g. notches/anti-notches [6, 23, 40, 45, 52] fabricated as trapping sites have been investigated extensively using both micromagnetic simulations and experimental observations. Such pinning features behave as potential wells or barriers [6, 40, 65, 66] depending on their shape and the chirality of the incoming DWs. However, as patterned magnetic structures continue to reduce in size, the role of patterned edges [67] as well as the limitation of fabrication techniques [68] becomes more important and challenging to write well defined geometrical pinning features below 100 nm. A possible alternative approach to this is to use ion irradiated pinning sites [69, 70] by effectively modifying the properties of the film in a controllable way in selected areas along the patterned structures. The modified areas along the structures

act as inherent pinning sites without necessarily changing the shape of the structures. This alternative technique of controlling DWs, using pinning sites arising from a controlled local modification of the magnetic properties of the nanowire, will be explored in **chapter 5**.

The nanowires are comprised of a multilayer thin film of Cr (3nm)/Py (10nm)/Cr (5nm) in which the local magnetic properties were varied by irradiation with *Ga* ions in a focused ion beam microscope. Cr was chosen as the material surrounding the Py layer because implantation of Cr is known to reduce the Curie temperature,  $M_s$ , magnetic anisotropy as well as altering the exchange constant [76, 84] of Py. Furthermore, the magnetic properties of Py are very highly sensitive to Cr content as low levels, around 8 at% Cr are sufficient to render the Py/Cr alloy paramagnetic at room temperature [85]. Experimental observations demonstrated that irradiation of energetic ion beams on ferromagnetic thin films have beneficial effects as they serve as versatile tool for the patterning or ordering [31, 32, 73] of the ultrathin ferromagnetic films. Tailoring of the magnetic properties like magnetic anisotropy, the saturation magnetisation, Curie temperature, magnetisation damping behaviour etc. of the thin film systems by the irradiation of different ion species is reported in references [4, 74–77]. One of the advantages of this technique is that by means of the ion irradiation, modification of the magnetic properties of laterally confined areas of the ferromagnetic films is possible in a controllable manner [32, 74, 79, 80]. However, property modifications of uncapped thin films by means of ion irradiation/implantation is limited by the sputter yield per incident ion. This is approximately 10 target atoms per incident 30 keV  $Ga^+$  [58, 81], depending on the sample irradiation history and mass of the target atom. An alternative approach is the tailoring of the magnetic properties of layered magnetic thin films [76, 77, 83] by radiation-induced interfacial mixing without significantly affecting the topography of the films. In the present investigation, a sandwich of tri-layer materials Cr/Py/Cr will be prepared by optimising the thickness of different layers using dynamic simulation package TRIDYN [86] (TRIDYN simulation package will be described in **chapter 2**) so that Cr concentration can be well controlled comparatively at low ion doses. It is expected that the combination of the irradiation and interlayer mixing will modify effectively the properties of this alloy system. Materials will be deposited by molecular beam epitaxy (MBE) and magnetron sputter deposition techniques. Using the dual

ion beam workstation, 30 keV  $Ga^+$  irradiation will be performed on the continuous films for different irradiation doses following the outcome of the TRIDYN simulations. Afterwards, low angle electron diffraction experiments will be carried out to quantify the integrated magnetic induction in the various exposed and unexposed areas of the film.

The nanowires will be patterned and irradiated in the FIB, a single irradiation line will be used to create a pinning site at an angle of 45 degrees to the wire length. Observation of the magnetic state of the nanowires will be realised using Lorentz microscopy. The change of wall structure and the dependence of the subsequent depinning field on the dose and wall type will be investigated systematically. To compare the experimental observations, micromagnetic simulations will also be conducted using the OOMMF package.

### 1.7.3 Magnetisation reversal processes in hybrid nanostructures

A part of the research work of this dissertation was performed in close collaboration with colleagues from HZDR, Institute of Ion Beam Physics and Materials Research, Dresden, Germany under DAAD-ARC project. The local modification of the magnetic properties [4,87] e.g. reduction of saturation magnetisation of thin Py film was realised with focused  $Ga^+$  beam irradiation. In this project, on a continuous  $16.9 \pm 0.8$  nm thick Py film, magnetically softer (irradiated) and harder (unirradiated) regions, which are in direct lateral contact by means of exchange coupling, were fabricated in Dresden using 30 keV focused  $Ga^+$  beam irradiation. The irradiation dose was  $6.24 \times 10^{15}$  ions/cm<sup>2</sup> and the width of the exposed and unexposed regions (stripes) were varied from 1000 nm to 200 nm. During magnetisation reversal process, it is expected to observe the formation of domain walls and domain configurations, which are different from that formed in the continuous thin films [88]. J. Fassbender et. al. [89] introduced previously artificial length scales to tailor magnetic properties for stripe patterns of width varied from 10  $\mu m$  to 1  $\mu m$ . Upon scaling the patterning size down into the nm regime, a transition from the tendency of a discrete switching to a collective switching of the stripe patterns may be observed due to the overlapping of the Néel wall tails of neighboring inter-stripe domain walls. Associated with the overlapping of Néel walls

is also the constriction of domain walls by the patterning size. In order to observe the influence of the downscaling of the patterning size on the domain wall formation and the magnetisation reversal in equivalent stripe structures, *in situ* magnetising experiments were performed using the high resolution Lorentz TEM imaging facilities available in Glasgow.

First of all, modification of magnetic properties in the exposed stripes was confirmed by measuring integrated magnetic induction using low angle electron diffraction experiments and assuming film thickness measured by using TEM cross-sectional image. Therefore, magnetisation reversal experiments were carried out using Fresnel and differential phase contrast (DPC) mode of Lorentz microscopy. Furthermore, quantitative analysis like domain wall width as a function of wall angle were investigated using also DPC mode of Lorentz microscopy. To assist the interpretation of the experimental observations micromagnetic simulations using OOMMF package were carried out extensively in Glasgow. The results will be discussed in **chapter 6**.

In the next chapter, materials deposition and nanofabrication techniques used for the present investigation will be described.

# Bibliography

- [1] C. H. Marrows, *Advances in Physics* **54:8** 585 (2005).
- [2] P. Weiss, *J. de Phys.* **6** 661 (1907).
- [3] W. Heisenberg, *Z. Phys.* **49** 619 (1928).
- [4] S. Chikazumi, *Physics of Ferromagnetism* (Oxford Science Publications), 1997.
- [5] M. C. Hickey, A. Atkinson, C. H. Marrows, B. J. Hickey, *J. Appl. Phys.* **103** 07D518 (2008).
- [6] D. McGrouther, *Effects of Focused Ion Beam Irradiation on Thin Ferromagnetic Films*, PhD thesis, University of Glasgow, 2004.
- [7] R. M. Bozorth, *Ferromagnetism* (D. Van Nostrand Company, Princeton, 1951).
- [8] M. Takahashi, *J. Appl. Phys.* **33** 1101 (1962).
- [9] L. Landau and E. Lifshitz, *Physik. Z. Sowjetunion.* **8** 153 (1935).
- [10] A. Aharoni, *An Introduction to the Theory of Ferromagnetism*, Oxford University Press (1996).
- [11] A. Hubert and R. Schäfer, *Magnetic domains* (Springer Verlag, 1998).
- [12] S. McVitie, J. N. Chapman, *J. Magn. Magn. Mater.*, **83** 97 (1990).
- [13] A. Hubert, *Phys. Stat. Sol.* **38** 699 (1970).
- [14] Y. Nakatani, A. Thiaville and J. Militat, *J. Magn. Magn. Mater.* **290** 750 (2004).
- [15] M. J. Donahue and D. G. Porter, Report No. NISTIR 6376 (National Institute of Standards and Technology, Gaithersburg, MD, 1999).

- [16] W. F. Brown, Jr., Phys. Rev. **58**, 736 (1940).
- [17] T. L. Gilbert, Phys. Rev. **100** 1243 (1955).
- [18] N. Inaba, Y. Uesaka, A. Nakamura, M. Futamoto, Y. Sugita, and S. Narishige, IEEE Trans. Magn. **33** 2989 (1997).
- [19] I. N. Krivorotov, N. C. Emley, J. C. Sankey, S. I. Kiselev, D. C. Ralph, and R. A. Buhrman, Science **307** 228 (2005).
- [20] P. M. Braganca, I. N. Krivorotov, O. Ozatay, A. G. F. Garcia, N. C. Emley, J. C. Sankey, D. C. Ralph, and R. A. Buhrman, Appl. Phys. Lett. **87** 112507 (2005).
- [21] G. M. Sandler, H. N. Bertram, T. J. Silva, and T. M. Crawford, J. App. Phys., **85** 5080 (1999).
- [22] C. Brownlie, S. McVitie, J. N. Chapman, and C. D. W. Wilkinson, J. Appl. Phys. **100** 033902 (2006).
- [23] C. W. Sandweg, N. Wiese, D. McGrouther, S. J. Hermsdoerfer, H. Schultheiss, B. Leven, S. McVitie, B. Hillebrands, and J. N. Chapman, J. Appl. Phys. **103** 093906 (2008).
- [24] A. Kunz, IEEE Trans. Magn. **42** 32219 (2006).
- [25] B. D. Cullity and C. D. Graham, Introduction to Magnetic Materials (Wiley, Hoboken, 2009).
- [26] R. C. O’Handley, Modern Magnetic Materials: Principles and Applications (Wiley, New York, 2000).
- [27] D. J. Craik and R. S. Tebble, Ferromagnetism and Ferromagnetic Domains, North-Holland Publishing Co. (1965).
- [28] Y. Liu, D. J. Sellmyer and D. Shindo, Handbook of Advanced Magnetic Materials, Springer (2006).
- [29] E. C. Stoner and E. P. Wohlfarth, Phil. Trans. Roy. Soc. **240** 599 (1948).

- [30] C. Haginoya, S. Heike, M. Ishibashi, K. Nakamura, K. Koike, T. Yoshimura, J. Yamamoto, Y. Hirayama, J. Appl. Phys. **85** 8327 (1999).
- [31] S. Landis, B. Rodmacq, B. Dieny, B. Dal’Zotto, S. Tedesco, M. Heitzmann, J. Magn. Magn. Mater. **226** 1708 (2001).
- [32] C.T. Rettner, M.E. Best, B.D. Terris, IEEE Trans. Magn. **37** 1649 (2001).
- [33] T. Ono, H. Miyajima, K. Shigeto, K. Mibu, N. Hosoi, and T. Shinjo, Science **284** 468 (1999).
- [34] D. Atkinson, D. A. Allwood, G. Xiong, M. D. Cooke, C. C. Faulkner, and R. P. Cowburn, Nature Mater. **2** 85 (2003).
- [35] G. S. D. Beach, C. Nistor, C. Knutson, M. Tsoi, and J. L. Erskine, Nature Mater. **4** 741 (2005).
- [36] K. Kondou, N. Ohshima, S. Kasai, Y. Nakatani, and T. Ono, Appl. Phys. Express **1** 061302 (2008).
- [37] P. Mhrke, T. A. Moore, M. Klui, J. Boneberg, D. Backes, S. Krzyk, L. J. Heyderman, P. Leiderer, and U. Rdiger, J. Phys. D **41** 164009 (2008).
- [38] K. Weerts, P. Neutens, L. Lagae, and G. Borghs, J. Appl. Phys. **103** 094307 (2008).
- [39] D. McGrouther, S. McVitie, J. N. Chapman, and A. Gentils, Appl. Phys. Lett. **91** 022506 (2007).
- [40] K. J. O’Shea, S. McVitie, J. N. Chapman, and J. M. R. Weaver, Appl. Phys. Lett. **93** 202505 (2008).
- [41] K. He, D. J. Smith and M. R. McCartney, Appl. Phys. Lett. **95** 182507 (2009) .
- [42] S. Glathe, M. Zeisberger, U. Hbner, and R. Mattheis, Phys. Rev. B **81** 020412 (2010).
- [43] N. Vernier, D. A. Allwood, D. Atkinson, M. D. Cooke, and R. P. Cowburn, Europhys. Lett. **65** 526 (2004).

- [44] J. Grollier, P. Boulenc, V. Cros, A. Hamzic, A. Vours, A. Fert, and G. Faini, Appl. Phys. Lett. **83** 509 (2003).
- [45] M. Hayashi, L. Thomas, C. Rettner, R. Moriya, Y. B. Bazaliy, and S. S. P. Parkin, Phys. Rev. Lett. **98** 037204 (2007).
- [46] L. Thomas, M. Hayashi, X. Jiang, R. Moriya, C. Rettner, and S. S. P. Parkin, Nature (London) **443** 197 (2006).
- [47] A. Yamaguchi, T. Ono, S. Nasu, K. Miyake, K. Mibu, and T. Shinjo, Phys. Rev. Lett. **92** 077205 (2003).
- [48] M. Tsoi, R. E. Fontana, S. S. P. Parkin, Appl. Phys. Lett. **83** 2617 (2003).
- [49] S. S. P. Parkin, US Patent, 6834005 (2004).
- [50] S.S.P. Parkin, M. Hayashi, L. Thomas, Science **320** 5873 (2008).
- [51] D. A. Allwood, G. Xiong, M. D. Cooke, C. C. Faulkner, D. Atkinson, N. Vernier, and R. P. Cowburn, Science **296** 2003 (2002).
- [52] D. A. Allwood, G. Xiong, C. C. Faulkner, D. Atkinson, D. Petit, and R. P. Cowburn, Science **309** 1688 (2005).
- [53] C. Brownlie, *A TEM Investigation of Controlled Magnetic Behaviour in Thin Ferromagnetic Films*, PhD thesis, University of Glasgow, 2007.
- [54] K. J. O'Shea, *Putting a leash on the domain wall: A TEM investigation into the controlled behaviour of domain walls in ferromagnetic nanostructures*, PhD thesis, University of Glasgow, 2010.
- [55] Y. Nakatani, A. Thiaville, and J. Miltat, Nature Mater. **2** 521 (2003).
- [56] M. T. Bryan, D. Atkinson and R. P. Cowburn, Appl. Phys. Lett. **85** 3510 (2004).
- [57] D. Atkinson, Journal of Physics: Conference Series **17** 33 (2005).
- [58] S. Glathe, R. Mattheis, and D. V. Berkov, Appl. Phys. Lett. **93** 072508 (2008).
- [59] T. W. Chiang, L. J. Chang, C. Yu, S. Y. Huang, D. C. Chen, Y. D. Yao, and S. F. Lee, Appl. Phys. Lett. **97** 022109 (2010).



- [60] J.I. Martin, J. Nogues, K. Liu, J.L. Vicent, I.K. Schuller, J. Magn. Magn. Mater. **256** 449 (2003).
- [61] A. A. Tseng, K. Chen, C. D. Chen, and K. J. Ma, IEEE Trans. Magn. **26** 141 (2003).
- [62] K. Gamo, Nucl. Inst. and Meth. in Physics Research B **121** 464 (1997).
- [63] J. Mayer, L.A. Giannuzzi, T. Kamino, and J. Michael, MRS Bulletin **32** 400 (2007).
- [64] J. N. Chapman, A. B. Johnston, L. J. Heyderman, S. McVitie, W. A. P. Nicholson, and B. Bormans, IEEE Trans. Magn. **30** 4479 (1994).
- [65] D. Petit, A. V. Jausovec, D. Read, and R. P. Cowburn, J. Appl. Phys. **103** 114307 (2008).
- [66] H. T. Zeng, D. Read, D. Petit, A. V. Jausovec, L. O'Brien, E. R. Lewis, and R. P. Cowburn, Appl. Phys. Lett. **94** 103113 (2009).
- [67] M. Herrmann, S. McVitie and J. N. Chapman, J. Appl. Phys. **87** 2994 (2000).
- [68] M. A. Basith, S. McVitie, D. McGrouther, J. N. Chapman and J. M. R. Weaver, J. Appl. Phys. **110** 083904 (2011).
- [69] A. Vogel, S. Wintz, J. Kimling, M. Bolte, T. Strache, M. Fritzsche, M. Y. Im, P. Fischer, G. Meier, and J. Fassbender, IEEE Trans. Magn. **46** 1708 (2010).
- [70] A. Vogel, S. Wintz, T. Gerhardt, L. Bocklage, T. Strache, M. Y. Im, P. Fischer, J. Fassbender, J. McCord and G. Meier, Appl. Phys. Lett. **98** 202501 (2011).
- [71] C. Chappert, H. Bernas, J. Ferreacute, V. Kottler, J. Jamet, Y. Chen, E. Cambril, T. Devolder, F. Rousseaux, V. Mathet, and H. Launois, Science **280** 1919 (1998).
- [72] W. M. Kaminsky, G. A. C. Jones, N. K. Patel, W. E. Booij, M. G. Blamire, S. M. Gardiner, Y. B. Xu, and J. A. C. Bland, Appl. Phys. Lett. **78** 1589 (2001).
- [73] H. Bernas, J.-P. Attan, K.-H. Heinig, D. Halley, D. Ravelosona, A. Marty, P. Auric, C. Chappert, and Y. Samson, Phys. Rev. Lett. **91** 077203 (2003).

- [74] D. McGrouther and J. N. Chapman, Appl. Phys. Lett. **87** 022507 (2005).
- [75] J. Fassbender and J. McCord, Appl. Phys. Lett. **88** 252501 (2006).
- [76] J. Fassbender, J. von Borany, A. Mücklich, K. Potzger, W. Möller, J. McCord, L. Schultz and R. Mattheis, Phys. Rev. B **73** 184410 (2006).
- [77] J. Fassbender, J. von Borany, A. Mücklich, K. Potzger, W. Möller, Nucl. Instr. and Meth. in Physics Research B **248** 343 (2006).
- [78] J. Fassbender and J. McCord, J. Magn. Magn. Mater. **320** 579 (2008).
- [79] D. Ozkaya, R. M. Langford, W. L. Chan, and A. K. Petford-Long, J. Appl. Phys. **91** 9937 (2002).
- [80] J. McCord, T. Gemming, L. Schultz, J. Fassbender, M. O. Liedke, M. Frommberger, and E. Quandt, Appl. Phys. Lett. **86** 162502 (2005).
- [81] P. Sigmund, Phys. Rev. **184** 383 (1969).
- [82] J. Ziegler, J. Biersack, U. Littmark, The Stopping and Range of Ions in Matter, Pergamon, New York, 1985 SRIM code /<http://www.srim.org>S.
- [83] C.C. Faulkner, D. Atkinson, D.A. Allwood, R.P. Cowburn, J. Magn. Magn. Mater. **319** 9 (2007).
- [84] L. Folks, R. E. Fontana, B. A. Gurney, J. R. Childress, S. Maat, J. A. Katine, J. E. E. Baglin and A. J. Kellock, J. Phys. D: Appl. Phys. **36** 2601 (2003).
- [85] R. M. Bozorth, Ferromagnetism (Piscataway: IEEE) 1993.
- [86] W. Möller, W. Eckstein, and J. P. Biersack, Comput. Phys. Commun. **51** 355 (1988); the TRIDYN code is available on [www.fzd.de](http://www.fzd.de)
- [87] J. Fassbender, D. Ravelosona, Y. Samson, J. Phys. D: Appl. Phys. **37** R179 (2004).
- [88] J. McCord, L. Schultz, and J. Fassbender, Adv. Mater. **20** 2090 (2008).
- [89] J. Fassbender, T. Strache, M. O. Liedke, D. Marko, S. Wintz, K. Lenz, A. Keller, S. Facsko, I. Mönch and J. McCord, New J. Phys. **11** 125002 (2009).

# Chapter 2

## Materials deposition and nanofabrication techniques

### 2.1 Introduction

The advancement in nanofabrication technology opens fascinating opportunities for engineering innovative magnetic materials and stimulates the demand for magnetic storage devices with higher density, faster speed, lower power consumption and smaller size than the current state-of-the-art devices. Amongst a variety of nanofabrication techniques, electron beam lithography (EBL) is widely used since the late 60s for high resolution submicron scale patterning of micro/nanostructures. This lithographic technique comprises a number of steps including resist spinning, pattern exposure, metallisation, removal of resist from the sample surface and lift off of the residual materials. The major advantages of EBL compare to its counterpart conventional optical lithography technique is the high resolution and versatility (multi-level capability) of pattern formation. Unlike photolithography, the ability to create any pattern without the need to fabricate expensive mask plates makes e-beam a highly flexible tool. However, the EBL technique [1, 2] is a collective term for several closely related processes and the time scale of this technique is couple of days. The processing steps of the EBL technique that will be described in the following sections is shown schematically in Fig. 2.1(a).

In the case of nanoscale patterning, for example, for writing a complex patterns by varying their sizes, EBL technique may be problematic to some extent. This is due to the variation of the amount of doses required for writing each patterns. Besides, the

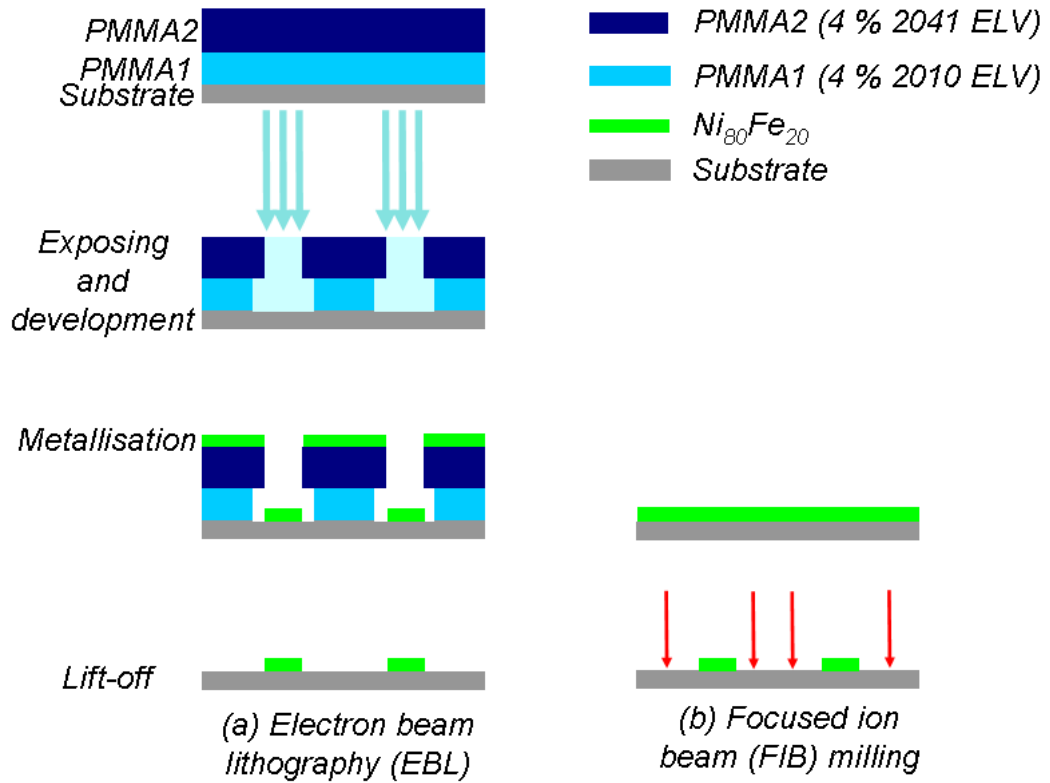


Figure 2.1: Schematic illustration of the processing steps of two alternative lithographic techniques. The processing steps for writing patterns using (a) EBL technique and (b) FIB milling technique. The latter technique is faster and a new addition to the range of nanofabrication techniques.

resolution limit in EBL is determined by the electron interaction with the molecules in the resist that can be divided into forward and backward scattering. A combination of high electron energy and small film thickness may reduce the influence of forward scattered electrons. But electrons penetrating through the resist and into the bulk substrate underneath will be partly backscattered into the resist and will also contribute to the resist exposure. These backscattered electrons are responsible for what's called the proximity effect: the dose at any point depends on the density of the pattern around this point. To correct the proximity effect commercial software is available but if the dose required for the patterns are varied according to their sizes, the correction always may not be possible [3].

An alternative approach, however, for writing patterns on thin continuous films may be the focused ion beam (FIB) milling technique. This technique is a new addition to the range of nanofabrication techniques and is comparatively faster than other current micro/nanofabrication techniques for the fabrication of prototype micro/nanostructures [1,4–8]. The processing steps of the focused ion beam milling technique are illustrated

schematically in Fig. 2.1(b). The FIB milling technique is capable of directly fabricating micro/nanostructures by milling the correct areas. However, there are several secondary effects that occur during FIB milling due to the heavy ions used for the milling process which may lead to undesired results. These include radiation induced damage and ion implantation.

In the present investigation (**chapter 5**), *in situ* ion induced pinning sites will be created at different areas of the nanowires fabricated by FIB milling of continuous multi-layer films. Therefore, prior to creating ion induced pinning sites in FIB milled nanowires, it is worthwhile to carry out a direct comparison of the magnetisation reversal behaviour of the nominally identical nanowires patterned by using both of these two techniques. The aim of this investigation is not to defend any technique by saying that FIB is better than EBL or vice versa. Instead the aim of the investigation is to go through the processes by fabricating nominally identical wires and thereby illustrating the differences and difficulties that arise from these two fabrication techniques. It has been seen from another study that nanoelements created by FIB with widths less than 100 nm were not able to be determined as magnetic using LTEM [9]. Therefore, in this project it was also intended to understand the scale limit in terms of the width of the wires up to which magnetic information can be extracted from patterns written using FIB milling.

The following sections will be described the substrates for deposition along with different deposition techniques used throughout this investigation. The processing steps of EBL and FIB techniques will also be illustrated. At the end of this chapter, the dynamic simulation package TRIDYN that will be used in **chapter 5** for optimising the thickness of the multi-layer thin films will be described briefly.

## 2.2 Substrate for deposition

The subject of interest of this dissertation is the TEM investigation of lithographically patterned ferromagnetic nanostructures on thin continuous films. To perform TEM investigations, the sample needs to be less than 100 nm thick for 200 keV electrons. The substrates used for the present studies are electron transparent  $\text{Si}_3\text{N}_4$  membrane depicted in Fig. 2.2. These membrane substrates consist of 35nm  $\text{Si}_3\text{N}_4$ , supported

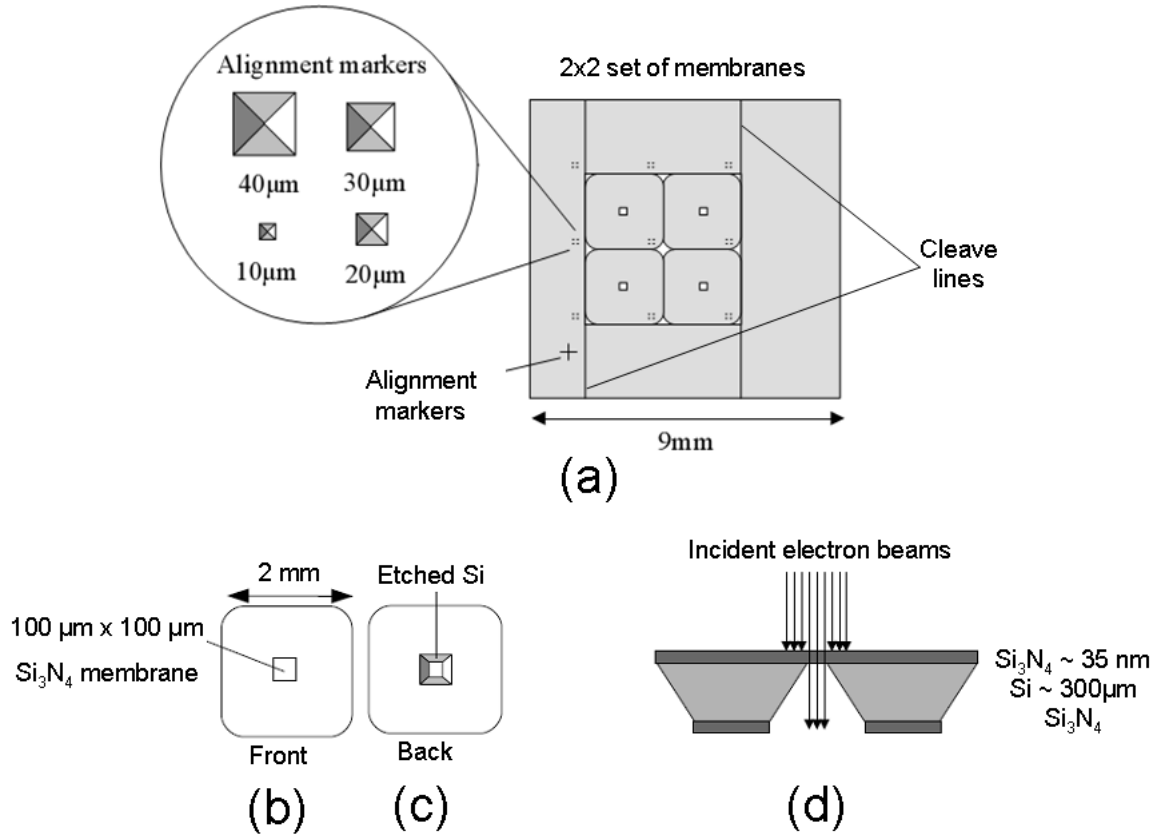


Figure 2.2: A schematic of the substrates used to fabricate thin film elements. (a) A  $2 \times 2$  membrane set containing etched markers is used for electron beam lithography, (b) Front, (c) back and (d) cross-sectional schematics of single Si<sub>3</sub>N<sub>4</sub> membrane.

on a Si frame with a  $100 \times 100 \mu m^2$  electron transparent window [10]. They are made by Kelvin Nanotechnology Ltd (KNT), based in the School of Electronics and Electrical Engineering at the University of Glasgow. The membranes particularly used for electron beam lithography are made in  $9 \times 9 mm^2$  blocks of  $2 \times 2 mm^2$  membranes. These blocks include etched markers to allow the beam to be positioned in the desired area, as shown in Fig. 2.2(a). The cleave lines shown in the same figure ensure safe separation of individual membranes for subsequent TEM investigations. Membranes were also collected from the edges of the 4 inches round wafers. These membranes have no markers and are used for focused ion beam milling and irradiation, Fig. 2.2(b).

## 2.3 Materials deposition

In order to deposit a thin continuous film of Permalloy (Py) and a multi-layer film of Cr/Py/Cr on Si<sub>3</sub>N<sub>4</sub> membrane, a number of deposition techniques including thermal evaporation, molecular beam epitaxy, and magnetron sputtering were used. The Py

films of the desired thickness were deposited using the thermal evaporation system available in the School of Physics and Astronomy, University of Glasgow. This evaporation system has some limitations for multi-layer film deposition. Therefore, a multi-layer polycrystalline film of Cr/Py/Cr was deposited onto  $\text{Si}_3\text{N}_4$  membrane using the molecular beam epitaxy system available in the HZDR, Institute of Ion Beam Physics and Materials Research, Dresden, Germany. In order to create a well defined uniaxial anisotropy into the continuous film, multilayer polycrystalline film of Cr/Py/Cr was also deposited by magnetron sputter deposition technique applying a magnetic field during deposition using the facilities available in IPTH Jena, Germany.

### 2.3.1 Thermal evaporation

In **chapter 4**, a direct comparison of the domain wall behaviour in Py nanowires patterned by electron beam lithography and focused ion beam milling was carried out. To pattern these nanostructures, a Py film of 20 nm thickness was deposited by thermal evaporation. This technique has the advantage of being simple to implement and allows a wide range of materials to be deposited. The thermal evaporation technique is based on evaporating source material inside a vacuum chamber where the material is heated to the point of evaporation. When a constant temperature and vapour pressure are obtained, the evaporated material travels directly to the target substrate, where they condense in the form of a thin film. A schematic of the thermal evaporation system, available in the School of Physics and Astronomy, University of Glasgow is depicted in Fig. 2.3. Using this evaporation technique, the deposition of the Py film was carried out under vacuum, around  $5 \times 10^{-6}$  mbar, to minimise contamination from other materials and to ensure a direct route for the metallic vapour from source to target. The raw material, in this case  $\text{Ni}_{80}\text{Fe}_{20}$ , is placed inside a ceramic coated tungsten wire crucible through which a large current is passed to heat the material resistively. The substrate is placed in a holder directly above the target material along with a shutter in between the substrate and target material. Once any oxide material is removed and a steady evaporation rate is achieved, the shutter is removed from beneath the substrate. The thickness of the deposited film is monitored by using a quartz oscillator and after the desired amount of material has been deposited, the shutter is replaced. The thickness of the deposited material monitored by the quartz crystal microbalance is subsequently

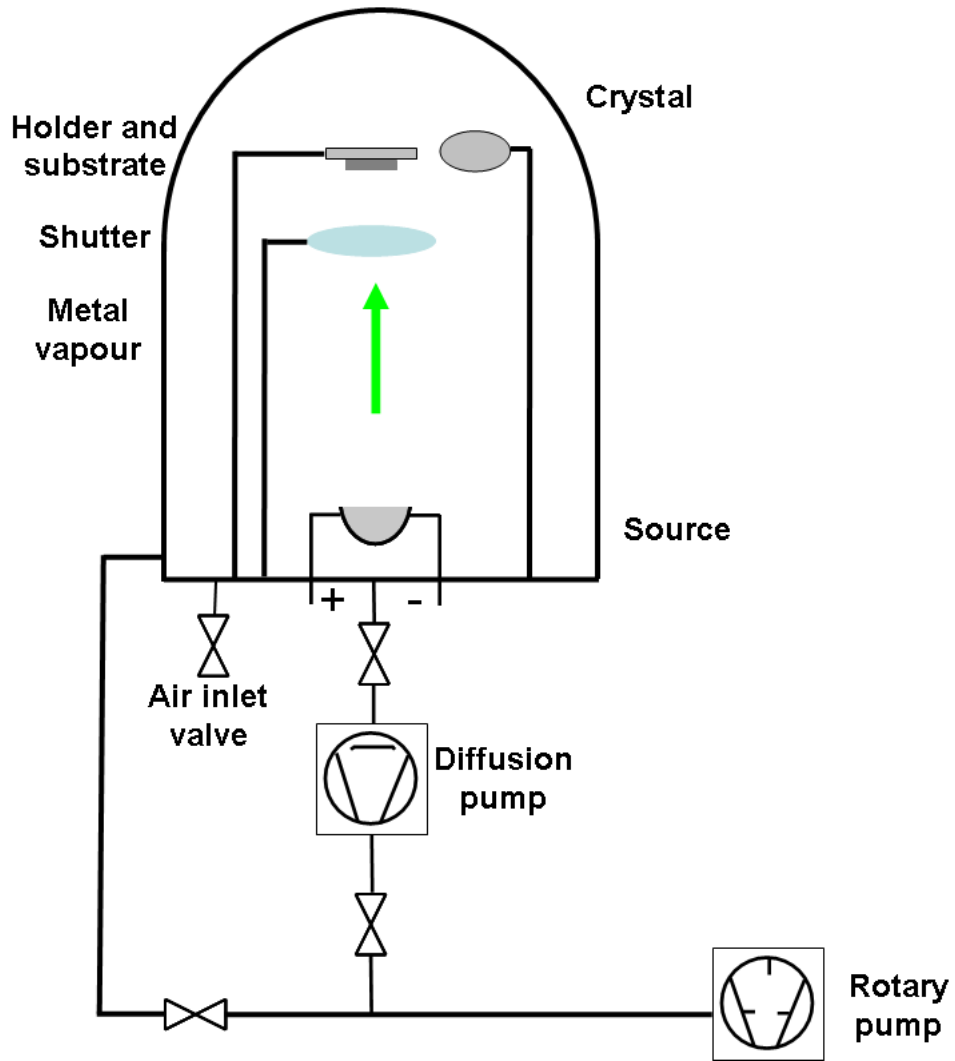


Figure 2.3: Schematic of the thermal evaporator used to deposit thin films.

calibrated using an atomic force microscope (AFM).

### 2.3.2 Molecular beam epitaxy

Epitaxy derives from Greek language meaning 'arranged on top of,' and molecular beam epitaxy (MBE) indicates creating a crystal structure by building up orderly layers of atoms or molecules on top of a substrate. The MBE technique was developed in 1960s in the Bell laboratories and since then has been widely used to grow single crystal structures and very high quality metallic/oxide thin films. The basic principle of the MBE deposition system involves generation of atomic or molecular beams using elemental sources evaporated from temperature controlled effusion cells or electron beam evaporation guns. The entire process is performed under ultrahigh vacuum ( $10^{-10}$  mbar [11]); therefore, the individual atoms or molecules are able to travel many cms before making any collisions with other atoms or molecules. Under this molecular beam



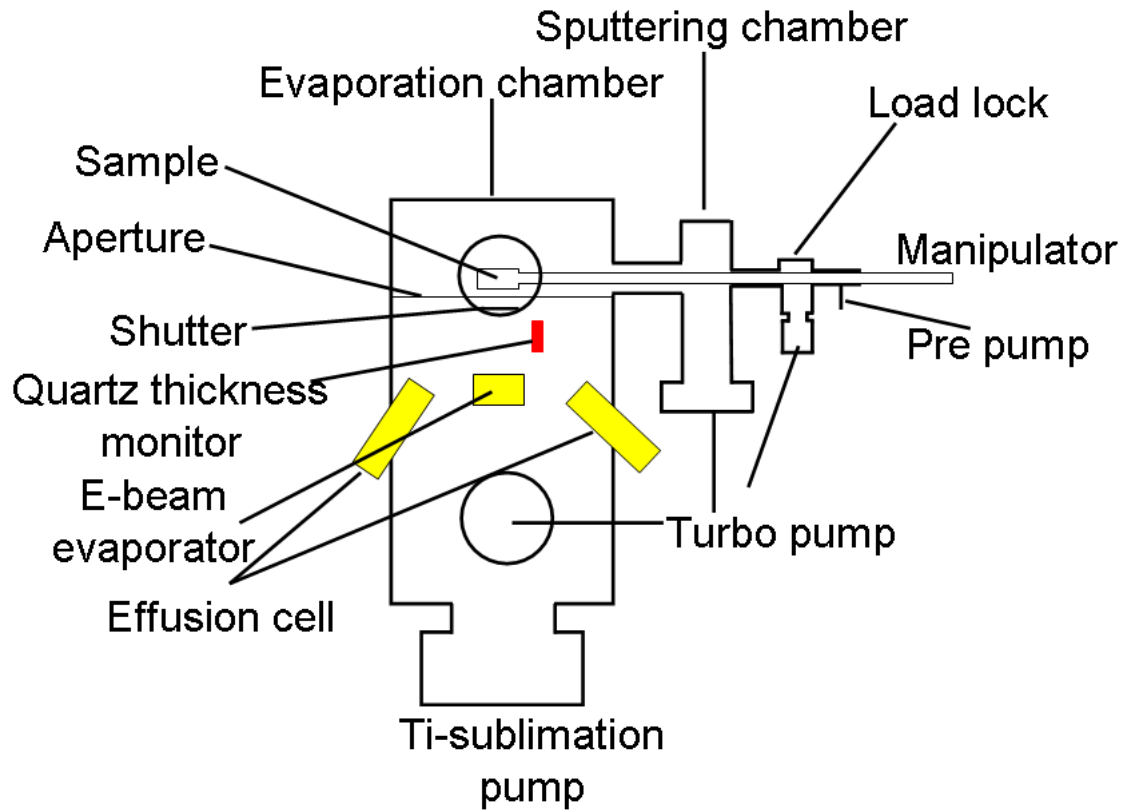


Figure 2.4: A schematic of the MBE system used for the multilayer thin films Cr/Py/Cr on  $\text{Si}_3\text{N}_4$  membrane.

condition, the mean free path between collisions in the thermal beams is significantly greater than the separation between the source and the substrate. The source contains the constituent element and the temperature of the source is chosen so that films of the desired composition can be obtained. MBE exhibits many advantages for single crystal film deposition, e.g. (i) evaporation at very low rates  $\text{\AA}/\text{s}$  (ii) deposition of films with good crystal structure, (iii) operation at ultrahigh vacuum conditions hence less contamination. However, using the MBE system it is also possible to deposit high quality multilayer polycrystalline films. In the present investigation, multilayer polycrystalline films of Cr/Py/Cr were deposited onto  $\text{Si}_3\text{N}_4$  membrane (results will be presented in **chapter 5**) by Dr. Maciej Oskar Liedke, using the MBE system available in the HZDR, Institute of Ion Beam Physics and Materials Research, Dresden, Germany. A schematic of the MBE system used for this deposition is shown in Fig. 2.4. The beams generated from the sources interact with heated membrane substrate to produce the film. The high vacuum is generated by three turbo molecular pumps and one titanium sublimation pump, leading to a pressure of the order of  $10^{-10}$  mbar. The sample can be clean by using a sputtering gun which is inside the cleaning chamber.

The deposition rate was very low, around 0.2-0.3 Å/s. The combination of the low growth rates and the use of a fast acting sample shutter facilitated to achieve the desired thickness (monitored by the quartz thickness monitor) of each layer.

### 2.3.3 Magnetron sputter deposition

When a solid target is bombarded by energetic particles like accelerated ions, a number of surface atoms are ejected from the target material and follow random trajectories. This phenomenon is known as sputtering (described further in section 2.5.3) and is commonly use for thin film deposition. The sputter deposition technique as shown schematically in Fig. 2.5 consists of a pair of planar electrodes, the anode where the substrate, in this case  $\text{Si}_3\text{N}_4$  membrane, is placed and the cathode (target) that is made up of the material to be deposited on the substrate. These electrodes are placed inside the low pressure vacuum chamber which is filled with an inert sputter gas such as Argon (Ar). Once a large voltage is applied between the electrodes, the emission of secondary electrons from the target material ionise the gas atoms generating a plasma. These Ar ions are then accelerated towards the cathode and a stream of atoms or clusters of atoms eject from the target on impact. The sputtered atoms are deposited onto exposed surfaces in the chamber, leading to the formation of a thin film onto the substrate. Electrons liberated in the ionisation process travel towards the anode and may, upon collision with atoms, further ionise the gas and keep the process ongoing. The idea of magnetron sputter deposition is to achieve higher yields and better performance by effectively utilising and combining strong electric and magnetic fields during the sputter process [12]. Electrons from the plasma and secondary electrons generated from the target during the sputter process are trapped by the magnetic field lines and accelerate towards the anode. Due to the Lorentz force, the electrons will follow helical trajectories around the magnetic field lines. Therefore, the electrons are forced to travel longer distances inside the chamber and thus induce more ionisation which in turn increases the sputter yield significantly. In the present investigation, thin films were deposited by magnetron sputter deposition technique and Ar gas was used as the sputter gas. The base pressure was  $10^{-8}$  mbar and the deposition rate was 0.55 Å/sec. The purpose of thin film deposition using magnetron sputter deposition technique is to create magnetic field induced anisotropy by applying a magnetic field during depo-

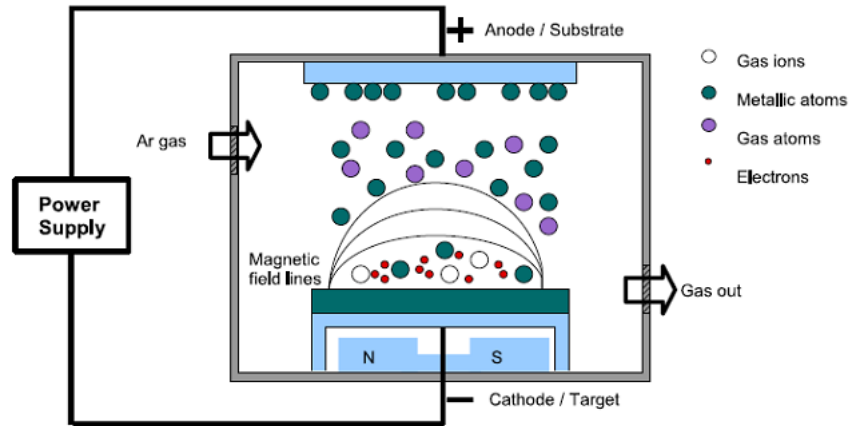


Figure 2.5: Schematically parallel plate DC magnetron sputtering system for thin film deposition.

sition. Therefore, magnetic nanowires/nanostripes were patterned along the uniaxial anisotropy axis. The results will be presented in **chapters 5 and 6**. The thin film was deposited by R. Mattheis from IPTH Jena, Germany.

## 2.4 Nanofabrication

Miniaturisation, i.e. all the way down to the atomic scales, with improved performance is the main theme of modern nanofabrication technology. Central to nanofabrication is lithography which can be classified by the radiation used: optical lithography in the case of photons, electron beam lithography for electrons and ion beam lithography for ionised atoms. Electron beam lithography and focused ion beam techniques were used to fabricate the structures investigated in this thesis. Electron beam lithography was used to fabricate planar nanowires on continuous Py film using an electron beam lithography tool available in the James Watt Nanofabrication Centre (JWNC), part of the School of Electronics and Electrical Engineering. Fabrication of nanowires/stripes were carried out using FIB milling/irradiation on continuous thin films using a dual FIB/SEM workstation available in the Kelvin Nanocharacterisation Center (KNC) part of the School of Physics and Astronomy, University of Glasgow.

### 2.4.1 Electron beam lithography

As was mentioned earlier, electron beam lithography (EBL) [1, 2] is actually a collective term for several closely related processes, including resist spinning, exposure,

development, metallisation etc. The following sections present a brief description of the e-beam writer and different lithographic processing steps.

### **E-beam system**

The EBL facility at JWNC is based on a Vistec VB6 UHR which uses a thermal field emission gun (FEG) capable of accelerating voltages of up to 100 keV [13]. A schematic diagram of the electron optical system is given in Fig. 2.6, indicating the main components. The electrons are generated by a field emission gun at the top of the column and directed along the optic axis with the aid of tilting and shifting coils. The condenser lenses C2 and C3 determine the spot size and beam current at the substrate. Therefore, during exposure a set of computer controlled deflection coils scan the probe in the in plane coordinates of the sample surface. The beam on the sample is focused by the objective lens and any deflections of the beam at the sample or any variations in sample height are corrected by the fine focusing coils. Any astigmatism in the beam is corrected by the stigmator coils. In addition, a final aperture is used to define the beam convergence angle to the substrate and the column is fitted with backscattered electron (BSE) detectors for imaging. The whole system operates under high vacuum and a series of pumps are operated below the stage to evacuate any gaseous contamination.

### **Pattern design and layout files**

To write the patterns on the substrate using the beam writer VB6, the design and job layout files must be sent to a control computer. In the present work, the pattern is initially designed using the computer-aided design (CAD) program L-edit. L-edit allows the user to create complex patterns by generating several individual structures. Moreover, using L-edit a number of layers can also be specified if multiple lithography steps are required. Like most CAD programs, L-edit produces file type, .gds, which is not compatible with the beam writer as the machine is only able to handle primitive shapes. Therefore, in order to convert the file to a suitable format further processing steps are mandatory.

Computer Aided Transcription System (CATS) is used to convert the \*.gds file to a VB6 compatible format. Then, the VB6 compatible file is sent to both the control computer and job layout program BELLE (Beamwriter Exposure Layout for Lithographic

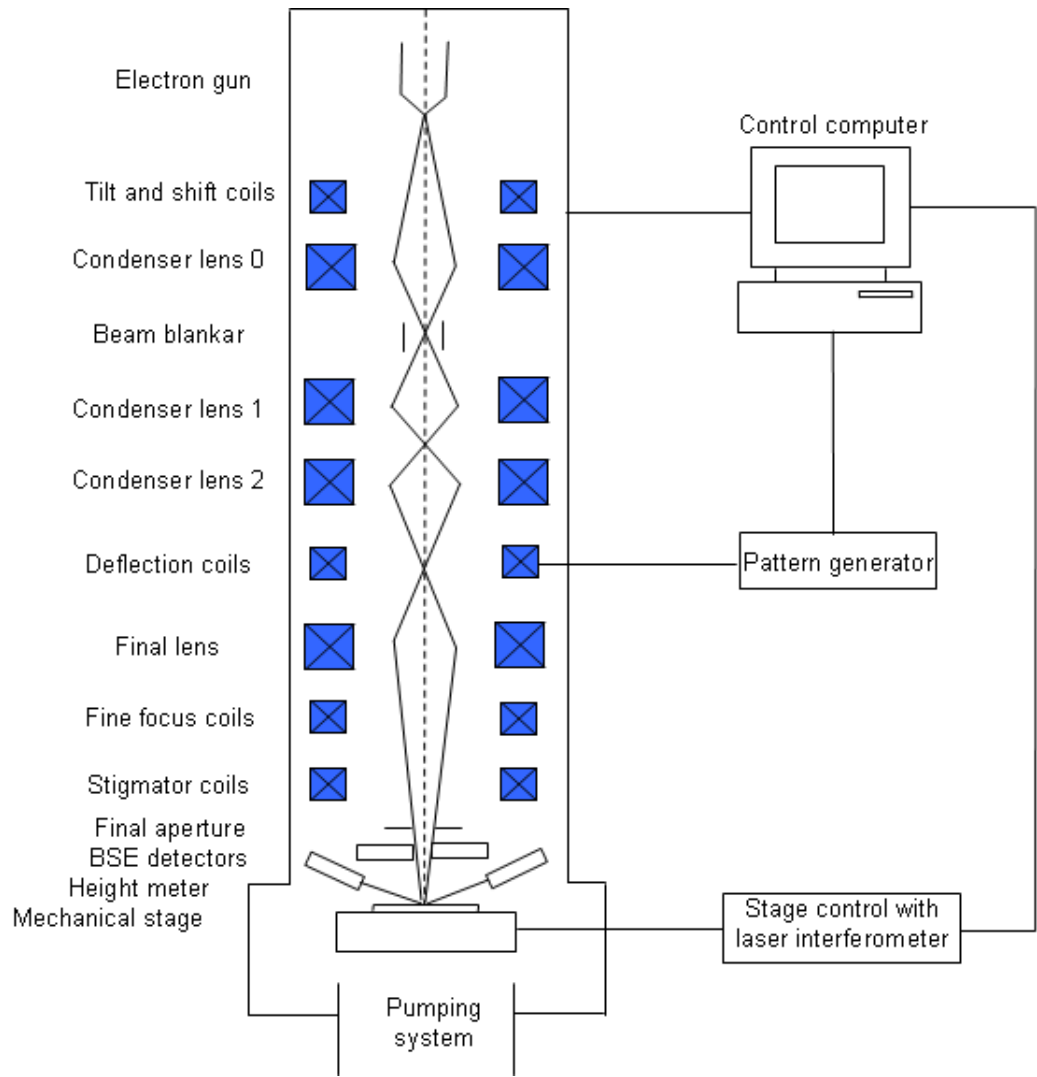


Figure 2.6: Schematic diagram of the VB6 beam writer used to pattern part of the structures in **chapter 4**.

Engineers) to produce a final layout file.

### Resist technology

Electrons can effectively expose any materials but due to their very light mass exposing of the electrons change properties of soft materials, such as photoresist or electron beam resist. The principal component of a resist is a high molecular-weight polymer dissolved in a liquid solvent. The polymer changes its structure when exposed to radiation, including electron radiation. Electron beam resist can be classified as either negative or positive resist. After exposure to electrons, the positive resist is weakened by chain scission to produce organic molecules of a lower molecular weight. As a result, the exposed resist become more soluble in the developing solution [14]. These lower molecular weights resist washes away by the solvent developer and eventually a

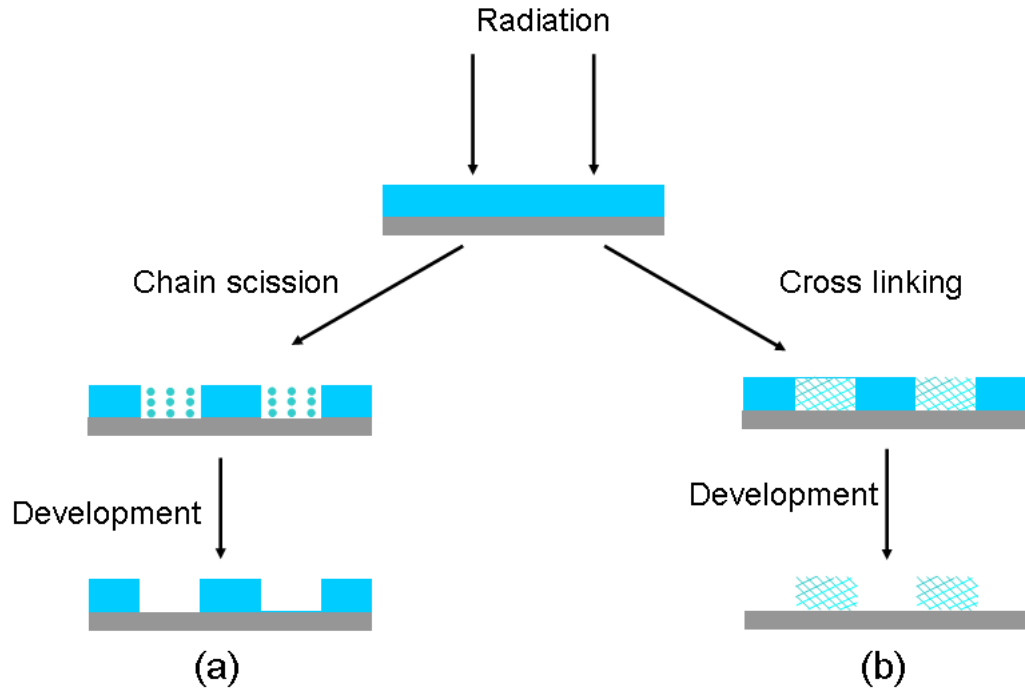


Figure 2.7: Schematic illustration of the resist profile of (a) positive and (b) negative single component resist. The positive resist is weakened by chain scission to produce organic molecules of a lower molecular weight. On the other hand, the negative resist is strengthened during exposure by random cross-linkage of main and side polymer chains and become less soluble in the developer.

positive tone pattern is formed in the resist film, Fig. 2.7(a). On the other hand, the negative resist is strengthened during exposure by random cross-linkage of main and side polymer chains and become less soluble in the developer, Fig. 2.7(b). Therefore, with negative resist, the unexposed resist portion is removed during the developing process. On the contrary, with positive resists only the unexposed portions remain after developing, as was explained earlier. Most commonly used positive resist Polymethyl Methacrylate (PMMA) was used for patterning nanowires in the present investigation and the size of the electron probe in conjunction with resist determined the resolution of the pattern generation.

### Resist development

The resist thickness depends on the PMMA concentration and spinning speed. In the present investigation, a bilayer PMMA resist was used for lift off process. The thickness of the bottom and top resist layers were 110 nm and 115 nm for 4% 2010 ELV and 4% 2041 ELV layers, respectively for a spinning speed of 5000 rpm. The substrate coated by resist is dried at 180<sup>0</sup> C for drying to remove solvent and to harden the resist. After

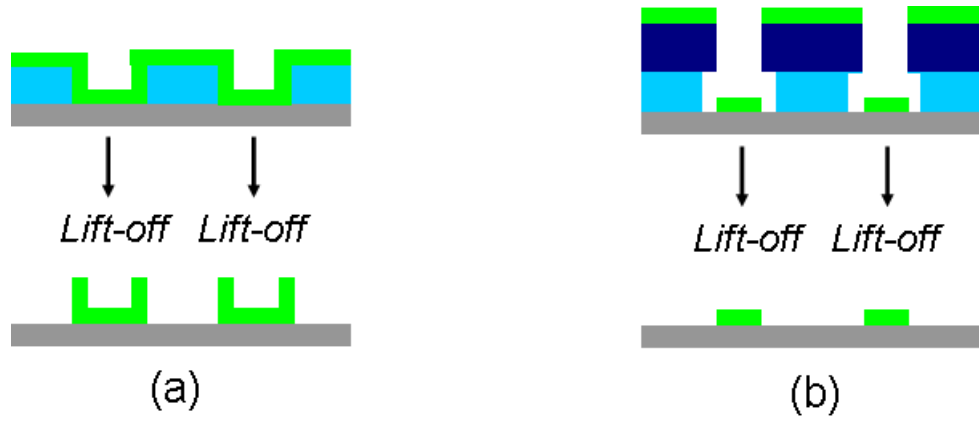


Figure 2.8: Schematic illustration of the resist and deposited metal profile with (a) a single resist layer and (b) a bilayer of electron sensitive resist. The later one facilitates the subsequent lift-off process of the resist, forming a suitable undercut profile.

the e-beam writing process of the patterns, 2.5:1 MIBK (methyl isobutyl ketone) and IPA (isopropyl alcohol) were used at 23<sup>0</sup> C, typically for 30 seconds, to develop the patterns. Prior to cleaning by the plasma cleaner, the substrate was nicely cleaned by IPA. Then metallisation and lift off were implemented as described in the following paragraphs.

### Metallisation and lift off

The Py film of desired thickness was deposited by thermal evaporation, which was described in section 2.3.1, covering the resist and areas where the polymer had been cleared.

In fact, to produce the desired patterns as designed in L-edit, the continuous metal film has to be divided into discrete structures. This can be achieved either by chemical etching or by lift-off. The latter process was used in this project to produce the structures in the present investigation. To accomplish the lift-off process, after metallisation the substrate is immersed in a solvent that dissolves the resist but does not attack the metal film. This step ensures that the polymer and any overlying metal was removed and the metal is only present in the regions specified by the pattern.

It is notable that the lift-off process is highly dependent on the quality of the resist profile. It is well known that using a single layer of resist to define a pattern is problematic for lift off. This is due to the tendency of the deposited metal to adhere to the sidewalls of the resist as well as to the surface to create a continuous film, as indicated in Fig. 2.8(a). This can drastically influence lift-off and even after resist removal, the

metals coating the sidewalls can remain on the substrate. This ultimately causes an unwanted build up of metal often known as flagging [15]. To overcome this problem, two layers of PMMA resists with different molecular weights (higher molecular weights on top of lower molecular weights) and different electron sensitivities are spun to get a suitable undercut profile as indicated in Fig. 2.8(b). In this case, the bottom layer of resist forms a wider mask than the top layer. When the material is deposited into the resist coated substrate, the top (narrower) mask defines the overall dimensions of the structure deposited. The underlying wider mask is not in contact with the deposited metal (Fig. 2.8(b)) and therefore facilitates the subsequent lift-off process of the resist, forming a suitable undercut profile in ideal case. However, in practice, a build up of metal on top of the PMMA resist was observed in the cross-sectional TEM images of the EBL patterned nanowires (results will be presented in **chapter 4**) indicating that after development all these resists were not removed. These TEM x-sectional images also ensures the presence of residual PMMA on top of the patterned structures. It is expected that during lift off the residual PMMA has taken position on top of the structures.

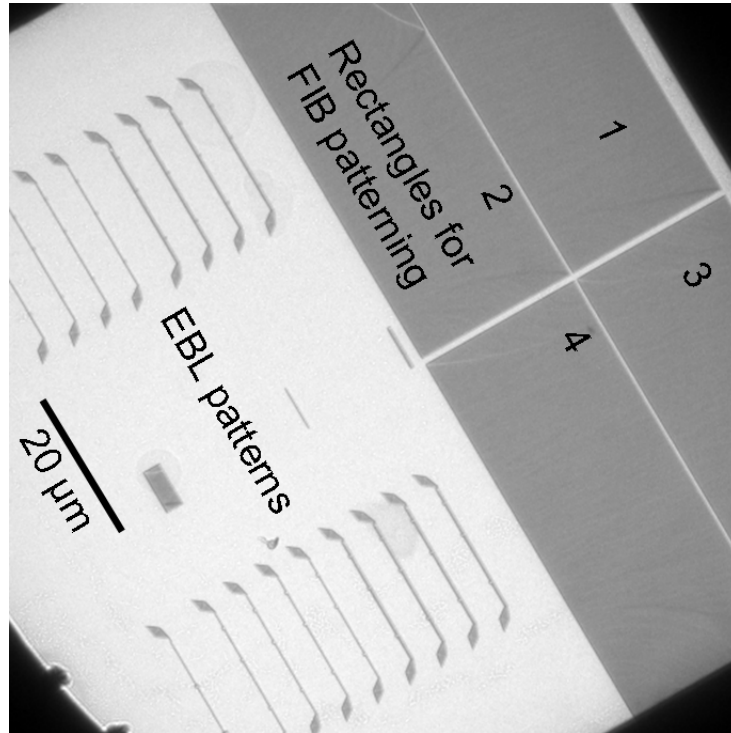


Figure 2.9: TEM image shows both the nanowires and rectangles written by using EBL technique in a single piece of membrane. Later on inside these rectangles, patterns were written using FIB milling.

In **chapter 4**, nominally identical permalloy nanowires fabricated onto a single electron



transparent  $\text{Si}_3\text{N}_4$  membrane using EBL and FIB milling techniques were compared as was already mentioned. The nanostructures were fabricated first by an EBL/lift off process onto one half of an electron transparent  $\text{Si}_3\text{N}_4$  membrane, as shown schematically in Fig. 2.9. In order to write identical structures using focused ion beam milling of a continuous film of Py, four large size rectangular patterns were also written using EBL onto the other half of the same membrane, as shown in Fig. 2.9. Therefore, after lift-off this membrane was inserted in the ion beam microscope to write the identical patterns inside these rectangles using FIB milling (FIB milling will be described in section 2.5.4).

## 2.5 Focused ion beam technique

### 2.5.1 Focused ion beam systems

Focused ion beam (FIB) systems operate in a similar fashion to a scanning electron microscope (SEM) except, rather than a beam of electrons, FIB systems use a finely focused beam of ions for imaging and milling. The basic components of a FIB system consist of an ion source, an ion column, a sample stage, detectors, and a vacuum chamber with auxiliary equipment. High resolution imaging and micromachining of materials needs a highly focused probe, which in turn requires to be formed from as small a source as possible, preferably of the order of 5 nm [16]. Of the existing ion sources for FIB, liquid metal ion sources (LMIS) are the most popular [8] as these sources provide the brightest and most highly focused beam. The operation and development of the LMIS was given in detail in references [17,18]. A schematic diagram of the ion beam column is shown in Fig. 2.10.

Amongst a variety of LMISs *Ga* is the most popular ion species used in FIB systems. Compare to other LMIS species such as In, Bi, Sn, ion source *Ga* is extensively used in commercial FIB systems because of its combination of low melting temperature (30°C), low volatility and low vapour pressure [16]. *Ga* based LMISs are typically more stable and consists of a spiral wound *Ga* reservoir and a tungsten needle. During operation, *Ga* flows from the reservoir to the needle tip by applying a fixed potential to the extraction electrode. Such a large fixed potential between the needle and extraction electrode generates strong electric field at the tip of the needle and thus the liquid *Ga*

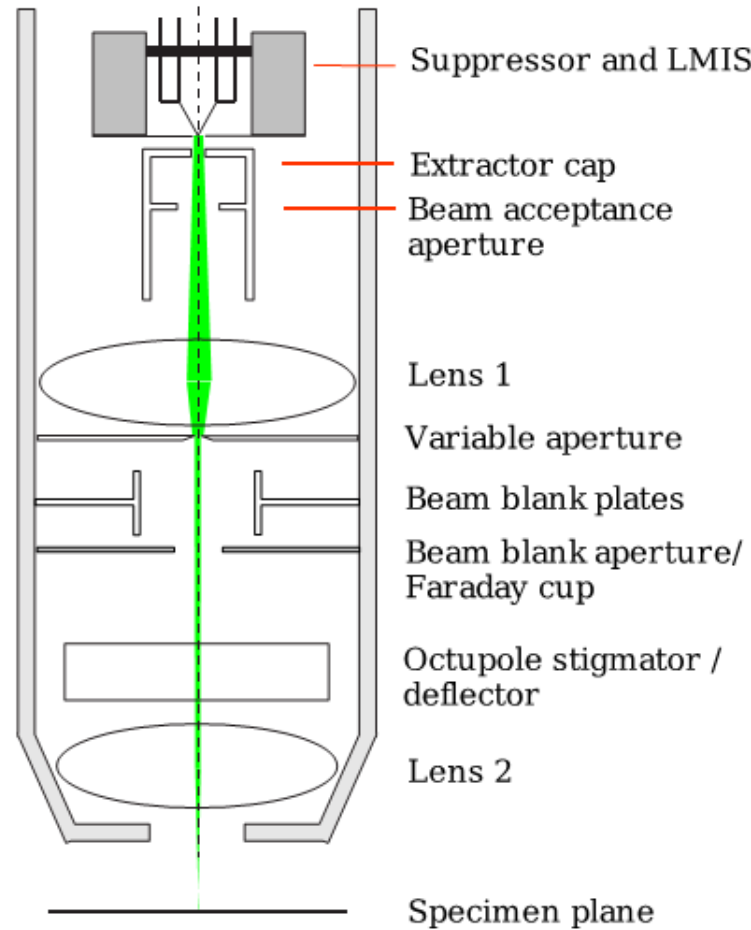


Figure 2.10: Schematic illustration of an ion column.

coating the tip of the needle is drawn into a Taylor cone with a tip radius of 5 nm. The typical emission current in FIB microscope is  $2.2 \mu\text{A}$ . The ions emitted from the LMIS enter an ion beam column which consist of a condenser and objective lens to define the  $\text{Ga}^+$  beam (energy typically 30 keV) and then focus it on the sample surface. The first of the two lenses operates at predetermined potential settings and executes to accelerate the ions through the beam diameter and current defining apertures. In FIB microscopes, the beam currents usually range from 1 pA to 20,000pA with corresponding profiles (FWHM) of 6 nm to 350 nm [19]. During irradiation the beam current is typically chosen so that the beam profile corresponds to the pixel spacing of the pattern to be irradiated. Amongst two electrostatic lenses in ion columns, the second lens controls the convergence of the beam at the specimen surface. The excitation of the lens is user controlled and is normally adjusted to focus the displayed on screen-image. The octupole stigmator/ detector assembly just above the second lens provides control of the scanning, shift and astigmatism of the beam. By selecting the

polarity and voltage of the detector both secondary ions and electrons can be collected to form an image.

### **2.5.2 Dual beam system**

FIB can also be incorporated in a system with both an ion beam and electron beam columns and commonly known as dual platform system. The dual platform FEI Nova NanoLab 200 SEM/FIB workstation that has been used as a tool in the present investigation offers several advantages over a single-beam FIB system. The dual beam system has advanced capabilities, especially for sample preparation and microscopy applications, in which the ion beam can be used for site-specific material removal and the electron beam can be used for imaging without concern of sputtering the sample surface. It is notable that property modifications of the magnetic thin film systems have been carried out in this thesis. Therefore, imaging with the ion beam would cause damage or unwanted property modification in the magnetic thin film samples. Beside this, it would be difficult to make accurate placement of the patterns on an electron transparent window only with an ion beam column.

In the FIB/SEM DualBeam system, the specimen is mounted on a grounded stage with three-axis translation, rotation, and tilt capabilities. The sample stage is designed to have a eucentric point such that the field of view is maintained at the location where the two beam cross when tilting the specimen. In the present investigation using the dual beam system, during operation of the ion beam, the stage is tilted through  $52^\circ$  and therefore the specimen surface was perpendicular to the incident ion beam, as is illustrated schematically in Fig. 2.11.

### **2.5.3 Ion-solid interactions**

The FIB system which was described above depends critically on the nature of the ion beam - solid interaction for milling, imaging and even for depositing material. When energetic ions interact with the surface of a solid material, they may lose energy to the electrons of the solid. This transfer of energy from the ion to the solid results in a number of different processes such as: (i) sputtering of neutral and ionised solid atoms, (ii) electron emission, (iii) displacement of atoms in the solid, (iv) emission of phonons etc [16]. Figure 2.12 shows schematically the electron and ion beam sample interaction

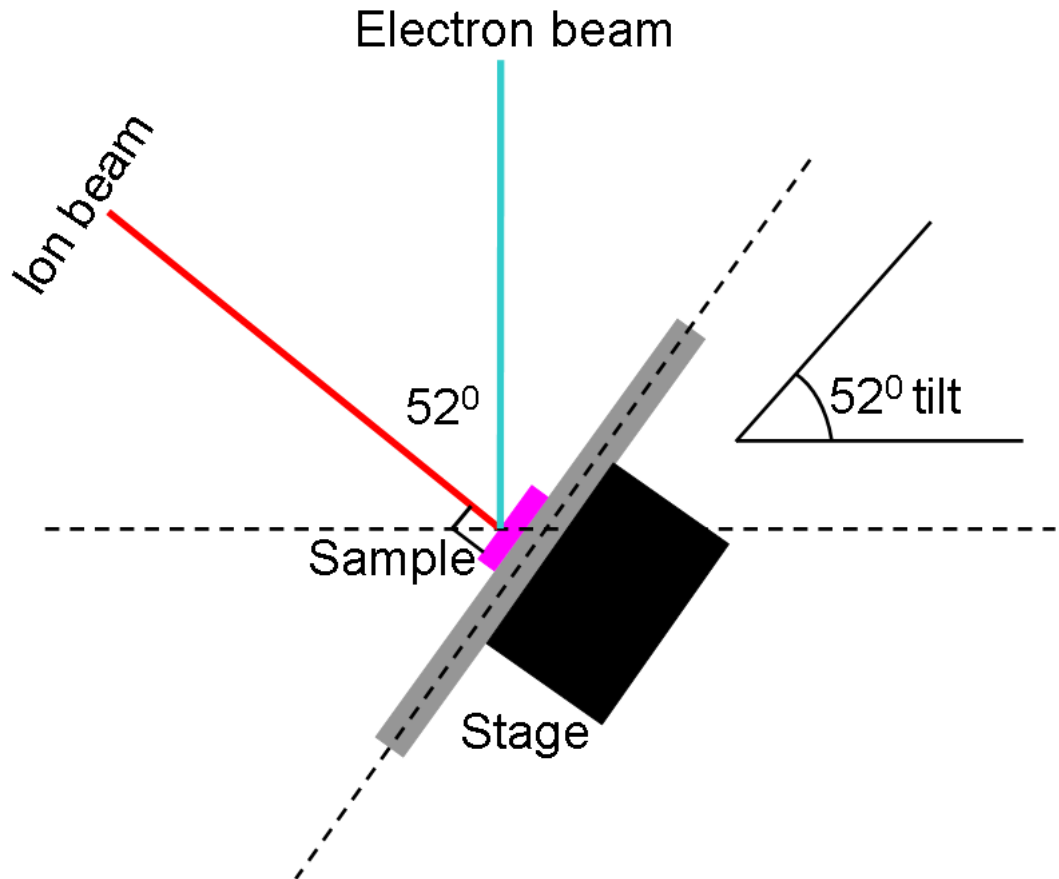


Figure 2.11: Schematic of the dual beam system, in which both electron and ion beams are co-focused at the eucentric point of the sample surface.

along with dual ion beam system.

Upon entering the solid, the ion initiates a 'collision cascade', a succession of encounters with host atoms. Schematic illustration of a collision cascade generated by a 30 keV  $Ga^+$  ion incident on a solid target is presented in Fig. 2.13. This collision cascade [20,21] model is the most widely accepted concept for ion-solid interactions. Depending on the ion energy, the collision cascade may involve a series of independent binary collisions. During successive collisions if the translational energy transferred to a target atom exceeds a critical value called the displacement energy, the atom will be ejected from its original site. This knocked out atom (primary recoil) may have sufficient energy to displace further target atoms (secondary recoils) from their initial sites, thus generating a volume where a huge number of atoms have excess kinetic energy. If a displacement collision occurs near the surface, and if the displacement energy is sufficient to overcome the surface binding energy of the target atom, the atom will be ejected from the solid and lead to sputtering. This sputtering is a dynamical collision

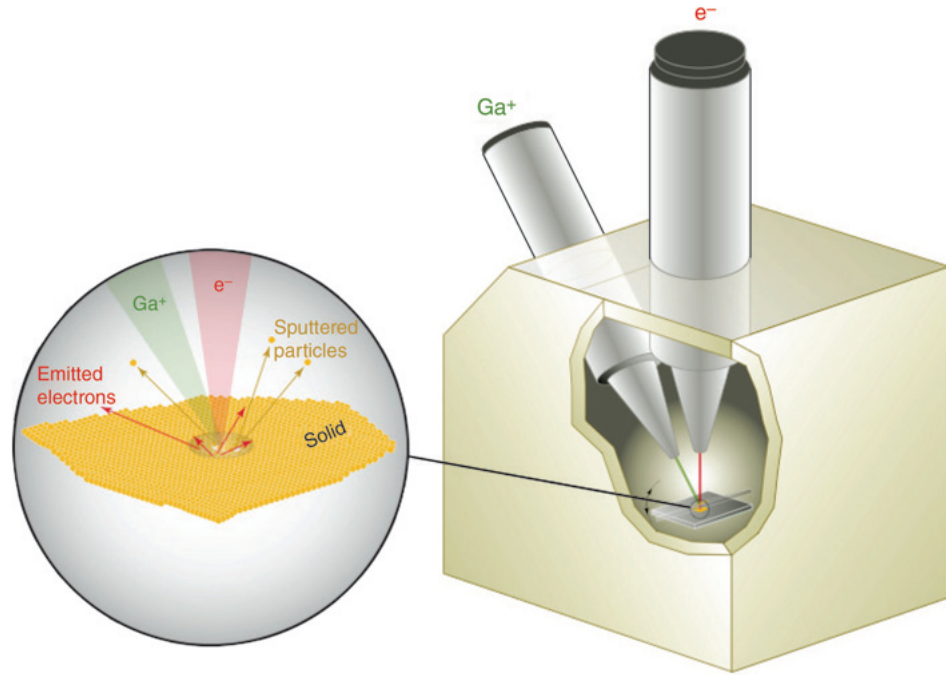


Figure 2.12: Schematic illustration of a dual-beam FIB-SEM instrument. Expanded view shows the electron and ion beam sample interaction. Figure adapted from reference [7].

process and is in fact the governing effect in FIB milling.

The sputtering yield is defined as the number of atoms ejected per incident ion and usually is a measure of the efficiency of the material removal from the solid target. As per the outcome of the Monte Carlo Simulation program TRIM or SRIM (transport, or stopping range, of ions in matter) [22] sputtering yields are between 1 and 20 atoms for normal incidence 30 keV per  $Ga^+$  [23]. The sputter yield is actually a function of many variables, including masses of ions and target atoms, ion energy, direction of incidence to the surface of the target, target temperature etc. If the ion energy is increased, then initially sputter yield also increases. But if the energy is increased enough so that the ions can penetrate deep into the target material, then the sputter yield starts to decrease. This is the stage of interactions when ions become trapped in the solid material [24], a process known as ion implantation. It may be stated that ion implantation is the addition of the incoming ions to the host material, at a depth near the end of the ion's projected range,  $R_P$ . It may also be noted that during sputtering, a portion of the ejected atoms may be redeposited into the sputtered region and ultimately make it difficult to control the amount of material removal by sputtering.

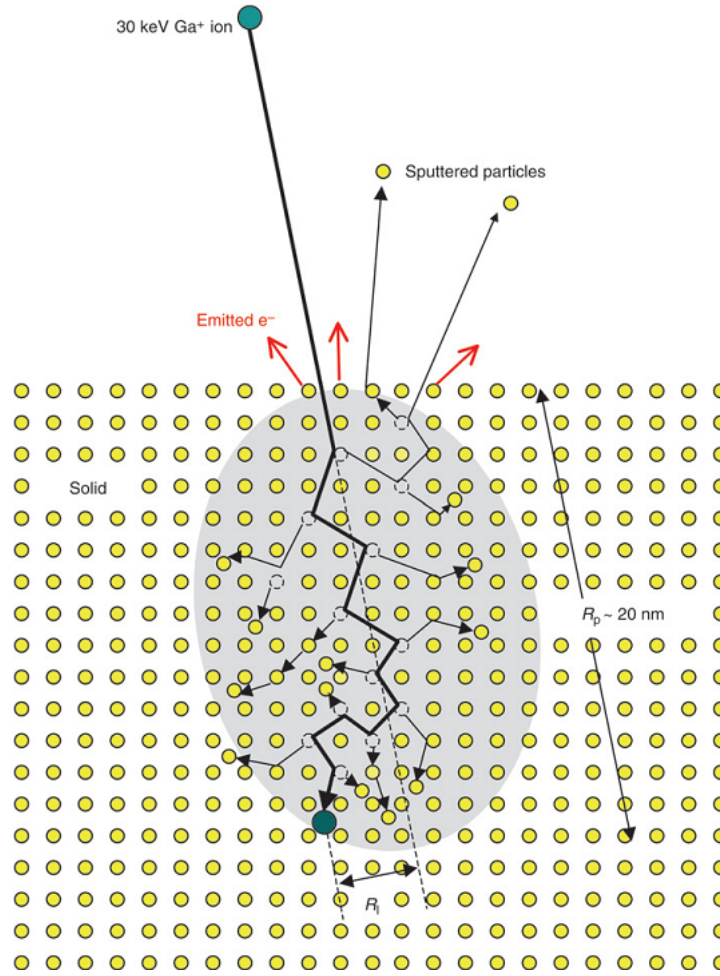


Figure 2.13: Schematic illustration of a collision cascade generated by a 30 keV  $Ga^+$  incident on a crystal lattice, showing the projected range  $R_p$  and lateral range  $R_l$  of the implanted ion. Figure adapted from reference [7].

### 2.5.4 FIB milling

As was described in the previous section, because of the sputtering action of the ion beam, the FIB systems can be used to locally mill away material in a controllable manner. In the present investigation, planar nanowires were fabricated from continuous thin films using the ion beam milling technique. In order to write high quality nanostructures using this subtractive ion beam technique, stage control parameters such as dwell time, pixel spacing and pattern size must be properly adjusted with the main beam energy control parameters [25]. A summary of the main parameters connected with the FIB milling technique is discussed in this section.

It was reported earlier [26,27] that the beam profile of the ion beam is approximately Gaussian. In order to define the nanostructures in the film, a 10 nm full-width-half maximum  $Ga^+$  ion probe (energy of 30 keV and current of 10 pA) was used. To write

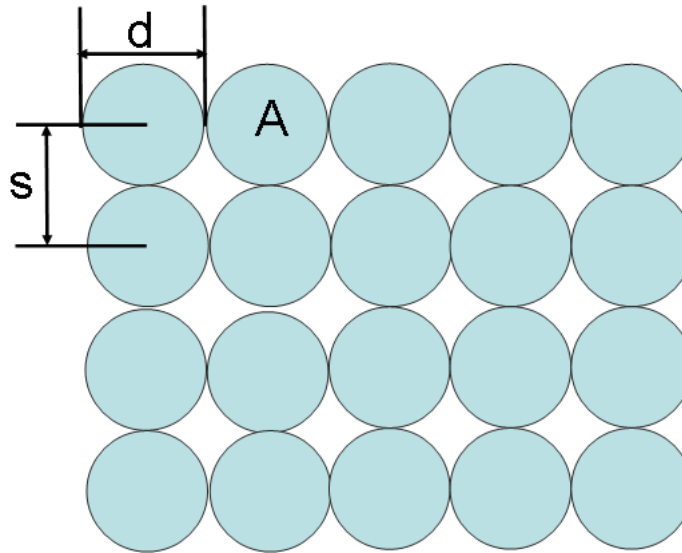


Figure 2.14: Schematic illustration of ion irradiation with 0% overlap, where  $d$  and  $s$  are equal and are the pixel size and pixel spacing, respectively.  $A$  is the area in  $\mu\text{m}^2$ .

a pattern using ion beam milling, the pattern should be first digitised into arrays of pixels, which are either defined by the user as part of the input file, or are the number of pixels on the FIB patterning screen. The absolute distance in  $\mu\text{m}$  or  $\text{nm}$  between two pixels (dwell points) in the pattern is known as pixel spacing. For milling and irradiation purposes, the beam current is typically chosen so that the beam diameter (FWHM) matches the pixel size,  $d$ , as shown in Fig. 2.14, therefore, the pixel overlap is set to zero. This is to ensure that each pixel receives the same dose and that the irradiation effects are homogeneous. The time that the beam is held on each pixel in the pattern is called dwell time. The dwell time per pixel is a parameter that can be directly controlled by the user. For nanoscale patterning, the beam dwell time should be chosen to be reasonable small to obtain more freedom in applying dose as the dose is a multiplication of beam dwell time and number of passes. The number of passes is calculated from the ratio of total dwell time / dwell time per pixel.

As stated earlier, in order to write a pattern in a continuous film, the pattern is digitised into arrays of pixels, arranged in rows (horizontal line) and columns (vertical lines). Two types of scanning procedure, raster and serpentine scans, as shown in Figs. 2.15(a,b), are normally used to steer the ion beam movement. The arrows shown in the figure indicate the direction of scanning. In raster scanning, the scan moves in the same direction throughout the procedure whereas the serpentine scan direction is reversed after each scan or pass. In schematics 2.15(a and b), the solid line delineates

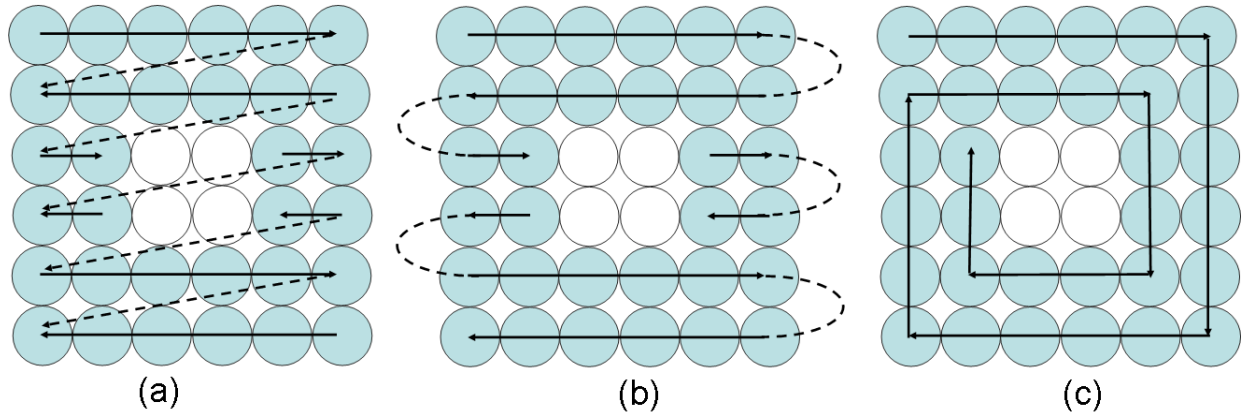


Figure 2.15: Scanning procedures with arrows indicating scanning direction: (a) raster scan (b) serpentine scan and (c) using a stream file generated by the ‘edgestream’ program.

the beam movement and milling can occur in any of the pixels scanned. On the other hand, dotted line illustrates the path taken by the returning passes of the beam. Therefore, in both cases due to the lag in beam blanking time or fly back of the beam as it returns to its starting position any unwanted modification of material that should remain unaffected may occur. This ultimately results in rough edges which will be detrimental to the definition of the pattern.

In the present investigation, the patterns were written using an externally generated stream files (the script was written by Dr. Damien McGrouther, University of Glasgow) containing a list of position coordinates and beam dwell times to be irradiated. These provide a greater control over the motion of the ion beam and ensure that every point receives the same dose. In order to create the stream files, the pattern was first designed in a graphics package and saved in a text based format (the portable grey map, \*.pgm format) so that it could be supplied to a program called ‘edgestream’ which converted the image information into the stream file format [6]. The custom program ‘edgestream’ uses a vector scanning strategy [6] to trace out shape edges rather than rastering, as shown in Fig. 2.15(c), and orders the co-ordinates to control the beam. This program also allows the pattern to be irradiated in several stages or cuts. This multistep approach is necessary to ensure that critical cuts are made in as short a time as possible, thus reducing the effects of stage drift on the definition of the pattern. For the NovaNanoLab 200 SEM/FIB, stage drift is estimated at 10 nm per minute and therefore the first cut was chosen to be small (milling area not the milling depth) so that the patterning (milling) time required less than 1 minute. Following cuts can be



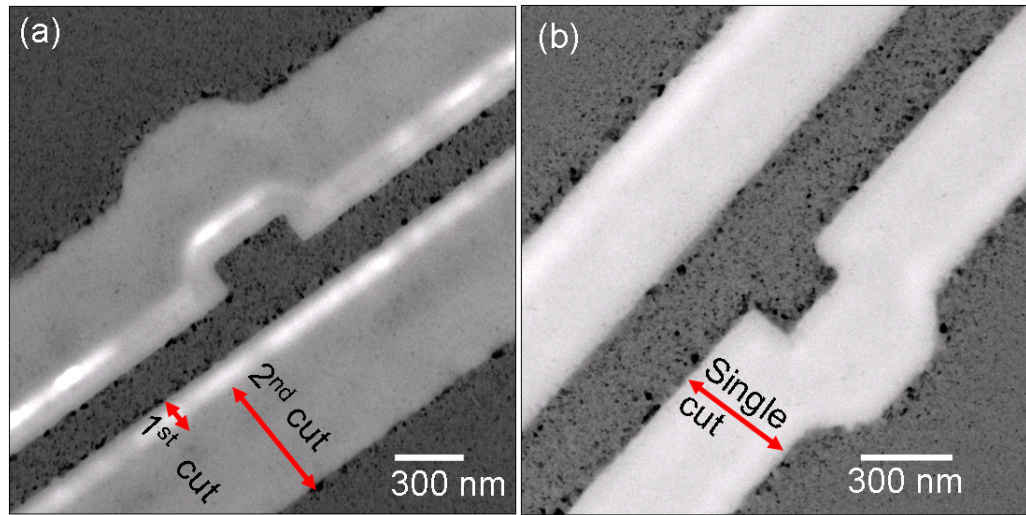


Figure 2.16: TEM bright field images show (a) the creation of holes at the interface of two milling cuts, (b) pattern written by a single cut approach.

larger as any further drift that occurs then will not affect the quality of the pattern definition significantly. During each cut, doses are controlled by the number of passes for a particular beam dwell time and patterning magnification. It is worth noting that, prior to commencing actual patterning, several minutes were allowed to elapse after the last stage movement to let the stage settle. However, during patterning, it was also observed that at the interface of the two cuts, sometimes the ion beam (10 pA beam current) milled the material including substrate completely and creates holes, Fig. 2.16(a), probably due to the dose overlapping from the extended tail of the ion beam. Therefore, to avoid these holes creation in between the two cuts, materials were kept unmilled for a few pixels. Alternatively, patterns were written using a single cut approach using the same beam current, Fig. 2.16(b) but with a reduced milling area. For writing this pattern, milling time was around 1 min, therefore stage drifting did not cause any significant influence. To compare the edge profile of the FIB patterns written by multiple cut approach keeping few pixels unmilled at the interface and single cut approach, TEM cross-sectional samples were prepared using FIB technique (x-sectional sample preparation will be described in section 2.5.6). The results will be addressed in **chapter 4** along with a discussion of the comparatively better techniques for milling.

### 2.5.5 FIB irradiation

The physical and technological consequences of ion beam technologies, in particular ion implantation and ion irradiation in semiconductors, metals and polymers have been

studied comprehensively over the past few decades [28–30]. However, only in relatively recent times [31, 32] magnetic patterning by means of ion irradiation has started to explore the interactions and opportunities for next generation technologies. In the present investigation, ion irradiations were performed to locally modify the magnetic properties of multi-layer (**chapter 5**) and single-layer (**chapter 6**) thin films as a function of irradiation dose using the dual platform.

As was mentioned in the previous section, one of the parameters that the user can control directly in the ion beam microscopy is the dwell time per pixel. The total dwell time for irradiation is given by

$$t = \frac{A \times z}{S \times I} \quad (2.1)$$

where  $A$  is the pattern area in  $\mu m^2$ ,  $z$  is the required milling depth at each pixel in  $\mu m$ ,  $I$  is the beam current in nA and  $S$  is the sputter rate in  $\mu m^3 nA^{-1} s^{-1}$ . The total milling time per pixel for a certain material, for a particular milling depth and beam current is calculated from sputter rate.

In terms of ions  $cm^{-2}$ , irradiation dose is used to calculate using the following expression [33]:

$$D = \frac{t \times I}{e \times A} \quad (2.2)$$

where  $D$  is the dose in ions  $cm^{-2}$ ,  $e$  is the charge on the  $Ga^+$ .

Therefore, for a particular irradiation dose, the total dwell time can be written as

$$t = De \frac{A \times 10^{-8}}{I \times 10^{-9}} \quad (2.3)$$

By rearranging the equations 2.1 and 2.3, the irradiation dose can be written as

$$D = \frac{z}{10eS} \quad (2.4)$$

By using the present version of the FEI software, it is not possible to directly input irradiation dose to the FIB in ions  $cm^{-2}$ . However, by using the above expression, irradiation dose can be obtained in ions  $cm^{-2}$  which is independent of beam current and area and is expressed in terms of variables that are at the users disposal. For ex-

ample, the sputter rate was chosen to have a value of 1000 when performing irradiation experiments. With this value for  $S$  a dose  $1 \times 10^{16} \text{ ions/cm}^2$  corresponds to the input of milling depth  $z = 1.6 \text{ }\mu\text{m}$ . In this way, by varying the milling depth, irradiation experiments were carried out by defining the irradiation dose in  $\text{ions cm}^{-2}$ . The results will be presented in **chapter 5**. TEM cross-sectional sample preparation using FIB milling is described in the next section.

### 2.5.6 TEM sample preparation using FIB technique

The first generation of focused ion beam (FIB) microscopes were mainly used for computer chip repair and circuit modification in semiconductor technology [7]. Since then, the dual beam system has become a powerful tool in TEM sample preparation [34–36]. The development of the advanced 'lift-out' technique has greatly enhanced TEM specimen preparation capabilities [37]. One of the most important advantages of the 'lift-out' technique over many other specimen preparation techniques [34] is the preparation of the TEM sample directly from the bulk specimen. However, the main disadvantage of this technique is that once the TEM sample is mounted on to a coated grid, then additional thinning of the sample is very difficult if it is ever required [34]. The initial attempts of this technique were based on an 'ex-situ' lift out (EXLO) of the specimen containing the feature of interest using a micromanipulator under an optical microscope [37]. The technique was then further developed, based on 'in-situ' lift-out and has recently achieved a paramount importance in TEM sample preparations. The 'in-situ' lift out technique is one of the most flexible FIB specimen preparation techniques since it offers all of the advantages of the EXLO technique with much less FIB re-deposited artefacts. TEM sample preparation processes using the FIB technique have been described in detail in several papers [7, 33, 38, 39]. In the present investigation, cross-sectional TEM samples were prepared using the FIB based 'in-situ' lift-out technique which is described precisely in a recent article [7].

As was mentioned earlier, the nanoscale patterning for the present investigation (results that will be described in **chapter 4**) was performed on a continuous film of Py that was deposited on to the electron transparent  $\text{Si}_3\text{N}_4$  membrane. The preparation of the x-sectional TEM samples of thin films is always challenging, however, the fragility of the  $\text{Si}_3\text{N}_4$  membrane makes it even more so. Nevertheless, attempts were made

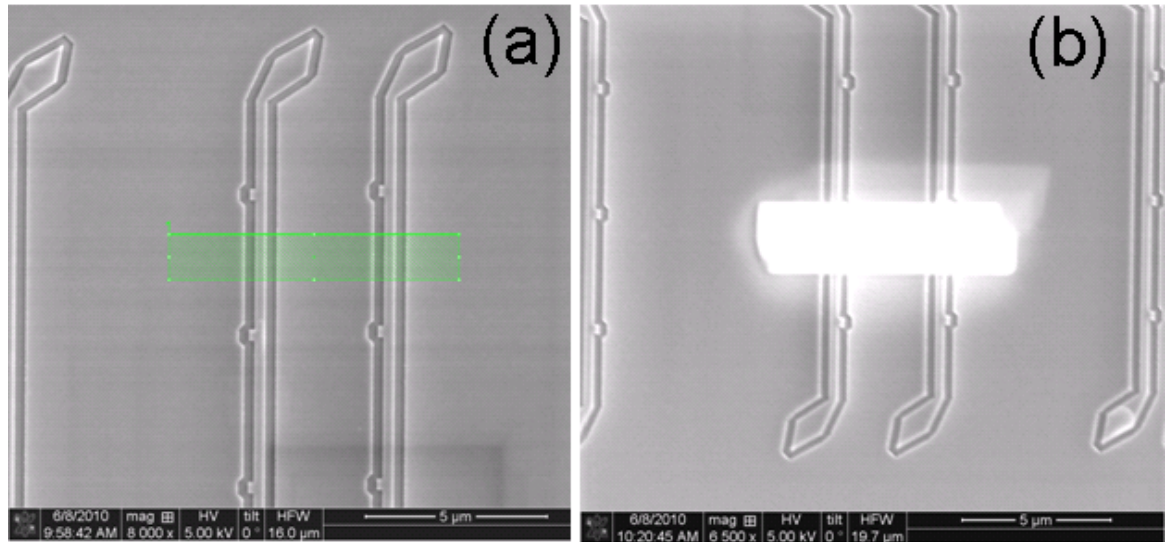


Figure 2.17: SEM images show (a) patterned nanowires written by FIB milling. The rectangular region show the area of interest for x-sectioning and (b) E-beam deposited Pt layer.

to make the TEM sample as thin as possible which is desirable both for high quality imaging and quantitative analytical microscopy. A brief description of the different processing steps of the x-sectional sample preparation for the present investigation is presented below along with the observed difficulties.

In order to obtain a thinner sample and to provide additional support during the milling process, prior to loading the sample inside the FIB chamber, approximately 200 nm Al was deposited in to the back side of the membrane. Additionally, 3 to 5  $\mu\text{m}$  glue which is a heat-cured resin was also deposited next to this Al layer to make the sample to be milled thicker. This was done to obtain additional support to hold the sample during initial rough milling using high beam current (1000 pA) and beam energy (30 keV). To distinguish between e-beam deposited Pt protective layer (described later) and the Py layer, about 5 -10 nm Al was also deposited on top of the Py layer. This Al layer may also serve as a protective layer of the metal surface to avoid any unwanted sputtering. The membrane was inserted in to the oven for a couple of hours to adhere this glue on its back surface.

Afterwards, the sample was mounted in the FIB chamber and using the electron beam about 500 nm Pt was deposited to protect [7,38] the area of the patterned nanowires from where the cross-section will be prepared as shown underneath the rectangle of Fig. 2.17(a,b). The Pt deposition was done by injection of precursor gas flow at the

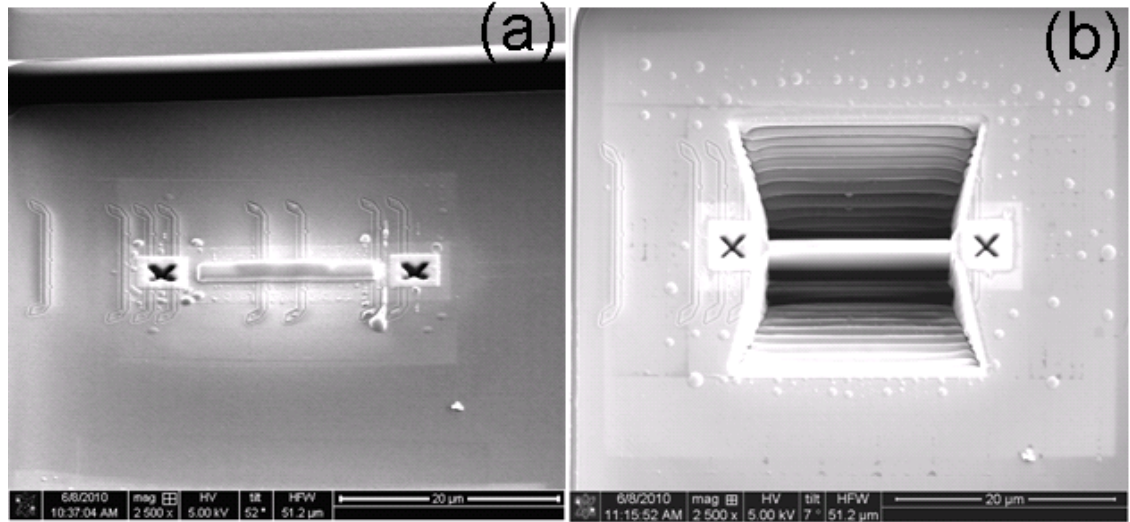


Figure 2.18: SEM image show (a) ion beam assisted Pt protective layer and (b) using 6000 pA beam current rough undercut.

specified area of the sample. It is notable that the Pt deposition can be achieved by injection of precursor gas using focused beams of ions (IBID-Pt, where IBID = ion-beam induced deposition) [40, 41] or electrons (EBID-Pt, where EBID= electron-beam-induced deposition) [42]. The Pt was deposited to prevent damage in the initial phase of the preparation caused by the energetic  $Ga^+$  to the surface of the patterns and also to avoid the spurious sputtering of the region of interest during the subsequent milling process. A large region of the film, including the e-beam deposited rectangle, was then coated by 1  $\mu m$  thick ion beam deposited Pt as shown in Fig. 2.18(a). Prior to the ion beam assisted Pt deposition, two cross-pads were created on either side of the patterns in the horizontal direction to delineate the location of the patterns during rough cutting using high beam currents. The thick layer of Pt was then deposited by the ion beam instead of the electron beam as the deposition rate of ion beam assisted Pt is much higher than that of the e-beam assisted Pt. Furthermore, the quality of the ion beam induced Pt is better due to the less carbon in its compositions than that of the e-beam deposited Pt. Afterwards, by defining a rectangular cross-section below and above the deposited strap, a rough undercut was performed using high current (6000 pA), as shown in Fig. 2.18 (b). Then using 1000 pA beam current and 30 keV beam energy a narrow rectangular undercut was performed and one side of the trenches were cut-out (Fig. 2.19(a)). Instead of the commonly used U shape cut, here it was preferred to make an L shape cut in order to get support to hold the sample.



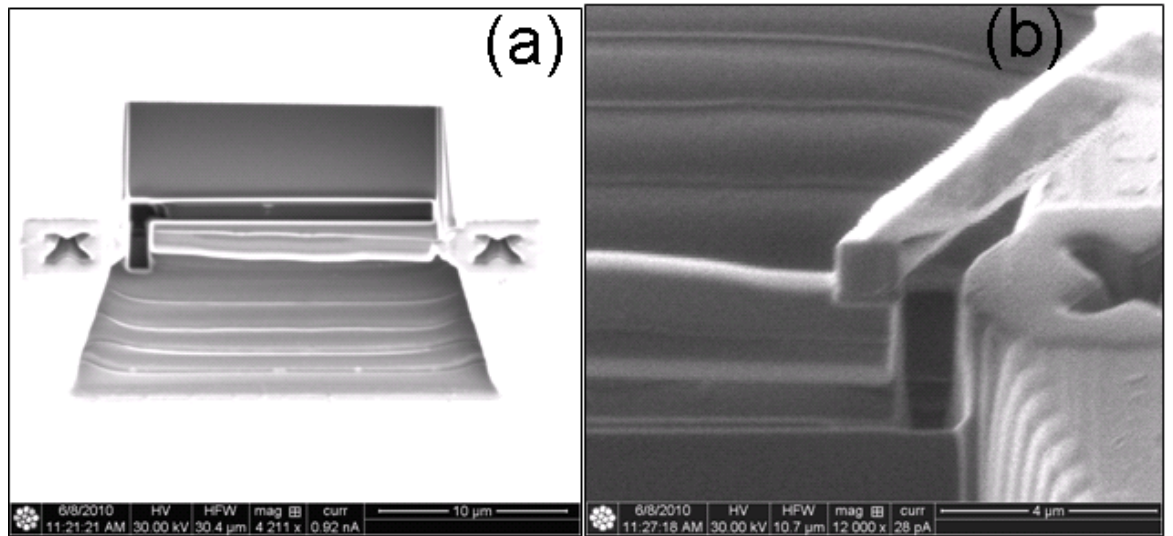


Figure 2.19: SEM image show (a) bulk trench cuts using 1000 pA current, (b) Omniprobe tip and the specimen was welded by depositing Pt.

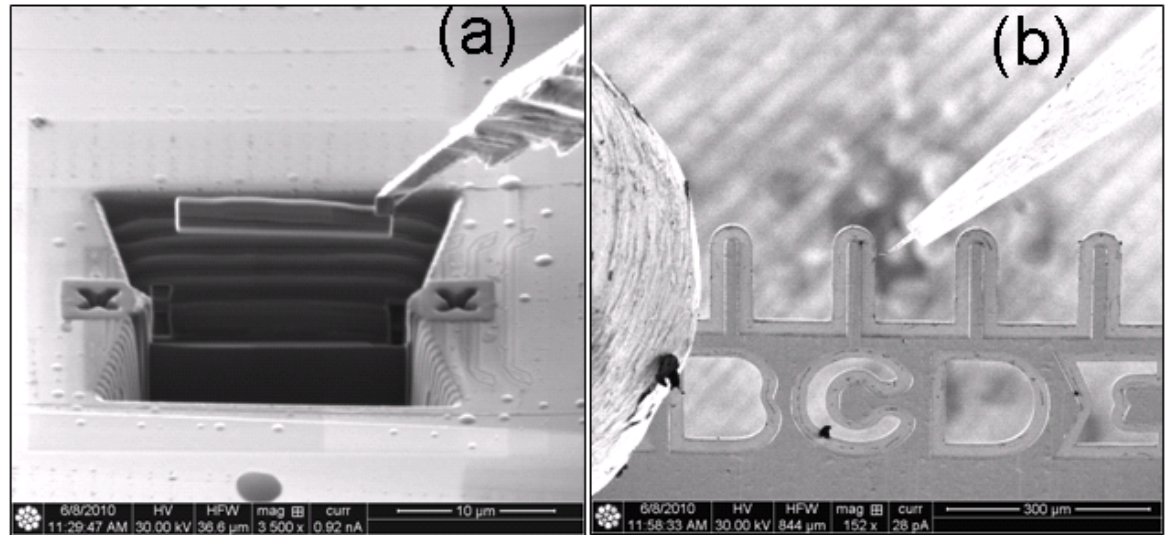


Figure 2.20: SEM images of (a) Pt attach lift-out of the sample with the Omniprobe needle and (b) TEM grid was mounted.

The Omniprobe was inserted and the Omniprobe tip was driven very gently to the coincident point. A small deposition box was defined to weld the Omniprobe tip and the specimen by depositing Pt, Fig. 2.19(b). The remaining material that holds the specimen in place was then released by milling a small rectangle. In this way the specimen is completely attached with the Omniprobe needle as shown in Fig. 2.20(a).

Afterwards the TEM grid was mounted (Fig. 2.20 (b)) and brought in contact. By depositing Pt, contact was established between TEM grid and the sample (Fig. 2.21(a)). The Omniprobe tip was released from the sample again by milling a rectangle and the

## Chapter 2: Materials deposition and nanofabrication techniques

sample was attached to the TEM grid as seen in Fig. 2.21(b). Using smaller beam currents (300 pA) thinning was performed by milling rectangles at two different tilt angles  $\pm 1.2^\circ$  from  $52^\circ$  until the thickness of the x-section reaches to 200 - 300 nm, Fig. 2.22(a). From this stage, the milling current was reduced to 100 pA to perform polishing at tilting angles  $\pm 1.0^\circ$  again from  $52^\circ$  to obtain a thickness of about 80 -100 nm. Using 30 keV beam energy this cleaning cross-section process was carried out from the front and backside (Fig. 2.22 (b)) of the specimen. Some bending (Fig. 2.22(b)) of the specimen arises in this stage of this x-sectional sample preparation. The beam

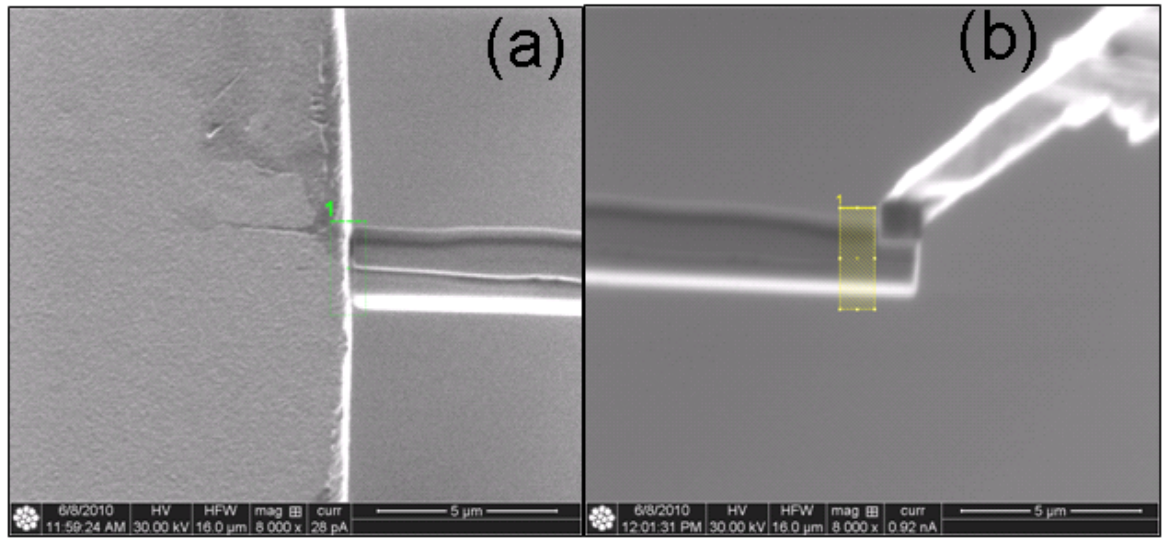


Figure 2.21: SEM images show (a) specimen was attached with the TEM grid and (b) the Omniprobe tip was released from the sample.

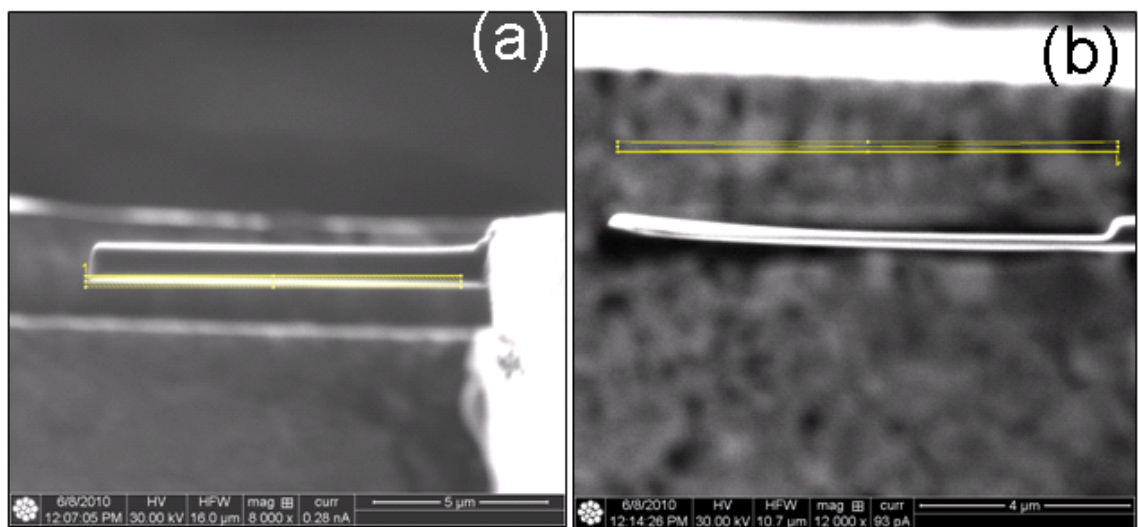


Figure 2.22: SEM images show that (a) thinning was performed at different tilt angles (1.2 degree) using 300 pA currents and 30 keV energy and (b) polishing using cleaning cross-section ( beam current 100 pA and energy 30 keV and tilt angle 1 degree).

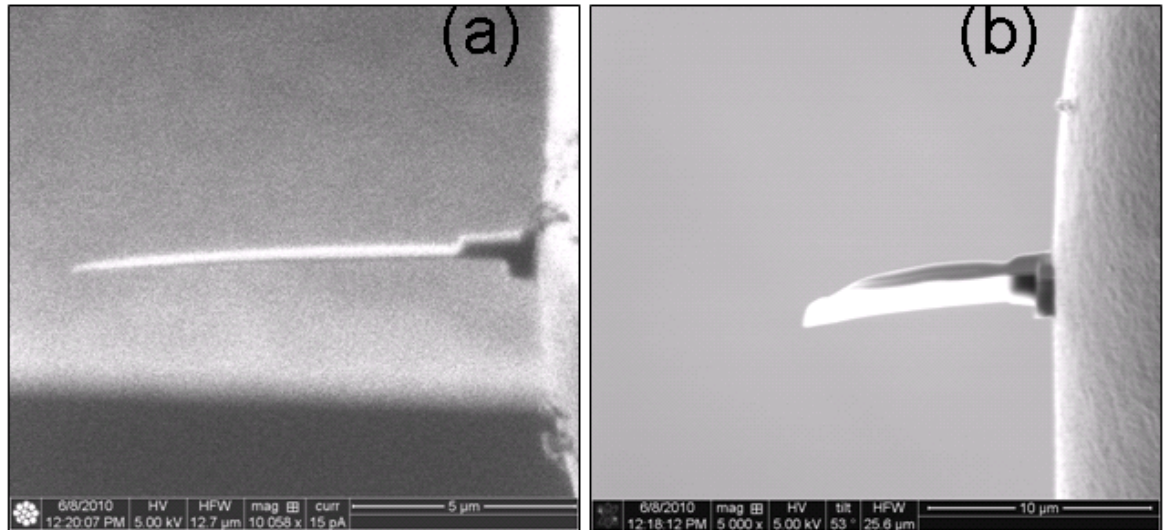


Figure 2.23: (a) Fine thinning of the sample using 5 keV beam energy and 16 pA beam current. (b) X-sectional sample for TEM imaging.

energy is immediately reduced to 5 keV to minimise the damage and *Ga* contamination. The specimen was thinned further using 5 keV beam energy and 16 pA beam current Fig. 2.23(a) to obtain a thickness of about 50 nm. Even though a reduced beam energy and beam current was used, however, further bending as well as twisting of the specimen was observed clearly. Therefore, at some point thinning process was being stopped. Therefore, it was not possible to obtain the same thickness of each of the sample. An SEM image of a x-sectional sample is shown in Fig. 2.23(b). Bright field TEM x-sectional images of the patterned nanowires will be shown in **chapter 4**.

## 2.6 TRIDYN simulation

In **chapter 5** of this dissertation, multilayer thin films of Cr/Py/Cr will be irradiated by varying ion doses to modify the magnetic properties of the films. When such a multilayer film is subject to ion irradiation, the incident ions cause mixing of atoms at the interfaces between the magnetic and non magnetic layers, a process which ultimately plays a vital role in modifying the properties of the films [43, 44].

It was described in section 2.5.3 that a beam of energetic ions interact with a solid substance is slowed down and scattered due to electronic interaction and nuclear collision. Computer simulations of the slowing down and scattering of energetic ions based on the binary collision approximation (BCA) have been established as a versatile tool for more than 40 years [45–47]. They have been employed to study the transport prop-



erties of implanted ions [47–51] as well as the phenomena associated with the atomic mixing [52,53], radiation damage [54,55] and sputtering [46,56]. Amongst a number of codes developed, 'The Stopping Range of Ions in Matter' (SRIM or TRIM) code written by Biersack and Haggmark [57] provides reasonably fast simulations in amorphous substances. Using the TRIM code, the penetration of any atomic ion, with energy between 500eV to 2GeV, into a bulk or multilayer target may be simulated. Any target compound may be selected by choice of target atoms and stoichiometry, and can consist of up to 8 layers of various thickness and composition. The original version of TRIM only considers the slowing down of the fast projectiles and ignores any target recoil atoms. The extended version of this code TRIM.SP [58] includes recoil atoms so that simulations of sputtering could be performed.

However, TRIM simulation does not account for the modification of the target substance during implantation. Thereby, reliable results are strictly valid only in the limit of low implantation fluences. In reality, at high fluences, a significant reordering of the lattice atoms due to the deposition of the projectiles and due to collision transport, including sputtering may occur. This ultimately leads to a change of the local concentrations in polyatomic or multilayered substances. Therefore, a dynamic version of the TRIM code has been developed [59–61] known as TRIDYN to simulate the resulting phenomena of ballistic effects such as incident ion implantation and reflection, sputtering and ion mixing for a target at zero temperature. Using TRIDYN simulation the calculation can be carried out for any ion species at any incident angle. The ion energy is limited by the BCA to  $> 10\text{eV}$  at low energies, whereas at high energies, the limit is determined by computation time and so is less suitable for MeV energies and above. In this investigation, the energy of the incident  $Ga^+$  beam is 30keV and therefore sits well within these limits. The version of the TRIDYN simulation code used for the present calculation is limited by a total of 5 elements. Therefore, during calculations, one approximation defining of the  $Si_3N_4$  substrate as pure Si was made. Ion doses were defined directly as ions per  $cm^2$ . The main use for this program during this research was to optimise the thickness of each layer of the multilayer system Cr/Py/Cr so that uniform Cr concentration can be well controlled in the Py layer, particularly at lower ion dose. The output of these calculations gave the depth profiles of each element in the target as a function of the incident ion dose. An example is shown in Fig. 2.24 for

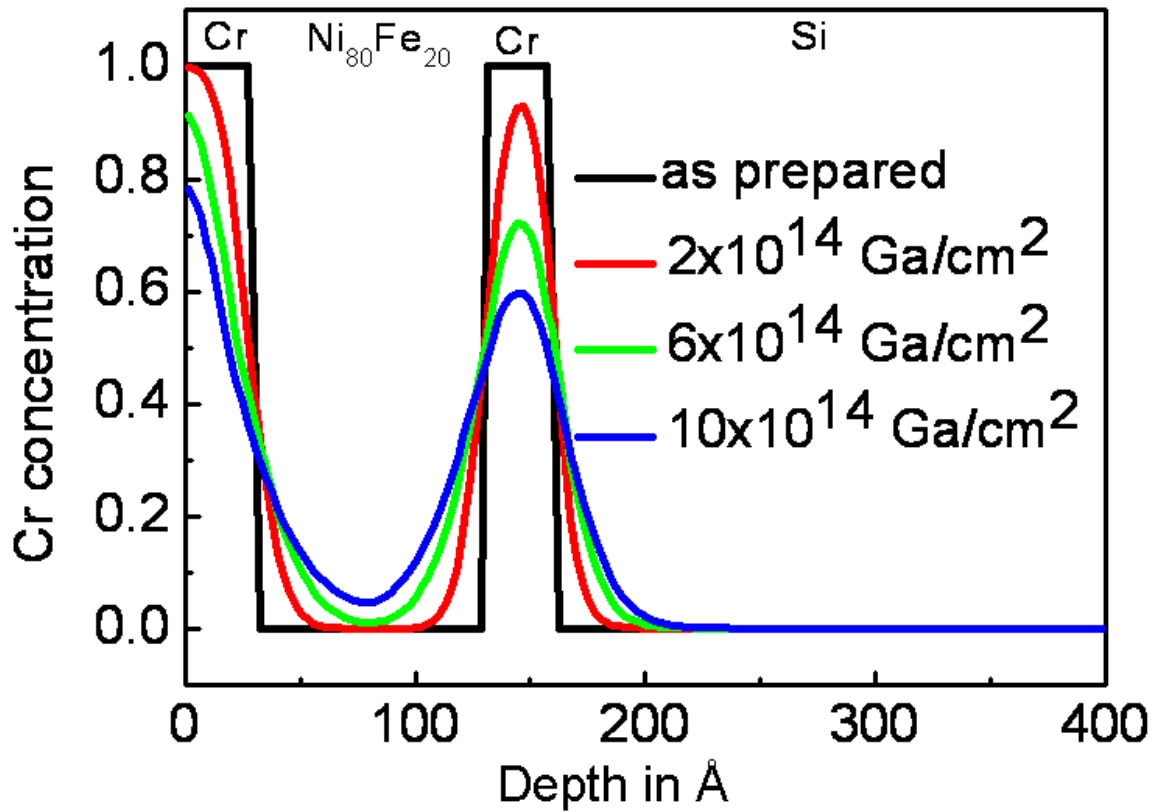


Figure 2.24: Tridyn simulation of Cr concentration profiles with varying dose.

a multilayer thin film system of Cr (3nm)/Py (10nm)/Cr (3nm). This ultimately gave a good indication of the amount of mixing that occurred between the layers due to a particular dose. TRIDYN simulations of the relative concentrations of the individual elements as a function of sample depth before implantation and after implantation at different doses is shown in Fig. 2.25. Atomic concentrations of each element as a function of depth profile provide important information to know the threshold dose below which there is no chance of any mixing of Si in the target. If Si is mixed then the ferromagnetic property e.g. coercivity of the film will be changed. Results from TRIDYN simulations gave us a guideline for realising experimentally micro-alloying locally in this alloy system. Outcomes of the simulations will be used in **chapter 5** to design the material systems and to perform the irradiation experiments.

The target of this investigation is to locally effectively modifying the ferromagnetic properties of Py in a controllable way by focused  $Ga^+$  irradiation. Cr was chosen because up to 8% Cr causes significant changes in magnetic behaviour. Therefore, in **chapter 5** large area irradiation experiments will be carried to observe the changes in magnetic behaviour of the Py film by radiation induced interfacial mixing. Finally,

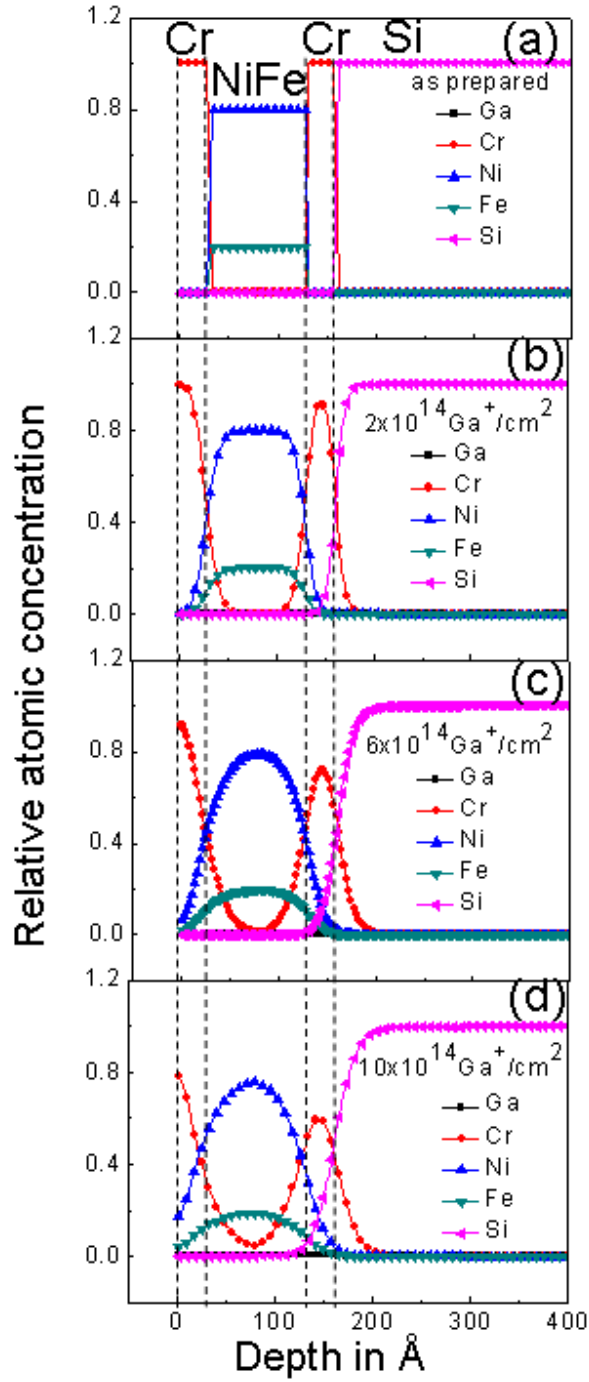


Figure 2.25: TRIDYN simulations of the relative concentrations of the individual elements as a function of sample depth before implantation (a), and for implantation doses of (b)  $2 \times 10^{14} \text{ ions/cm}^2$ , (c)  $6 \times 10^{14} \text{ ions/cm}^2$ , and (d)  $10 \times 10^{14} \text{ ions/cm}^2$ .

isolated nanowires will be patterned using FIB milling of thin continuous film and a single irradiation line will be exposed to create pinning site to control magnetic domain walls.

# Bibliography

- [1] J. I. Martin, J. Nogues, K. Liu, J.L. Vicent, Ivan K. Schuller, J. Magn. Magn. Mater. **256** 449 (2003).
- [2] A. A. Tseng, K. Chen, C. D. Chen, and K. J. Ma, IEEE Trans. Magn. **26** 141, (2003).
- [3] D. Mailly, The European Physical Journal **172** 333 (2009).
- [4] J. Fassbender, J. McCord, J. Magn. Magn. Mater. **320** 579 (2008).
- [5] C.C. Faulkner, D. Atkinson, D.A. Allwood, R.P. Cowburn, J. Magn. Magn. Mater. **319** 9, (2007).
- [6] D. McGrouther, S. McVitie, J. N. Chapman, A. Gentils, Appl. Phys. Lett. **91** 022506-1(2007).
- [7] J. Mayer, L.A. Giannuzzi, T. Kamino, and J. Michael, MRS Bulletin **32** 400 (2007).
- [8] A. A. Tseng, J. Micromech. Microeng. **14** R15-R34, (2004).
- [9] X. Kong, S. McVitie, J. N. Chapman, J. M. W. Weaver and C. D. W. Wilkinson, J. Vac. Sci Tech., submitted for publication.
- [10] B. Khamsehpour, C. D. W. Wilkinson, J. N. Chapman and A. B. Johnston, J. Vac. Sci. Technol. B **14** 3361 (1996).
- [11] N. N. Ledentsov, Growth processes and surface phase equilibria in molecular beam epitaxy. New York : Springer, 1999)
- [12] R. S. Rastogi, V. D. Vankar, and K. L. Chopra, Simple planar magnetron sputtering source, Review of Scientific Instruments **58** 1505 (1987).

- [13] S. Thoms and D. Macintyre, Introduction to ebeam lithography training course, School of Electronics and Electrical Engineering, University of Glasgow, 2006.
- [14] M. Khoury and D. K. Ferry, J. Vac. Sci. Technol. B **14** 75 (1996).
- [15] C. Brownlie, *A TEM Investigation of Controlled Magnetic Behaviour in Thin Ferromagnetic Films*, PhD thesis, University of Glasgow, 2007.
- [16] C. A. Volkert and A. M. Minor, MRS Bulletin **32** 389 (2007).
- [17] J. Meingallis, J. Vac. Sci. Technol. B **5** 469 (1987).
- [18] J. Orloff, Rev. Sci. Instrum. **64**, 1105 (1993).
- [19] XT Novananolab User Manual 4022 262 52351.
- [20] P. Sigmond, Phys. Rev. **184** 383 (1969).
- [21] P. Sigmond, J. Mater. Sci. **8** 1545 (1973).
- [22] J.F. Ziegler, J.P. Biersack, U. Littmark, The Stopping Range of Ions in Solids (Pergamon Press, New York, 1984). The SRIM code is available online at [www.srim.org](http://www.srim.org) (accessed February 2007).
- [23] A. Benninghoven, F.G. Rdenauer, H.W. Werner, Secondary Ion Mass Spectrometry: Basic Concepts, Instrumental Aspects, Applications and Trends (John Wiley, New York, 1987).
- [24] I. Brodie and J. J. Muray, 1992 Particle beams: sources, optics, and interactions The Physics of Micro/Nano-Fabrication (New York: Plenum) chapter 2.
- [25] J. H. Kim, J.H. Boo, and Y.J. Kim, Thin Solid Films **516** 6710 (2008).
- [26] J. Melngailis, J. Vac. Sci. Technol. B **5** 469 (1987).
- [27] A. Kieslich, Reithmaier J P and Forchel A, J. Vac. Sci. Technol. B **12** 3518 (1994).
- [28] J.W. Mayer, L. Eriksson, J.A. Davies, Ion Implantation of Semiconductors, Academic Press, New York, 1970.
- [29] J.S. Williams, J.M. Poate (Eds.), Ion Implantation and Beam Processing, Academic Press, Sydney, 1984.

- [30] M. I. Guseva, G. V. Goedevea, Phys. Stat. Sol. (a), **95** 385 (1986).
- [31] C. Chappert, H. Bernas, J. Ferreacut, V. Kottler, J. Jamet, Y. Chen, E. Cambril, T. Devolder, F. Rousseaux, V. Mathet, and H. Launois, Science **280** 1919 (1998).
- [32] W. M. Kaminsky, G. A. C. Jones, N. K. Patel, W. E. Booi, M. G. Blamire, S. M. Gardiner, Y. B. Xu, and J. A. C. Bland, Appl. Phys. Lett. **78** 1589 (2001).
- [33] B. D. Huey and R. M. Langford, Nanotechnology **14** 409 (2003).
- [34] L.A. Giannuzzi , F.A. Stevie, Micron **30** 197 (1999).
- [35] M.W. Phaneuf , Micron **30**, 277 (1999).
- [36] R. Anderson, Proceedings of Microscopy and Microanalysis, **8** 44 (2002).
- [37] T. Yaguchi, T. Kamino, T. Ishitani, R. Urao, Microsc. Microanal. **5** 363 (1999).
- [38] T. Ishitani and T. Yaguchi, Micr. Res. and Tech. **35** 320 (1996).
- [39] E.C.G. Kirk, D.A. Williams, H. Ahmed, Inst Phys Conf Ser **100** 501 (1989).
- [40] C. Y. Nam, J. Y. Kim, J. E. Fischer, Appl. Phys. Lett. **86** 193112 (2005).
- [41] G. D. Marzi, D. Iacopino, A. J. Quinn, G. Redmond, J. Appl. Phys. **96** 3458 (2004).
- [42] V. Gopal, E. A. Stach, V. R. Radmilovic, Appl. Phys. Lett. **85** 49 (2004).
- [43] Y. G. Wang, D. McGrouther, S. McVitie, M. McKenzie, and J. N. Chapman, J. Appl. Phys. **100** 073901 (2006).
- [44] T. Devolder, Phys. Rev. B **62** 5794 (2000).
- [45] D.P. Jackson and D.V. Morgan, Contemp. Phys. **14** 25 (1974).
- [46] M.T. Robinson, in: Sputtering by Particle Bombardment I, ed. R. Behrisch (Springer, Berlin-Heidelberg-New York, 1981) p. 74.
- [47] H.H. Andersen, Nucl. Instr. and Meth. B **18** 321 (1987).
- [48] M.B. Anttila, A. Fontell and K.B. Winterbon, Rad. Eff. **33** 13 (1977).

- [49] U. Littmark, G. Maderlechner, R. Behrisch, B.M.U. Schemer and M.T. Robinson, Nucl. Instr. and Meth. **132** 661 (1976).
- [50] W. Eckstein, H. Verbeek and J.P. Biersack, J. Appl. Phys. **51** 1194 (1980).
- [51] W. Möller, Nucl. Instr. and Meth. **209/210** 773 (1983).
- [52] T. Ishitani and R. Shimizu, Appl. Phys. **6** 241 (1975).
- [53] F. Ferrieu, Rad. Eff. **62** 231 (1982).
- [54] M.T. Robinson and I.M. Torrens, Phys. Rev. B **9** 5008 (1974).
- [55] M. Hou, Nucl. Instr. and Meth. **182/183** 153 (1981).
- [56] D.E. Harrison, Jr., Rad. Eff, **70** 1 (1983).
- [57] J.P. Biersack and L.G. Haggmark, Nuci. Instr. and Meth. **174** (1980) 257.
- [58] J.F. Ziegler, J.P. Biersack and U. Littmark, Stopping Power and Ranges of Ions in Matter, vol. 1, ed. J.F. Ziegler (Pergamon, New York, 1985).
- [59] W. Möller and W. Eckstein, Nucl. Instr. and Meth. B2 814 (1984).
- [60] W. Möller and W. Eckstein, Nucl. Instr. and Meth. B7 and 8 645 (1985).
- [61] W. Möller and W. Eckstein, Comput. Phys. Commun. **51** 355 (1988).

# Chapter 3

## Instrumentation and characterisation techniques

### 3.1 Introduction

The branch of transmission electron microscopy (TEM) in which the observed contrast is understood in terms of the Lorentz force acting on the moving electrons as they travel through a thin magnetic film is known as Lorentz microscopy. *In situ* Lorentz transmission electron microscopy (LTEM) is the main characterisation technique used in this project for qualitatively and quantitatively determining the magnetisation behaviour of the magnetic nanostructures. The spatial resolution of *in situ* TEM is well suited for nanostructural observation as well as for high quality magnetic imaging of the behaviour of individual structures. In this chapter, the basic principles of TEM and the modes of operation, including Fresnel and differential phase contrast, used for the present investigation are described. Low angle electron diffraction experiments exercised in Lorentz TEM to determine the integrated magnetic induction of the magnetic thin film systems (assuming that film thickness is known), are also briefly described in this chapter.

### 3.2 Transmission electron microscopy

The spatial resolution of an optical microscope is limited by the wavelength of its illumination, so the best optical microscopes are only able to resolve features down to a few hundred nanometres [1]. A high spatial resolution (tens of nanometer) is required however to understand the fundamental properties of the thin film systems



or patterned structures studied in this thesis. To overcome this resolution limit, the concept of an electron microscope was first proposed by the German physicists Ernst Ruska and Max Knoll. The first electron microscope was built in 1931 [2], shortly after the publication of De Broglie's famous theory of electron wave-particle duality in 1925 [3]. Inspired by Einstein's photon description of electromagnetic radiation, Louis de Broglie [3] hypothesised that electrons exhibit wave-like characteristics, with the possibility of wavelengths far shorter than visible light:

$$\lambda = \frac{h}{p}, \quad (3.1)$$

where  $h = 6.625 \times 10^{-34} \text{ J.s}$  is Planck's constant and  $p$  is the momentum of the particle. This ultimately leads to the idea of designing an electron microscope using the electron wave to overcome the resolution limitation of conventional optical microscopes.

The wavelength,  $\lambda$ , of electrons accelerated by a potential difference,  $V$ , is related to their energy,

$$\lambda = \frac{h}{\sqrt{2m_0eV}}, \quad (3.2)$$

where  $m_0$ ,  $e$  are the rest mass and the charge of the electron.

Nowadays, TEMs typically operate using accelerating voltages in the range 100-300 kV and therefore the relativistic kinetic energy of electrons must be taken into consideration. By considering the relativistic effect, equation 3.2 is modified to become:

$$\lambda = \frac{h}{\sqrt{2m_0eV(1 + \frac{eV}{2m_0c^2})}}, \quad (3.3)$$

where  $c$  is the speed of light in vacuum. With a voltage of 200 kV, the operating voltage of both conventional and Lorentz TEMs used in this work, the wavelength is found to be 2.51 pm. This wavelength is much shorter than interatomic distances, however, due to aberrations in electromagnetic lenses, electron microscopes are not capable of this wavelength limit of resolution. Nevertheless, in an electron microscope, imaging is possible with much higher resolution. As a result, since the mid-1970s, the modern versions of commercial TEMs have been equipped to resolve individual columns of atoms in crystals with resolution down to the atomic scale and below [1]. The following section describes the principal components of the conventional TEM and

the modifications that allow Lorentz microscopy to be performed.

### 3.3 The electron gun

In a TEM, electrons penetrate a thin specimen and are then imaged by appropriate lenses, in broad analogy with the optical microscope. The difference is that in a TEM, the illumination system is replaced by the electron beam, and the glassy lens (in optical microscope) is substituted by electromagnetic lens in a high-vacuum column. It is convenient to divide the TEM up into three main components: the illumination system, the objective lens/stage, and the imaging system. The illumination system comprises the gun and the condenser lenses. The two microscopes used for the present investigation, a FEI T20 and Philips CM20, use two kinds of electron sources; a thermionic and a field emission source, respectively. Thermionic sources, typically tungsten and  $LaB_6$ , produce electrons when heated sufficiently to exceed the work function of the particular material.

On the other hand, field emission sources produce electrons from the source material when an intense electric field gradient is applied to it. The source material in a field emission gun (FEG) is typically a tungsten needle oriented single crystal and acts as a cathode with respect to two anodes. The first anode extracts the electrons from tip and the second one accelerates them down the microscope column. To allow field emission, the tip must be free of contaminants which can be achieved by operating under high vacuum conditions ( $< 10^{-10}$  Torr), a process referred to as cold-field emission. By moderately heating the tip, the surface is maintained in a pristine condition and the electrons are thermally assisted in overcoming the barrier, a process known as Schottky-field emission. Schottky emitters are coated with zirconia ( $ZrO_2$ ) that acts to lower the work function and enhance emission. The Philips CM20, the microscope used for *in situ* magnetisation experiments, is fitted with such a source.

The important properties of an electron source are the brightness and spatial coherence [1]. The word 'brightness' is defined as the current density per unit solid angle of the source. The spatial coherence is associated with the source size. The extremely small source size associated with a FEG means that: (a) the beam is highly spatially coherent, (b) the current density is very large, and (c) the brightness is correspondingly

high. FEGs are particularly compatible to imaging techniques like differential phase contrast (DPC) imaging practiced in scanning transmission electron microscopy (will be described later in section 3.7.3) that require a small probe to scan over the surface of the sample.

## **3.4 The microscope column**

In any conventional TEM (CTEM) such as the FEI T20, electrons leaving the gun region enter the condenser system of the microscope column. The condenser system, generally consisting of two condenser lenses and an condenser aperture, acts to control the electron intensity, spot size and convergence at the sample, with the use of a series of magnetic lenses and apertures, as illustrated schematically in Fig. 3.1. Electromagnetic lenses in a TEM control the beam trajectory from the gun to the viewing screen and are responsible for all the basic operational functions of the instrument, for example, magnifying and focusing the electron beam, the images and diffraction patterns. The magnetic lenses used in electron microscopes consists of an iron core called a polepiece with a hole (or bore) drilled through it. There are usually two polepieces in one lens, an upper and lower polepiece, separated by a gap and surrounded by a coil of copper wire to generate a magnetic field when a current is passed through it. The advantage of a magnetic lens compared to the light optical equivalent is that the user can control the strength of the field and the path of the electrons by changing the current through the coils and thereby can change the focus.

The resolution of the microscope is defined as the shortest distance between points in the images that is distinguishable by the observer. The major problem with magnetic lenses in comparison to light optical lenses is that the resolved power (resolution) of the TEM is limited by the aberrations (an intrinsic artefacts/defects of the electromagnetic lenses). In a magnetic lens, it is limited mainly by the spherical aberration which arises from an inhomogeneous lens field (aberration correction is now possible [4]). Such an inhomogeneous field acts to focus off-axis electrons more strongly than on-axis rays. The further off-axis an electron is, the more strongly it is bent towards the axis. Consequently, a point object is imaged as a disk of finite size surrounded by a series of diffraction rings and ultimately limits the resolution of the system. In the case of

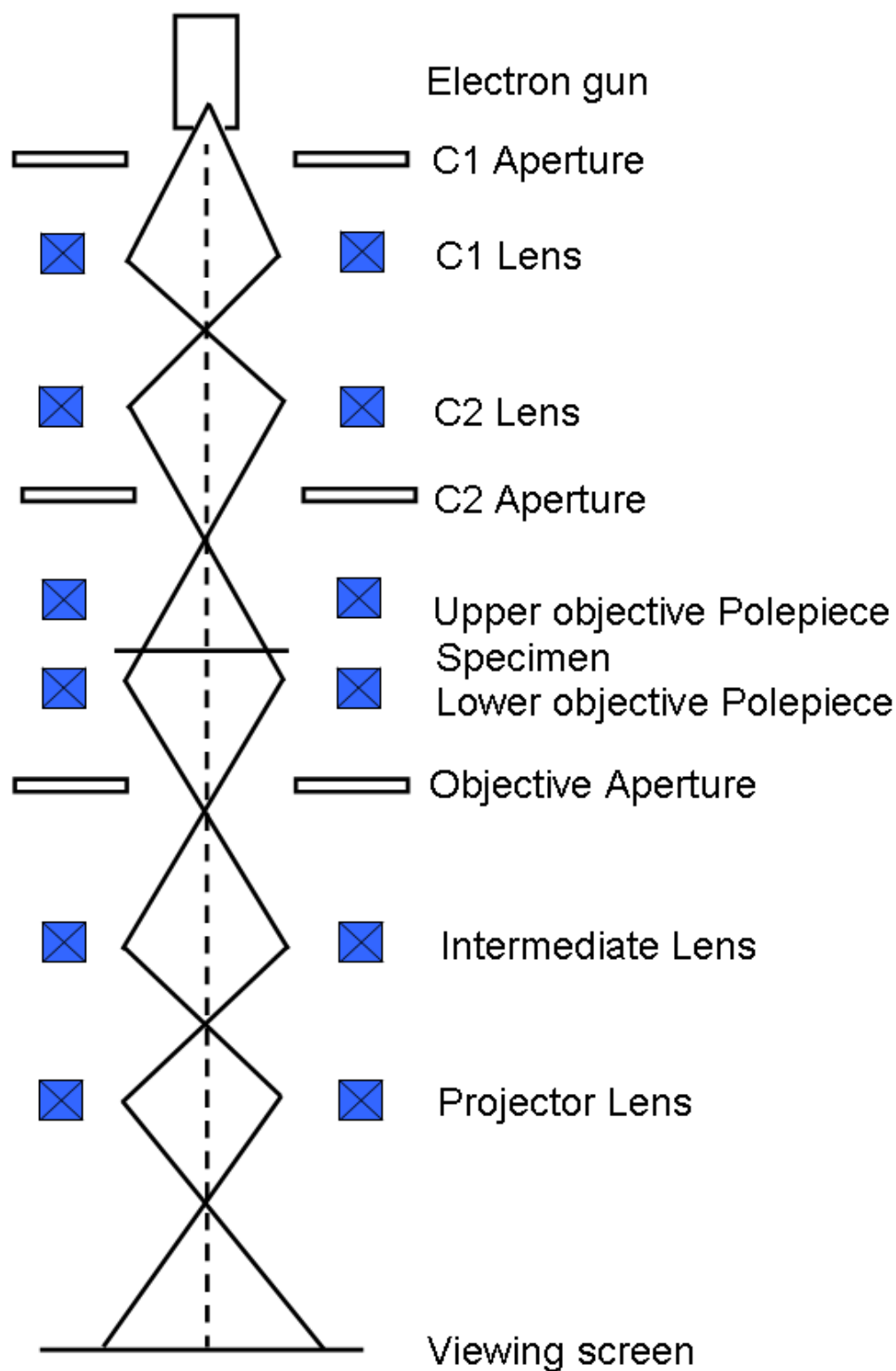


Figure 3.1: Schematic ray diagram of a typical CTEM column illustrating the positions of the various lenses and apertures used to form an image.

Fresnel imaging, lens defocus dominates and determines the resolution of the system, therefore, the effect of spherical aberration can be ignored. For DPC imaging, the finite size of the probe, determined by the condenser system and upper twin lens, is the limiting factor in resolution and not spherical aberration.

The condenser lenses are the first lenses encountered by the electron beam after leaving the gun. In all microscopes used for the work in this thesis there are two main condenser lenses, C1 and C2. The C1 lens forms a demagnified image of the gun cross-over and determines the diameter of the beam on the sample. The user controllable lens, C2, alters the intensity of the illumination by varying the convergence angle of the beam. Further control over the illumination conditions are obtained by the aperture strip. The C1 and C2 apertures control the spot size of the beam incident on the sample and the maximum convergence angle of the beam, respectively. C2 apertures are inserted below the condenser lens system and typically their sizes vary from 20  $\mu m$  to 200  $\mu m$ . Notably, selecting a smaller aperture produces a beam with greater coherence, but with lower total current.

In a CTEM, the specimen is situated between the upper and lower polepieces of the objective lens; the main imaging lens that determines the resolution of the microscope. Electrons, after exiting the condenser lens system, enter the upper polepiece of the objective lens system and are incident on the specimen. A series of intermediate and projector lenses are situated below the objective lens to further magnify and project the image onto the viewing screen. The mode of operation of the microscope, either imaging or diffraction, is selected by the intermediate lens (will be discussed in section 3.5).

#### Image acquisition

In all electron microscopes, electrons scattered by the specimen are detected by the electron detectors which are able to translate the variations in the scattered electron wavefunction to intensity variations that can be observed by the operator. In CTEMs, a viewing screen, coated with a scintillator material and situated at the bottom of the microscope, emits light when an electron strikes its surface. Additionally, in most modern microscopes images are recorded with a digital detector like charge coupled device (CCD) camera situated below the viewing screen. The scintillator plate converts the electron image into a light image and is then transferred to the surface of the pixelated CCD through a fibre optic plate. Images captured by the camera are sent to a computer screen for automatic viewing and further processing of the data.

### 3.5 Structural characterisation

In the present investigation, physical nanostructures of the patterned ferromagnetic thin film elements were characterised by using the two most fundamental operations mode performed in a TEM: electron diffraction pattern and imaging. Electron diffraction experiments were carried out to extract information on the composition of the as-deposited and ion irradiated specimens. Bright field plan view as well as cross-sectional TEM imaging were performed routinely to observe the morphology of the patterned nanowires, particularly around their edges.

#### Electron diffraction

Electron diffraction is a phenomenon which refers to the scattering of electron waves when it encounters a thin crystalline specimen. If two plane waves are incident at an angle,  $\theta$ , on a set of lattice planes ( $hkl$ ), within the crystal, they will be reflected at an equal angle and will interfere with one another (Fig. 3.2(a)). The path difference of two waves is  $2d \sin \theta$ , where  $d$  is the interplanar spacing of the ( $hkl$ ) planes. To obtain the maximum interference, it must satisfy the Bragg's law [5]:

$$n\lambda = 2d \sin \theta \quad (3.4)$$

where,  $\lambda$  is the wavelength of the electrons,  $n$  is an integer number that represents the interference order. When the angle of incidence (measured between the incident direction and the planes) is equal to a Bragg angle  $\theta_B$ , equation 3.4 can be rewritten as,

$$\lambda = 2d \sin \theta_B \quad (3.5)$$

by considering integer  $n=1$  in equation 3.4. In the case of electron diffraction,  $\lambda \ll d$ , therefore, using small angle approximation, equation 3.5 can be rewritten as,

$$\lambda = 2\theta_B d = \theta d \quad (3.6)$$

where,  $\theta = 2\theta_B$  is the angle of scattering of the electron resulting from the diffraction process [6].

Electrons that are Bragg scattered emerge from the crystal suffering a deflection of  $2\theta$  with respect to the incident beam direction, Fig. 3.2(a). Since all electrons that pass

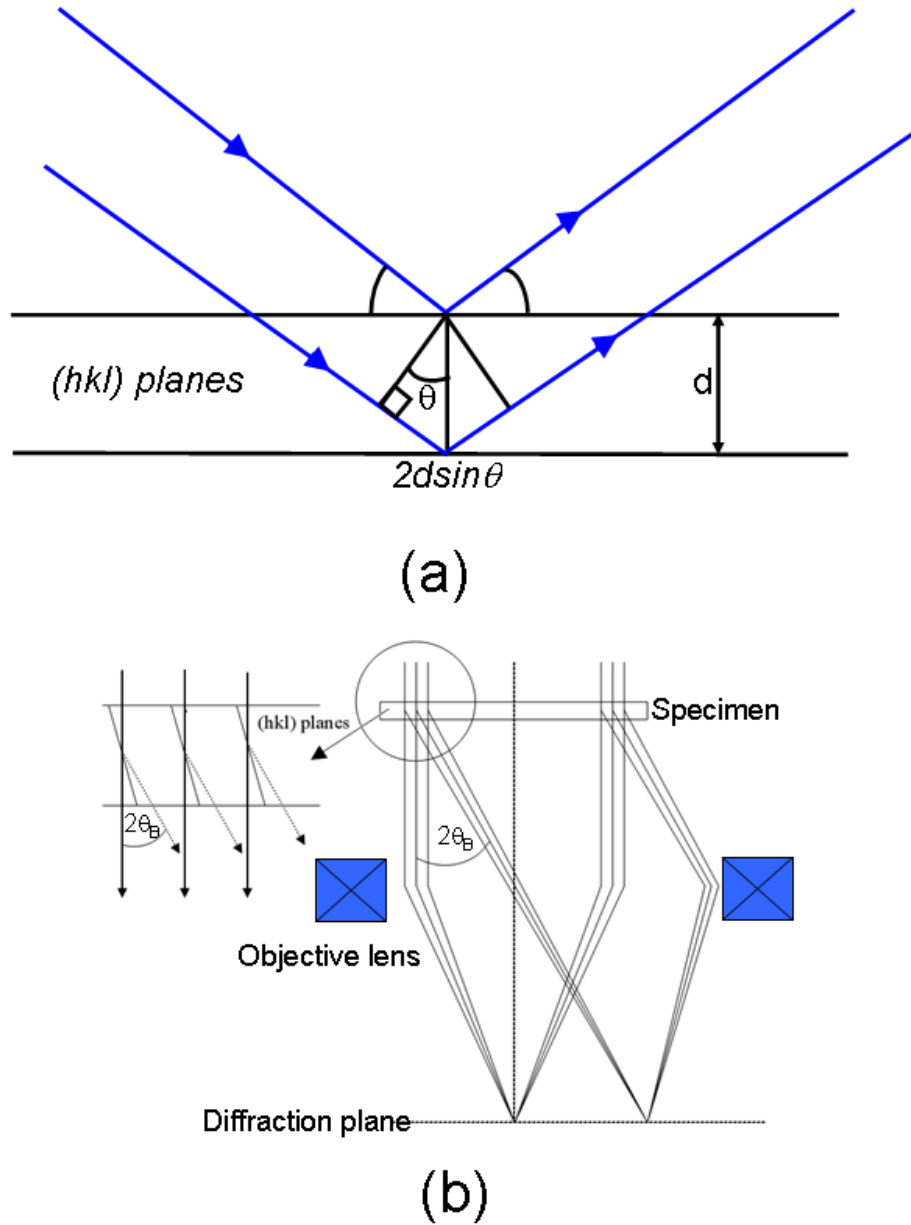


Figure 3.2: Schematically electron diffraction on crystal lattice: (a) two incident waves reflecting on  $(hkl)$  planes are in-phase when their path difference is equal to an integer number of wavelengths, and (b) principle of electron diffraction in the TEM.

through the specimen are brought to focus in the back focal plane of the objective lens, the diffraction pattern is produced in this plane.

An electron beam passing through a polycrystalline material like  $Ni_{80}Fe_{20}$  will produce a diffraction pattern consisting of a series of concentric rings, Fig. 3.3(a). The intensity of the centre of the pattern indicates that the majority of electrons are not scattered and travel directly through the specimen. Electrons diffracted in this manner emerge from exit surface of the specimen at various angles and are focused by the objective lens forming a diffraction pattern in its back focal plane. This relates to the next section

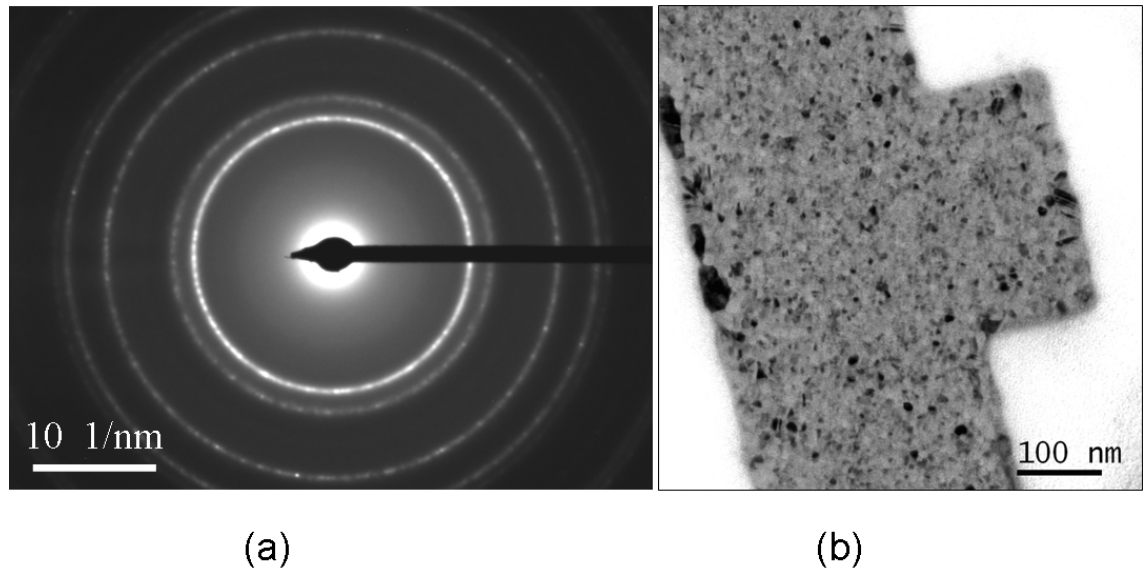


Figure 3.3: (a) An example diffraction pattern obtained in a CTEM (b) Plan view TEM bright field image of a permalloy nanowire patterned by FIB milling showing the grain structure.

and is illustrated in Fig. 3.4.

Notably, polycrystalline specimens contain small crystallites also known as grains, within which the atoms are arranged regularly, however, the direction of atomic alignment varies randomly from one crystallite to the next. The grain structure of a polycrystalline material can therefore be seen in a TEM bright/dark field image as an intensity variation between different regions. TEM bright field image, Fig. 3.3(b) shows the grain structure of a Py nanowire patterned by focused ion beam milling. Note the larger grains around the edge of the nanowire which will be discussed in **chapter 4**.

It should also be noted that, in a single crystal diffraction experiment, the electron wavelength, beam direction and d spacing for each set of planes are fixed. Therefore, only certain lattice planes are able to satisfy the Bragg condition and produce an intense beam. The beams for each of these allowed reflections results in a series of spots not ring like Fig. 3.3(a). A spot diffraction pattern, effectively a 2d map of the reciprocal lattice. The ring patterns is a superposition of all possible spot patterns from the different orientations.



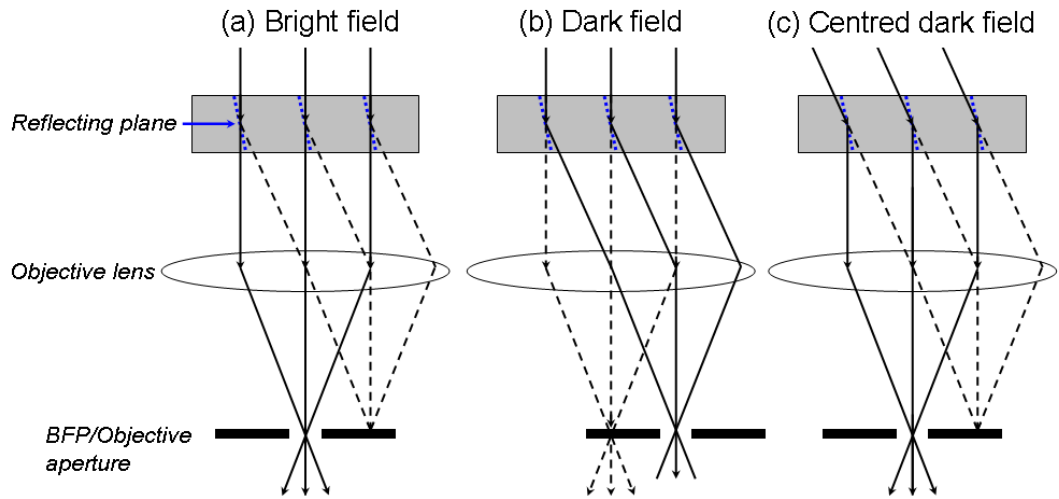


Figure 3.4: Principle of bright-field and dark-field imaging: (a) bright-field image, (b) dark-field image and (c) centred dark-field image.

### 3.6 Bright field and dark field imaging

As already mentioned the two basic modes of TEM operation are diffraction and imaging. In the diffraction mode, the diffraction pattern is viewed by changing the strength of the intermediate lens so that the back focal plane of the objective lens (at which the DP is formed) becomes the object plane of the intermediate lens, Fig. 3.4 (a). On the other hand, in the imaging mode, the image is formed on the screen by setting the intermediate lens so that the object of this lens is the image of the objective lens produced at the image plane.

Figure 3.3(a) shows a selected area diffraction pattern in which bright central spot formed by the direct electrons and several rings produced by the scattered electrons as was mentioned earlier. An image can be formed in the TEM by selecting either the undiffracted beam of electrons (central spot) or some or all of the scattered electrons using an objective aperture. Images formed by centring the objective aperture around central spot as shown schematically in Fig. 3.4(a) are known as bright field images. TEM BF image, Fig. 3.3(b), is an example of a 20 nm thick permalloy nanowire patterned by focused ion beam milling on thin continuous film. Here image contrast arises as a result of variations in electron scattering across the specimen. The permalloy wire causes a greater scattering of electrons than the milled area, hence the wire appears darker in the image. BF image, Fig. 3.5(a) was recorded from the centre region of the wire and also shows clearly the dark grains.

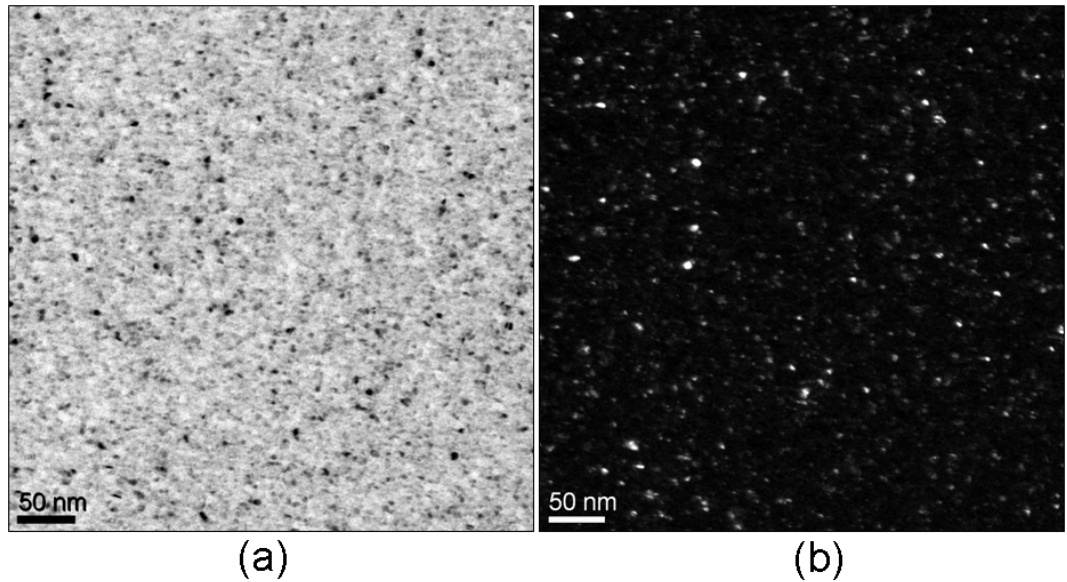


Figure 3.5: An example of (a) bright field (BF) and (b) dark field (DF) plan-view images of the centre region of the nanowire patterned by FIB milling

Instead of selecting the undiffracted beam of electrons to form the image, if the objective aperture is moved and centred around one (or some) of the diffracted beams, then a dark field (DF) image is formed, Fig. 3.4(b). However, in common dark-field imaging, the electrons selected by the aperture in Fig. 3.4(b) travel off-axis and consequently suffer aberrations and astigmatism. To overcome this, the alternative approach is to tilt the incident beam onto the specimen at an angle equal to the Bragg angle, Fig. 3.4(c). Therefore, the scattered electrons will now travel down the optic axis and the direct electrons off-axis. The objective aperture is then centred around the scattered beam to produce the image, an operation commonly known as centred dark field imaging. Figure 3.5(b) is an example of a centred dark field image which was recorded from the centre of the patterned nanowire. The BF image has a higher intensity whereas the DF is less intense but can provide a high contrast of grain/crystallites. During the course of this investigation, TEM plan view and cross-sectional BF imaging was mainly used to observe the morphology of the patterned nanowires, particularly around their edges.

### 3.7 Magnetic imaging in TEM

Magnetic nanostructures and thin film systems display novel magnetisation reversal behaviour as a function of size and shape. Detailed knowledge of the reversal process

is necessary for a greater understanding of their fundamental properties and also for the realisation of the technological applications to which they are suited [7–10]. During magnetisation reversal, basic micromagnetic information such as the nature of the domain walls and many other related phenomena can be obtained using a number of microscopy techniques. These include, transmission electron microscopy (Lorentz TEM, electron holography), scanning electron microscopy (spin-polarised SEM - SEMPA), optical Kerr microscopy, magnetic force microscopy (MFM), scanning tunnelling microscopy (spin-polarised STM), X-ray magnetic circular dichroism (PEEM-XMCD), etc [11,12]. Among them, Lorentz microscopy provides very high spatial resolution and is well suited for *in situ* investigation of the magnetisation behaviour of the magnetic nanostructures. Lorentz microscope technique will be described in the next sections.

### 3.7.1 Lorentz microscopy

Lorentz microscopy is the main imaging technique used for the present investigation of the magnetisation behaviour of the patterned magnetic nanostructures on thin continuous films. The main microscope used is a Philips CM20 FEG TEM/STEM has been optimised for magnetic imaging [13] and was used for *in situ* magnetisation experiments. In conventional TEMs, electrons, after exiting the condenser lens system, enter the upper pole piece of the objective lens. The specimen is situated in the space between the upper and lower pole-pieces of the objective lens. This lens focuses the electron beam to produce a diffraction pattern in its back focal plane and produces a high vertical magnetic field of up to few Tesla which is a problem to study magnetic structure. In the modified CM20, two additional mini-lenses, known as Lorentz lenses, have been inserted to replace the function of the objective lens and thus create a field-free environment for imaging magnetic specimens in both the Fresnel and differential phase contrast (DPC) imaging modes. This microscope also has a scanning capability used for the DPC mode of Lorentz microscopy, as to be discussed in section 3.7.3.

Magnetic imaging using Lorentz TEM [12, 14] rely on small deflections of electrons on passing through thin magnetic specimens. These deflections are a consequence of the Lorentz force and are used to generate contrast in a magnetic sample [15]. When electrons are incident on a thin magnetic specimen, the interaction of electrons with the specimen can be described by both classical and quantum mechanical approaches

by considering electrons as particles and waves, respectively. This is illustrated in the following sections.

### Classical approach

In Lorentz microscopy, if the electrons are considered as particles, magnetic contrast is generated by the deflection of electrons on passing through a magnetic specimen with a component of induction perpendicular to the electron trajectory. Electrons travelling along the  $z$ -axis through a magnetic sample with an in-plane magnetisation, as in Fig. 3.6, will experience deflection in the  $x$ -direction as a result of the Lorentz force,  $\mathbf{F}_L$  given by,

$$\mathbf{F}_L = -e[(\mathbf{v} \times \mathbf{B})] \quad (3.7)$$

$\mathbf{B}$  is the magnetic induction in the specimen,  $e$ ,  $\mathbf{v}$  are the electron charge and velocity. For a parallel beam, which is incident perpendicular to the plane of the specimen (parallel to the  $z$  - axis), the deflection angle due to Lorentz force is given by [16]:

$$\beta_L(x) = \frac{e\lambda}{h} \int_{-\infty}^{+\infty} B_{\perp}(x, y) dz \quad (3.8)$$

where  $B_{\perp}(x, y)$  is the magnitude of the in-plane component of magnetic induction at point  $(x, y)$ ,  $e$  is the magnitude of the electron charge,  $\lambda$  is the electron wavelength and  $h$  is Planck's constant.

For a specimen of thickness  $t$ , with uniform in-plane magnetisation and saturation magnetic induction  $B_s$ , the above expression can be simplified to

$$\beta_L = \frac{e\lambda B_s t}{h} \quad (3.9)$$

with  $B_s = \mu_0 M_s$  where  $M_s$  is the saturation magnetisation. The deflection is thus

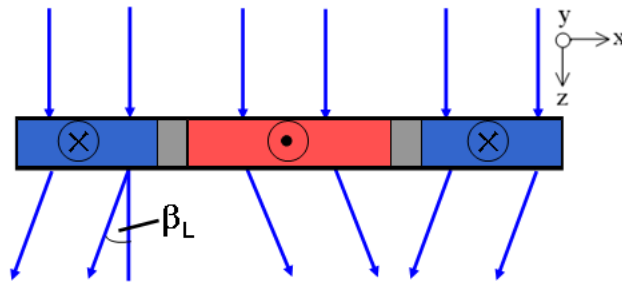


Figure 3.6: Schematically deflection of the electrons due to Lorentz force when passing through a thin magnetic specimen.

proportional to the thickness-induction product.

In the two microscopes used in this work, a FEI T20 and Philips CM20, electrons are accelerated to energies of 200 kV. For a 20 nm thick film with an in plane saturation induction of  $B_s = 1$  T, the deflection angle  $\beta_L$  is  $1.2 \times 10^{-5}$  rad at 200 kV. This means that the magnitude of the deflection angle due to Lorentz force is much smaller than the angle of Bragg diffraction which is of the order of  $10^{-2}$  rad.

### **Quantum mechanical approach**

The above classical description by considering electrons as particles is sufficient to qualitatively explain the principles of Lorentz microscopy. However, to extract quantitative magnetic information, a quantum mechanical approach using the Aharonov-Bohm effect [17] is essential. In a quantum mechanical point of view, the motion of the electron is considered as a wave and the specimen is a phase object. The electrons on passing different paths through a piece of magnetic material is experienced a magnetic phase shift,  $\phi_m$  due to the interaction with magnetic vector potential  $\mathbf{A}$ , and electrostatic phase shift,  $\phi_e$  induced by electrostatic potential,  $V$ .

Electrons travelling along different paths will experience a phase shift,  $\phi_m$ , given by

$$\phi_m(r) = -\frac{e}{\hbar} \int_{-\infty}^{+\infty} (\mathbf{A} \cdot \hat{\mathbf{n}}) dz \quad (3.10)$$

where  $\hat{\mathbf{n}}$  is the unit vector parallel to the beam and  $\mathbf{A}$  is the magnetic vector potential which can be written as a 3-D function

$$\mathbf{A}(\mathbf{r}) = \frac{1}{4\pi} \int \int \int \frac{\nabla \times \mathbf{B}(\mathbf{r}')}{|\mathbf{r} - \mathbf{r}'|} d^3r' \quad (3.11)$$

which is a convolution of  $\nabla \times \mathbf{B}(\mathbf{r})$  and the geometric function  $\frac{1}{4\pi r}$  with  $r = |\mathbf{r}|$ .

$$\mathbf{A}(\mathbf{r}) = \frac{1}{4\pi r} \otimes \nabla \times \mathbf{B}(\mathbf{r}) \quad (3.12)$$

However,  $\nabla \times \mathbf{B}(\mathbf{r})$  can be written in terms of conduction,  $\mathbf{J}_c$ , displacement,  $\mathbf{J}_D$ , and Amperian current densities,  $\mathbf{J}_M$ ,

$$\nabla \times \mathbf{B} = \mu_0(\nabla \times \mathbf{H}) + \mu_0(\nabla \times \mathbf{M}) = \mu_0(\mathbf{J}_C + \mathbf{J}_D) + \mu_0(\mathbf{J}_M) \quad (3.13)$$

Ignoring conduction and displacement currents,  $\mathbf{A}(\mathbf{r})$  can be rewritten as,

$$\mathbf{A}(\mathbf{r}) = \frac{\mu_0}{4\pi r} \otimes \nabla \times \mathbf{M}(\mathbf{r}) \quad (3.14)$$

By inserting this into the phase equation, one can write

$$\phi_m(r) = -\frac{e\mu_0}{4\pi\hbar r} \otimes \int_{-\infty}^{+\infty} (\nabla \times \mathbf{M}) \cdot \hat{\mathbf{n}} dz \quad (3.15)$$

By assuming the film lies in the xy-plane, the beam is incident along the z-direction and the magnetisation is uniform through the film thickness,  $t$ ,

$$\phi_m(r) = -\frac{e\mu_0 t}{4\pi\hbar r} \otimes (\nabla \times \mathbf{M}(\mathbf{r})) \cdot \hat{\mathbf{z}} \quad (3.16)$$

This relation indicates that Lorentz microscopy can be considered as Amperian current microscopy, with the electron phase dependent on the local magnetisation curl component parallel to the electron beam direction. Fresnel images are dominated by out of plane curl for magnetic effects.

From here DPC images can be obtained by taking the derivative of the electron phase perpendicular to the electron beam [18, 19],

$$\nabla \phi_m(r) = -\frac{e}{\hbar} \int_{-\infty}^{+\infty} (\nabla \times \mathbf{A}) \times \hat{\mathbf{n}} dz \quad (3.17)$$

By substituting  $\mathbf{B} = \nabla \times \mathbf{A}$ , equation 3.17 can be rewritten as,

$$\nabla \phi_m(r) = -\frac{e}{\hbar} \int_{-\infty}^{+\infty} (\mathbf{B} \times \hat{\mathbf{n}}) dz = -\frac{2\pi}{\lambda} \beta_L \quad (3.18)$$

This equation shows that the phase gradient is equivalent to the deflection angle. This makes the classical and quantum approaches equivalent.

The electrostatic phase shift,  $\phi_e$  induced by electrostatic potential,  $V$  is given by,

$$\phi_e = \frac{\pi V t}{\lambda E} \quad (3.19)$$

where  $V$  is the mean inner potential of the material, 21 V for permalloy [20],  $t$  is the thickness of the sample,  $\lambda$  is the wavelength of the electron wave and  $E$  is the electron accelerating voltage.

The total phase change is therefore the sum of the two phase contributions,

$$\phi(r) = \phi_m + \phi_e \quad (3.20)$$

Therefore, if the interaction between the electrons and magnetic induction is considered as a change in phase of the incident electron wave, then, Lorentz microscopy may be considered as a branch of phase contrast microscopy. A number of modes including Fresnel, DPC and Foucault represent different methods of capturing the phase change of an electron beam on passing through a magnetic specimen. In the present investigation, only Fresnel and DPC imaging modes were used and are described in the following sections.

### 3.7.2 Fresnel imaging

The Fresnel mode of Lorentz microscopy is a powerful technique for *in situ* studies of magnetisation reversal behaviour in patterned ferromagnetic thin films. This technique can be easily implemented for observing domain walls in patterned/continuous thin films by simply defocusing the imaging lens an amount of  $\Delta$  (defocus) below or above the object plane, Fig 3.7 (a). Schematic diagram 3.7(a) illustrates that electrons passing through an in-plane magnetised film are deflected in opposite direction by the neighbouring  $180^\circ$  anti-parallel magnetic domains. Magnetic domain walls become visible in a defocused image as alternating black and white lines due to alternating convergence and divergence of the electron beam at the wall position, whilst the domains themselves appear with near-uniform electron intensity. The edge contrast that appears on either side of the wall, Fig. 3.7(a) is also notable and will be discussed further later on.

Generally, increasing the defocus gives rise to an increase of the contrast of the Fresnel image, albeit at the cost of poorer resolution. Fresnel images 3.7(b-g) show at three different defocus values, a clockwise vortex domain wall in permalloy nanowires patterned by electron beam lithography (b-d) and focused ion beam milling (e-g). In this patterned nanowire, the central  $180^\circ$  Néel wall along with the vortex core are clearly visible; the two darker lower angle sidewalls are just visible at either side of the central wall. Beside the DW contrast, edge contrast is also visible along the edges of

the nanowires. As an example, in Fresnel images 3.7(b), the thick black fringes that appear along the upper edge of the diamond shape pad and lower edge of the straight wire, marked by A and B, respectively, indicates that these two sections are magnetised in opposite directions and is consistent with a DW existing at the corner position between the pad and the wire. However, the contrast at the edge of the wire is not purely magnetic contrast because of the variation of electrostatic phase at the edge. For wires fabricated by FIB, significant grain growth was observed along the edges of the nanowires (will be addressed further in **chapter 4**). Diffraction contrast from

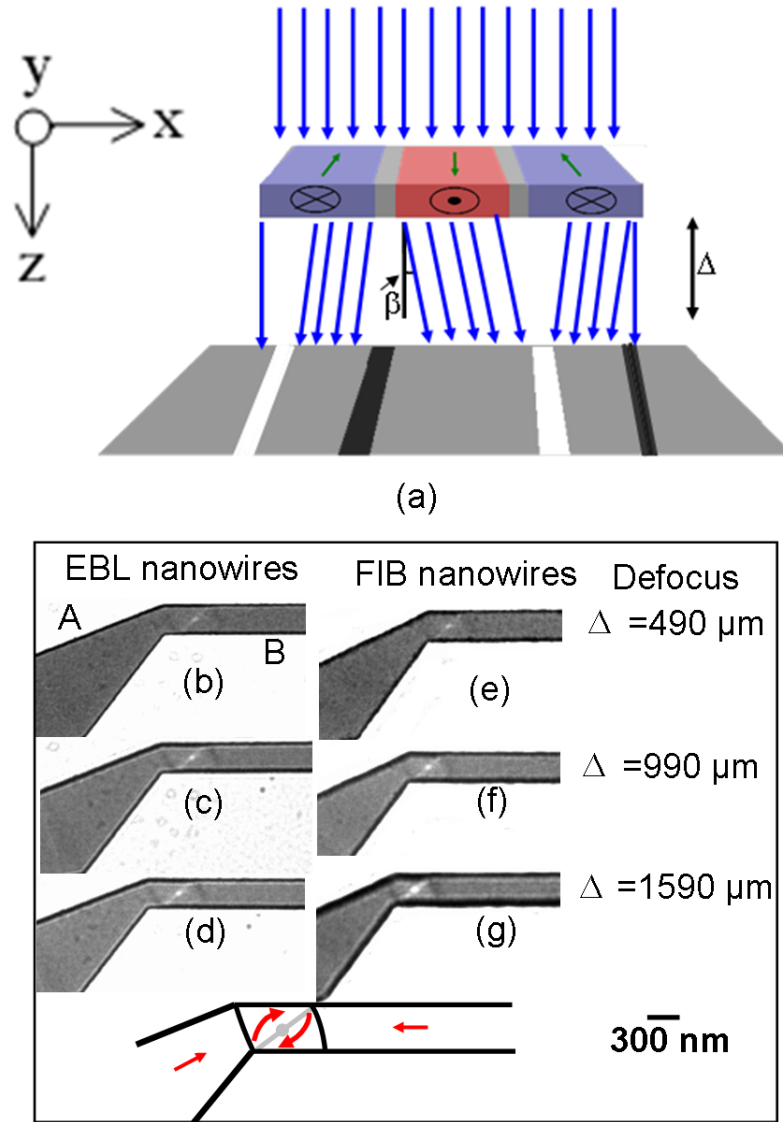


Figure 3.7: (a) Schematic illustration of the principle of Fresnel imaging mode. The main imaging lens is defocused a distance  $\Delta$  above or below the specimen plane to observe contrast at the positions of domain walls and at the edges of the element. Fresnel images (b-g) demonstrate a vortex domain wall at different values of  $\Delta$  in nanowires patterned by electron beam lithography (b-d) and focused ion beam milling (e-g).



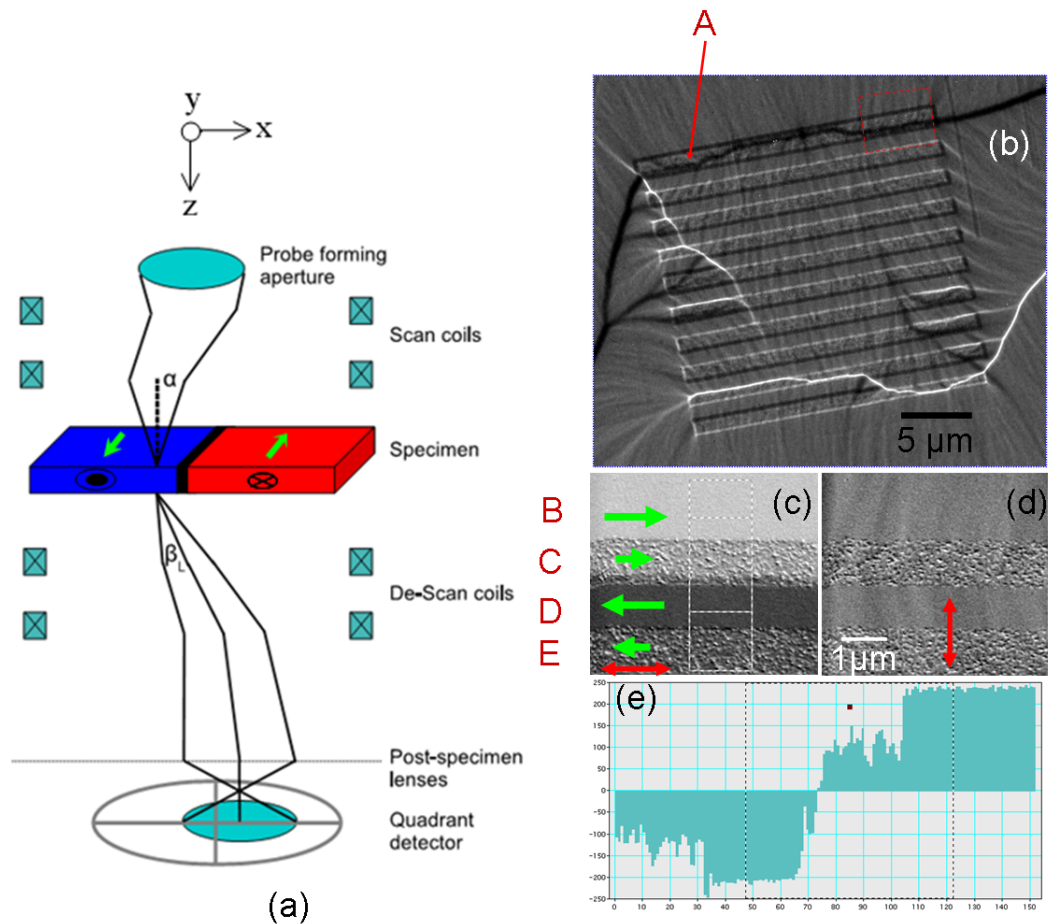
the crystallites is also an issue along with the electrostatic edge contrast. At smaller defocus, images (b,e) edge contrast is not very prominent but wall contrast is also not very clearly visible as well. Using a larger defocus, images (d,g), increases the magnetic contrast, however the image resolution becomes poorer. Hence, a compromise must be made for choosing defocus value to maximise the magnetic contrast whilst preserving the image detail and images (c,f) with intermediate defocus value may be a good choice in this example.

The Fresnel technique involves defocus with resolution at best, 30 nm. However, the advantages of Fresnel imaging for studying magnetic specimens include its simple operation and the high levels of contrast. The real-time *in situ* imaging i.e. allowing reversal sequences to be recorded during magnetising experiments is another notable advantage of this technique. However, in order to extract magnetic information quantitatively e.g. domain wall width that will be measured in **chapter 6**, differential phase contrast mode of Lorentz TEM was used. This particular mode of Lorentz TEM is described in the next section.

### 3.7.3 Differential phase contrast imaging

Differential phase contrast (DPC) mode of Lorentz microscopy [16, 21, 22] provides a greater spatial resolution (down to less than ten nanometres [21]) than Fresnel imaging as the images acquired are in-focus. DPC is one of the leading techniques to image the magnetic nanostructure and was used in this thesis (**chapter 6**) to investigate the details of the switching behaviour in narrower stripe patterns written by focused ion beam irradiation. The domain width as a function of wall angle in the continuous film and also in the patterned film was also calculated using DPC images. These results will be presented in **chapter 6**.

The microscope used for the Fresnel imaging has a scanning capability and is used also for the DPC mode of Lorentz microscopy. The principle of DPC imaging mode is illustrated schematically in Fig. 3.8(a). The DPC technique requires the field emission gun to create a very highly monochromatic electron beam and the beam is focused to a small probe. The probe is controlled to scan across the specimen by scanning coils and emerges as a cone of illumination which subsequently falls onto a segmented detector, as illustrated in Fig. 3.8(a). In the absence of a magnetic sample, the beam will



of integrated orthogonal magnetic induction perpendicular to the electron trajectory are obtained. A bright field image is also obtained by simply summing the signals from all four quadrants. In this way, the parallel acquisition of magnetic and physical images of the specimen can be achieved. Fresnel image, Fig. 3.8(b) shows a reversal sequence recorded during magnetising experiments performed on alternate unirradiated and irradiated stripe patterns on  $16.9 \pm 0.8$  nm thin continuous permalloy film (in details results will be presented in **chapter 6**). The irradiated stripes were written by focused ion beam technique using a 30 keV  $Ga^+$  ion beam with a current of 10 pA. An ion dose of  $6.24 \times 10^{15}$  ions/cm<sup>2</sup> was applied on the irradiated stripes. During this stage of the experiment, an 180° black contrast domain wall propagate along the irradiated stripe marked by 'A'. Due to the presence of 180° domain wall, the magnetisation in the irradiated and non-irradiated stripes of either side of the wall have opposite components along the stripe axis.

Figures 3.8(c) and (d) show a pair of orthogonal DPC images of the stripe patterns recorded from red rectangular region of Fresnel image, Fig.3.8(b). Red arrows in Figs. 3.8(c) and (d) indicate the direction of magnetic induction each image is sensitive to. In the induction map along the stripe axis, the continuous film and the uppermost irradiated stripe marked by B and C, respectively, is much brighter compare to the intensity of the unirradiated and irradiated stripes marked by D and E, respectively of the other side of the domain wall. The intensity profile taken from the marked region perpendicular to the domain wall showing these four regions, Fig.3.8(e). By using the difference signals from this intensity profile of the unirradiated and irradiated

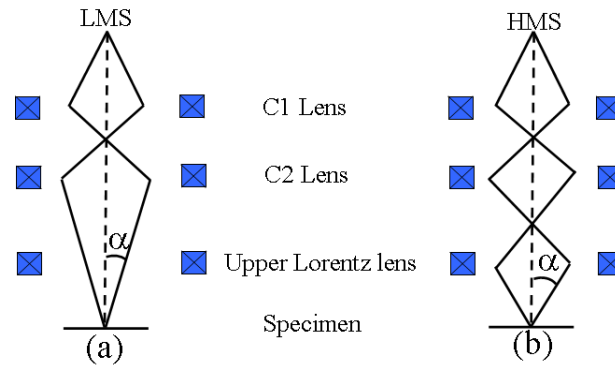


Figure 3.9: (a) Schematic illustration of the low magnification scanning (LMS) in which the upper Lorentz lens is switched off to form a larger probe at the specimen. (b) Schematically high magnification scanning (HMS) mode in which the Upper Lorentz lens is switched on to achieve a smaller probe at the specimen.

stripes, it is possible to calculate magnetic deflection angle  $\beta_L$  of the unirradiated and irradiated stripes. If  $\beta_L$  is known, then we can calculate integrated magnetic induction using equation 3.9. In this present investigation, we have measured the reduction of integrated magnetic induction of the Py film due to  $Ga^+$  irradiation. Notably, FIB induced grain growth was observed in **chapters 5 and 6** due to  $Ga^+$  irradiation directly in the micron size irradiated stripes. This ultimately made the signals of the irradiated stripes bit more noisy. Therefore, we have measured the reduction of integrated magnetic induction of the Py film due to  $Ga^+$  irradiation using low angle electron diffraction experiments (this technique will be described in section 3.10) instead of DPC images.

The DPC mode is an in-focus imaging mode and the resolution of the image produced in the DPC mode is limited by the diameter of the probe. This varies depending on the mode of operation, either low magnification scanning (LMS) or high magnification scanning (HMS). In LMS mode, the upper Lorentz lens is turned off, resulting in a larger probe at the specimen and a probe convergence angle, ( $\alpha$ , of around  $150 \mu rad$ ), as shown in Fig. 3.9(a). On the other hand, in HMS mode, Fig. 3.9(b), the upper Lorentz lens is switched on to form a finer probe below 10 nm with large probe angle, around 1 mrad. Therefore, using a HMS mode a greater useful magnification is achievable with very high spatial resolution by scanning a smaller area of the specimen with a finer probe. In the present investigation, using the HMS mode of Lorentz microscopy, domain wall width was calculated as a function of wall angle both in the continuous Py film and also in the patterned constrained film. The results will be presented in **chapter 6**.

The advantages of the DPC technique are that it can be used to obtain quantitative magnetic information at a very high spatial resolution of below 10 nm, provided a FEG microscope is used. In DPC images, due to the phase gradient experienced by the electron beam between areas containing the magnetic specimen and those with the supporting substrate, edge contrast arising from electrostatic phase contribution is also present. However, as DPC is an in-focus mode though, these fringing effects are less than in Fresnel images. The main disadvantage of DPC technique is the instrumental complexity and operational difficulty compared with the fixed-beam imaging modes. Notably, micromagnetic simulations provide a useful guide to assist interpretation of

the experimentally observed micrograph's captured using both Fresnel and DPC mode of Lorentz TEM. In the next section Lorentz image calculation will be described with the aid of examples of nanowire structures.

### 3.8 Lorentz image calculation

Micromagnetic simulations using OOMMF package were carried out routinely during the course of this investigation. One example of this theoretical modelling can be observed in **chapter 4** where nanowires were patterned on thin continuous films by two different fabrication techniques, EBL and FIB. However, TEM cross-sectional images showed that the edge profiles of the patterned nanowires were varied with fabrication techniques. The propagation of domain wall along these patterned nanowires were investigated by *in situ* magnetisation experiments and were compared between nanowires patterned using alternative fabrication processes. For a greater understanding of the DW behaviour as they propagate along these patterned nanowires, micromagnetic simulations were carried out for ideal (rectangular) edge profiles and also for experimentally observed edge profiles of the patterned nanowires. From the outcome of a given simulation, Fresnel and DPC images may be calculated providing certain microscope parameters are known.

The interaction of the electrons passing through a region of magnetic induction is the basis for the generation of contrast in Lorentz microscopy, because of the deflections experienced by the electrons. Lorentz images of the simulated elements may be calculated using the phase of the electron wave (as was introduced in section 3.7.1),

$$\phi_m(r) = -\frac{e\mu_0 t}{4\pi\hbar r} \otimes (\nabla \times \mathbf{M}(\mathbf{r})).\hat{\mathbf{z}} \quad (3.21)$$

In order to calculate the Lorentz images from the magnetisation distribution, the phase associated with a magnetic object is considered in terms of the magnetic vector potential. In real space, this expression involves a convolution between two functions and is difficult to compute. This problem, however, becomes far easier to compute in Fourier space. This is due to the fact that in Fourier space, a convolution can be written as a straight multiplication of the Fourier transforms of the two functions, allowing faster processing. The Fourier transform produces a complex number valued output image

that can be displayed as separate real and imaginary parts. All image calculations were performed using the Fast Fourier Transform algorithm available in the TEM software package, Digital Micrograph. To calculate the magnetic electron phase, scripts were written by Dr. Stephen McVitie and Mr. Gordon White at the University of Glasgow, using the algorithm proposed by Mansuripur [23]. The calculation of DPC and Fresnel images from the electron phase will be discussed in the following sections:

#### DPC image calculation

In the DPC mode of Lorentz microscopy, the beam is scanned across the specimen and an in focus image is formed by a segmented detector that converts phase changes into intensity variations. DPC images are then obtained by taking the derivative of the electron phase perpendicular to the electron beam which is equivalent to Lorentz deflection angle as shown in equation 3.18

$$\nabla\phi_m(r) = -\frac{e}{\hbar} \int_{-\infty}^{+\infty} (\mathbf{B} \times \hat{\mathbf{n}}) dz = -\frac{2\pi}{\lambda} \beta_L \quad (3.22)$$

Therefore, it is notable that DPC mode quantitatively measures the integrated induction perpendicular to the beam. Figure 3.10 is a schematic illustration of the derivative of the phase shift for both a magnetic (a) and non-magnetic (b) specimen along the x-direction. For a magnetic thin film specimen, the finite width of the domain walls has been ignored and magnetic phase is represented by a simple triangular wave. As was illustrated in Fig. 3.10(a), a positive phase gradient is observed in the outermost

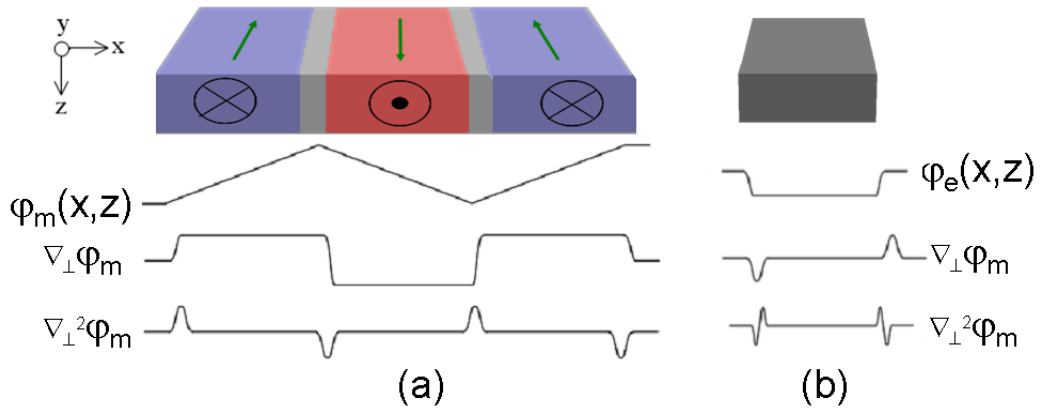


Figure 3.10: Schematically the phase change incurred by the electrons on passing through (a) a magnetic and (b) a non-magnetic specimen. The schematic of derivative of the phase and the Laplacian, for a small defocus value, are given below accordingly.

domains, whereas in the central domain the phase gradient is negative. Therefore, a brighter and darker regions of intensity will be observed corresponding to the outermost and the central domain, respectively. For a nonmagnetic specimen, the phase shift depends on the sample shape and thickness variations. A rectangular element of uniform thickness is shown in Fig. 3.10(b) to illustrate the phase shift for a non magnetic element.

The electrostatic phase contribution to the image appears only at the edges of the specimen and within the element there is no electrostatic contribution. Figure 3.11 shows an example calculation of a vortex domain wall in a permalloy wire containing an anti-notch, simulated using OOMMF. The magnetisation components are given in Figs. 3.11(a-c), with the calculated magnetic and electrostatic phase in Figs. 3.11(d,e). The magnetic phase was calculated using the process detailed above, whereas, the electrostatic phase was calculated using equation  $\phi_e = \frac{\pi V t}{\lambda E}$  and multiplying by a mask of the wire. For Fresnel imaging, the electrostatic phase is more important as it involves defocus. By differentiating the magnetic phase along the x and y directions the calculated DPC images shown in Figs. 3.11(f,g) were produced. The calculation of the Fresnel intensity is discussed in the next section.

### **Fresnel image calculation**

It has been shown that the intensity of the Fresnel image in the low-defocus regime is linearly dependent with defocus and Laplacian of the phase shift [24]

$$I(\mathbf{r}, \Delta) = 1 - \frac{\Delta \lambda}{2\pi} \nabla_{\perp}^2 \phi(\mathbf{r}) \quad (3.23)$$

where  $\lambda$  is the electron wavelength,  $\Delta$  is the defocus and  $\nabla_{\perp}^2$  is the Laplacian relating to the in plane co-ordinates. The derivation assumes that higher order terms in defocus are neglected. However, Fresnel imaging is generally considered to be non-linear imaging technique. A quick check against the linear imaging conditions is to look at the wall width measurements from the images as a function of defocus as was done in reference [24]. It is expected that within the linear range of imaging the measured wall width would be constant, however, outside of this range the width should increase with defocus. Notably, in the latter case, a linear increase of wall width is predicted from classical optics for divergent walls [25]. Therefore, if the linear region is not applicable,

then quantification of the wall width using Fresnel imaging is misleading. However, as was mentioned earlier, the advantages of Fresnel imaging for studying magnetic specimens include its simple operation which allows reversal sequences to be recorded during magnetising experiments. During the course of this investigation, in **chapters 4 and 5** using Fresnel mode of Lorentz TEM, we have investigated the formation, propagation, pinning and depinning of domain walls along the patterned nanowires under the application of magnetic fields. However, in order to extract magnetic information quantitatively e.g. domain wall width in **chapter 6**, we have used differential phase contrast mode of Lorentz TEM.

In this investigation, all image calculations were performed using the Fast Fourier Transform algorithm available in digital micrograph. Notably, in order to calculate

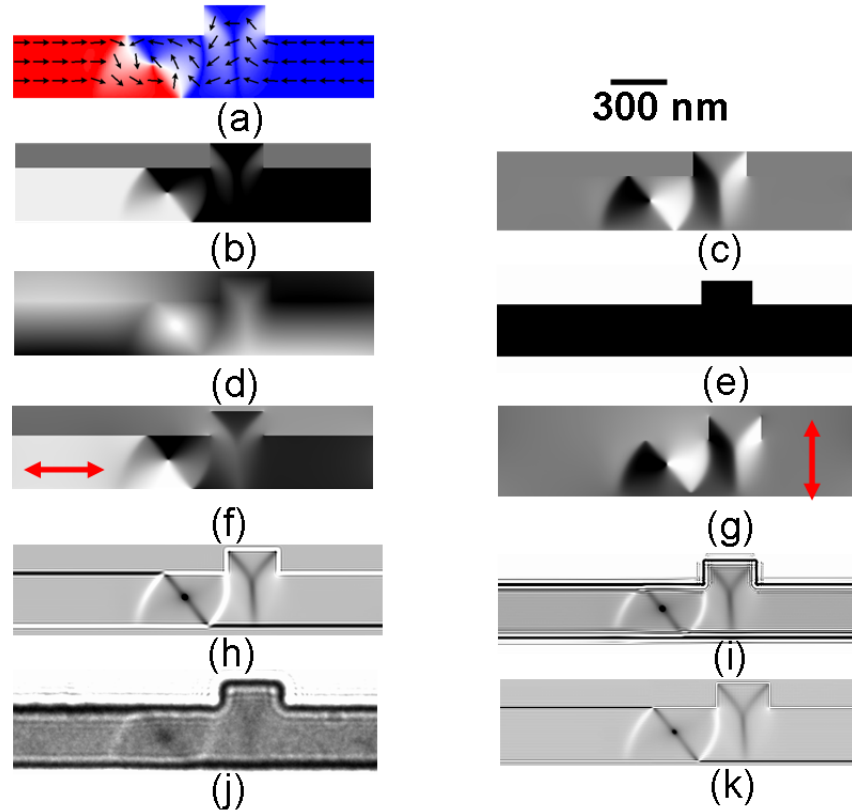


Figure 3.11: Experimental Fresnel image of a vortex domain wall in a 20 nm thick permalloy nanowire containing an anti-notch is compared with simulated Lorentz images. (a) Magnetisation as calculated from OOMMF simulation. (b) and (c) are the x and y components of the magnetisation. From this the (d) magnetic and (e) electrostatic phase are calculated. (f) and (g) are the orthogonal components of the magnetic induction where arrows are indicating the sensitivity direction. (h) Fresnel image contrast from purely magnetic phase and including electrostatic and amplitude effect (i). (j) is an experimental image for comparison. The out of plane component of magnetisation curl (k) is in good agreement with the Fresnel contrast.



the Lorentz images from the magnetisation distribution, it is necessary to consider the phase in terms of the magnetic vector potential. In real space, this expression involves a convolution which is difficult to calculate. This problem, however, becomes far easier to compute when we convert to Fourier space. In Fourier space, a convolution can be written as a straight multiplication of the Fourier transforms of the two functions, allowing faster processing. By considering a uniform incident electron wave with unit amplitude is assumed the exit wave is then calculated by a multiplication of the Fourier transform of the incident wave and the transfer function based on a Lorentz lens where, spherical aberration term  $C_s = 8000$  mm, TEM operating voltage  $V = 200$  kV and electron wavelength  $\lambda = 2.5$  pm. An inverse Fourier transform of the exit wave multiplied by its complex conjugate gives the image intensity. Using the earlier example of the vortex domain wall, the Fresnel image intensity is calculated from magnetic phase only and unit amplitude, Fig. 3.11(h), at a defocus of  $200 \mu\text{m}$ . A good agreement with the experimental image (Fig. 3.11(j)) is observed at the position of the domain wall along with the DW contrast inside the anti-notch, however there are significant differences at the edges of the wire due to the electrostatic phase contribution. By including electrostatic phase and amplitude effects in the calculation, a better representation of the experimental Fresnel intensity was achieved as shown in Fig. 3.11(j).

It may be mentioned also that the Fresnel image intensity can be calculated with adequate knowledge of the microscope parameters and the out of plane component of the magnetisation curl, when the linear imaging conditions are applicable. The out of plane magnetisation curl, Fig. 3.11(k) also represents a good agreement with the experimental Fresnel image.

## 3.9 *In situ* Magnetising experiments

During the course of this investigation, Lorentz microscopy (Philips CM 20 TEM/STEM) was routinely used to image static magnetic states of the magnetic structures as well as to study their dynamic behaviour by applying magnetic fields *in situ*. In the Philips CM20, the external magnetic field is generated by weakly exciting the objective lens and by using the Lorentz lenses to image the magnetic structure. When a user variable electrical current flows through the objective lens coils, a magnetic field,  $\mathbf{H}$  which is

parallel to the optical axis of the microscope, is produced in the specimen region. The direction of the field, either up or down, can be controlled by passing the electrical current through the lens coils in the forward or reverse directions, respectively. When the specimen is placed in the horizontal position ( $0^\circ$  tilt), the applied field is completely out-of-plane. By tilting the specimen at an angle  $\theta$  (Fig. 3.12), a magnetic field component that is parallel to the specimen plane is introduced. The magnitude of this component is given by:

$$H_{\parallel} = H \sin \theta \quad (3.24)$$

The maximum field that can be applied by tilting  $\theta = 90^\circ$  (though imaging is not pos-

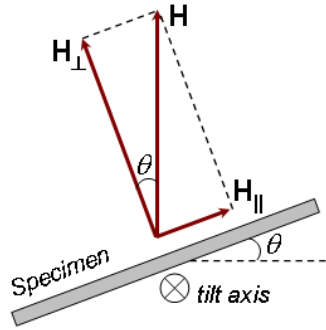


Figure 3.12: Generating a magnetic field parallel to the specimen plane by tilting the specimen.

sible at this tilt) is determined by the objective lens current and can have a maximum field value of around 7000 Oe. One notable issue associated with this technique is that the component of field perpendicular to the specimen can influence the magnetisation. This sensitivity to the perpendicular component lowers the in-plane field necessary to reverse a particular structure [24]. This is less sensitive for continuous thin films which have a large out-of-plane demagnetising factor.

### 3.10 Low angle electron diffraction (in CM 20)

Although not an imaging technique like DPC, using low angle electron diffraction technique practiced in Lorentz TEM, quantitative data can be extracted by direct observation of the magnetic structure in the split central diffraction spot [14, 16]. This technique may be interpreted classically as a map of the Lorentz deflection angles present in the region of specimen under investigation in TEM. However, the main requirement is that the magnification of the intermediate and projector lenses of the

electron microscope is sufficient to provide visible the small Lorentz deflections which is typically of the order of  $12 \mu\text{rad}$  for 20 nm thick Py film. Therefore, camera length in the range 50 to 1000 m are typically required. Such a large value of camera length is achievable in the Philips CM20 TEM, the microscope used for performing low angle diffraction experiments in the present investigation. Another important requirement is the high spatial coherence in the illumination system and this is also achievable in the CM 20 TEM as the microscope is equipped with a FEG source.

The electron waves which are incident on the sample as plane waves, after leaving the sample their magnetic phase ( $\phi$ ) change can be expressed as by the exponential function,

$$e^{i\phi} \quad (3.25)$$

here

$$\phi = \frac{2\pi e B_s t x}{h} \quad (3.26)$$

This is the form of the wavefunction modified after passing through the sample where  $x$  is the distance of the electron waves prior to leave the sample plane.

The principle of this method is best described by consideration of the diffraction image of a region of a magnetic specimen which includes a  $180^\circ$  wall, Fig. 3.13(b). Schematic diagram, Fig. 3.13 (a), illustrates that all rays passing through domains with their magnetisation in a particular direction converge to a single point in the back focal plane of the imaging lens. Thus for an  $180^\circ$  wall structure (the film is

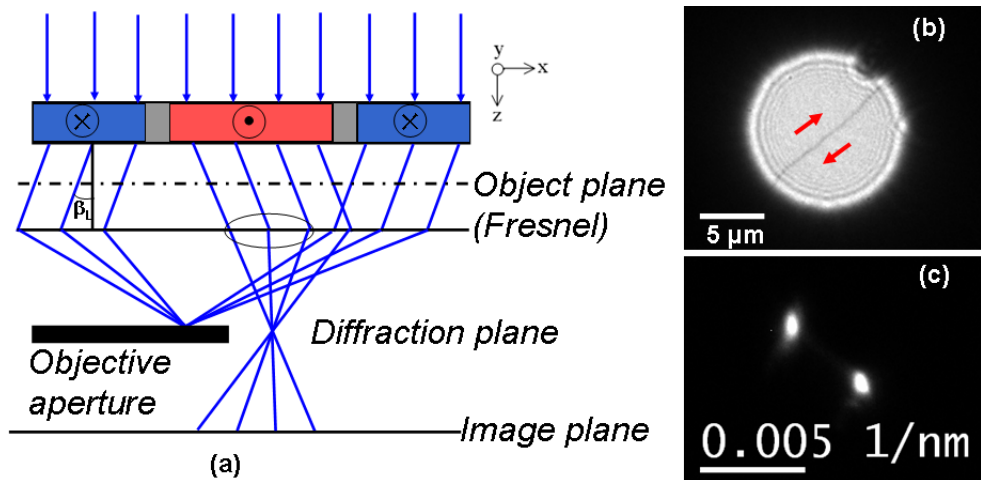


Figure 3.13: (a) Schematic representation of the split central diffraction spot containing  $180^\circ$  domain walls. (b) Fresnel image show a  $180^\circ$  domain wall in a continuous thin film. (c) Two diffraction spots recorded by illuminating the area in image (b).

Cr(3nm)/Py(10nm)/Cr(5nm)/membrane, will be presented in **chapter 5**) in which domains pointing alternately parallel and anti-parallel, Fig. 3.13(b), the main features of the diffraction pattern are two spots, Fig. 3.13(c) whose angular separation is  $2\beta$  from classical point of view.

A diffraction pattern can be regarded in terms of reciprocal space as well as scattering angles. The above equation (equation 3.26) can be rewritten as,

$$\sin\phi = \sin\left(\frac{2\pi e B_s t x}{h}\right) \quad (3.27)$$

In terms of the spatial frequency, this equation can be written as

$$\sin\phi = \sin(2\pi K x) \quad (3.28)$$

Therefore,

$$K = \frac{e B_s t}{h} \quad (3.29)$$

This equation indicates that half of the distance between these two spots, Fig. 3.13(c), is proportional to the  $B_s t$  for diffraction image of a region of magnetic specimen which includes an  $180^\circ$  wall. Notably,  $B_s t$  measurement is very useful when verifying quality of films or seeing local variations such as irradiated films. If the thickness of the film is correctly known, then  $B_s t$  of the film can be measured correctly. It is notable that low angle electron diffraction experiments provide global information from the whole of the illuminated specimen area rather than local information. It is necessary to be careful that the high intensity in the diffraction spots does not cause damage to the imaging system used, for example, CCD TV camera. In **chapter 5** large area irradiation experiments will be carried out and low angle diffraction experiments will be performed to measure  $B_s t$  of the unirradiated and irradiated regions.

# Bibliography

- [1] D. B. Williams, C. B. Carter, *Transmission Electron Microscopy: A Textbook for Materials Science*, volume 1: Basic, 2004, Springer, ISBN-10: 030645324X.
- [2] E. Ruska, Rev. Mod. Phys. **59** 627 (1987).
- [3] L. de Broglie, *La nouvelle dynamique des quanta*, Électrons et Photons: Rapports et Discussions du Cinquième Conseil de Physique. Solvay (1928).
- [4] N. Tanaka, Sci. Technol. Adv. Mater. **9** 014111 (2008).
- [5] M. De Graef, *Introduction to conventional transmission electron microscopy*, Cambridge University Press, 2003, ISBN 0 521 62995 0.
- [6] R.F. Egerton, *Physical Principles of Electron Microscopy*, Springer, 2008, ISBN 978-0-387-25800-3.
- [7] G. A. Prinz, Science **282** 1660 (1998).
- [8] G. A. Prinz, J. Magn. Magn. Mater. **200** 57 (1999).
- [9] D. A. Allwood, G. Xiong, C. C. Faulkner, D. Atkinson, D. Petit, R. P. Cowburn, Science **309** 1688 (2005).
- [10] S. P. Parkin, M. Hayashi, and L. Thomas, Science **320** 190 (2008).
- [11] H. Hopster, HP Oepen, editors, *Magnetic Microscopy of Nanostructures*, Springer, 2005.
- [12] M. Tanase, A. K. Petford-Long, Microscopy Research and Technique **72** 187 (2009).
- [13] J. N. Chapman, A. B. Johnston, L. J. Heyderman, S. Mcvitie, W. A. P. Nicholson and B. Bormans, IEEE Trans. Magn. **30** 383 (1994).

- [14] J. N. Chapman and M. R. Scheinfein, J. Magn. Magn. Mater. **200** 729 (1999).
- [15] M. E. Hale, H. W. Fuller, and H. Rubinstein, J. Appl. Phys. **30** 789 (1959).
- [16] J. N. Chapman, J. Phys. D: Appl. Phys. **17** 623 (1984).
- [17] Y. Aharonov and D. Bohm, Phys. Rev. **115** 485 (1959).
- [18] S. McVitie, G. S. White, J. Scott, P. Warin and J. N. Chapman, J. Appl. Phys. **90** 5220 (2001).
- [19] S. McVitie and G. S. White, J. Phys. D: Appl. Phys. **37** 280 (2004).
- [20] K. J. O'Shea, *Putting a leash on the domain wall: A TEM investigation into the controlled behaviour of domain walls in ferromagnetic nanostructures*, PhD thesis, University of Glasgow, 2010.
- [21] J. N. Chapman, R. Ploessl and D. M. Donnet, Ultramicroscopy **47** 331 (1992).
- [22] J.N. Chapman, A.B. Johnston, L.J. Heyderman, S. McVitie, W.A.P. Nicholson, B. Bormans, IEEE Trans. Magn. **30** 4479 (1994).
- [23] M. Mansuripur, J. Appl. Phys. **69** 2455 (1991) .
- [24] S. McVitie, M. Cushley, Ultramicroscopy **106** 423 (2006).
- [25] H. Gong, J. N. Chapman, J. Magn. Magn. Mater. **67** 4 (1987).

# Chapter 4

## Nanostructures patterned by EBL and FIB milling: a direct comparison

### 4.1 Objective and motivation

Understanding and controlling magnetic domain wall (DW) behavior in ferromagnetic nanowires is of fundamental scientific interest and important for their potential applicability in future spintronic devices such as magnetic logic [1] and race-track memory [2]. Micromagnetic simulations [3, 4], magneto-optic Kerr effect magnetometry [5, 6], off-axis electron holography [7] and magnetic imaging techniques [8, 9] have contributed useful information for a greater understanding of the magnetic properties of DWs. To ensure the reliable operation of devices, performance variability must be reduced and high quality nanofabrication is extremely important. Previous reports [10, 11] indicate that the structural roughness at the edges of the nanostructures produced by fabrication processes affect the magnetic properties of the nanostructures. Amongst a variety of nanofabrication techniques, electron beam lithography (EBL) is widely used for high resolution submicron scale patterning of magnetic materials. EBL is a multilevel fabrication technique though this technique requires a number of steps including resist spinning, pattern exposure, metallisation, removal of resist from the sample surface and lift off of the residual materials. By contrast, focused ion beam (FIB) based fabrication is essentially a one step patterning process of a continuous film and is an excellent tool for rapid device proto-typing [8]. Nevertheless, FIB has some disadvantages [12] especially due to the heavy  $Ga^+$  used for the milling process.

These include radiation induced damage and ion implantation. The extent to which the magnetic properties of nanostructures are affected by the differences in physical properties produced by patterning structures using EBL and FIB techniques has not been studied extensively. Therefore, in the present investigation, nominally identical permalloy nanowires fabricated by these two nanofabrication techniques are compared through characterisation of their physical nanostructure and magnetic behavior.

### 4.2 Material deposition and nanofabrication

A permalloy film of 20 nm thickness was deposited by thermal evaporation (the process was described in **chapter 2**) onto a single electron transparent  $\text{Si}_3\text{N}_4$  membrane for the fabrication of nanowires using two different fabrication techniques. The structure of the fabricated nanowires is shown in Fig. 4.1 which contains three 320 nm wide and 140 nm height rectangular protrusions referred to as anti-notches. Two wire widths were chosen for study, 320 and 150 nm, and both ends of the wire were connected to diamond shaped pads to allow control over the formation of DWs. Nanostructures

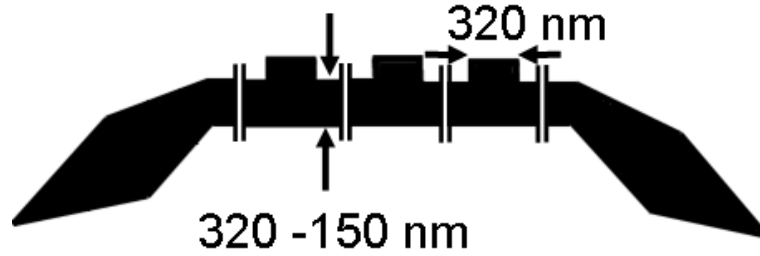


Figure 4.1: Schematic of the nanowire geometry. The distance between the anti-notches has been reduced for this schematic indicated by vertical bars.

were fabricated first by an EBL/lift off process onto one half of the membrane as shown in the TEM image in Fig. 4.2(a). The schematic diagram in Fig. 4.3 illustrates the different processing steps of EBL/lift off technique, described elaborately in **chapter 2**. During the fabrication of the nanostructures using EBL/lift off technique, four large area rectangles were also fabricated onto the other half of this membrane, 4.2(a). Therefore, identical structures were written inside these large rectangles containing the same film of permalloy, as shown in Fig. 4.2(b), using FIB. This was done to ensure that the same film thickness and quality of the deposited permalloy was used for patterning using both the techniques. For FIB patterning, a FEI Nova NanoLab 200 SEM/FIB



Schematically pattern written in the Si substrate

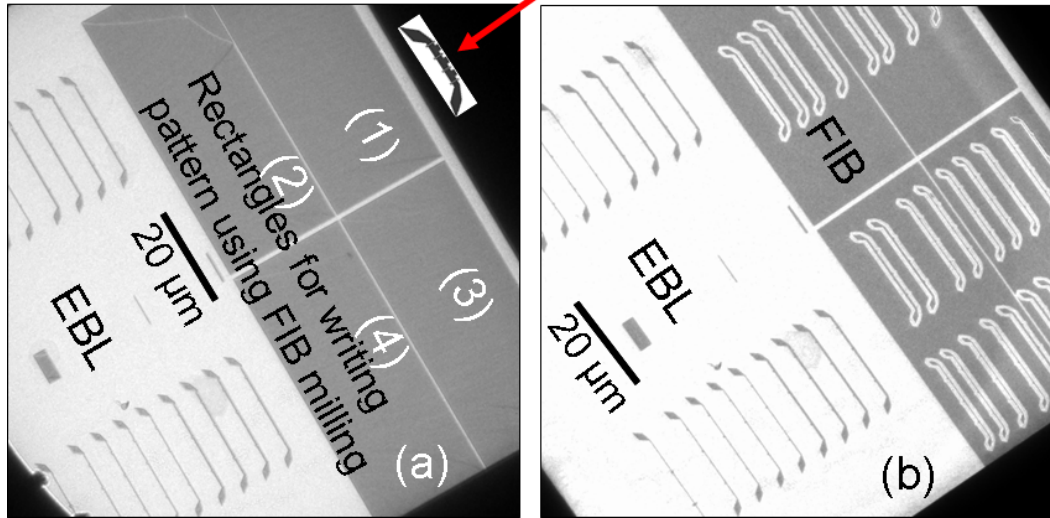


Figure 4.2: (a) Patterns were written onto one half of the membrane using EBL/lift off techniques. Four large size rectangles were also written using EBL technique onto the other half of the membrane. Later on identical patterns were written into these rectangles using FIB milling. (b) TEM image shows the patterns written by EBL and FIB techniques onto a single membrane on which the Py film of the same thickness and quality was deposited.

workstation with a 10 nm full-width-half maximum  $Ga^+$  ion probe (energy of 30 keV and current of 10 pA) was used. The FIB pattern generation involved a two-step vector milling strategy [8] as was described in **chapter 2**. Instead of using a single step for milling, a multistep approach was chosen in such a way that a critical cut was made in as short a time as possible, thus the effects of stage drift on the definition of the pattern was reduced. For the NovaNanoLab 200 SEM/FIB, stage drift is estimated at 10 nm per minute and therefore the first cut was chosen to be small (tens of nm) so that the patterning time required was less than 1 minute. Following cuts were larger as any further drift that occurred then did not affect the quality of the pattern definition significantly. During each cut, doses were controlled by the number of passes for a particular beam dwell time and patterning magnification. In practice, initially a pattern was written by FIB milling on the Si substrate, parallel to the rectangular boxes, as shown schematically at the top of Fig. 4.2(a). Therefore, prior to commencing actual patterning inside the rectangular boxes containing Py film, several minutes were allowed to elapse after the last stage movement to let the stage settle and thereby reduce stage drifting. Then only by ion beam shifting, array of patterns were written inside

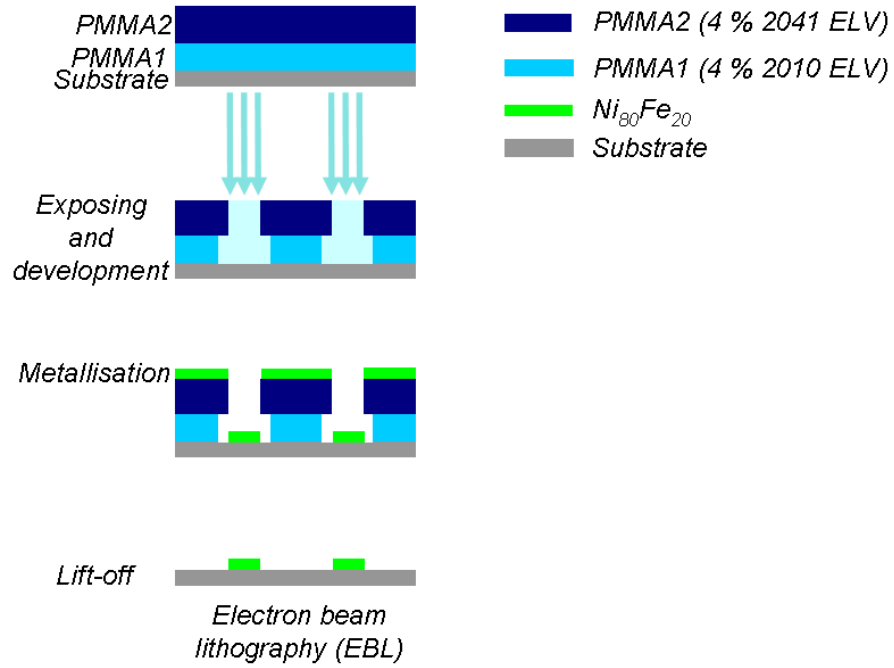


Figure 4.3: Schematically different processing steps of EBL/lift off technique as was described in **chapter 2**.

the boxes 1 and 2, as shown in the TEM image 4.2(b). To write arrays of patterns in another areas of the these two boxes or inside boxes 3 and 4, the same process was followed, i.e. again one pattern was written in the Si substrate, then several mins elapsed before starting patterning inside the boxes by beam shifting. During fabrication using this dual beam system, imaging was done only using the electron beam, never using ion beam in order to avoid any unwanted property modification in the continuous Py thin film as well as the Py in the patterned nanowires. Structural and magnetic characterisation of the patterned nanowires were described in the next section.

## 4.3 Structural characterisation

### 4.3.1 Plan-view TEM images

Conventional TEM was used to investigate the physical structure of the patterned nanowires. Figure 4.4(a) and (b) show TEM bright field images of the plan view of 320 nm wide nanowires patterned by EBL (a) and FIB (b). These images reveal polycrystalline films with well defined anti-notches produced by both methods. Higher magnification TEM bright field images of the plan view of 320 nm wide nanowires patterned by EBL and FIB techniques are shown in Figs. 4.4(c) and (d), respectively.

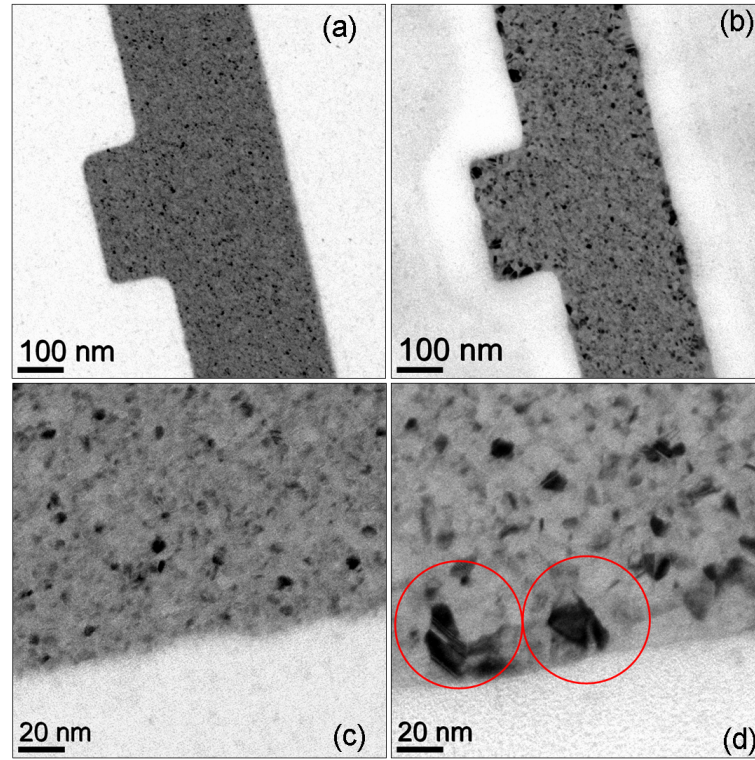


Figure 4.4: TEM bright field images of the plan view of 320 nm wide nanowires patterned by EBL (a) and FIB (b). Higher magnification TEM bright field images of the plan view of 320 nm wide nanowires patterned by EBL (a) and FIB (b). Circle marked regions indicate grain growth along FIB patterned nanowire edge (b).

The measured edge roughness is of the order of the mean grain size, 5 -10 nm, observed in the continuous film. The grain structure of the EBL nanowires, as shown in Fig. 4.4(c), reveal a log-normal distribution [14] of the grain size peaked around this mean value as was measured for polycrystalline film prepared in the same way [15,16]. For wires fabricated by FIB, significant grain growth was observed up to a distance of 30 to 40 nm from the wire edges, as marked by circles in Fig. 4.4(d). The size of these larger grains varied from 20 to 30 nm. The grain size distribution was measured from dark field images recorded from the centre of the patterned nanowires. The measurement was done by using the image processing software package Digital Micrograph (DM). The methodology for measuring grain size using DM was described in Ref. [15]. It is notable that the size of the larger grains appeared along the wire edge of the FIB patterned nanowires were also measured using DM from a number (more than 10) dark field and bright field TEM images. These images were recorded from different areas of different FIB patterned nanowires. However, the grain size distribution about the centre of the FIB patterned wires is similar to the EBL/continuous film. Therefore, the

differences between the physical nanostructure of the patterned nanowires are clearly associated with the regions close to the edge of the wires. The long extended tail of the  $Ga^+$  beam affect the edges of the nanowires and will be discussed in the next section. In a related study this effect was observed for nanoelements with a width of  $< 100$  nm, where the grain growth was seen in the entire structure and actually was seen to be amorphous when the width was less than 60 nm [17]. In that study the proximity of the edges meant that there was effectively no non-irradiated region in the centre of the structure unlike in this study.

### 4.3.2 Cross-sectional TEM images

Cross-sectional (x-sectional) TEM samples of the patterned nanowires were prepared using a FIB based 'in-situ' lift-out technique [12] to observe the details of the physical structure of the nanowires around their edges. As was mentioned in **chapter 2**, the preparation of the x-sectional TEM samples of thin films is always challenging, however, the fragility of the  $Si_3N_4$  membrane makes it even more so. Nevertheless, attempts were made to make the TEM sample as thin as possible which is desirable for good imaging. To obtain a thinner sample and to provide additional support during milling process prior to loading the sample inside the FIB chamber, approximately 200 nm Al was deposited on the back side of the membrane. Moreover, a few micron of glue was also deposited on the back side of the membrane just after Al deposition. This was done to obtain additional support during initial rough milling using high beam current (1000 pA) and beam energy (30 keV). Then the membrane substrate in which patterns were written was inserted inside the FIB chamber and the samples were prepared using the process described elaborately in section 2.5.6 of **chapter 2**. After preparing the TEM lamella, bright field TEM images were recorded to observe the morphology of the nanowires, particularly around their edges. Figures 4.5(a,b) show TEM bright field images of the wire edges of a 320 nm wide EBL nanowire. The individual layers are labeled in image 4.5(a,b). In the x-sectional images of the EBL sample, Figs. 4.5(a,b), the top layer is an electron beam deposited platinum (Pt) protective layer. The white band around the edge structure is residual PMMA and its thickness is approximately 3-5 nm which is consistent with the measured residual PMMA thickness after acetone removal during lift-off [18]. Furthermore these images reveal a tapered edge structure

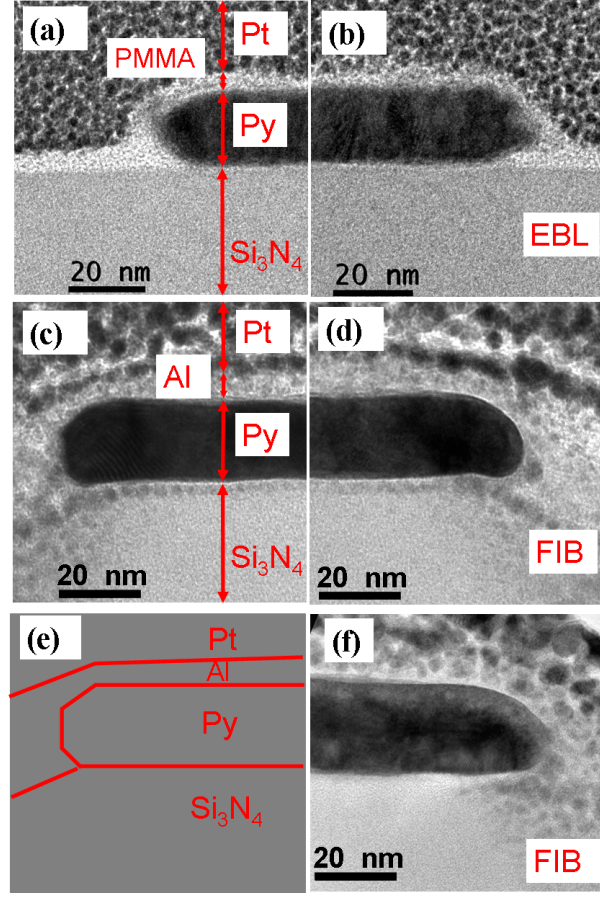


Figure 4.5: X-sectional TEM bright field images showing the wire edges of the 320 nm wide nanowires patterned by EBL (a,b). The individual layers are labeled in (a). X-sectional TEM bright field images showing the wire edges of the 320 nm wide nanowires patterned by FIB (c,d). Figure (e) is showing schematically the individual layers of image (c). X-sectional image (f) is showing the one edge of a 150 nm wide FIB patterned nanowire.

of the patterned nanowire. Formation of the tapered edge structure in this case may be due to shadowing associate with a build-up of metal during evaporation on the residual PMMA resist to the side of the nanowire. By comparison x-sectional TEM images 4.5(c,d) show the wire edges of a 320 nm wide FIB milled nanowire. Figure 4.5(e) is a schematic showing the individual layers of Fig. 4.5(c). To distinguish between the Py layer and Pt over layer, about 5 nm of Al was deposited on top of the Py prior to Pt deposition. In the case of the EBL patterned nanowire, the residual PMMA meant that such an intermediate layer was unnecessary. A comparison of the edge structure from the x-sectional images of the EBL and FIB samples indicate that in both cases the edge profile is not vertical but tapered, though in the case of the FIB structure the tapering is slightly less symmetric. Whilst in the case of the EBL nanowires the tapering may be in part due to residual resist, in the case of the FIB

nanowires this is clearly due to the interaction of the  $Ga^+$  beam with the film during the milling process. However in both cases the edge structure can be described as well defined. A x-sectional TEM image from a FIB milled 150 nm wide wire, 4.5(f), also demonstrates a well defined edge profile of this narrower wire consistent with that observed in the wider nanowires.

From the plan view images 4.4 and cross-sectional TEM bright field images 4.5, it is apparent that the main difference between the wires fabricated by the two processes is the grain structure observed along the edges of the nanowires, in particular the formation of larger grains along edges of the FIB milling nanowires. The purpose of focused  $Ga^+$  beam milling here is to generate isolated patterns of magnetic thin film without the need for time consuming steps of the lithography process. However, it is well known that the profile of the  $Ga^+$  beam has a long exponential tail in addition to the central Gaussian profile of the ion beam [19,20]. Therefore, during the sputtering process, the  $Ga^+$  implantation from the extended tail of the ion beam may affect the ferromagnetic properties of the Py particularly along the edges of the nanowires. Modification of the ferromagnetic properties, including reduction of saturation magnetisation of magnetic thin film systems due to ion implantation/irradiation, have been reported earlier [21–26]. Notably these investigations were performed by ion irradiation/implantation on continuous films and property modifications arose as a direct result of the ion implantation/irradiation the thin film systems. By contrast, in the present investigation, the observed modification occurring along the wire edges of the FIB milled Py nanowires appears to be due to residual irradiation from the extended tail of the  $Ga^+$  beam. This point will be further discussed in the micromagnetic modeling section of this chapter.



### 4.3.3 Double cut vs single cut approaches for pattern generation

It was already mentioned that for FIB patterning, instead of using a single milling step, a multistep approach was chosen so that stage drift that occurs does not significantly affect the quality of the pattern definition. But one unwanted problem is that at the interface of the two cuts, sometimes the ion beam (10 pA beam current) mills through the whole film, Fig. 4.6(a), probably due to the dose overlapping from the extended tail of the ion beam. In the worst case, this ultimately damages the whole membrane as shown in the SEM image, Fig. 4.6(b). Therefore, to avoid this damage between the two cuts, materials were kept unmilled for a few pixels. Alternatively, patterns were written using a single cut, Fig. 4.6(c) by reducing the size of the element and the milling area so that the total milling time is around 1 min for a particular pattern. Therefore, stage drifting did not cause any significant influence on the pattern definition. To compare the edge profile of the FIB milling patterns written by a single cut approach with that of the multiple cut approach, TEM cross-sectional samples were also prepared using FIB technique described in section 2.5.6, **chapter 2**.

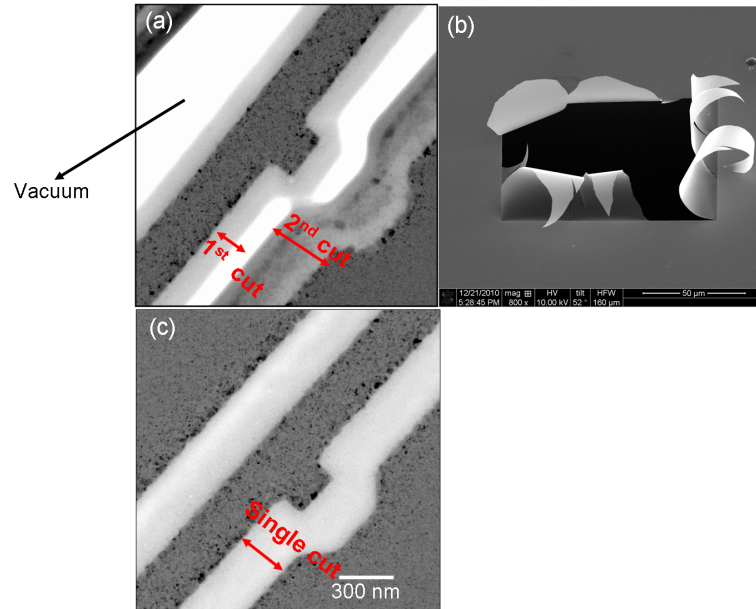


Figure 4.6: TEM bright field images showing the nanowires patterned by a (a) two cut approach, (b) SEM image showing the extreme damage due to the milling of the film and (c) TEM image demonstrating the single cut approach.

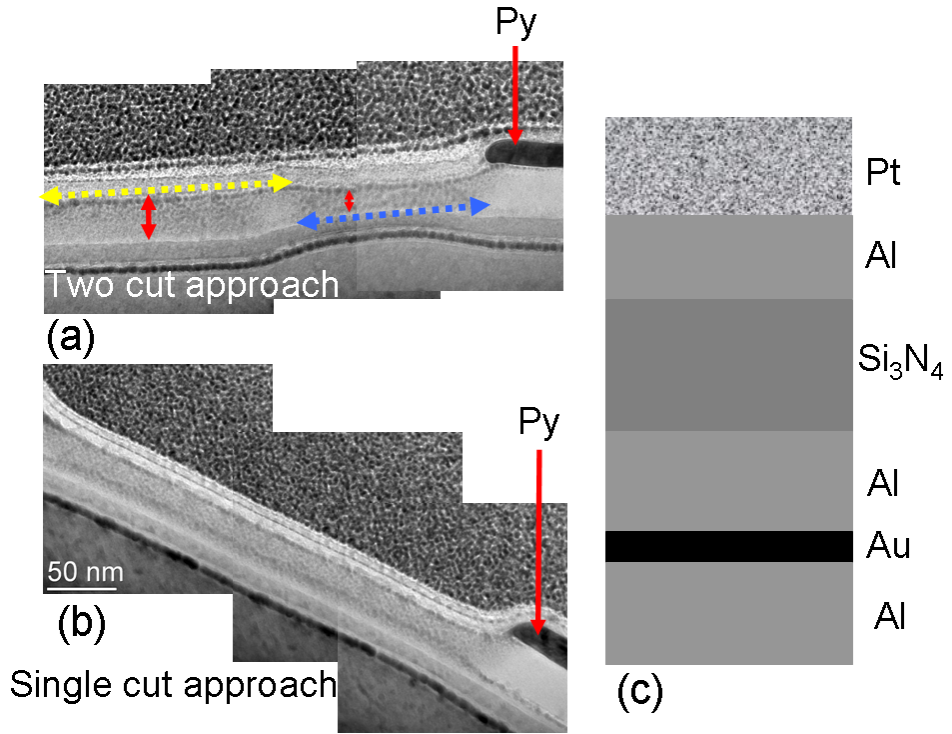


Figure 4.7: Left edges of the nanowires written by a multiple cut approach (a) and single cut approach (b) along with milling areas. The individual layers in the milling areas in images (a) and (b) are shown schematically in the schematic (c).

The x-sectional TEM image show in Fig. 4.7(a) the left edge of a nanowire written by multiple cut approach along with the milling area of the 1st cut (blue dotted line) and part of the 2nd cut (yellow dotted line). The left edge of a nanowire written by the single cut approach, along with the milling area, is also shown in the x-sectional TEM image of Fig. 4.7(b). The individual layers in the milled region are shown schematically in Fig. 4.7(c). The edge profile of the nanowire written by multiple cut approach, Fig. 4.7(a) is well defined, but a modification of the surface of the membrane in the area of the 1st cut is clearly visible. Particularly the  $\text{Si}_3\text{N}_4$  membrane in this milling area was found to shrink about two third of it's total thickness. This actually results an apparent deformation of the underlying membrane. On the other hand, the edge profile of the nanowire patterned by single cut approach was also well defined, but any damage and deformation of the membrane as a consequence of the over milling was not observed like multicut approach. Therefore, in future patterns were written using this single cut approach by using FIB milling. For a comparison with the surface of the membrane patterned by EBL, a general view of a TEM x-section of a nanowire pattern by EBL technique is also shown in Fig. 4.8(a). The individual layers around either side of the



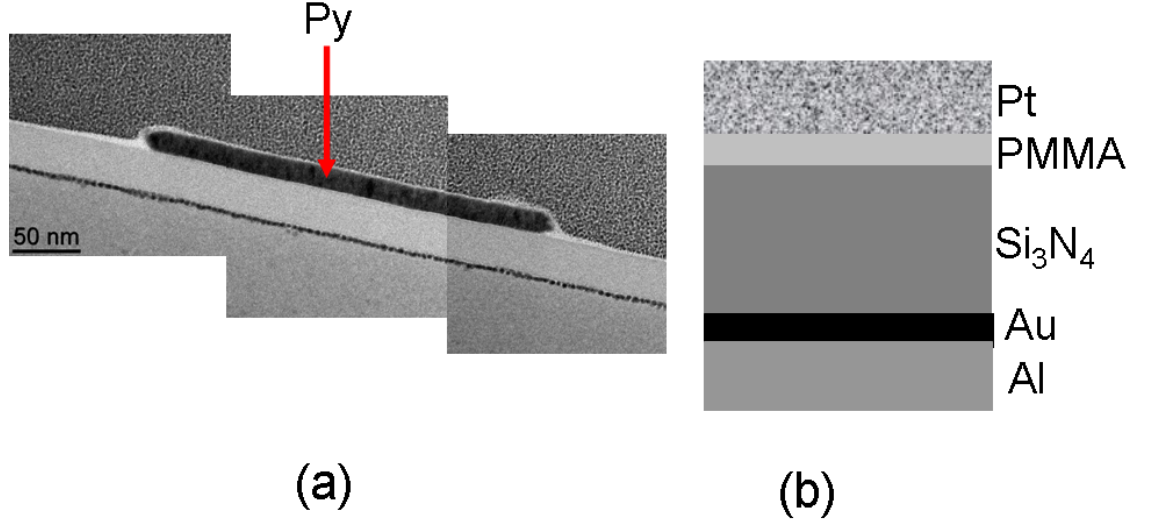


Figure 4.8: A TEM x-sectional image shows an overview of a nanowire patterned by EBL technique. The individual layers in the either edges of the nanowire are shown schematically in (b).

nanowire are shown schematically, Fig. 4.8(b). This image clearly indicates the well defined edge profile of the EBL patterned nanowire along with the unembellished Si<sub>3</sub>N<sub>4</sub> membrane surface in either side of the pattern.

## 4.4 Magnetic characterisation

### 4.4.1 Formation of domain walls

*In situ* magnetisation experiments were carried out using Fresnel mode of Lorentz TEM to investigate and compare the magnetic behavior of DWs as they propagate along the EBL and FIB patterned nanowires. It has been seen from another study that nanoelements created by FIB with widths less than 100 nm were not able to be determined as magnetic using LTEM [17]. Therefore, in this project we intended to understand the scale limit in terms of the width of the wires up to which magnetic information can be extracted from patterns written using FIB milling. That's why nominally identical permalloy nanowires, with widths down to 150 nm, were fabricated onto a single electron transparent Si<sub>3</sub>N<sub>4</sub> membrane. Formation of the DWs at the corner position between the pad and the 320 nm wide wires were achieved by applying a magnetic field close to the hard axis and then relaxing the field to zero as described in reference [27]. For nanowires of 320 nm width and 20 nm thickness, the favoured wall structure is a vortex DW (VDW) according to the DW structure phase diagram, Fig. 4.9 [28]. For

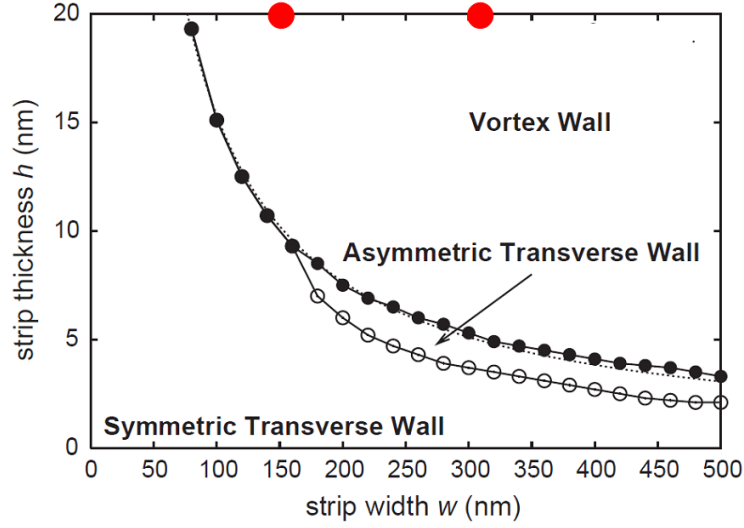


Figure 4.9: Domain wall structure phase diagram proposed by Y. Nakatani et al [28]. The red circles indicate the location within the domain wall structure phase diagram of the wire geometries considered for the investigation in **chapter 4**.

the formation of DWs at the corner position between the pad and the wire, a magnetic field was applied at an angle of 2-4 degrees counter clockwise (ccw) from the hard axis and relaxed to zero. From 120 observations involving 24 wires, it was observed that if magnetic field is applied about 2-4 degree counter clockwise from hard axis and relaxed to zero, then a transverse DW, Fig. 4.10(a) is formed 84% of the time while a clockwise (cw) VDW is formed in the remaining 16%. Under the application of a small magnetic field along the wire axis, the transverse DW transferred into ccw VDW, Fig. 4.10(c), as it moved into the uniform section of the wire. Alternatively, for the cw VDW formation a magnetic field was applied at an angle of 10-12 degrees counter clockwise from the hard axis and relaxed to zero. In this case, it was observed from 120 observations that around 80% of the time a cw VDW is formed at the corner position between the pad and the wire, Fig. 4.10 (e). In the remaining 20 % experiments, at the corner position either an asymmetric TDW is formed or did not form any micromagnetic wall structure. These proportions of the formation different wall structures by applying an offset angle magnetic field are in consistent with a previous investigation [29] for related wire structure patterned by EBL. In a number of previous investigations, topographically defined trapping sites such as notch/anti-notch of different geometries were used to know the exact position of DWs [6, 8, 9, 16, 30] in ferromagnetic nanowires. In the present investigation, the structure of the fabricated nanowires were contained three 320 nm wide and 140 nm height rectangular protrusions referred to as anti-notches to

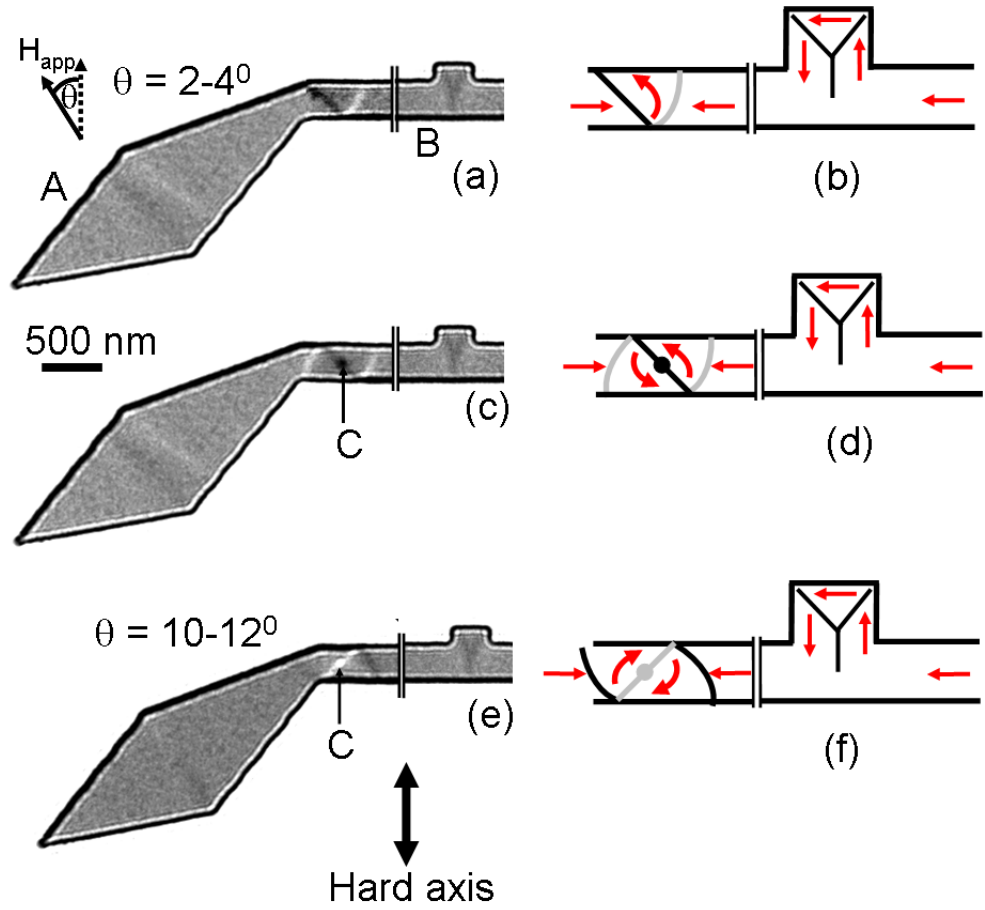


Figure 4.10: Formation of the asymmetric transverse DW (a), ccw VDW (c) and cw VDW (e) at the zero field in 320 nm wide EBL patterned nanowires. DWs of different chiralities were formed by applying a magnetic field at different angles counter clockwise from the hard axis and relaxing to zero. For the formation of a ccw VDW, a magnetic field was applied at an angle of 2-4 degrees whereas for a cw VDW formation, the angle of the applied magnetic field was increased to 10-12 degrees. (b, d and f) are the corresponding schematics of (a, c and e). 'A' and 'B' indicate the black thick fringe at the upper edge of the diamond shaped pad and lower edge of the straight wire, respectively. 'C' denotes the vortex core.

allow control of the position of DWs in the patterned nanowires.

Figures 4.10(b, d and f) are the corresponding schematics of 4.10(a, c and e) and showing magnetisation distributions deduced from the images. Also visible in Figs. 4.10(a, c and e) is a dark Y-shaped contrast at the anti-notches. From the schematics in Figs. 4.10(b, d and f) it can be seen that this results from the magnetisation in the nanowire following the edge of the anti-notch resulting in the Y-shaped domain wall structure.

In the Fresnel mode of LTEM, the magnetic DW contrast is clearly visible along with edge contrast appearing along the wire edges [9]. In Fresnel images 4.13 (a and c), the appearance of a thick black fringe along the upper edge of the diamond shaped pad

(marked by A) and lower edge of the straight wire (marked by B) clearly indicates that these two sections are magnetised in opposite directions and is consistent with a DW existing between the pad and the wire. The appearance of the vortex, white or black (indicated by C), depends on the sense of rotation of the magnetisation around it.

#### 4.4.2 Propagation of domain walls

Following the formation of DWs, a magnetic field was applied along the wire axis to drive the VDWs towards the anti-notches of the nanowires. The DW propagation experiments were carried out for both chiralities of VDW in nanowires of both width patterned by EBL and FIB. In terms of reproducibility of the magnetizing behaviour there were 4 identical nanowires for each width and preparation method and each measurement was based on repeated cycles of 4 identical nanowires. Therefore the fields quoted in the following results are based on an average of 20 measurements for each event for a given chirality in a wire of a given width for each preparation method. The error comes from the spread of the recorded data. Each set of measurements started from the states shown in Fig. 4.10 and then followed the sequence of propagation, pinning and depinning as the field increased. The state would then be reset and the measurement repeated.

Fresnel images 4.11(a and b) show a ccw VDW at zero field in a 320 nm wide wire patterned by EBL and FIB, respectively. Figure 4.11(c) is the corresponding schematic showing the magnetisation distribution deduced from the images. By applying a magnetic field of 17 Oe, the DWs move and are pinned prior to the anti-notches of both EBL and FIB wires as shown in Figs. 4.11(d and e), respectively. The ccw VDW was pinned prior to the anti-notch as the magnetisation in the leading domain of the DW has a component antiparallel to that in the adjacent anti-notch as can be seen from schematic 4.11(f). A further field increase to  $\sim 62$  Oe results in the DW depinning and propagating through the anti-notch of the EBL nanowire leaving the wire nearly uniformly magnetised, Fig. 4.11(g). After the depinning of the DW, a vortex of ccw chirality appears inside the anti-notch as a black spot, Fig. 4.11(g). At an applied magnetic field of  $\sim 57$  Oe, Fig. 4.11(h), the magnetisation reversal is completed in the FIB nanowire without a vortex forming inside the anti-notch. Here the thicker dark fringe runs along the upper edge of the wire and weak white DW contrast appears in-

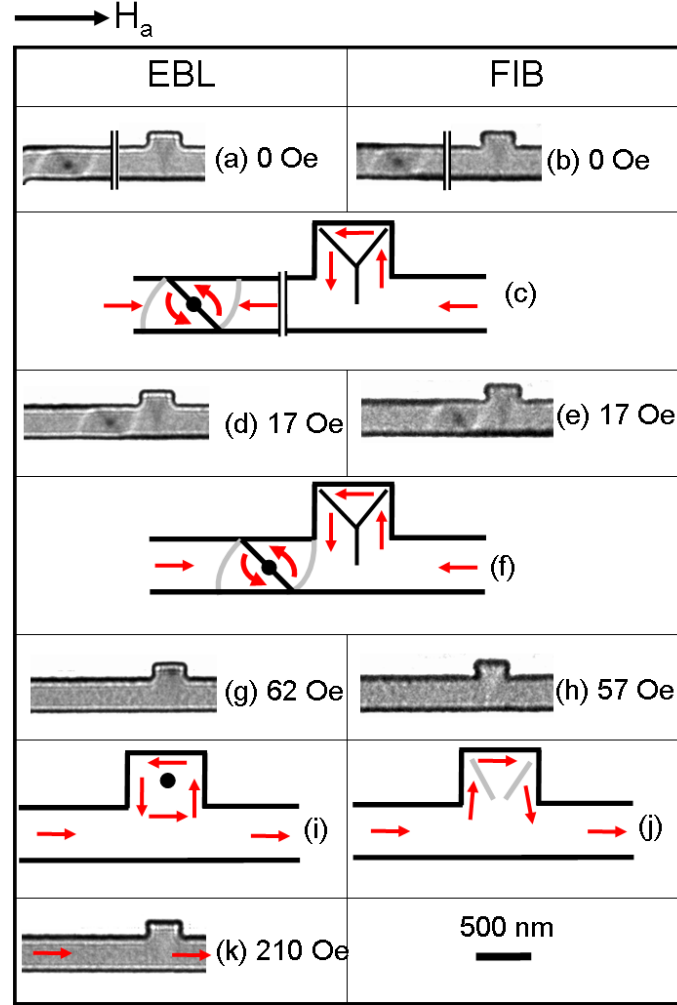


Figure 4.11: Fresnel images of a ccw VDW at zero field in 320 nm wide nanowires patterned by EBL (a) and FIB (b). (d and e) are showing ccw VDW is pinned prior to the anti-notches. State after DW depinning is showing (g and h). Completion of reversal in EBL wire is showing (k). Schematic interpretation of (a and b) is (c), (d and e) is (f) and (g and h) are (i and j), respectively.

side the anti-notch after the depinning of the DW, which has a similar but opposite configuration to the black Y-shaped domain wall observed earlier but modified by the applied field. The schematic interpretation of Figs. 4.11(g and h) are (i and j), respectively. Finally at  $\sim 210$  Oe, the vortex structure is annihilated from the anti-notch of the EBL patterned nanowire, Fig. 4.11(k).

Fresnel images 4.12(a and b) show the situation for cw VDWs at zero field in 320 nm wide wires fabricated by EBL and FIB, respectively with a schematic of the magnetisation distribution shown in Fig. 4.12(c). An applied magnetic field of 12 Oe for both cases results in the leading part of the DW entering the anti-notches as shown in Figs. 4.12(d,e). The magnetisation distribution in Fresnel images (d and e) are shown in the schematic (f). As the leading part of the VDWs now have a component parallel

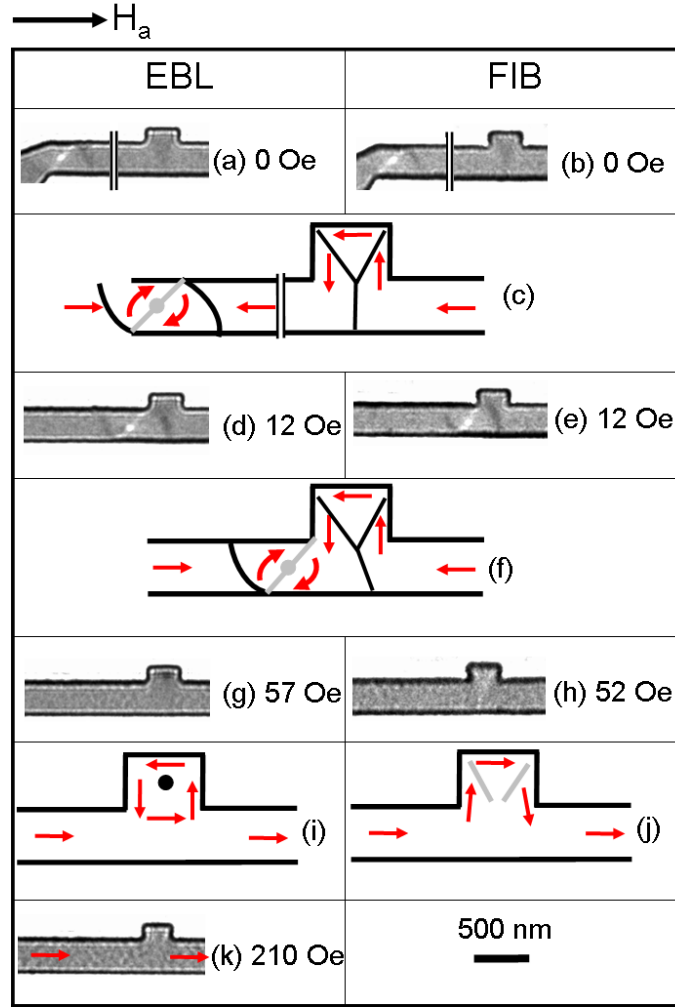


Figure 4.12: Fresnel images (a) and (b) are showing a cw VDW at zero field in 320 nm wide nanowires fabricated by EBL and FIB, respectively. (d and e) are showing part of the cw VDW merged inside the anti-notches. (g and h) are showing state after DW depinning. (k) is showing completion of reversal in EBL wire. (c) is the schematic of (a and b), (f) is the (d and e) and (i and j) are the schematics of (g and h), respectively.

to the magnetisation at the left side of the anti-notch the VDWs and the Y-shaped domain walls effectively merge. A further field increase to  $\sim 57$  Oe results in the DW depinning from the anti-notch of the EBL nanowire, Fig. 4.12(g). It is noted that after the depinning of the DW, a ccw vortex structure formed inside the anti-notch of the EBL nanowire, as seen by the presence of the black spot in Fig. 4.12(g). In the FIB milled nanowire, the DW depins at  $\sim 52$  Oe and weak white DW contrast is formed inside the anti-notch as shown in Fig. 4.12(h). Figures 4.12(i and j) are the schematics of (g and h), respectively. Under the application of a magnetic field of  $\sim 210$  Oe, the vortex structure is totally removed from the anti-notch of the EBL nanowire, Fig. 4.12(k).

These results show that DW depinning fields at anti-notches are higher for the ccw

## Chapter 4: Nanostructures patterned by EBL and FIB milling: a direct comparison

vortex domain walls compared to those of the cw vortex domain walls in accordance with previous results on triangular shaped anti-notches in EBL nanowires [9]. In the present investigation however the comparison of the EBL and FIB nanowires indicates that DW depinning fields at the anti-notches are lower for the FIB nanowires compared to their equivalent EBL nanowires for both cw and ccw VDWs. Furthermore it is noted that after reversal of the EBL nanowires residual ccw vortex structures are present inside the anti-notch for both chiralities of the incoming DWs, these are not observed in the FIB nanowires after depinning. The presence of these vortices appears irrespective of the chirality of the depinned DWs and it is noted that the same field is required to annihilate the vortex in either case. Thus the presence of the vortex after depinning does appear to be a residual structure in the anti-notch and not connected to the depinned wall.

Table 4.1: Domain wall depinning field dependency on the fabrication technique and chiralities of the DWs in 320 and 150 nm wide nanowires. Each experimentally measured field is an average from 4 identical nanowires each of which were measured from separate magnetising cycles. Field values are the mean values of the repeated experiments and error bars represent their standard deviation. The vortex annihilation fields are also inserted inside the table 4.1. Domain wall depinning fields for rectangular (rec.) and sloped (slop.) edge profiles of the nanowires obtained from micromagnetic simulations are also included inside the bottom part of the table 4.1.

Fabrication technique	Wire width (nm)	Domain wall depinning field (Oe)		Vortex annihilation field (Oe)
		ccw	cw	
EBL	320	$62 \pm 2$	$57 \pm 2$	$210 \pm 5$
FIB	320	$57 \pm 2$	$52 \pm 2$	— — —
EBL	150	$150 \pm 5$	$118 \pm 5$	$210 \pm 5$
FIB	150	$129 \pm 5$	$100 \pm 8$	— — —
Micromagnetic simulation	320 (rec. edge)	160	100	300 (ccw/cw VDW)
	320 (slop. edge)	120	100	240 (ccw/cw VDW)
	150 (rec. edge)	360	200	300 (cw VDW)
	150 (slop. edge)	320	190	240 (cw VDW)

Experiments were also performed on EBL and FIB patterned 150 nm wide nanowires which contain anti-notches of width 320 nm and height 140 nm. Like the 320 nm wide wires, a ccw vortex structure appeared inside the anti-notches of the EBL nanowires after the DWs of both ccw and cw chiralities had depinned from the anti-notches. The vortex annihilation field for both chiralities of DWs in 150 nm wide nanowires was

again seen to be at  $\sim 210$  Oe, i.e. the same as for 320 nm wide EBL nanowires. Again this vortex structure did not appear after the DWs depinned from the anti-notches of the FIB patterned nanowires at this width. Table 4.1 gives the DW depinning field dependency on the fabrication technique and the chiralities of the DWs along with vortex annihilation field where appropriate. DW depinning fields are higher for the narrower wires compared to the wider wires but also show that FIB nanowires have lower depinning fields for each chirality of DW at both widths.

The comparative study of the DW depinning in the EBL and FIB nanowires have shown that the depinning fields are comparable in both cases although consistently lower for the FIB nanowires which may be due to differences in edges crystallinity already seen in TEM images. It has been seen from another study that nanoelements created by FIB with widths less than 100 nm were not able to be determined as magnetic using LTEM [17]. In that case the whole of the magnetic structure appeared to be modified by residual irradiation from the FIB, whereas in this study there is a clearly defined affected edge and non affected internal regions. In the next section we show how micromagnetic simulations can be used to gain an insight into the differing behavior of the EBL and FIB nanostructures based on the possible edge modification in the case of the latter and taking account of previous studies of ion implantation of permalloy.

### 4.4.3 Micromagnetic simulation

The micromagnetic simulations were carried out using freely available code, object oriented micromagnetic framework (OOMMF) developed by the NIST group at Gaithersburg [31]. This simulation package was described elaborately in **chapter 1**, section 1.5. The parameters used for the simulations were standard for Py: saturation magnetisation  $M_s = 8.6 \times 10^6$  A/m, exchange stiffness constant  $A = 1.3 \times 10^{-11}$  J/m, magnetocrystalline anisotropy  $K = 0$  and damping coefficient  $\alpha = 0.5$ . The measured damping parameter  $\alpha$  for Py estimates between 0.013 and 0.03 [32–34]. However, a damping parameter of 0.5 was used throughout to speed up the computations as was mentioned earlier in **chapter 2**. A cell size of  $5 \times 5 \times 5$  nm<sup>3</sup> (exchange length for Py) was used. The rest of the parameters are actually standard for Py and are commonly use for simulations Py nanowires [3, 4, 6, 27, 28] using OOMMF package. Notably, the quality of the Py deposited by thermal evaporation technique was checked by using



## Chapter 4: Nanostructures patterned by EBL and FIB milling: a direct comparison

---

DPC and low angle electron diffraction techniques by measuring saturation magnetic induction  $B_s$  ( $B_s = \mu_0 M_s$ , where,  $M_s$  is the saturation magnetisation). The measured  $B_s$  for Py deposited by using thermal evaporation technique in Glasgow was around 0.5 to 0.6 T which is much less than the standard value 1 T. This implies that for the experimentally used Py film  $M_s$  is less than the standard value ( $8.6 \times 10^6$  A/m). However, we have used the standard parameters of Py for simulations as our intention here is to use the simulated results as a guide to understand the experimental observations and to check the qualitative agreement between simulated and experimental results. It is also notable that in this chapter for the comparison of the domain wall behaviour in the nanowires patterned by the two alternative techniques, we have used the Py film deposited onto a single piece of  $\text{Si}_3\text{N}_4$  membrane. This actually ensured us that for this comparison, the same quality of Py film was used. Micromagnetic simulations were performed in this chapter for ccw and cw VDWs in 320 nm and 150 nm wide nanowires which contain 320 nm wide and 140 nm high anti-notches.

TEM cross-sectional images, Figs. 4.5(a-d, f) demonstrated a variation in the edge profile of the patterned nanowires. Therefore, to conduct simulations initially two different edge profiles were considered. These are shown as schematic cross-section of the wires in Figs. 4.13(a,b) in which (a) was designed as an ideal structure with a rectangular cross-section and (b) was structured based on the TEM x-sectional image of Fig. 4.5 (d), as a representative of the experimental edge profile which was sloping rather than vertical. Such an edge profile was modelled by dividing the thickness of the wire into four separate layers, as shown in the schematic in Fig. 4.13(b). The bottom layer (layer 1) had the dimensions of the width of the wire with the subsequent layers (layers 2-4) had their width reduced by three cells, thus creating a tapered edge profile.

The DW depinning fields obtained from micromagnetic simulations are shown in the lower part of table 4.1 along with experimentally observed field values. These simulations have confirmed the chirality dependence of the depinning fields i.e. the ccw vortex wall has a higher depinning field than the cw wall. The simulations also show that the wider wires have lower depinning fields than the narrower ones which are consistent with the experimental observations. The effect of the edge structure is evident in that the characteristic fields, i.e. DW depinning and vortex annihilation, are higher for a

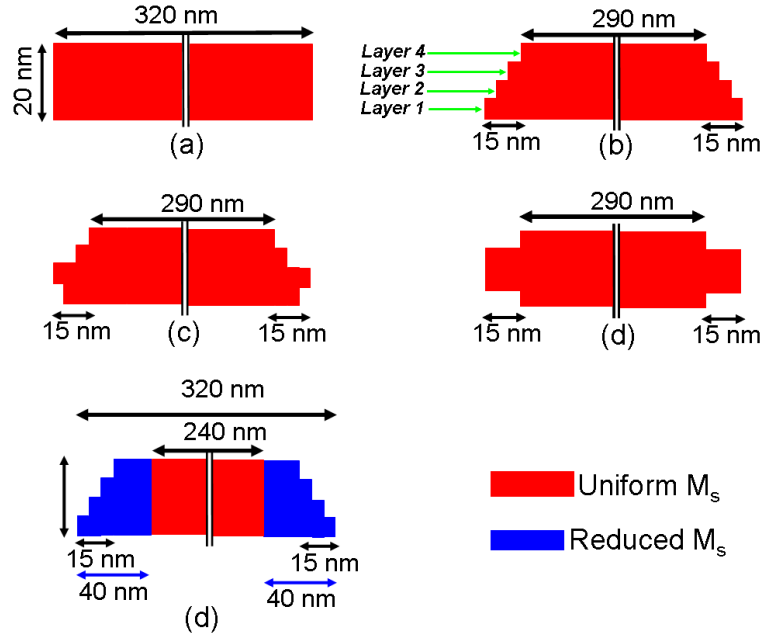


Figure 4.13: Simulations were carried out by varying the edge profiles. Schematic cross-section of the ideal nanowires with rectangular edge (a) and sloped edge (b). (c and d) The edge profile of the nanowires based on the x-sectional TEM images 4.5 (a and c). (e)  $M_s$  were reduced up to a distance of 40 nm along the wire edge in the nanowire (b). The width of the nanowires has been reduced for this schematic indicated by vertical bars.

rectangular edge profile compared to that of the sloped edge profile for all cases considered here. As is the case with previous OOMMF simulations, the predicted fields are all much larger than the observed experimental values with simulations being carried out at 0K [6,35], however the trends of the higher characteristic fields for rectangular edges narrower wires are reproduced (refer to table 4.1). Whilst the sloped edge structure accounts for lower characteristic fields like the experimental FIB structures it does still retain the residual vortex structure after DW depinning. Although in the case of the ccw VDWs in the 150 nm wide wires the simulated depinning fields are greater than the vortex annihilation field seen in the cw DW depinning. Figures 4.14(a-d) show the sequence of Fresnel images simulated for a ccw DW moving through a nanowire, which shows good agreement with the process for the EBL fabricated nanowire in Fig. 4.11. However, a clear difference between experimental and simulated Fresnel images is that the former always appear more blurry. It was mentioned in **chapter 1** section 1.5 that simulated elements do not contain any structural roughness. In reality, element edges contain structural roughness produced by the fabrication processes and ultimately affect the magnetic contrast give rise to other contrast like diffraction and electrostatic

contrast. Such defects are difficult to simulate accurately and play a role when the outcome of the simulations is compared with experimental observations.

In simulations, the edge profile of the nanowires were further varied based on the x-sectional TEM images 4.5(a and c) and these are shown as schematic cross-sections of the wires in Figs. 4.13(c and d), respectively. Again, to introduce the edge profile of Fig. 4.13 (c), the width of layer 2 had the dimensions of the width of the wire and then the layers 1, 3 and 4 had their width reduced by a couple of cells. To build up the edge profile 4.13 (d), the width of the layer 2 and 3 was same as the wire width and the layers 1 and 4 were decreased by 3 cells. In each case, the width of the nanowire was 320 nm and a ccw VDW was considered. The DW depinning fields for these two edge profiles of the nanowires were exactly equal to that of the edge profile of the representative nanowire shown as schematic cross-section of the wires in Fig. 4.13(b). Only the vortex annihilation field was slightly higher (10 Oe ) for these two edge profiles compared to the representative edge profile 4.13(b) of the nanowire. Therefore, results from micromagnetic simulations demonstrate that the characteristic DW depinning fields are reduced for a non vertical edge of a patterned nanowire.

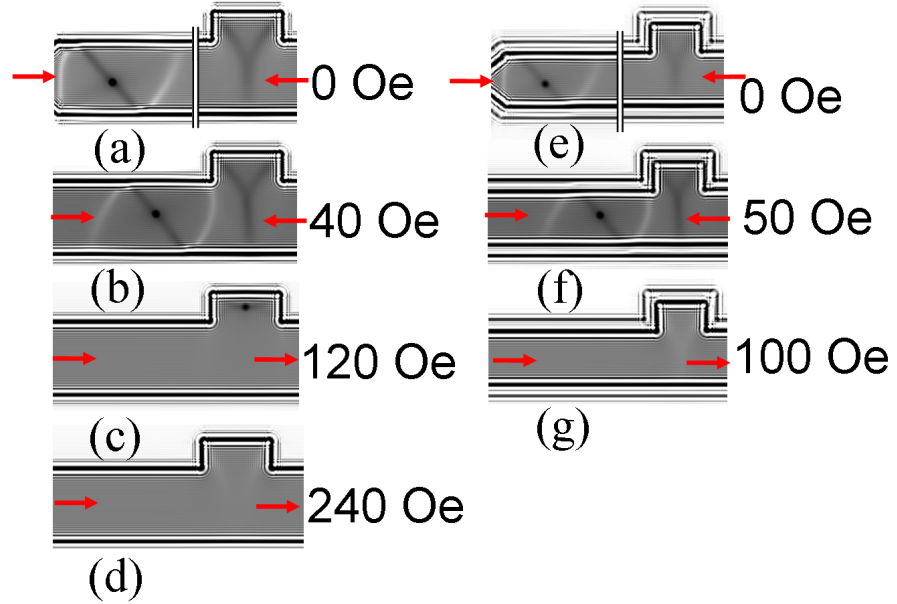


Figure 4.14: Simulated Fresnel images (a-d) show the magnetisation reversal process in 320 nm wide nanowire (sloped edge) with uniform  $M_s$  throughout the wire. A DW has moved through the anti-notch and a vortex structure is formed inside the anti-notch, as shown in (c). Simulated Fresnel images (e-g) are showing the reversal process of the nanowire of same geometry but with  $M_s$  of 50% along the wire edge. The DW has moved through the anti-notch without the presence of the vortex structure, as shown in (g).

## Chapter 4: Nanostructures patterned by EBL and FIB milling: a direct comparison

---

Although these initial simulations have shown that the characteristic DW depinning fields are reduced for a sloped edge nanowire however they do not explain why no residual vortices are seen in the anti notches after DW depinning. As mentioned earlier, it was assumed that during the milling process of the nanowires by focused  $Ga^+$  beam, the wire edges were affected by  $Ga^+$  implantation due to the extended tail of the  $Ga^+$  beam. Previously studies have looked at the effect on films irradiated homogeneously with 30 keV  $Ga^+$ , for example investigation [21] was carried out using Magneto-optic Kerr effect measurements at room temperature on  $Ni_{80}Fe_{20}$  (15.5nm)/ $Ni_{80}Cr_{20}$ (9.0nm). This study demonstrated coercivity changes in a  $100\ \mu m^2$  area even for mildly dosed ( $8 \times 10^{14}\ ions/cm^2$ ) samples that did not receive more than 1 at.% of  $Ga^+$ . However, a dramatic reduction in the Curie temperature was observed for doses of  $1 \times 10^{16}\ ions/cm^2$  due to direct  $Ga^+$  implantation. It may also be noted here that doping  $Ni_{80}Fe_{20}$  alloys with other metal such as Cr also causes the Curie temperature and saturation magnetisation to be reduced, and that at 8 at% Cr the alloy becomes paramagnetic at room temperature [36]. Therefore, to clarify the experimentally observed two-step reversal process in the case of EBL patterned nanowires and one step process for FIB nanowires, micromagnetic simulations were also carried out by varying the saturation magnetisation ( $M_s$ ) of Py along nanowire edges.

To observe the influence of the reduction of  $M_s$  along the wire edge, a similar wire structure of Fig. 4.13(b) but with a reduced  $M_s$  up to a distance of 40 nm from the wire edge was considered, as shown schematically in the blue marked region in Fig. 4.13(e). As was mentioned earlier, in the plan view bright field image 4.4(d), most of the large size grains were observed up to a distance of 40 nm from the wire edge of the FIB milled nanowire. This was the basis for reducing  $M_s$  in simulations up to this distance of the wire edges.

The simulations were performed by varying  $M_s$  up to a distance of 40nm from the wire edge along the edges for a ccw VDW in a 320 nm wide and 20 nm thick wire as shown in the schematic cross-section 4.13(e). The  $M_s$  value in the central part of the wire remained at 100%. The dimension of the anti-notch was fixed as before, i.e. 320 nm wide and 140 nm high.  $M_s$  values along the wire edge were reduced from 100% down to 40% and results were plotted in Fig. 4.15. This figure shows that if  $M_s$  is reduced along the wire edges the DW depinning field decreases by around 20% compared to the

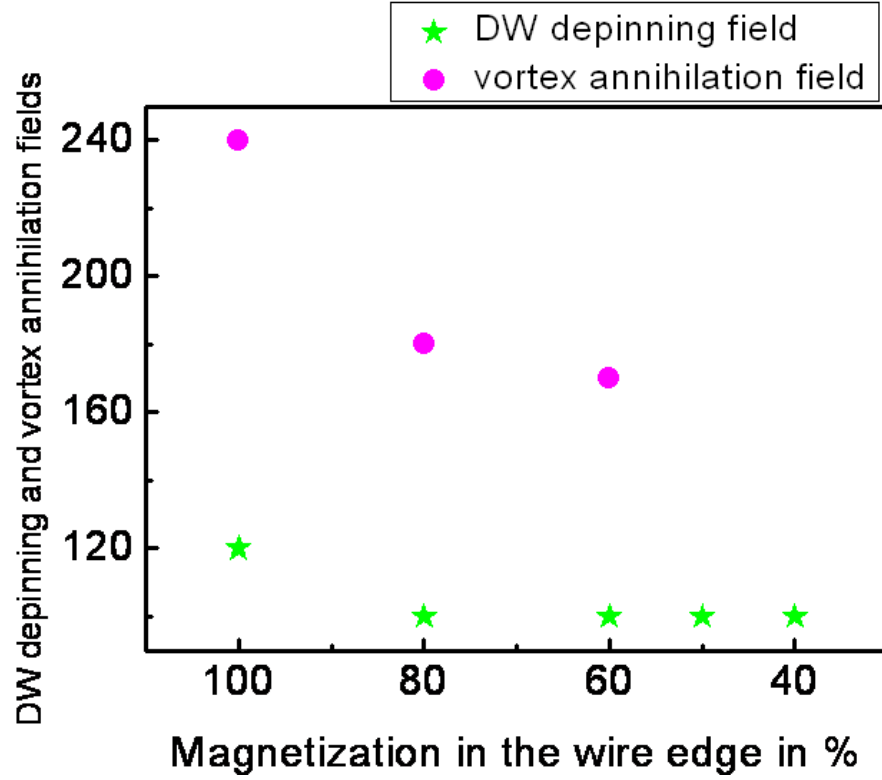


Figure 4.15: DW depinning field and vortex annihilation fields as a function of  $M_s$  along the wire edge. The simulations were carried out for a ccw VDW in a 320 nm wide and 20 nm thick wire as shown in the schematic cross-section 4.13(e)

unmodified wire. Additionally it can be seen that the vortex annihilation field inside the anti-notch also reduces with reduced  $M_s$  along the wire edge. However when  $M_s$  is reduced to 50 % along the wire edge, the ccw vortex structure is no longer formed inside the anti-notch of the wire. To illustrate this the reversal process for a 50 %  $M_s$  along the wire edge of a 320 nm wide wire is shown in Figs. 4.14(e-g). This suggests that the experimental results, Figs. 4.11(b,e and h) and 4.12(b,e and h) for FIB patterned nanowires may be consistent with reduced edge  $M_s$ , due to  $Ga^+$  implantation.

## 4.5 Summary

In the present investigation, high quality nanostructures were fabricated by using EBL and FIB techniques and characterised by TEM imaging. Bright field images revealed significant grain growth along the wire edges of the FIB patterned nanowires. However, TEM x-sectional images have confirmed that well defined edge profiles are produced in nanowires patterned using both EBL and FIB techniques. Magnetising experiments using the Fresnel mode of Lorentz TEM revealed differences in the magnetic behavior

between EBL and FIB patterned nanowires, notably small but reproducible differences in the depinning fields and the absence of residual vortices in the anti-notches of the FIB nanowires. Evidence from micromagnetic simulations suggest that this different reversal process between the nanowires fabricated by the FIB techniques may be associated with the reduction of  $M_s$  along the wire edges. Such a reduction of  $M_s$  along the wire edges reduces the DW depinning fields and is consistent with the experimentally observed magnetisation behavior of the FIB milled nanowires. Indeed this point is consistent with a study of nanoelements with dimensions  $< 100$  nm in which the entire element appeared to be affected by the residual irradiation from the FIB [17]. The difference in the reversal process between EBL and FIB patterned nanowires are also demonstrated by the formation of a ccw vortex structure inside the anti-notches of the EBL nanowires after the depinning of DWs in contrast to the FIB nanowires where no such vortex structures formed. The presence of these vortices could potentially be very problematic for nanowire applications where a series of domain walls pass through wires in proposed memory and logic applications [1, 2]. Therefore for the wire dimensions considered here FIB may actually be beneficial as a fabrication method. However it must be noted that the edge modification induced by the FIB method does have implications particularly if smaller dimensions are to be fabricated and this certainly needs to be carefully considered when using this method.

# Bibliography

- [1] D. A. Allwood, G. Xiong, C. C. Faulkner, D. Atkinson, D. Petit, R. P. Cowburn, Science **309** 1688 (2005).
- [2] S. P. Parkin, M. Hayashi, and L. Thomas, Science 320, 190 (2008).
- [3] M. T. Bryan, T. Schrefl, and D. A. Allwood, Appl. Phys. Lett. **91** 142502 (2007).
- [4] Atkinson, D. S. Eastwood, and L. K. Bogart, Appl. Phys. Lett. **92** 022510 (2008).
- [5] D. A. Allwood, G. Xiong, and R. P. Cowburn, Appl. Phys. Lett. **85** 2848 (2004).
- [6] D. Petit, A. V. Jausovec, D. Read, and R. P. Cowburn, J. Appl. Phys. **103** 114307 (2008).
- [7] M. Kläui, H. Ehrke, U. Rdiger, T. Kasama, R. E. Dunin-Borkowski, D. Backes, L. J. Heyderman, C. A. F. Vaz, J. A. C. Bland, G. Faini, E. Cambril, and W. Wernsdorfer, Appl. Phys. Lett. **87** 102509 (2005).
- [8] D. McGrouther, S. McVitie, J. N. Chapman, and A. Gentils, Appl. Phys. Lett. **91** 022506 (2007).
- [9] K. J. O'Shea, S. McVitie, J. N. Chapman, and J. M. R. Weaver, Appl. Phys. Lett. **93** 202505 (2008).
- [10] M. T. Bryan, D Atkinson and R P Cowburn, Appl. Phys. Lett. **85** 3510 (2004).
- [11] D. Atkinson , Journal of Physics: Conference Series **17** 33 (2005).
- [12] J. Mayer, L.A. Giannuzzi, T. Kamino, and J. Michael, MRS Bulletin, 32, 400 (2007).
- [13] J. N. Chapman, A. B. Johnston, L. J. Heyderman, S. McVitie, W. A. P.Nicholson, and B. Bormans, IEEE Trans. Magn. **30** 4479 (1994).

- [14] D.T. Carpenter, J.M. Rickman, K. Barmak, J. Appl. Phys. **84** 5843 (1998).
- [15] D. McGrouther, *Effects of Focused Ion Beam Irradiation on Thin Ferromagnetic Films*, PhD thesis, University of Glasgow, 2004.
- [16] S. Turnbull, *Characterisation of focused ion beam nanostructures by transmission electron microscopy*, PhD thesis, University of Glasgow, 2008.
- [17] X. Kong, S McVitie, J. N. Chapman, J. M. W. Weaver and C. D. W. Wilkinson, J. Vac. Sci Tech., submitted for publication.
- [18] D. S. Macintyre, O.Ignatova, S.Thoms, I.G.Thayne, J. Vac.Sci. Technol. B **27(6)**, 2597 (2009).
- [19] J. Melngailis, J. Vac. Sci. Technol. B **5** 469 (1987)
- [20] A. Kieslich, Reithmaier J P and Forchel A, J. Vac. Sci. Technol. B **12** 3518, (1994).
- [21] W. M. Kaminsky, G. A. C. Jones, N. K. Patel, W. E. Booi, M. G. Blamire, S. M. Gardiner, Y. B. Xu, and J. A. C. Bland, Appl. Phys. Lett. **78** 1589 (2001).
- [22] D. Ozkaya L, R. M. Langford, W. L. Chan, and A. K. Petford-Long, J. Appl. Phys. **91** 9937 (2002).
- [23] J. Fassbender and J. McCord, Appl. Phys. Lett. **88** 252501 (2006).
- [24] C.-M. Park and J.A. Bain, J. Appl. Phys. **91** 6830 (2002).
- [25] C.-M. Park and J.A. Bain, IEEE Trans. Magn. **38** 2237 (2002).
- [26] J. Fassbender, J. von Borany, A. Mcklich, K. Potzger, W. Mller, J. McCord, L. Schultz and R. Mattheis, Phys. Rev. B **73** 184410 (2006).
- [27] C. Brownlie, S. McVitie, J. N. Chapman, and C. D. W. Wilkinson, J. Appl. Phys. **100** 033902 (2006).
- [28] Y. Nakatani, Y. A. Thiaville, J. Miltat, J. Magn. Magn. Mater. **290** 750 (2005).
- [29] C. Brownlie, *A TEM Investigation of Controlled Magnetic Behaviour in Thin Ferromagnetic Films*, PhD thesis, University of Glasgow, 2007.



- [30] K. J. O'Shea, *Putting a leash on the domain wall: A TEM investigation into the controlled behaviour of domain walls in ferromagnetic nanostructures*, PhD thesis, University of Glasgow, 2010.
- [31] M. J. Donahue and D. G. Porter, Report No. NISTIR 6376 (National Institute of Standards and Technology, Gaithersburg, MD, 1999).
- [32] I. N. Krivorotov, N. C. Emley, J. C. Sankey, S. I. Kiselev, D. C. Ralph, and R. A. Buhrman, *Science* **307** 228 (2005).
- [33] P. M. Braganca, I. N. Krivorotov, O. Ozatay, A. G. F. Garcia, N. C. Emley, J. C. Sankey, D. C. Ralph, and R. A. Buhrman, *Appl. Phys. Lett.* **87** 112507 (2005).
- [34] G. M. Sandler, H. N. Bertram, T. J. Silva, and T. M. Crawford, *J. App. Phys.*, **85** 5080 (1999).
- [35] A. Himeno, T. Okuno, T. Ono, K. Mibu, S. Nasu, and T. Shinjo, *J. Magn. Magn. Mater.* **286** 167 (2005).
- [36] R. M. Bozorth, *Ferromagnetism* (Piscataway: IEEE) 1993.

# Chapter 5

## Controlling of domain walls in planar nanowires by ion irradiated features

### 5.1 Objective and motivation

The previous chapter (**chapter 4**) illustrated a direct comparison of the domain walls' behaviour in ferromagnetic nanowires patterned by electron beam lithography and focused ion beam milling. *In situ* magnetising experiments using Lorentz TEM explored differences in the magnetic behavior between nanowires patterned by these two alternative fabrication techniques at the final stage where the VDW moved through the anti-notches. Another notable observation was that the DW depinning fields are lower in the FIB patterned nanowires compared to those of the EBL patterned nanowires. In order to perform this comparison, domain walls (DWs) in the patterned nanowires were controlled using a rectangular geometrical feature referred as anti-notch. The ability to control precisely the motion of magnetic domain walls (DWs) in ferromagnetic nanowires is crucial for the future realisation of proposed magneto-electronic (or spintronic) devices [1,2] as well as for greater understanding of fundamental nanomagnetic behavior [3,4]. Previous investigations have demonstrated that topographically defined trapping sites such as notch/anti-notch of different geometries allow control of the position of DWs [5–9] in ferromagnetic nanowires. The strength of these trapping/pinning features depends on the feature geometry dimensions and the spin distribution of the incoming DWs [6,7,9]. However, as patterned magnetic structures are reduced in size, the role of edges [10] and the fabrication techniques used will become limiting fac-

tors [11] making it challenging to write well defined notch/anti-notch structures below 100 nm. A possible alternative approach is to use ion irradiated features [12–14] that controllably modify the properties of the film in selected regions within the patterned structures. The modified areas may act as inherent pinning sites without necessarily changing the geometry of the nanowires. This alternative technique of controlling DWs is explored in this chapter. Field-driven pinning and depinning of DWs by such non topographic pinning features were observed directly using the Fresnel mode of Lorentz TEM. Prior to conducting pinning/depinning experiments, property modifications of the thin continuous film system were investigated as a function of irradiation dose in the TEM.

## 5.2 Property modification by ion irradiation

Modification of materials' properties by ion implantation and ion irradiation in semiconductors, metals and polymers has been studied comprehensively over the past few decades [15–17]. However, in recent times magnetic patterning has been studied by local modification of the magnetic properties of thin continuous films by means of ion irradiation [18–20]. Focused ion beam (FIB) implantation/irradiation has been shown to be capable of modifying magnetic properties such as the coercivity, saturation magnetization  $M_s$  [20, 21] and local anisotropy direction [22] in continuous permalloy (Py) films. Another investigation demonstrated that  $M_s$  as well as the effective magnetic layer thickness is modified due to the sputtering of target atoms by means of 30 keV Ni ion implantation [23] in an uncapped 20 nm thick Py film. This investigation indicates that ion implantation of an uncapped film is limited by the sputter yield per incident ion. An alternative approach for tailoring magnetic properties such as the coercivity, saturation magnetisation and local anisotropy direction of layered magnetic films is radiation-induced modification of interfaces [24–26]. In multilayered ferromagnetic films, where interfaces are present, magnetic properties have been shown to be even more sensitive to FIB irradiation [27–29]. In a recent investigation [30], tailoring of the magnetic properties of layered magnetic films  $\text{Ni}_{81}\text{Fe}_{19}/\text{Au}$  by radiation-induced modification of interfaces was also explored. That study demonstrated the ability of a FIB to modify locally the magnetic properties of ultra thin, in-plane magnetised

capped films due to ion beam mediated intermixing of the layers. In another investigation [12], magnetic properties of multilayer systems consisting of a Py layer of either 10nm or 20nm, and one or more non-magnetic layers of Al or Au were irradiated in a FIB with a 30keV  $Ga^+$  source. The presence of the non-magnetic layers allowed irradiation induced mixing with the magnetic layer, effectively creating alloyed regions with different properties to the rest of the film.

In this investigation, we demonstrate the novel creation of non-topographic DW pinning sites, defined directly by FIB irradiation, where the pinning strength and structure of the DWs pinned is strongly controlled by the irradiation dose. In the present investigation, a tri-layer thin film of Cr/Py/Cr was purposely created to optimise sensitivity to ion irradiation through localised beam induced alloying of the Py and Cr in a FIB microscope. Cr was chosen as the material surrounding the Py layer because implantation of Cr is known to reduce the Curie temperature,  $M_s$ , magnetic anisotropy as well as altering the exchange constant [24–26] of Py. Furthermore, the magnetic properties of Py are very highly sensitive to Cr content as low levels, around 8 at% Cr are sufficient to render the Py/Cr alloy paramagnetic at room temperature [31], as shown in the schematic diagram Fig. 5.1. Notably, the structural and magnetic properties of Cr implanted 20 nm thick Py on top of a Ta buffer layer was investigated recently [24] as a function of saturation magnetisation. This investigation also demonstrated that ferromagnetism is destroyed for an implantation fluence of  $1.5 \times 10^{16} \text{ ions/cm}^2$ , which corresponds to a doping concentration of about 8 at. % Cr throughout the Py film. In the present investigation, it is thereby expected that the combination of the irradiation and interlayer mixing will modify effectively the properties of this alloy system.

### 5.3 Optimisation of materials thickness using TRIDYN simulation

The material thicknesses used experimentally were suggested from results carried out using the TRIDYN simulation program [32] (this package was described in **chapter 2**, section 2.6) so that we could get something approaching a uniform Cr concentration in the Py layer. This was done by noting the concentration of Cr in the Py film for a particular ion dose. The  $Ga^+$  energy is 30 keV and irradiation direction is normal to

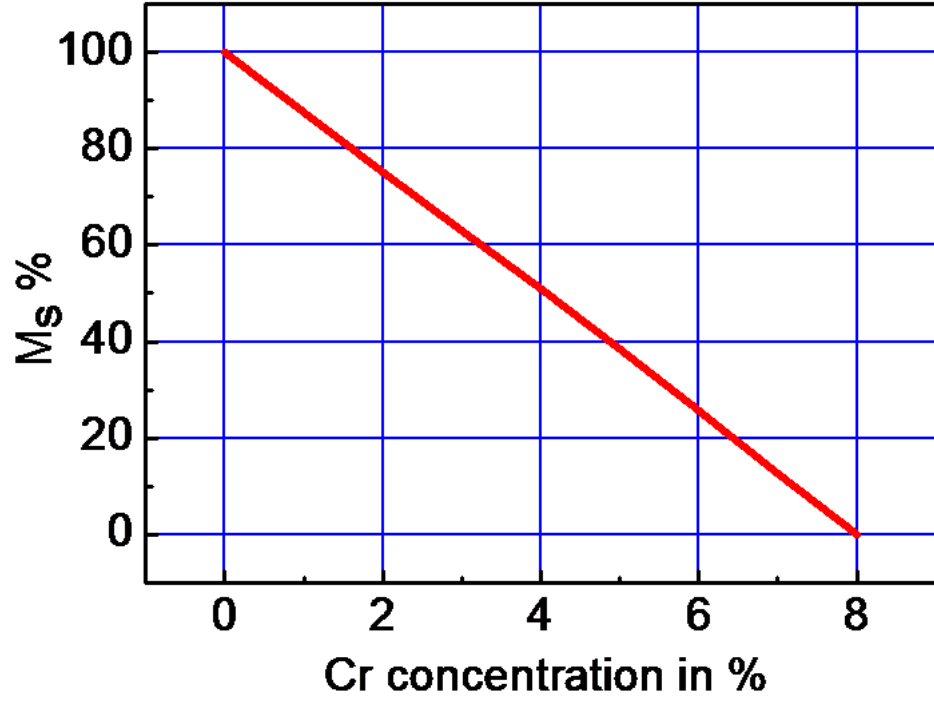


Figure 5.1: Reduction of saturation magnetisation  $M_s$  due to doping Cr in Py as a function of Cr concentration. Data was adapted from reference [31].

the surface. As a substrate, Si was used instead of  $\text{Si}_3\text{N}_4$  due to the limited number of elements available in the TRIDYN code used in this project. Initially a Py thickness of 20 nm was considered for this alloy system. However, the Cr concentration at the centre of the Py film in material system  $\text{Cr}(5 \text{ nm})/\text{Py}(20 \text{ nm})/\text{Cr}(5 \text{ nm})$  was zero for an ion dose of up to  $1 \times 10^{15} \text{ ions/cm}^2$  as shown in Fig. 5.2. The same figure shown a small amount of Cr (2.5 at. %) at the centre of the Py film for an ion dose of  $4 \times 10^{15} \text{ ions/cm}^2$ . These clearly indicate that from this combination it is not possible to obtain a significant amount magnetic property modification at ion doses of the order of magnitude of  $10^{14} \text{ ions/cm}^2$ . Then the thickness of the Py layer was reduced to half (10 nm) and also the thickness of the top and bottom Cr layers were varied. The Cr concentration at the centre of the Py layer was calculated from each of these combinations and the data were plotted in Fig. 5.2. For the combination of  $\text{Cr}(3 \text{ nm})/\text{Py}(10 \text{ nm})/\text{Cr}(5 \text{ nm})/\text{substrate}$  (red color spots), the Cr concentration at the centre of the Py film was higher and therefore such a material system shown schematically in Fig. 5.3 (a) was considered for the present investigation. The asymmetry of the top and bottom Cr layer was crucial to obtain comparatively uniform Cr concentration in a controllable manner.

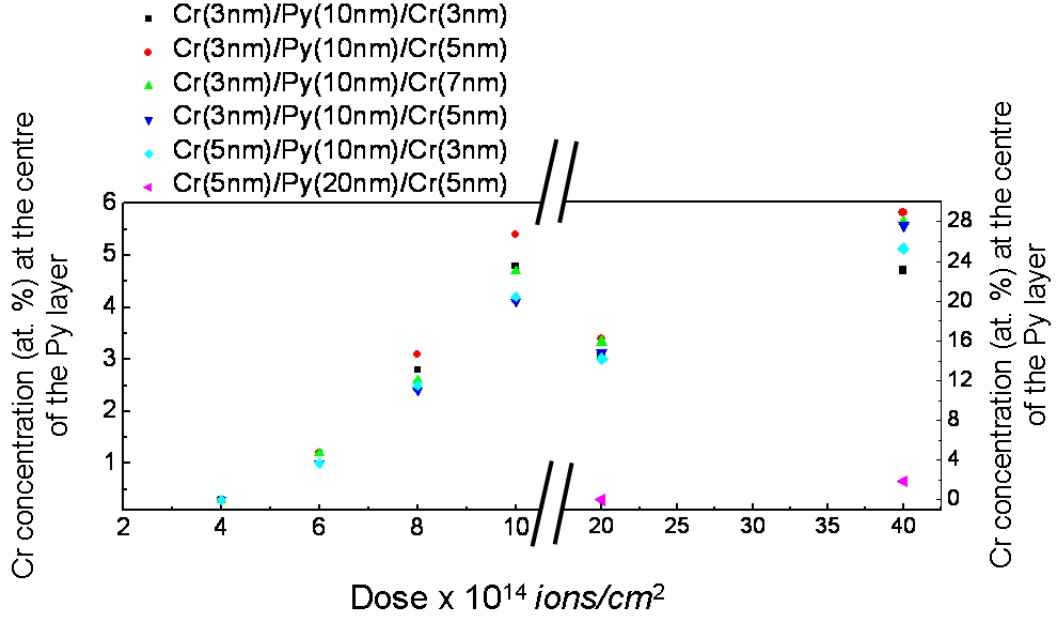


Figure 5.2: The amount of Cr concentration at the centre of the Py film as a function of dose for different combinations of Cr/Py/Cr/substrate thin films. Cr concentration at the centre of the Py is higher for a combination of Cr(3 nm)/Py(10 nm)/Cr(5 nm) (red colour).

Figure 5.3(b) shows Cr concentration in each layers of this material system as a function of sample depth for different ion doses. The histograms, Figs. 5.3(c-f), show separately the Cr concentration in the Py layer for ion doses (c)  $4 \times 10^{15}$  ions/cm<sup>2</sup> (d)  $8 \times 10^{15}$  ions/cm<sup>2</sup> (e)  $12 \times 10^{15}$  ions/cm<sup>2</sup> and (f)  $16 \times 10^{15}$  ions/cm<sup>2</sup>. In the histograms (c-f) the dark cyan regions are paramagnetic as the Cr concentrations in these regions are  $> 8$  at.%. Ferromagnetism gradually decreases from histograms c to f as Cr concentration increase in the Py film. For an ion dose of  $16 \times 10^{15}$  ions/cm<sup>2</sup>, Fig. 5.3(f) which corresponds to a Cr concentration of  $> 8$  at. % throughout the film, the ferromagnetism completely vanishes and the material becomes paramagnetic. It should be noted that the simulation and actual doses in practice may differ somewhat and so what we expect is that the ferromagnetism will decrease with dose but perhaps not at the exact level predicted by these simulations.

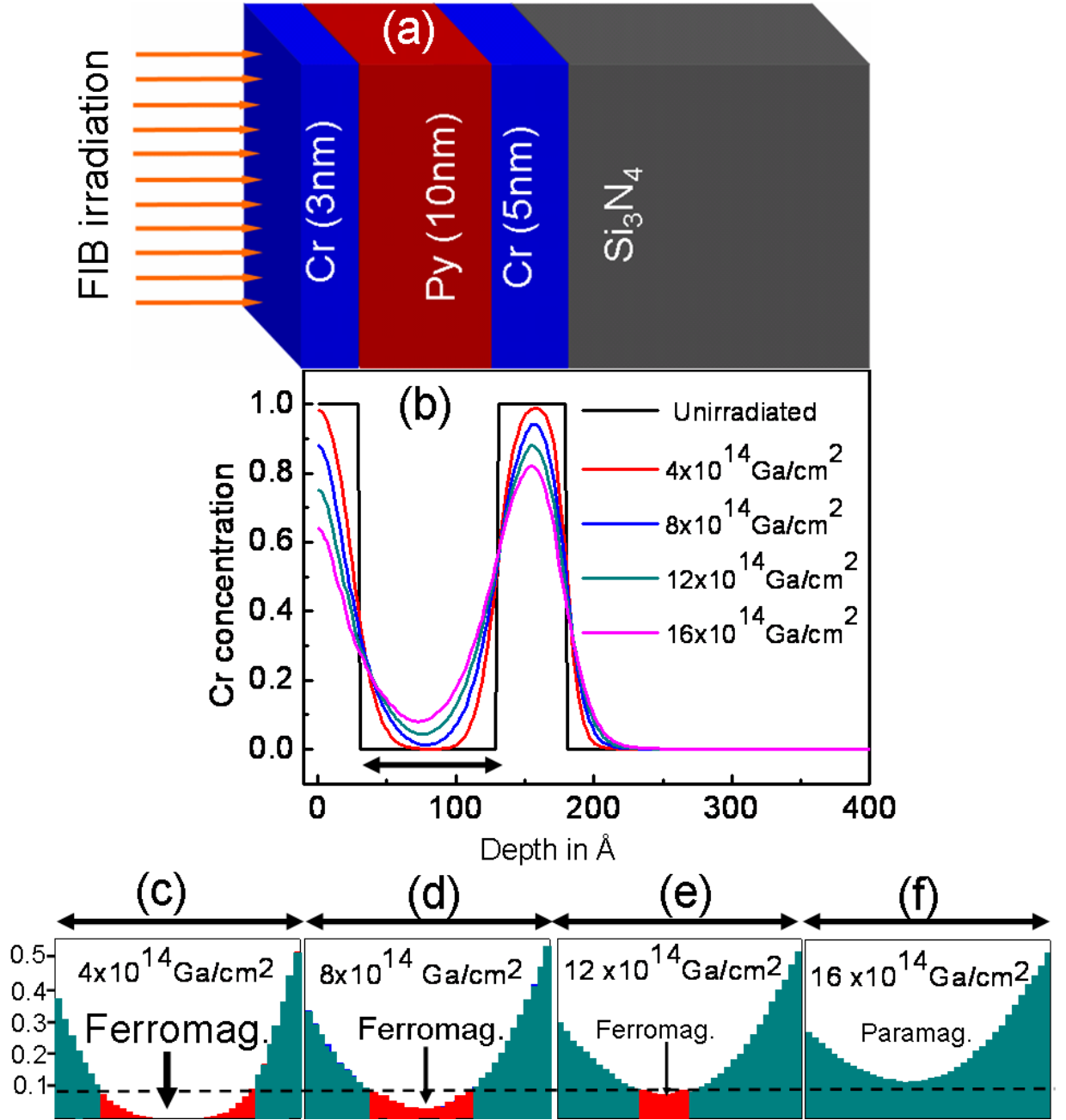


Figure 5.3: (a) Schematically multi-layer thin film system considered for the present investigation. (b) The Cr concentration as a function of sample depth for different ion doses obtained from TRIDYN simulation. (c-f) Histograms show the amount of Cr concentration in the Py layer for different ion doses.

## 5.4 Materials deposition

Thin film of Cr(3 nm)/Py(10 nm)/Cr(5 nm) was deposited on top of Si<sub>3</sub>N<sub>4</sub> membrane by molecular beam epitaxy technique (the technique was described in **chapter 2**) available in the HZDR, Institute of Ion Beam Physics and Materials Research, Dresden, Germany. Polycrystalline Py was deposited at a rate 0.2-0.3 Å/s on top of Si<sub>3</sub>N<sub>4</sub> window membrane suitable for TEM experiments. This MBE deposited film was

not suitable for magnetic characterisation as we did not observe a reproducible magnetic behaviour during the magnetisation experiments. This issue will be discussed further later on in section 5.8.1. Therefore, a multilayer polycrystalline film of Cr(3 nm)/Py(10 nm)/Cr(5 nm) was deposited by magnetron sputter deposition technique without breaking vacuum at a rate not exceeding  $0.55 \text{ Å/s}$  on top of  $\text{Si}_3\text{N}_4$  membrane. During the deposition of the magnetic material an in-plane field was applied to produce a uniaxial magnetic anisotropy direction using the facilities available in IPTH Jena, Germany. It is noteworthy that this becomes very important in having wires with reproducible DW behaviour as will be discussed later on in section 5.8.2. Magneto-optic

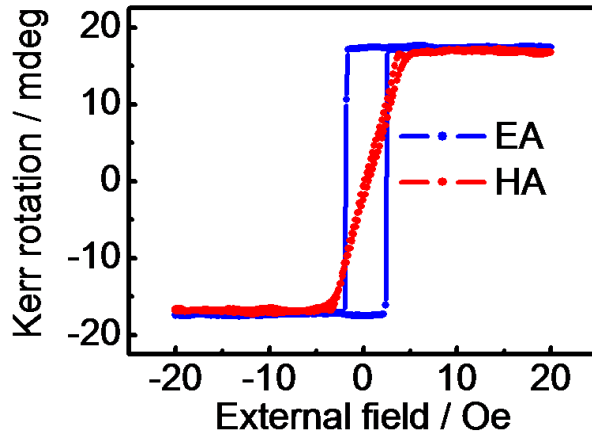


Figure 5.4: MOKE easy (EA) and hard axis (HA) hysteresis loops for the as-deposited film with field induced anisotropy.

Kerr effect magnetometry was used to obtain easy and hard axis hysteresis loops of the as-deposited film (the measurement was done by Mr. Thomas Streche, HZDR, Institute of Ion Beam Physics and Materials Research, Dresden, Germany). Kerr magnetometry measurements showed well defined uniaxial anisotropy of the as deposited Py film, Fig. 5.4. The anisotropy field  $H_K$  for the hard axis direction and the coercivity  $H_C$  for the easy axis direction are measured to be  $3.9 \pm 0.2 \text{ Oe}$  and  $2.2 \text{ Oe}$ , respectively.

## 5.5 FIB irradiation

One of the main ideas of this project is to modify locally the ferromagnetic properties of Py by microalloying due to a combined effect of the  $\text{Ga}^+$  irradiation and interfacial atomic mixing as shown schematically in Fig. 5.5.

In order to investigate the effective local modification of the multi-layer thin film system due to radiation induced interfacial mixing, stripe patterns were written on continuous



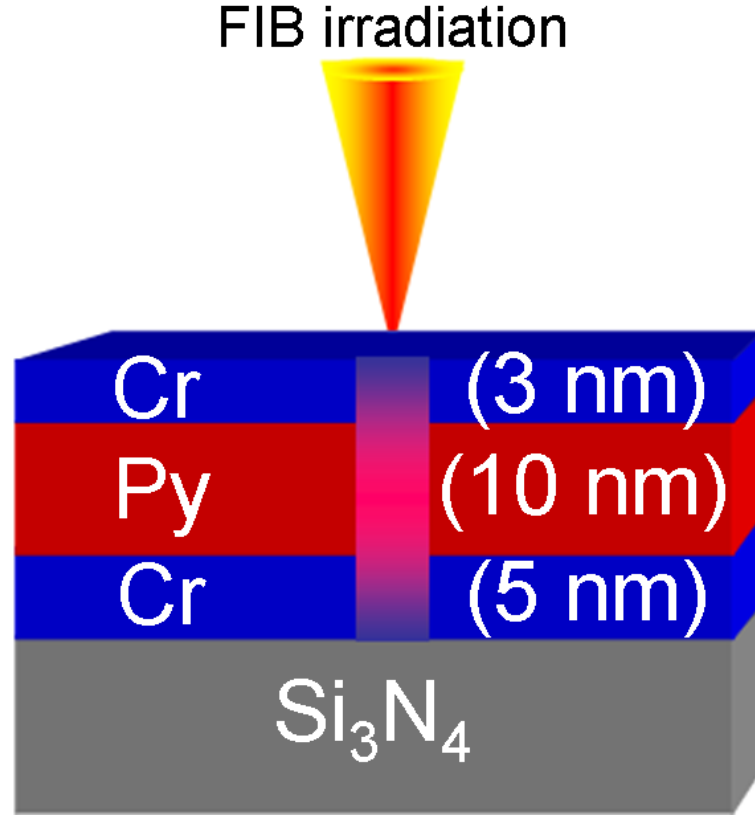


Figure 5.5: Schematic illustration of micro-alloying due to a combined effect of the focused  $Ga^+$  irradiation and interfacial atomic mixing.

thin film of Cr(3 nm)/Py(10 nm)/Cr(5 nm) deposited by MBE technique. Notably, these MBE deposited films were studied first. The alternate unirradiated and irradiated stripe patterns of width 1000 nm and length 10  $\mu m$  is illustrated schematically in Fig. 5.6. FIB irradiation was carried out using 30 keV  $Ga^+$  energy and a beam current of 93 pA using a FEI Nova NanoLab 200 SEM/FIB workstation. Irradiation of the nominal  $Ga^+$  doses of  $d \times 10^{14}$  ions/cm<sup>2</sup> ( $d = 4, 8, 12, 16$  and  $20$ ) in each stripe was applied automatically across  $Si_3N_4$  window membrane by using the in-built scripting language [33].

Figure 5.7(a) shows the plan view TEM bright field image of the as deposited unirradiated continuous multi-layer film. Figure 5.7(b) shows the plan view bright field image of the unirradiated and irradiated stripe patterns. The irradiated material can be easily distinguished from the unirradiated film by the increase in grain size from 5-10 nm to 20-30 nm. An increase of grain size after  $Ga^+$  irradiation has been reported for 30 nm  $Ni_{80}Fe_{20}$  on carbon-coated copper TEM-grids [21, 34]. In **chapter 4** significant grain growth was observed up to a distance of 30 to 40 nm from the wire edges of the FIB patterned nanowires, as marked by circles in Fig. 4.4(d). It was assumed that

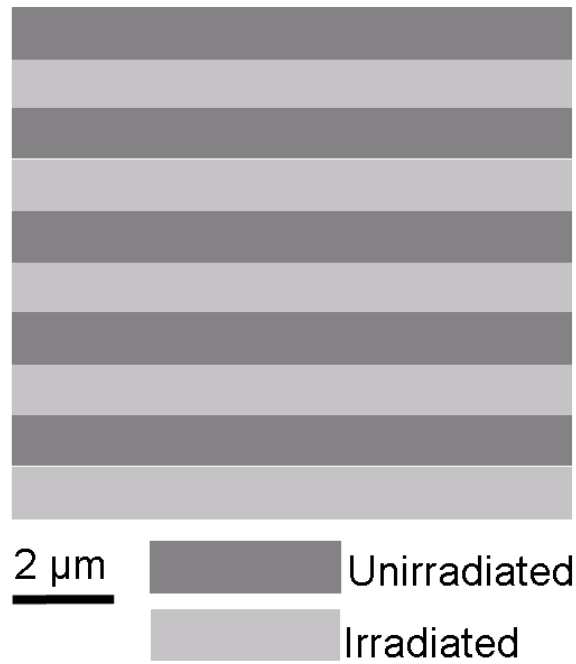


Figure 5.6: Schematically alternate unirradiated and irradiated stripe patterns written on thin continuous film using focused ion beam.

during the milling process of the nanowires by focused  $\text{Ga}^+$  beam, the wire edges were affected indirectly by  $\text{Ga}^+$  irradiation due to the extended tail of the  $\text{Ga}^+$  beam and therefore FIB induced grain growth was observed along the wire edges. In contrast, here FIB induced grain growth was observed due to  $\text{Ga}^+$  irradiation directly in the micron size irradiated stripes.

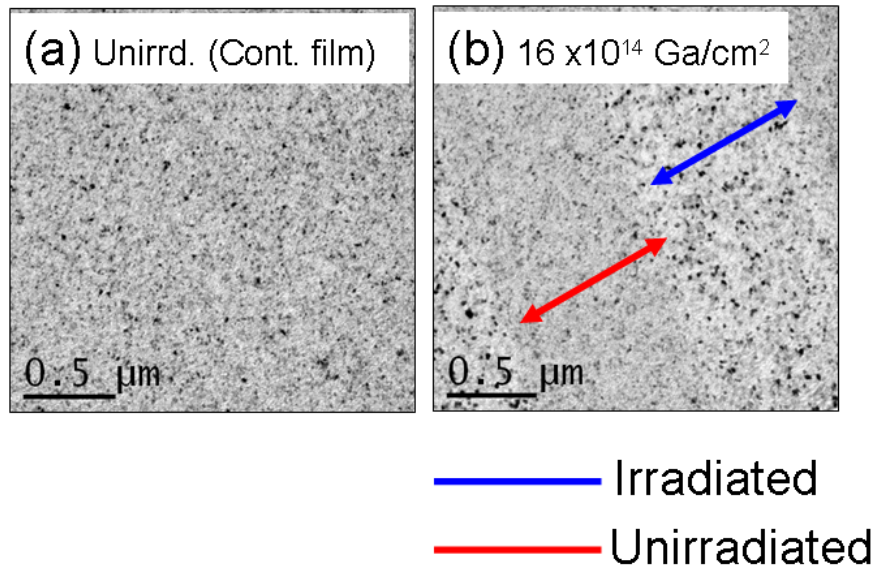


Figure 5.7: TEM bright field images of the (a) unirradiated continuous film and (b) alternate unirradiated irradiated stripe patterns. The average grain size in the irradiated stripe is larger than that of the unirradiated stripe.

## 5.6 Modification of the material system: low angle electron diffraction experiments

After successfully conducting FIB irradiation as irradiated stripes surrounded by alternative unirradiated stripe patterns, low angle electron diffraction experiments [35] were carried out using Lorentz microscopy. This technique was described in **chapter 3** (section 3.10). In order to carry out this diffraction experiment, we were able to form a state with a 180° degree wall perpendicular to the stripes, then studied it using Fresnel mode of Lorentz TEM. The wall is connected from unirradiated film to the patterned stripes as shown in Fig. 5.8(a). By illuminating an area of anti-parallel alignment of magnetisation of the unirradiated film (marked by red circles in Figs. 5.8(a)), pairs of diffraction spots were formed. From such an anti-parallel alignment of magnetisation region of the continuous film, formation of two diffraction spots was expected. Whereas by illuminating an area of anti-parallel alignment of magnetisation of the alternate unirradiated and irradiated region (marked by blue circle) we also see a pair of spots though with a smaller separation. Given that the dose is expected to reduce the magnetisation in the irradiated region, therefore, it is perhaps a bit surprising that only two spots are visible. However, for all doses this effect was observed, the only change being the separation of the spots. The dose of the irradiated region was  $4 \times 10^{14} \text{ ions/cm}^2$ , the lowest dose used for this experiment. A careful observation of the distances between the two pairs in Figs. 5.8(b) and 5.8(c) indicate that the distance between two spots formed from the hybrid region is smaller compared to that of the unirradiated film region. Diffraction patterns were taken from another region, Fig. 5.8(d) in which the dose of the irradiated stripes was  $8 \times 10^{14} \text{ ions/cm}^2$ . Pairs of diffraction spots were recorded from this region and the separation between the two spots was again smaller compared to that of the unirradiated film region and also of the region irradiated by ion doses of  $4 \times 10^{14} \text{ ions/cm}^2$ . The Lorentz deflection angle present in the region of the continuous film or patterned region under investigation is expected to be proportional to the saturation magnetic induction ( $B_s = \mu_0 M_s$ ) times film thickness  $t$ , i.e.  $\beta_L = \frac{e\lambda B_s t}{h}$  for a uniformly magnetised material with no stray field present. Therefore, the separation between two diffraction spots of a pair is higher if the deflection takes place from a region containing two uniformly magnetised and

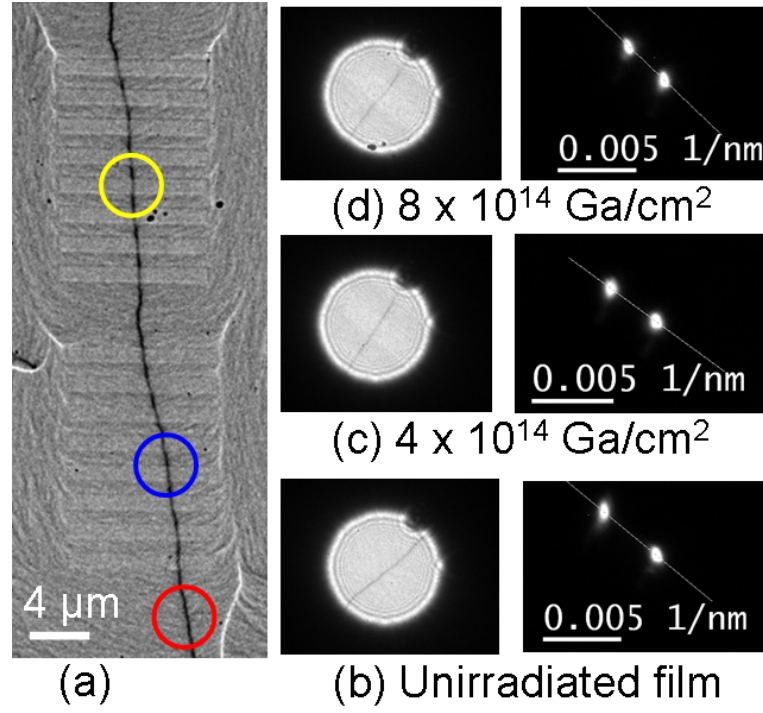


Figure 5.8: (a) Fresnel image show the formation of a DW perpendicular to the stripes. Diffraction patterns were taken against  $180^\circ$  DW from (b) unirradiated continuous film, (c and d) irradiated regions. Irradiation doses were  $4 \times 10^{14} \text{ ions/cm}^2$  (c) and  $8 \times 10^{14} \text{ ions/cm}^2$  (d).

anti-parallel aligned domains, Fig. 5.8(b). It is expected that the magnetisation of the irradiated region is lower compared to that of the unirradiated region. Hence, the separation between two diffraction spots of a pair might be smaller if the deflection takes place from a region containing a reduced magnetised and anti-parallel aligned domains. Therefore, in principle four diffraction spots were expected for the patterned region, either Fig. 5.8(c) or Fig. 5.8(d), two from the non-irradiated material and the other two from the material with reduced saturation magnetisation value, as was illustrated in the schematic Fig. 5.9(a). Notably, the predicted spots from Fig. 5.9(a) are based on a calculated deflection due to the magnetisation only. However, in practice only two diffraction spots were observed from the patterned region as was seen in Figs. 5.8(c) or 5.8(d).

Using the low angle electron diffraction technique in Lorentz microscopy, by illuminating the area under investigation we are sensitive to the integrated magnetic induction not the integrated magnetisation. This is very important when stray field are present and may contribute significantly to the observed deflection. It is well known from the theory of electromagnetism that the normal component of magnetic induction is con-

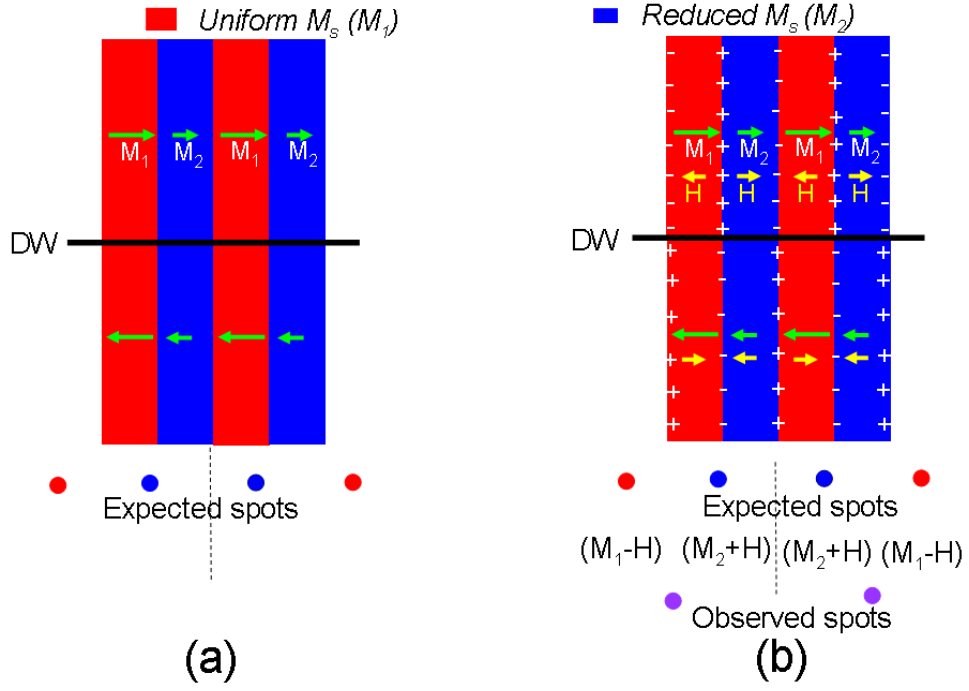


Figure 5.9: (a) A schematic of magnetisation direction of the unirradiated and irradiated regions against an  $180^\circ$  DW. Two pairs of diffraction spots were expected from such an anti-parallel alignment of unirradiated and irradiated magnetisation regions. (b) Schematic illustration of stray magnetic fields originated from the surface charges in the uniformly magnetised and reduced magnetised regions. Pairs of diffraction spots were observed experimentally due to the influence of oppositely oriented stray magnetic fields in the unirradiated and irradiated regions.

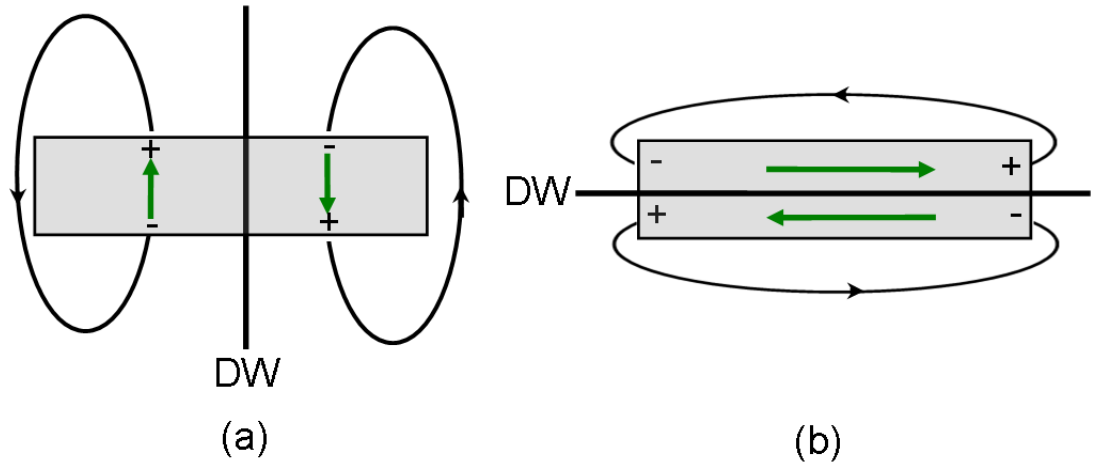


Figure 5.10: The schematic diagrams show stray magnetic fields when DW is formed (a) perpendicular to the long stripe and (b) parallel to the same stripe. The influence of stray magnetic fields in the integrated magnetic induction is significant when DW is formed perpendicular to the long stripe (a) and is negligible when DW is formed parallel to the long stripe (b).

tinuous across a boundary i.e.  $\nabla \cdot \mathbf{B} = 0$ , one of Maxwell's equation. Since  $\nabla \cdot \mathbf{B} = 0$ , the divergence of  $\mathbf{M}$  can be expressed as  $\nabla \cdot \mathbf{M} = -\nabla \cdot \mathbf{H}$ . This non zero divergence of  $\mathbf{M}$  gives rise to surface charge (surface is the region between two different media) [3]

which was shown schematically in Fig. 5.9(b). The amount of stray field originates from these surface charges are same both in the unirradiated and irradiated stripe regions but points opposite to the magnetisation of the unirradiated stripe and along the irradiated stripe regions as was illustrated in Fig. 5.9(b). Therefore, the continuity of the  $\mathbf{B}$  field ensures that the combination of magnetisation and stray field in each region (unirradiated and irradiated) give almost the same contribution to the integrated induction and hence this is the reason that only one spot is observed for each area either side of the domain wall, Fig. 5.9(b) even though the magnetisation can vary considerably.

The influence of stray magnetic fields may be described with the aid of schematic Fig. 5.10. It's influence in the integrated magnetic induction is significant when DW is formed perpendicular to the long stripe as shown in Fig. 5.10(a) and is negligible when DW is formed parallel to the long stripe, schematic Fig. 5.10(b) as in the latter case, the charge is appeared at the far end of the stripe. In this investigation, DW is formed perpendicular to the stripe patterns and therefore, the combination of magnetisation and stray field in each region (unirradiated and irradiated) contributed to the integrated induction as was described using schematic diagram Fig. 5.9(b). Therefore, two diffraction spots were observed instead of four from the oppositely magnetised unirradiated and irradiated stripe patterns. However, in **chapter 6** we will see that DW is formed along the stripe patterns as shown in the schematic Fig. 5.10(b) and in that case the influence of stray magnetic fields is negligible. In the absence of stray magnetic fields, the integrated magnetic induction is equivalent to saturation magnetisation. Therefore, four diffraction spots was observed for the stripe pattern, two from oppositely magnetised non-irradiated regions and the other two from the oppositely magnetised regions with reduced saturation magnetisation value. These results will be presented in **chapter 6**, section 6.4.

Based on the continuity of the normal component of  $\mathbf{B}$  a calculation was performed using the image processing software package Digital Micrograph (DM). The "model" assumes uniform magnetisation in each region being the full  $M_s$  of the material and a reduced amount that can be varied according to the radiation dose. Thereby, alternate unirradiated and irradiated stripe patterns were created for modeling. The magnetisation of the irradiated stripe is reduced within an interval of 5% from its maximum

value. Examples of such an alternate stripe patterns were shown here along with their magnetisation values, in Figs. 5.11(a) and (b), respectively. The magnetisation of the unirradiated and irradiated stripes are 100 % and 50 %, respectively. It was described

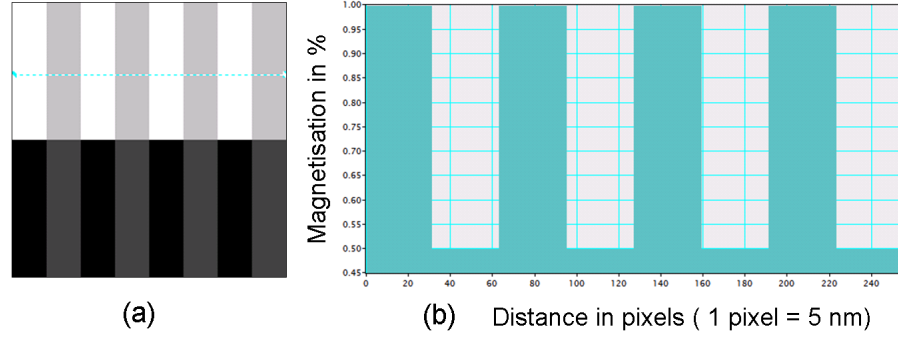


Figure 5.11: (a) Using image processing software package DM, alternate uniformly magnetised and reduced magnetised (50 %) stripes were created including an  $180^\circ$  DW. (b) is a profile of the magnetisation in the upper region.

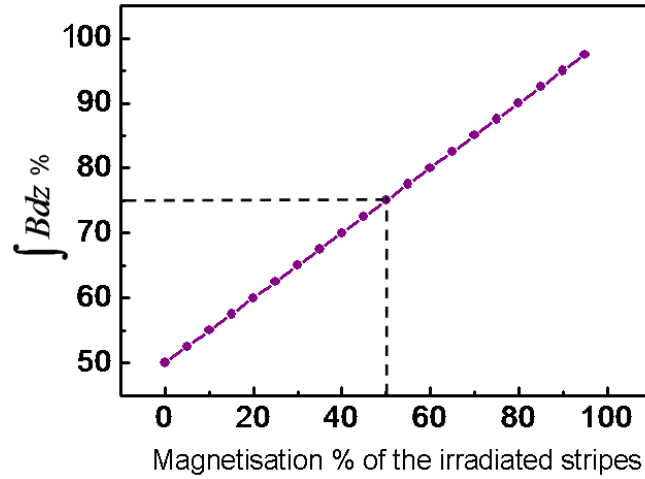


Figure 5.12:  $\int \mathbf{B}dz$  % as a function of the magnetisation of the irradiated stripe. The vertical axis is a normalised value of integrated induction scaled to  $B_s t$  of the unirradiated film. The magnetisation of the unirradiated stripe is 100 %.

in **chapter 3** that the gradient of the magnetic phase is proportional to  $\int (\mathbf{B} \times \hat{\mathbf{n}}) dz$ . Therefore, by calculating the gradient of the magnetic phase using the available scripts written by Dr. Stephen McVitie and Mr. Gordon White at the University of Glasgow, the value of  $\int \mathbf{B}dz$  was calculated and plotted in Fig. 5.12. It is essential to clarify here that scaling to  $M_s$  is of the unirradiated film and the deflection is to  $B_s t$  of the unirradiated film. For example, if the magnetisation of the unirradiated and irradiated stripes are 100 % and 50 %, respectively (marked by dotted line in Fig. 5.12) then the calculated  $\int \mathbf{B}dz$  is 75 %, which indicates that  $\mathbf{H} = 25$  %. Therefore, one can say that due to the influence of the stray magnetic fields the magnetisation of the unirradiated

stripe was decreased 25% and that of the irradiated stripe was increased 25%. Based on this theoretical modeling  $\mu_0 M_s t$  was deduced as a function of the irradiation doses in the irradiated stripes. These values were plotted in Fig. 5.13 along with the observed values of  $\int \mathbf{B} dz$  by calculating the separation between two diffraction spots, for example Fig. 5.8(c) for which the dose of the irradiated stripe was  $4 \times 10^{14} \text{ ions/cm}^2$ . Figure 5.13 shows that  $\int \mathbf{B} dz$  and deduced  $\mu_0 M_s t$  decreases as a function of ion doses of the irradiated stripe patterns. But from irradiated ion dose  $16 \times 10^{14} \text{ ions/cm}^2$ ,  $\int \mathbf{B} dz$  is almost half of the  $B_s t$  of the unirradiated continuous film and then for a further increase of the ion doses, experimentally observed  $\int \mathbf{B} dz$  is no longer decreases. As was mentioned earlier, the normal component of  $\mathbf{B}$  is continuous across the boundary, therefore one can write using the schematic 5.9(b),

$$(\mathbf{M}_1 - \mathbf{H}) = (\mathbf{M}_2 + \mathbf{H}) \quad (5.1)$$

Therefore,

$$\mathbf{H} = (\mathbf{M}_1 - \mathbf{M}_2)/2 \quad (5.2)$$

If  $\mathbf{M}_1$  is 100 % and  $\mathbf{M}_2$  is zero, then  $\mathbf{H} = 50\%$  of  $\mathbf{M}_1$ . Hence, if the magnetisation of the irradiated stripe is zero, then  $\int \mathbf{B} dz$  will no longer decrease from half of the initial value of magnetisation of the unirradiated stripe. This argumentation is also supported by the calculated  $\int \mathbf{B} dz$  using DM as Fig. 5.12 clearly demonstrate that, if the magnetisation of the unirradiated and irradiated stripe patterns are 100 % and 0 %, respectively then  $\int \mathbf{B} dz$  is 50%. From Fig. 5.13 it is apparent that magnetisation is changed as a function of irradiation doses. This clearly indicates that modifications of this material system were achieved by micro-alloying due to a combined effect of the  $Ga^+$  irradiation and interfacial atomic mixing. Now the question which may arise is that at higher irradiation dose e.g.  $16 \times 10^{14} \text{ ions/cm}^2$  whether the system becomes paramagnetic or still some ferromagnetism remains there. Figure 5.14 (a) shows Fresnel image in which DW is appeared along the micron sized ( $1 \mu m$ ) irradiated stripe surrounded by unirradiated stripes. The irradiation dose was  $16 \times 10^{14} \text{ ions/cm}^2$ . The Fresnel image 5.14 (a) does not provide any clear indication of the wall contrast appeared in the ion irradiated region. Diffraction patterns were taken from unirradiated continuous thin film and patterned film regions. Figures 5.14(b) and (c) show



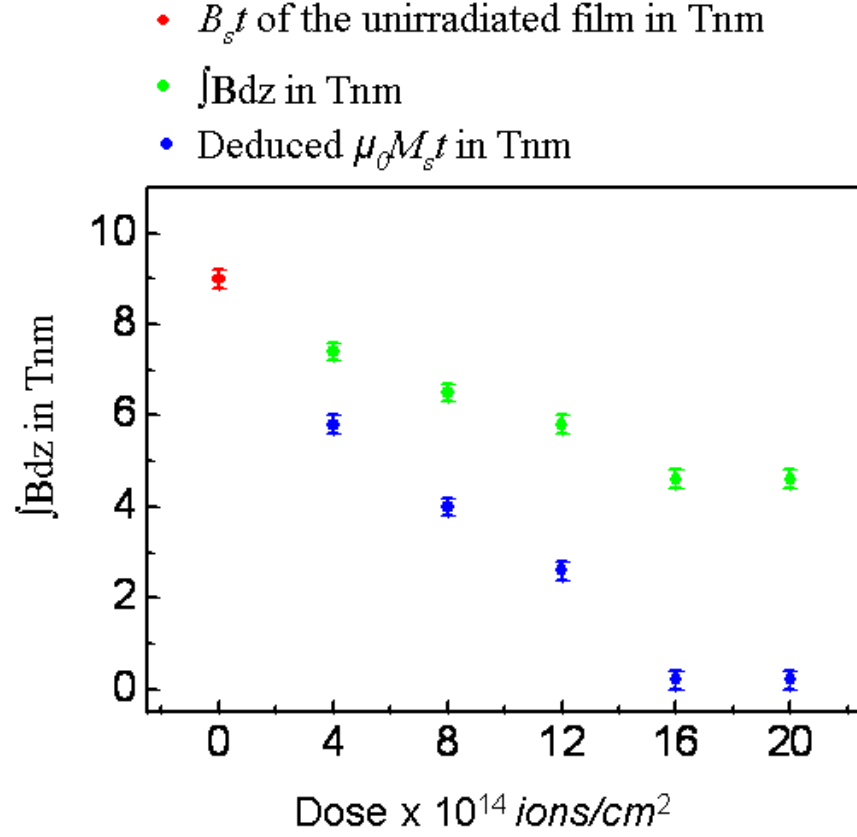


Figure 5.13:  $\int B dz$  and deduced  $\mu_0 M_s t$  as a function of the irradiation ion doses.

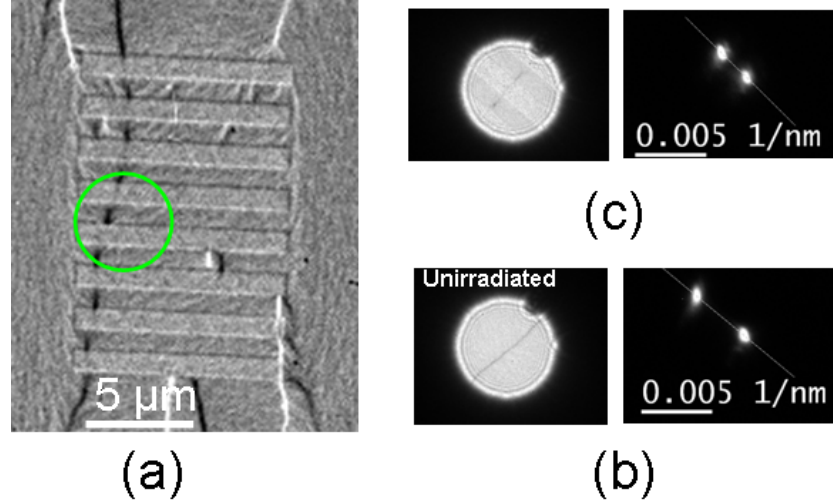


Figure 5.14: (a) Fresnel image showing black contrast domain wall along alternative unirradiated and ion irradiated stripe patterns. Diffraction patterns from (b) unirradiated continuous film region and (c) alternative unirradiated and irradiated region. The irradiation dose was  $16 \times 10^{14} \text{ ions/cm}^2$

the diffraction pattern captured from unirradiated continuous film and ion irradiated patterned film region, respectively. In the patterned region two diffraction spots were formed like Figs. 5.8(c and d). However, the  $\int B dz$  in the patterned region was slightly

higher than that half of the unirradiated continuous film region and therefore at irradiation dose  $16 \times 10^{14} \text{ ions/cm}^2$  the deduced magnetisation is not exactly zero but very close to zero. As was also seen in Fig. 5.13, by a further increment of the irradiation dose to  $20 \times 10^{14} \text{ ions/cm}^2$ ,  $\int \mathbf{B} dz$  does not change. In order to make sure that whether the region irradiated with higher doses becomes paramagnetic or not, alternate unirradiated and irradiated larger size (width:  $6 \mu\text{m}$ ) rectangles were written, Fig. 5.15. The irradiation doses varied as before and domain wall contrast formed along these rectangles are clearly visible upto an irradiation dose of  $12 \times 10^{14} \text{ ions/cm}^2$ . For an irradiation dose of  $16 \times 10^{14} \text{ ions/cm}^2$  and above, DW contrast does not appear inside the rectangles. Diffraction patterns taken from regions (a-e) of Fig. 5.15 are shown respectively in Figs. 5.16 (a-e). The separation between these diffraction spots are reduced as a function of doses upto an irradiation dose of  $12 \times 10^{14} \text{ ions/cm}^2$ . Notably, for an irradiation dose of  $16 \times 10^{14} \text{ ions/cm}^2$ , only one diffraction spot was observed. This may be an indication to say that due to this amount of ion irradiation the region appears to be rendered non-ferromagnetic. Notably, in this case, due to the presence of stray magnetic fields, an accurate quantification of the reduced  $B_s t$  as a function of irradiation dose from the separation of the diffraction spots is not possible.

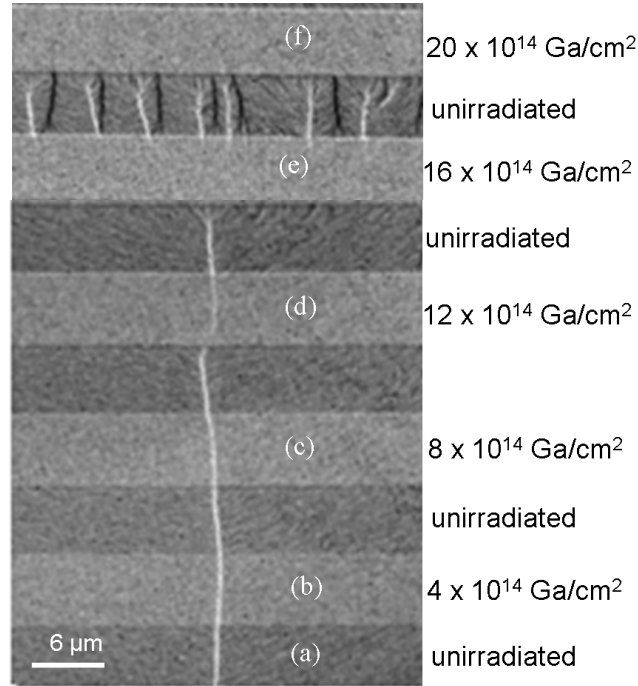


Figure 5.15: Fresnel image showing white contrast domain wall along alternate unirradiated and ion irradiated large size rectangles. The irradiation dose was  $d \times 10^{14} \text{ ions/cm}^2$  ( $d = 4, 8, 12$  and  $16$ ) in the rectangles b to e, respectively

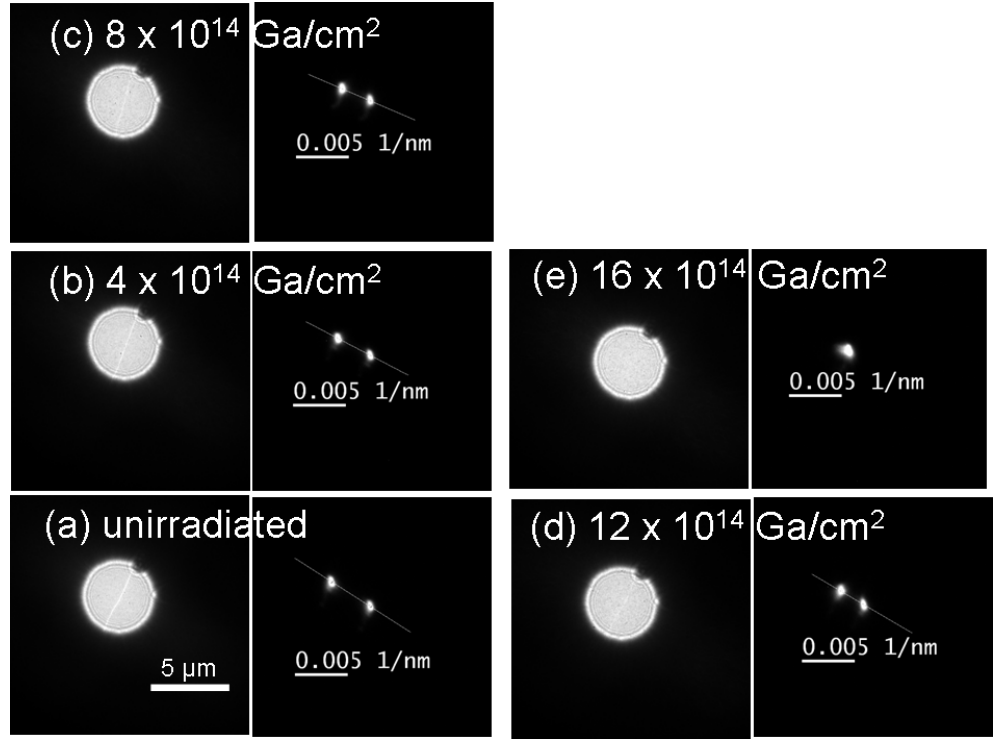


Figure 5.16: Diffraction pattern taken from unirradiated film region (a) and patterned regions (b-e), respectively as a function of doses

## 5.7 Patterning of nanowires and pinning features

In the present stage of this investigation, isolated nanowires were written by FIB milling using a 10 pA aperture of a FEI Nova NanoLab 200 SEM/FIB workstation ( $Ga^+$ ). The patterns were written using a single cut approach as was described in **chapter 4**. The structure of the fabricated nanowires of width 500 nm is shown schematically in Figs. 5.17(a), (b) and (c).

In nanowire Fig. 5.17(a) either side of the straight wire is connected to a diamond shaped pad so that the formation a of domain wall can be achieved reproducibly at the corner position between the pad and wire by applying a magnetic field close to the hard axis and relaxing the field to zero [36]. The right end of the nanowire 5.17(b) was connected to a diamond shaped pad like 5.17(a) to allow control over the formation of DWs whereas left end was terminated to a triangular end shapes to prevent nucleation of the DWs from this end. The other nanowire, Fig. 5.17(c) was designed as an L-shaped wire [7] in which both ends were connected to a triangular end shapes and DW was expected to form at the bend corner upon the application of a magnetic field and relaxing the field to zero. Different wire structures were chosen for the formation of

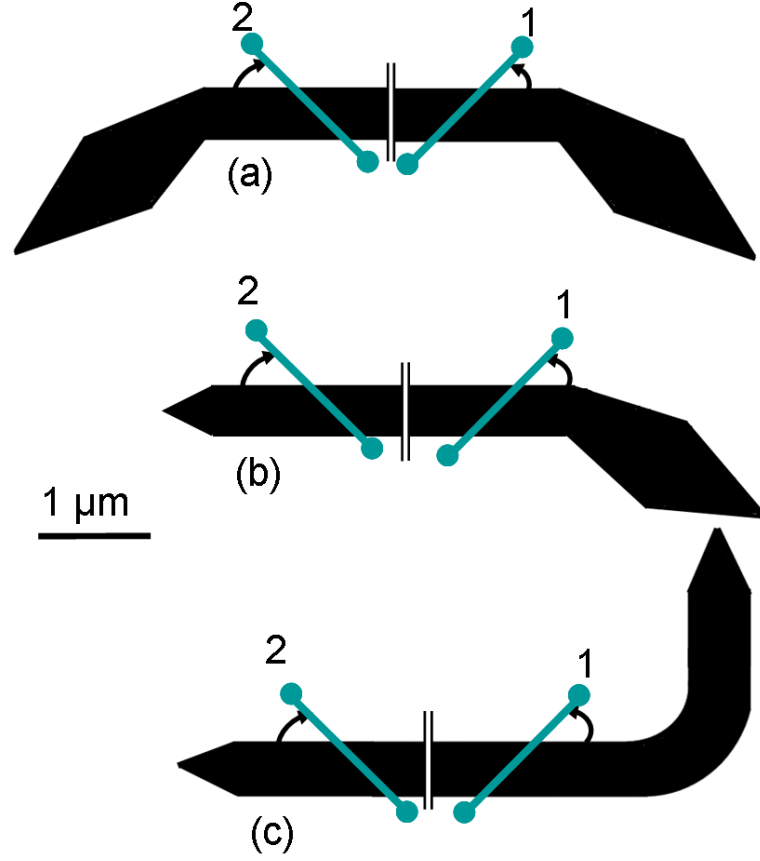


Figure 5.17: (a, b and c) Schematics of the nanowire geometry. The length of the wire axis has been reduced for this schematic, indicated by vertical bars. Ion irradiated pinning sites were indicated by the two lines oriented at  $\pm 45^\circ$  and marked as pinning sites 1 and 2 in each nanowire.

an asymmetric TDW with magnetisation pointing up and down during TEM investigations. In each nanowire, two irradiated lines were written at an angle oriented  $\pm 45^\circ$  from the wire axis and referred as pinning sites 1 and 2, as shown in the schematics 5.17(a, b and c). Heavily irradiated marker spots of diameter 300 nm were positioned at the end of the each line to allow identification of the line's location during TEM investigation as this was not generally visible. Patterning of the isolated nanowires and irradiation of pinning sites and marker spots were performed using a 10 pA aperture of an FEI Nova NanoLab 200 SEM/FIB workstation ( $Ga^+$  LMIS operated at 30 keV). The ion beam was scanned once along a line for creating irradiation lines 1 and 2, and by varying the beam dwell time irradiation doses were varied along the lines. Nominally the doses of the irradiated sites corresponded to  $d \times 10^{15} \text{ ions/cm}^2$  ( $d = 4, 8, 12, 16$  and  $20$ ). Three wires of each structure were written using exactly the same ion beam milling condition and irradiation line doses. Figure 5.18(a) shows a plan view TEM bright field (BF) image of a patterned nanowire in which the pinning site

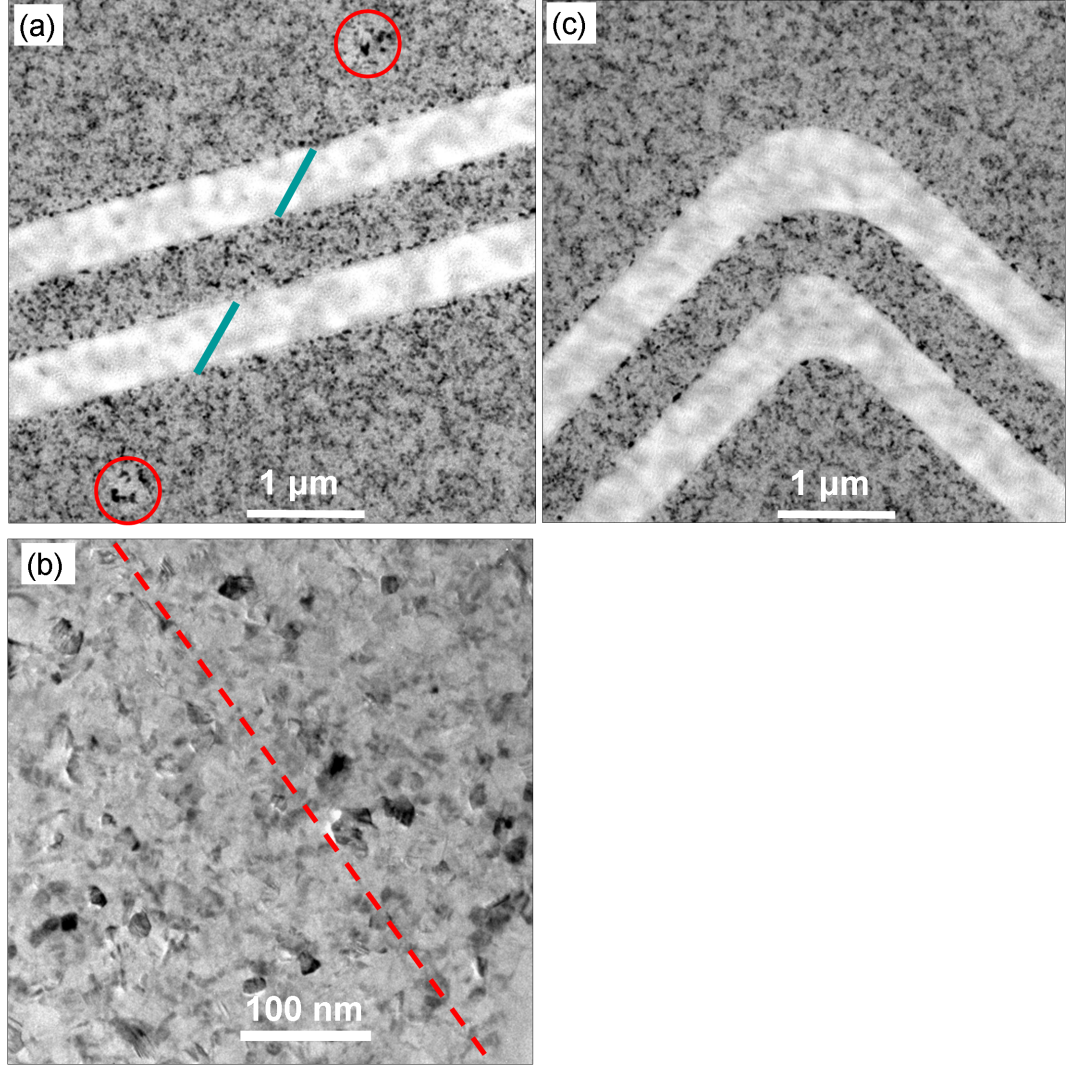


Figure 5.18: (a) TEM image shows the nanostructures written by FIB milling along with a schematic of the direction of the irradiated site 1 (cyan). Red circles are indicating the position of the marker spots. (b) TEM image at the centre of the nanowire along which irradiation line was written. The location of the line is between the red dots on the image. (c) TEM BF image shows the bend corner of an L-shaped nanowire.

was irradiated with the highest dose of  $20 \times 10^{15} \text{ ions/cm}^2$ . A higher magnification BF image, 5.18(b), was recorded from the centre of the nanowire along which the irradiation line was written and the location of the line indicated between the red dots. It is apparent, and a little surprising, that even at this high dose level no visible effect on the grain structure of the nanowire could be discerned in high magnification BF TEM images. TEM BF image, Fig. 5.18(c), shows the bend corner of an L-shaped nanowire patterned by FIB milling. These BF images ensure the well defined wire edge of the patterned nanowire. In the next stage of this investigation, *in situ* magnetising experiments were carried out using the Fresnel mode of Lorentz TEM to show how DWs along the patterned nanowires can be controlled reproducibly at the irradiated sites.

LTEM imaging was performed in a Philips CM20 field emission gun TEM equipped with Lorentz lenses and suitable for performing *in situ* magnetising experiments [35]. This method was described in detail in **chapter 3**.

## 5.8 *In situ* magnetizing experiments

### 5.8.1 Patterns generation on isotropic film

Patterning of the nanowire was realised by FIB milling, as was already mentioned, of the thin continuous isotropic multilayer film. The pinning sites 1 and 2 were irradiated with nominal doses mentioned earlier. However, we did not observe reproducible DW behaviour in the nanowires patterned on thin isotropic film. Therefore, results for few irradiation line doses are described herewith instead of all nominal ion doses. Figures 5.19(a-d) show the magnetisation reversal sequence in a 500 nm wide nanowire with corresponding schematics 5.19(e-h), respectively, in which irradiation line dose is  $12 \times 10^{15} \text{ ions/cm}^2$ . Figure 5.19(a) shows an asymmetric transverse type of domain wall formed at the corner position between the pad and the wire. Formation of the DW in these nanowires throughout this investigation was performed by applying a magnetic field ( $H_i$ , schematic 5.19(e)) close to the hard axis and then relaxing the field to zero [36]. For straight nanowires of 500 nm width and 10 nm Py thickness, the expected wall structure at ground energy state is a vortex DW (VDW) according to the DW structure phase diagram [37]. However, Fig. 5.19(a) and the corresponding schematic 5.19(e) show the formation of an asymmetric transverse DW (TDW) for the shape of the nanowire considered for the present investigation. It is noteworthy that we are forming a DW at the edge of the straight section and the end pad, so perhaps the energetics are different than from a straight wire. Contrast at the edges of the wires as was described in **chapter 4** were used as a reference for the direction of magnetisation in the wire. By applying a magnetic field ( $H_a$ , schematic 5.19(f)), opposite to the direction of the magnetisation in the nanowire, the initial asymmetric TDW, Fig. 5.19(a), moves to and is pinned at the pinning site 1 in the nanowire, Fig. 5.19(b). As shown in the schematic Fig. 5.19(f), on arriving at the pinning site 1, the type of the DW structure remain unchanged i.e asymmetric TDW with magnetisation points up at the centre of the wall. By a further field increment to 17 Oe, the DW



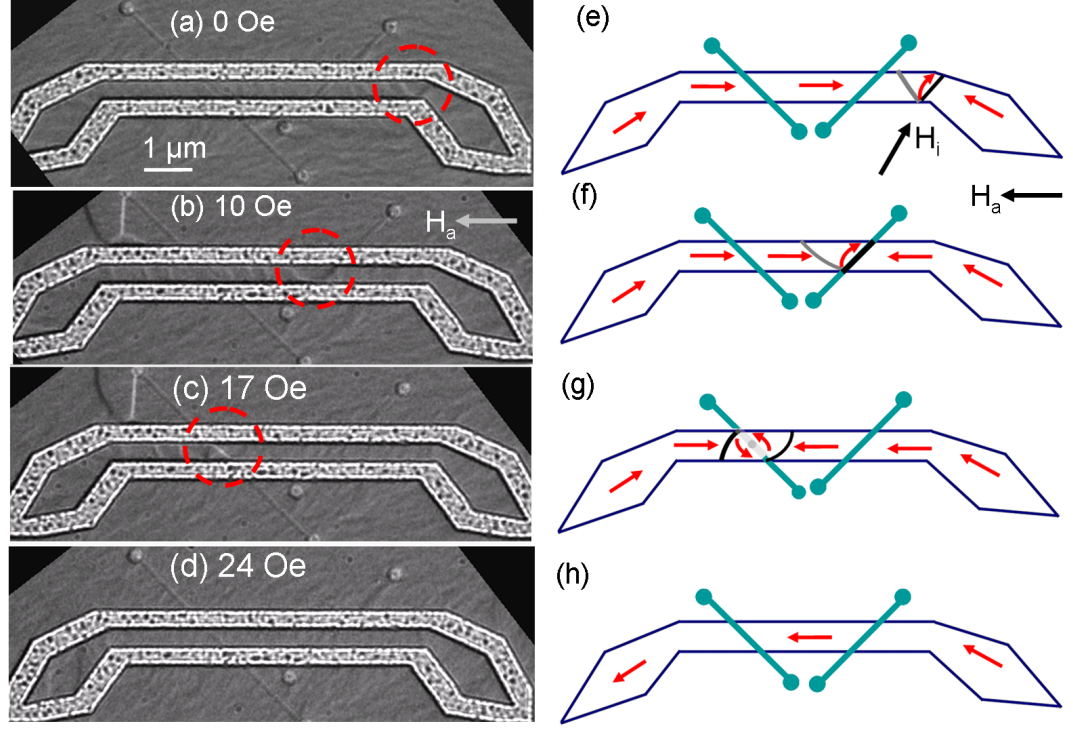


Figure 5.19: Pinning and depinning of DWs as a function of applied magnetic fields at irradiation sites 1 and 2. The irradiation dose is  $12 \times 10^{15} \text{ ions/cm}^2$ . The corresponding schematics of (a-d) are (e-h), respectively.

depinned from site 1 and is pinned at site 2, Fig. 5.19(c). On arriving at pinning site 2, the DW not only pinned there but also the wall structure transformed to a ccw VDW. Beside DW contrast significant ripple contrast along the wire axis is also visible in the Fresnel images (a, b and c). The magnetisation ripple is observed as a consequence of dispersion in the film and was described briefly in **chapter 1**. The ripple arises due to the preference of the magnetic moment for each crystallite to lie along crystallographic 'easy-axes' nearest to the net direction for the magnetic domain. Here, the ripple clearly suggests considerable deviation of the magnetisation from the nanowire axis and was problematic for reproducible DW behaviour. This issue will be discussed further later on. In this nanowire, upon the application of a magnetic field of 24 Oe, ccw VDW depinned from site 2 completing the reversal process. Figures 5.20(a-d) show the magnetisation reversal sequence in another 500 nm wide nanowire only this time irradiated with doses of  $16 \times 10^{15} \text{ ions/cm}^2$ . The corresponding schematics of (a-d) are (e-h), respectively. By applying a magnetic field of 10 Oe, initial asymmetric TDW comes to and is pinned at site 1 as a highly modified cw VDW. The applied magnetic field against magnetisation direction probably distorted the right end of the wall structure. Although the wall structure looks like a vortex, the vortex core is not clearly

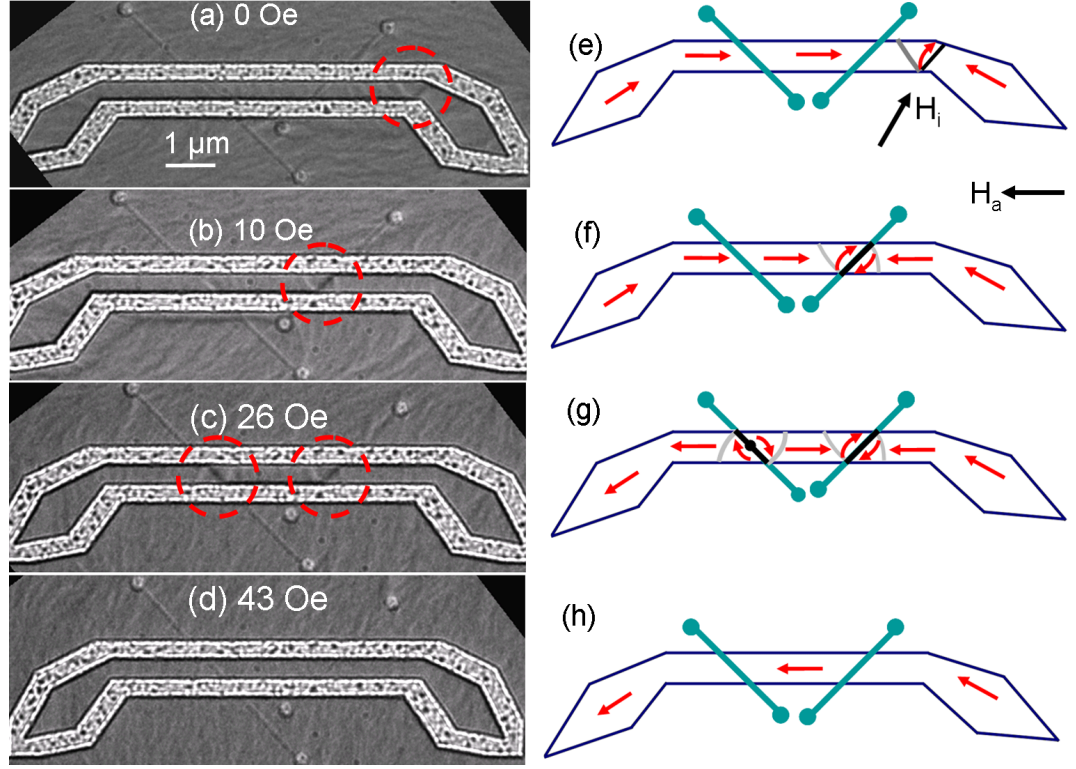


Figure 5.20: Pinning and depinning of DWs as a function of applied magnetic fields at irradiation sites 1 and 2. The irradiation dose is  $16 \times 10^{15} \text{ ions/cm}^2$ . Reversal of the nanowire was started also from the other end of the wire and consequently a tail to tail VDW is pinned at site 2 as shown in image (c). Figures (e-h) are the corresponding schematics showing the magnetisation distribution deduced from the image (a-d).

seen. This modified micromagnetic wall structure remained stable at this site, until at a field of 26 Oe, when a second domain wall is seen at the next pinning site, 5.20(c). This is a tail to tail domain wall with a black core and is formed into the wire due to the reversal of the other end of the wire. In a separate experiment the field required to reverse the magnetisation of this nanowire is found to be  $27 \pm 2$  Oe. However, an applied magnetic field of 43 Oe was required to annihilate the two walls Fig. 5.20(d). Notably, the purpose of this investigation is to control DW reproducibly by the non topographic pinning sites and to measure the strength of these pinning potentials as a function of ion irradiation doses. Therefore, whilst *in situ* magnetising experiments demonstrate that DWs can be controlled using these ion irradiated pinning features, the reversal of the other end of the wire is an obstacle to measure their strength as a function of irradiation doses.

In order to overcome this difficulty, the geometric structure of the patterned nanowire Fig. 5.17(a) was changed. In that case, the right end of the nanowire 5.17(b) was still connected to the diamond shaped pad but left end was terminated to a triangular end



shape to prevent nucleation of the DWs from this end. Alternatively, another nanowire, Fig. 5.17(c) was designed as an L-shaped wire [7] in which both ends were connected to a triangular end shape as was described in section 5.7. Two different wire structures were chosen for the formation of asymmetric TDWs with magnetisation pointing up and down during TEM investigations, as was also mentioned earlier. In the present stage of this investigation, to check the reproducibility of this investigation and also to ensure that reversal does not start from the other end of the nanowire, three L-shaped nanowires were written using the same milling condition. The pinning sites in these nanowires were also irradiated with the same amount of ion doses.

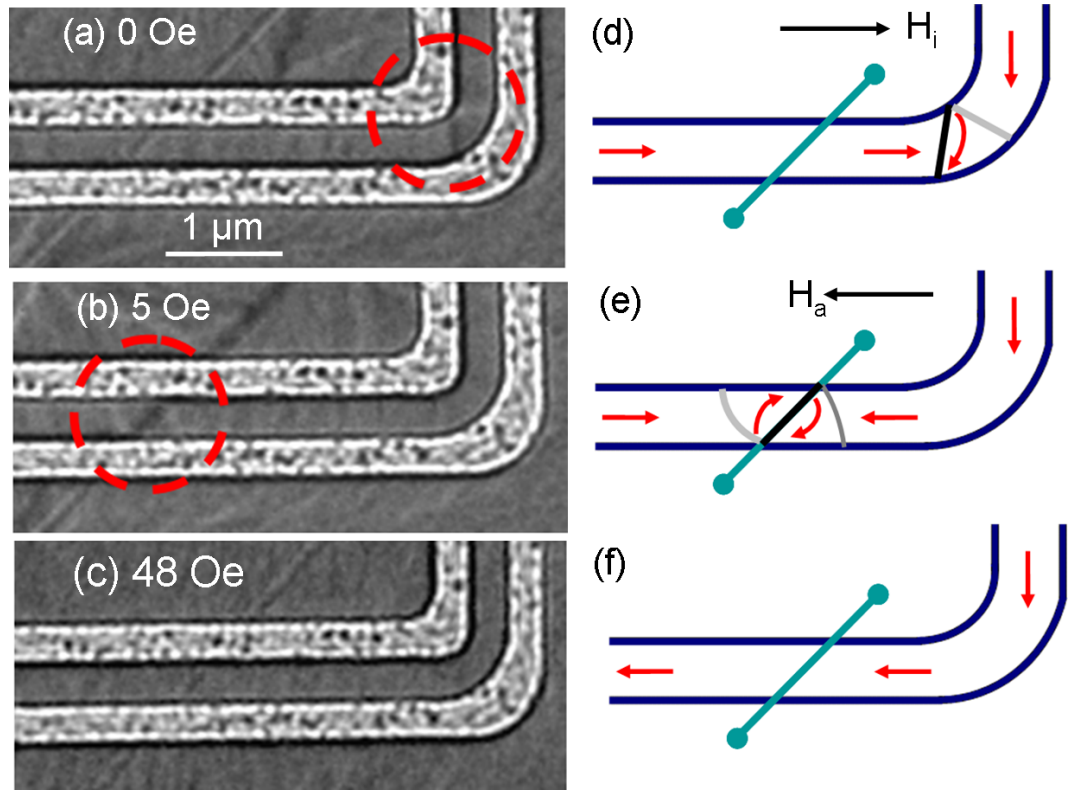


Figure 5.21: Pinning and depinning of DWs as a function of applied magnetic fields at site 1 which were irradiated with an ion doses of  $20 \times 10^{15} \text{ ions/cm}^2$ . The schematic diagrams of (a, b and c) are (d, e and f), respectively.

Figure 5.21(a-c) show a typical pinning/depinning in such a 500 nm wide L-shaped nanowire patterned on the same isotropic continuous film in which the pinning sites 1 and 2 were irradiated with an ion dose of  $20 \times 10^{15} \text{ ions/cm}^2$ . The schematic diagrams of Fig. 5.21(d-f) show the magnetisation distribution in the images (a-c). Figure 5.21(a) demonstrates the formation of an asymmetric TDW at the bend corner of the L-shaped nanowire by applying a magnetic field  $H_i$  along the long axis of the wire as shown in the schematic of Fig. 5.21(d) and relaxing the field to zero. Upon the application of

a magnetic field of 5 Oe, DW come to pinning site 1 and is pinned there. The DW remained stable in this position and the wall structure looks like a cw VDW though the vortex core is not seen. By a further field increment to 48 Oe, DW depinned from this pinning site and magnetisation reversal of this nanowire was completed. Therefore, in an L-shaped nanowire in which both end were terminated with a triangular end shape prevents the nucleation of a DW from the other end of the nanowire upon the application of magnetic fields. Figure 5.22(a-c) show the pinning/depinning of

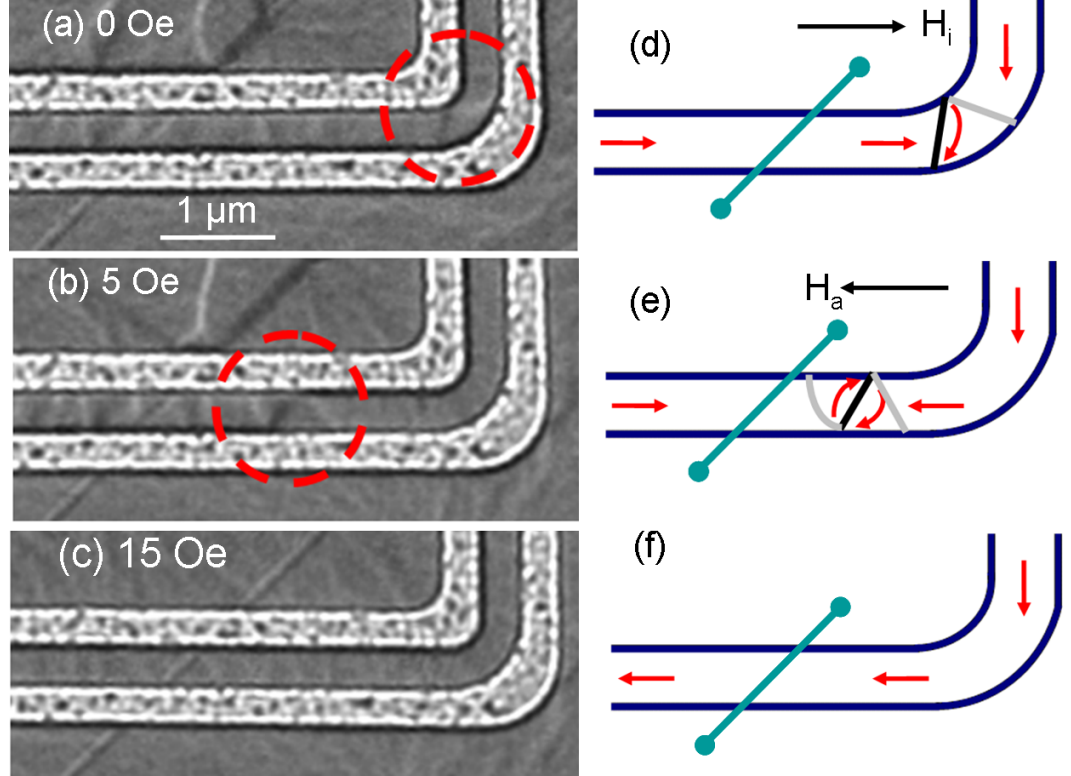


Figure 5.22: Patterned nanowire showing the presence of strong ripple contrast which ultimately influenced the reversal process including pinning and depinning of DWs at irradiation sites. The irradiation dose was same of wire Fig. 5.21 i.e.  $20 \times 10^{15} \text{ ions/cm}^2$ .

another 500 nm wide L-shaped nanowire in which pinning sites 1 and 2 were irradiated with the same ion dose i.e.  $20 \times 10^{15} \text{ ions/cm}^2$ . Figure 5.22(a) show the formation of an asymmetric TDW at the bend corner of this L-shaped nanowire. Along the long axis of this nanowire, the ripple contrast which was described earlier is clearly observed. The magnetisation ripple arise due to a deviation of the magnetisation from uniformity and runs perpendicular to the average direction of the magnetisation as was described earlier. To move this DW, a magnetic field  $H_a$  was applied along the long axis towards the pinning site 1. In contrast to the Fresnel image Fig. 5.21(b), the initial asymmetric TDW in this case did not move to the pinning site and instead

is pinned at a position prior to reaching site 1. By a further field increment to 15 Oe, the DW moves and the wires reverses completely without any pinning of the DW at the irradiated sites. In principle, it is expected that in these isolated nanowires magnetic shape anisotropy will be dominating and magnetisation will lie along the edge of the nanowires. In practice, the appearance of the strong ripple contrast clearly indicates a deviation of the local magnetisation direction along the wire axis. As a result, by comparing Fig. 5.21 and Fig. 5.22, it is obvious that in spite of patterning the nanowires using the same milling condition and irradiating the pinning sites with the same ion doses, the pinning/depinning strength and their mechanism differ due to local non uniform magnetisation distribution along the patterned nanowire. This actually raises the question of reproducibility of pinning and depinning of DWs along the patterned nanowires using these ion irradiated features. Therefore, in the next stage of this investigation, materials were deposited in such a way that anisotropy can be created in the continuous film and thereby nanowires can be patterned along the anisotropy direction so that locally a less variation of magnetisation due to dispersion is appeared.

### 5.8.2 Patterns generation on anisotropic film

Materials of nominally identical thicknesses were deposited using magnetron sputter deposition and field induced anisotropy was created during deposition, as was described in section 5.4. Nanowires of geometric structures 5.17(b) and (c) were written using FIB milling technique along the anisotropy direction and thereby *in situ* magnetising experiments were carried out using LTEM. Nanowires presented in this section were fabricated by a focused nominal ion beam dose of  $9 \times 10^{15} \text{ ions/cm}^2$ .

Fig. 5.23(a) shows the formation of an asymmetric transverse DW (TDW) for the shape of the nanowire ( schematic 5.17(b)) considered for the present investigation. Figure 5.23(e) is the corresponding schematic showing the magnetisation distribution deduced from the image 5.23(a). Figures 5.23(b, c and d) demonstrate the DW pinning/depinning under the application of a magnetic field in a nanowire in which irradiation sites 1 and 2 were irradiated with an ion dose of  $4 \times 10^{15} \text{ ions/cm}^2$ . The schematic diagrams of the images (b , c and d) are (f, g and h), respectively. By applying a magnetic field ( $H_a$ , schematic 5.23(f)), towards the pinning sites, the initial asymmet-

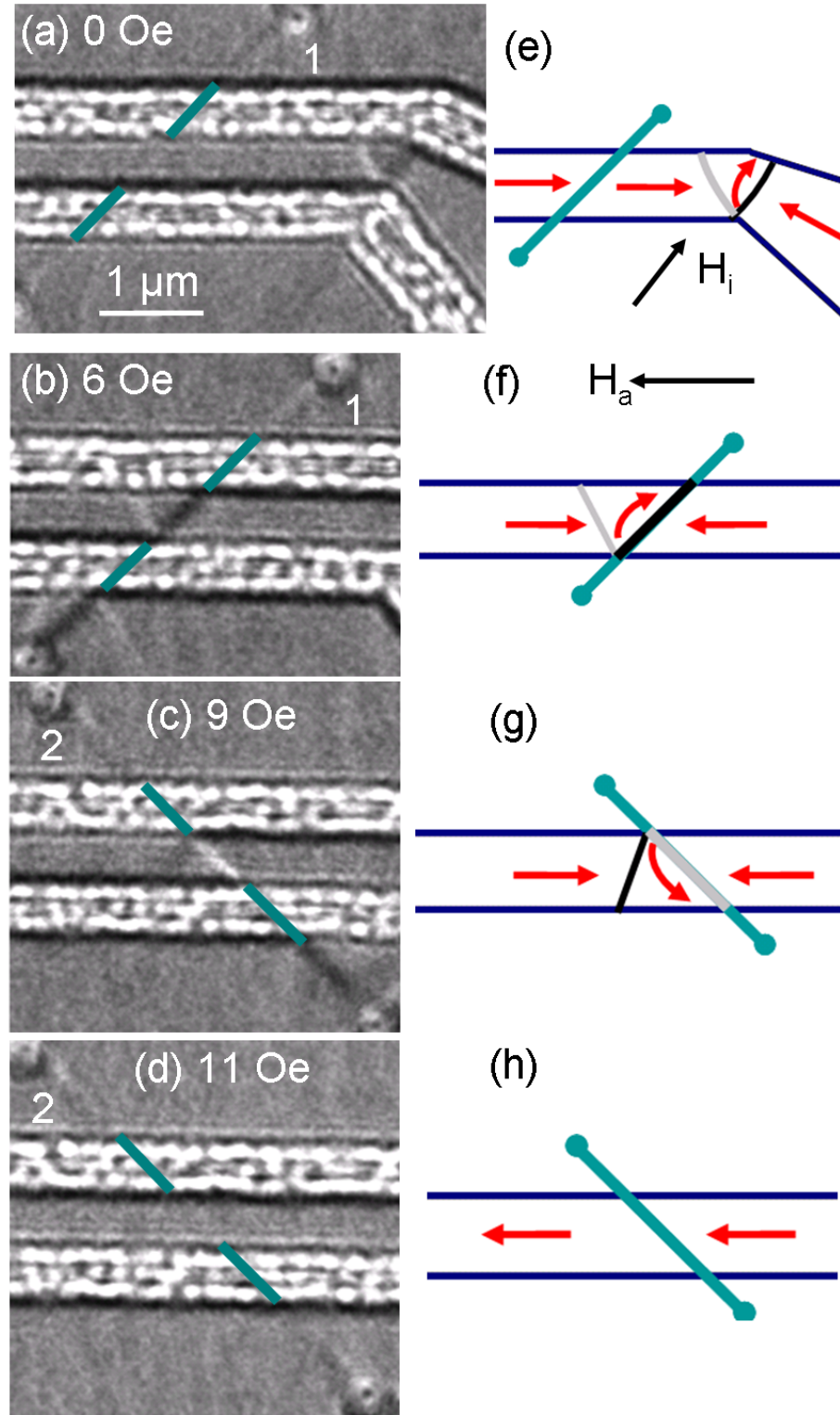


Figure 5.23: Fresnel image (a) showing the structure of an asymmetric TDW (magnetisation points up) in a wire with a schematic of the magnetisation shown in Fig. (e). DW is initially pinned at site 1 without changing it's structure and later on pin again at site 2 after depin from 1. The ion irradiation dose is  $4 \times 10^{15} \text{ ions/cm}^2$ . Schematic interpretation of (b, c and d) are (f, g and h), respectively. Fresnel image (d) shows the completion of the reversal process.

ric TDW, Fig. 5.23(a), moves to and is pinned at the pinning site 1 in the nanowire, Fig. 5.23(b). The sense of magnetisation of the wall structure is seen to be unchanged

at the pinning site 1. With a further field increase to 9 Oe, the DW was depinned from the pinning site 1 and is pinned now at site 2, as shown in Fig. 5.23(c). On arriving at site 2, the sense of the magnetisation of the asymmetric TDW was changed and transformed from pointing up to down. By a further field increment to 11 Oe, the DW was depinned from site 2 and the magnetisation reversal was completed, Fig. 5.23(d) and the strong edge contrast appeared along the upper edge of the nanowire. The experiments carried out throughout this investigation were repeated ten times for three wires of same irradiation line doses. Therefore, from 30 observations, pinning of DW at site 1 and then again at 2 was observed for 40% experiments. In the remaining 60 % experiments, as soon as DW is pinned at the pinning site 1, the sense of the magnetisation of the asymmetric TDW was changed and transformed from pointing up to down. In this case, the DW never pinned again at site 2. The fields required to depin the DW from pinning sites (referred as DW depinning field) were inserted in table 5.1 as a function of irradiation doses.

Table 5.1: Type of the micromagnetic wall structure on arriving at the pinning site irradiated with different ion doses under the application of magnetic fields. DW depinning fields as a function of irradiation doses for two different types of initial wall structures. Error bars depict the standard deviation for 30+30=60 observations for both initial TDW structure with magnetisation points up and down involving six nanowires irradiated with same line dose.



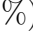
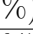


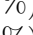
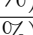

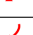
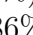
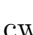
Dose : $d \times 10^{15}$ $ions/cm^2$	Initial TDW structure : magnetization points up (  )		Initial TDW structure : magnetization points down (  )	
	DW pinned at site 1 as a	Depin. field (Oe)	DW pinned at site 1 as a	Depin. field (Oe)
4	TDW:  (40%) TDW:  (60%)	$11 \pm 1$ $16 \pm 4$	TDW:  (40%) TDW:  (60%)	$16 \pm 2$ $20 \pm 4$
8	TDW:  (20%) TDW:  (80%)	$65 \pm 8$ $79 \pm 10$	TDW:  (25%) TDW:  (75%)	$55 \pm 4$ $64 \pm 8$
12	TDW:  (14%) VDW: cw (86%)	$76 \pm 4$ $75 \pm 2$	TDW:  (80%) VDW: cw (20%)	$80 \pm 4$ $76 \pm 4$
16	VDW: cw (100%)	$79 \pm 2$	VDW: cw (100%)	$79 \pm 4$
20	VDW: cw (100%)	$82 \pm 4$	VDW: cw (100%)	$82 \pm 4$

Figure 5.24(b and c) demonstrates the pinning of an initial asymmetric TDW at site 1 which was irradiated with ion doses of  $8 \times 10^{15} ions/cm^2$ . The corresponding schematics of Figs. 5.24(b and c) are 5.24(e and f), respectively. At the pinning site 1, the sense



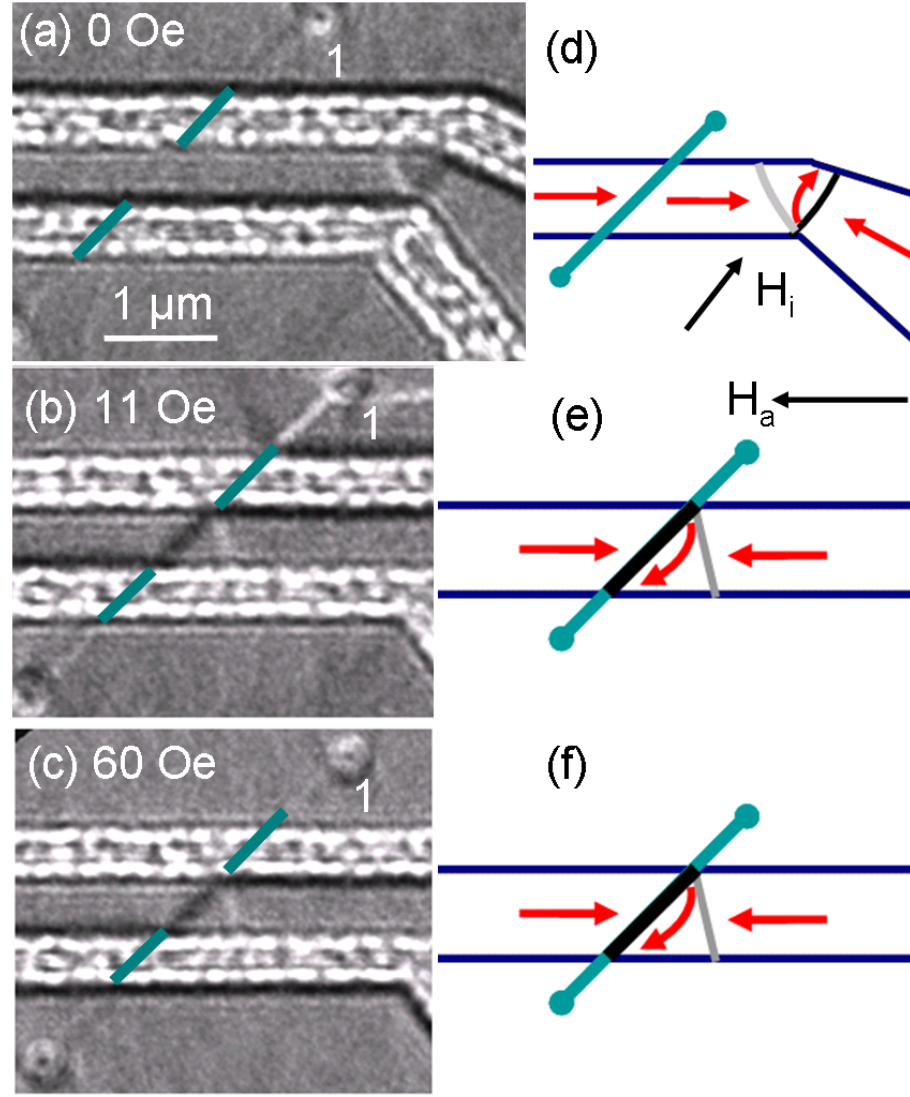


Figure 5.24: (a) Initially formed asymmetric TDW with magnetisation points up at the centre of the wall. (b) DW is pinned at site 1 by changing the magnetisation direction points from up to down. The ion irradiation dose is  $8 \times 10^{15} \text{ ions/cm}^2$ . Fresnel image (c) shows that DW remains stable at this position. Schematic diagrams (d, e and f) demonstrate the magnetisation distribution in Fresnel images (a, b and c), respectively.

of magnetisation of the initial wall structure has been changed and transformed from pointing up to down. The DW remained stable at the pinning site 1, Fig. 5.24(b) and DW depinning field was increased dramatically (refer to table 5.1) compared to that of the line doses of  $4 \times 10^{15} \text{ ions/cm}^2$ . Notably for such an irradiation doses, the DW never pinned again in the pinning site 2 probably due to the higher depinning field.

At higher irradiation line dose, for example  $16 \times 10^{15} \text{ ions/cm}^2$ , on arriving at irradiation site 1, the initial asymmetric TDW, Fig. 5.25(a) is transformed to a clockwise vortex DW (cw VDW), as shown in Fig. 5.25(b). Figure 5.25(e) is the corresponding schematic showing the magnetisation distribution deduced from the image 5.25(b).

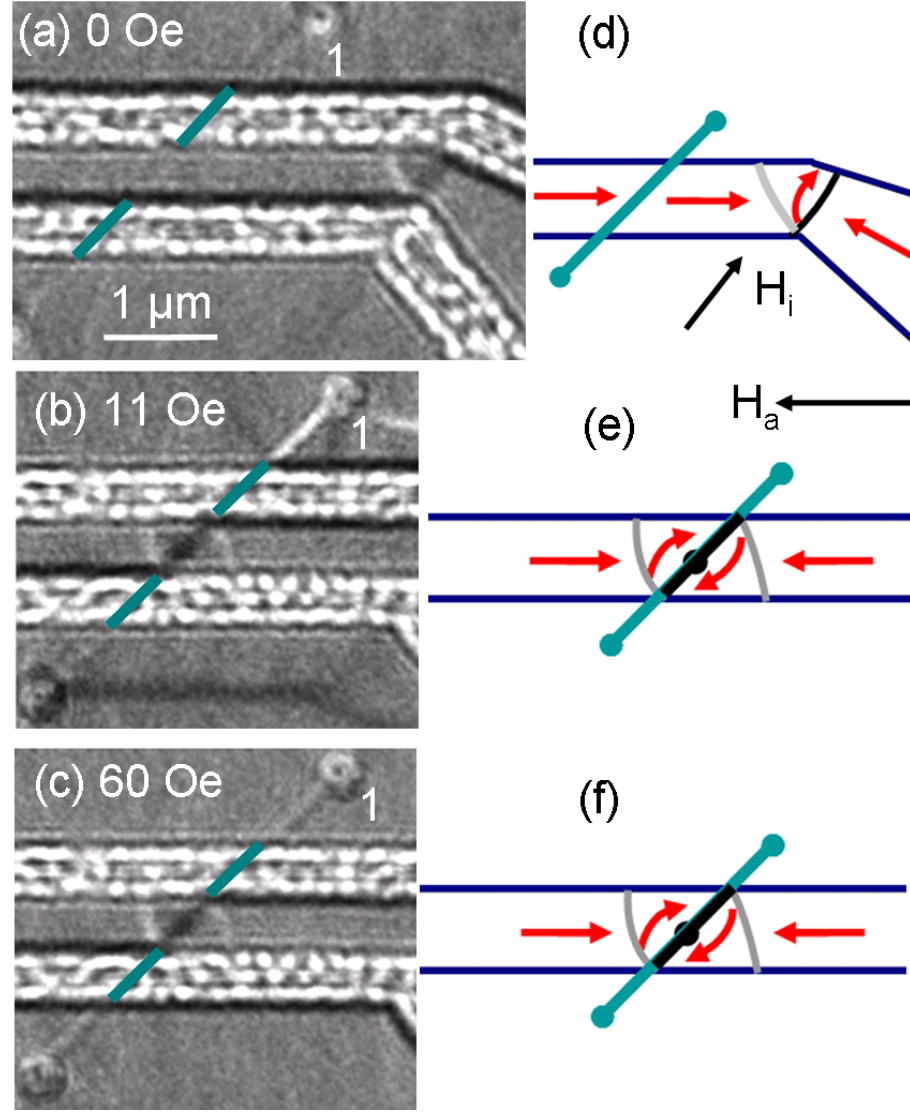


Figure 5.25: Initially formed asymmetric TDW (a) is pinned with transforming wall structure to a cw VDW (b). The irradiation dose at sites 1 and 2 were  $8 \times 10^{15} \text{ ions/cm}^2$ . Fresnel image (c) shows that cw VDW remains stable at pinning site 1. Schematic interpretation of images (a, b and c) are (d, e and f) respectively.

The DW is remained stable at this pinning site, Fig. 5.25(c) although the right end of the micromagnetic wall structure in Figs. 5.25(b and c) is slightly modified probably due to the effect of the Zeeman field and looks pretty much a slightly distorted vortex compared to the VDW structure observed in related nanowires [7, 11, 38].

In order to investigate the dependency of the potential behavior of pinning sites 1 and 2 on the sense of DW magnetisation, L-shaped nanowires, schematic 5.17(c), were fabricated and pinning sites 1 and 2 were irradiated by the nominal ion doses as was mentioned earlier. Formation of the DWs in the L-shaped nanowires were achieved by applying a magnetic field along the wire axis as shown in the schematic Fig. 5.26(c) and relaxing the field to zero. The micromagnetic wall structure formed at the bend corner

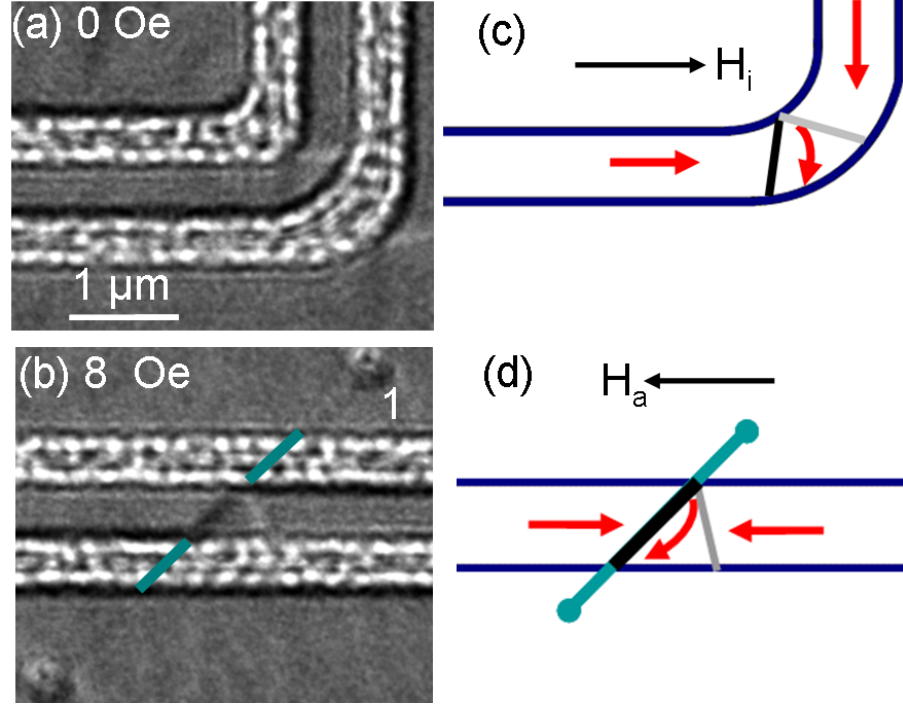


Figure 5.26: (a) Initially formed asymmetric TDW with magnetisation points down at the centre of the wall in the bend corner of an L-shaped nanowire. (b) DW is pinned at site 1 without changing the magnetisation direction. The ion irradiation line dose is  $4 \times 10^{15} \text{ ions/cm}^2$ . Schematic diagrams (c and d) demonstrate the magnetisation distribution in Fresnel images (a and b), respectively.

of this nanowire was again an asymmetric TDW, whereas at the centre of the wall the magnetisation points down instead of up, as observed in the previous experiments. Under the application of magnetic fields towards the pinning sites, the DW is pinned at site 1 (irradiation dose  $4 \times 10^{15} \text{ ions/cm}^2$ ), Fig. 5.26(b) without changing the wall structure. The schematic diagrams of (a and b) are (c and d), respectively. Initially formed micromagnetic wall structure Fig. 5.27(a) was also found to pin at this site by changing the magnetisation direction pointing from down to up, Fig. 5.27(b). After depinning this DW from site 1, DW is pinned again at site 2 and the magnetisation direction at the centre of the wall points up to down, Fig. 5.27(c). The schematic diagrams Figs. 5.27(d, e and f) shows the magnetisation distribution in the Fresnel images (a, b and c), respectively.

At higher irradiation line doses, for example  $16 \times 10^{15} \text{ ions/cm}^2$ , the initial asymmetric TDW, Fig. 5.28(a) is transformed to a clockwise vortex DW (cw VDW) as soon as DW is pinned at the irradiation site 1, Fig. 5.28(b). This is consistent with the previous investigation in which the magnetisation at the centre of the initially formed asymmetric TDW was pointed up. Figure 5.28(d) is the corresponding schematic showing



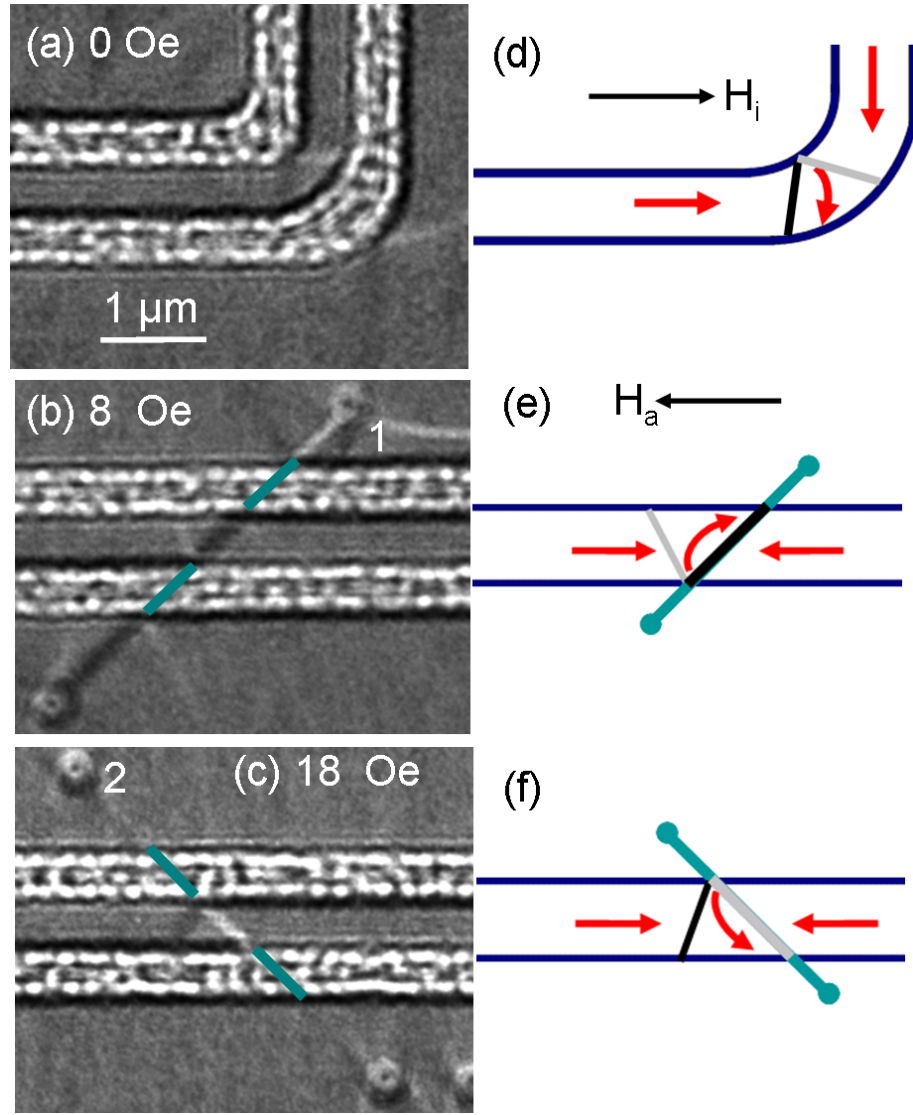


Figure 5.27: Fresnel image (a) showing the structure of an asymmetric TDW (magnetisation points down) in the bend corner of an L shape wire. DW is initially pinned at site 1 by changing it's structure and later on pin again at site 2 after depin from 1. The ion irradiation dose is  $4 \times 10^{15} \text{ ions/cm}^2$ . Schematic interpretation of (a, b and c) are (d, e and f), respectively.

the magnetisation distribution deduced from the image Fig. 5.28(b). Under the application of magnetic fields, the micromagnetic wall structure appeared at pinning site 1 in the L-shaped nanowires and the corresponding depinning field as a function of irradiation doses are inserted in table 5.1.

Magnetic imaging carried out in this investigation using LTEM demonstrates that micromagnetic wall structure can be controlled reproducibly by the non topographic pinning sites. These ion irradiated sites provided a well defined stable location for DWs. In order to check the reproducibility of the experimental findings, six nanowires of two different wire structures Figs. 5.17(b and c) were patterned for each ion irradiation line

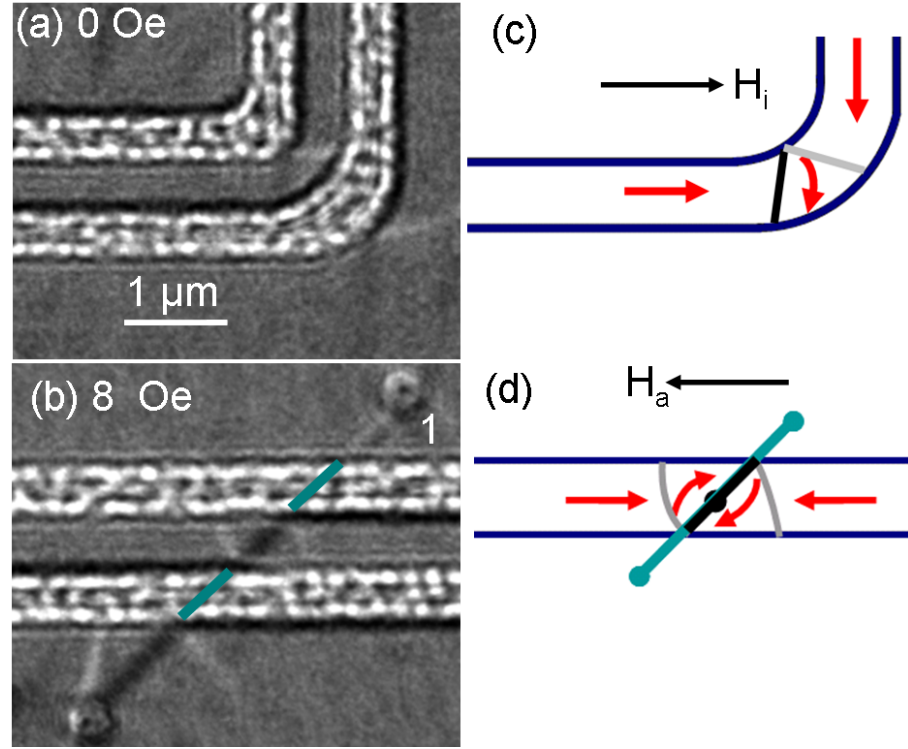


Figure 5.28: (Fresnel image shows that initially formed asymmetric TDW (a) is pinned and transform to a cw VDW (b) under the application of magnetic fields. The irradiation line dose is  $16 \times 10^{15} \text{ ions/cm}^2$ . Magnetisation distribution in Fresnel images (a and b) are shown schematically in (c and d), respectively.

dose. During the *in situ* magnetising experiments using LTEM, repeated experiments demonstrate that the propagation and pinning/depinning of DWs were consistent along all these patterned nanowires. This consistency indicate that creation of the field induced anisotropy during the material deposition and thereby writing of the patterns along this anisotropy direction played a vital role to establish the reproducibility of these experiments. As was described earlier, patterns written on the isotropic film did not reveal a reproducible magnetic behaviour.

Having established the experimental proof of the reproducible controlled pinning and depinning of DWs by using these non topographic pinning sites, we will now discuss the physics behind the strength and mechanism of these pinning features. By creating a local pinning site, we actually modify the magnetic properties of the Py film locally due to a combined effect of ion irradiation and Cr mixing from top and bottom layers. These modified magnetic properties include a reduction in the Curie temperature and  $M_s$  as well as a change in the exchange constant as was already mentioned. Therefore, in the schematic illustration, Fig. 5.29(a) the isolated nanowires can be divided into two sections; either side of the wire with an unmodified magnetic properties (defined

by FM1) and the ion irradiated site with a modified properties of the film (defined by FM2).

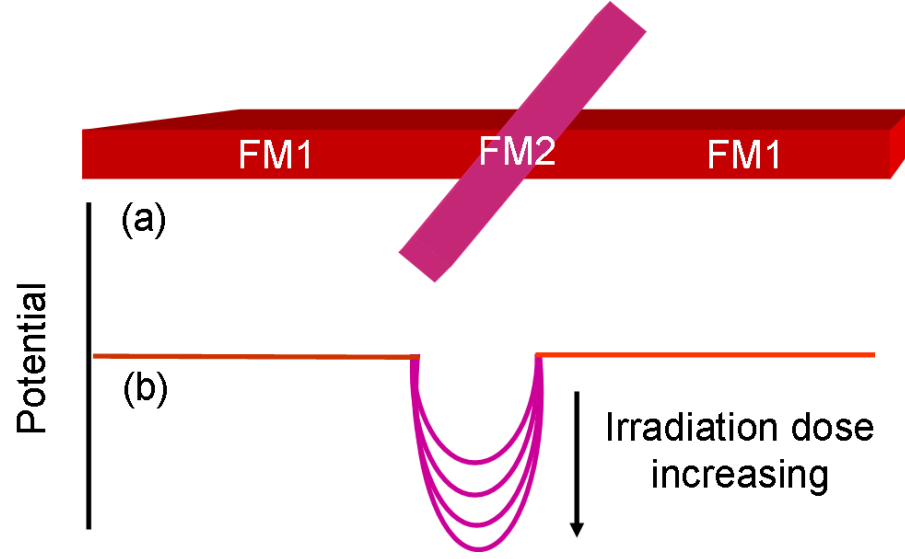


Figure 5.29: (a) Schematic diagram shows that the ferromagnetic (FM1) properties of the nanowire are unmodified at either side of the pinning site. At the pinning site the magnetic property is modified and denoted by FM2. (b) Schematic diagram illustrates that the pinning site behaves as an attractive potential well for DW and the well gets deeper for higher irradiation doses. The vertical axis is a measure of potential. Notably, higher irradiation dose allows DW to change structure.

A local modification of magnetic properties creates an attractive potential well which is a local minimum in potential energy. The experimentally obtained depinning fields are a measure of the strength of this well. The well gets deeper, Fig. 5.29(b) for higher irradiation dose, and therefore a high field is required to depin the DW from the well. In this way, the strength of this pinning potential was tuned by changing the dose of the irradiated feature. Notably, as soon as a DW comes into this potential well, the wall energy changes and thus a DW positioned along the irradiated line becomes energetically favourable. At higher irradiation doses, for both wire structures, initial asymmetric TDWs with either magnetisation pointing up or down were transformed into a cw VDW to explore the energy landscape of this potential well. Therefore, we may say that the irradiated site has the possibility of pinning, transforming and filtering the DWs. In order to gain further insight into the energy landscape of the potential well, we have performed micromagnetic simulations of the propagation of a DW driven by an external magnetic field.

## 5.9 Micromagnetic simulation

Micromagnetic simulations were carried out using freely available code, object oriented micromagnetic framework (OOMMF) developed by the NIST group at Gaithersburg [39]. The parameters used for the simulations were standard for Py:  $M_s = 8.6 \times 10^6$  A/m, magnetocrystalline anisotropy  $K = 0$  and damping coefficient  $\alpha = 0.5$ . A cell size of  $5 \times 5 \times 5$  nm<sup>3</sup> was used. These parameters are standard for Py and are commonly use for micromagnetic simulations of nanowires as was mentioned in **chapter 4**. In this chapter, *in-situ* magnetisation experiments were carried out for Py film deposited by MBE and sputter deposition technologies. Using low angle diffraction experiments, we have measured the integrated magnetic induction  $B_s t$  (t is the thickness) of the Py film deposited by MBE technique. The measured  $B_s t$  for a nominally 10 nm thick continuous Py film was  $9.0 \pm 0.2$  Tnm. As we did not observe reproducible magnetic domain wall behaviour for MBE deposited Py film, therefore, during the course of this investigation we did not measure accurately the thickness of the Py film. However, from  $B_s t$  value we can assume that the saturation magnetic induction for this film is close to 1 T (the standard value). Furthermore, the  $B_s$  of the magnetron sputter deposited Py film was measured in **chapter 6** using low angle electron diffraction technique. The measured  $B_s$  is 1 T (within an error limit of less than 2 %) for sputter deposited Py film that was used for magnetic investigations in **chapter 6**. It may also be noted here that the thickness of the film was measured from TEM cross-sectional image (this will be described in **chapter 6**) which was fairly accurate. One set of Py film investigated in **chapter 5** was deposited using the same sputter deposition machine (the deposition condition described in **chapter 6** was also nominally same). As was mentioned earlier,  $B_s = \mu_0 M_s$ , where,  $M_s$  is the saturation magnetisation, therefore, in **chapters 5 and 6** there was not any difference between the measured and the standard vale of  $M_s$  ( $8.6 \times 10^6$  A/m) that was used for OOMMF simulations.

Micromagnetic simulations were performed in this chapter for an asymmetric TDW in a 300 nm wide and 10 nm thick Py nanowire in which a pinning site oriented approximately at 45° from the wire axis were created as shown in the schematic Fig. 5.30(a). For modelling this pinning site, a matrix of 8 (horizontal) x 4 (vertical) cells were build up and then each matrix was displaced horizontally in the leftward direction

by two cells. Schematic Fig. 5.30(b) shows part of the 8 (horizontal) x 4 (vertical) cells modelled pinning site.

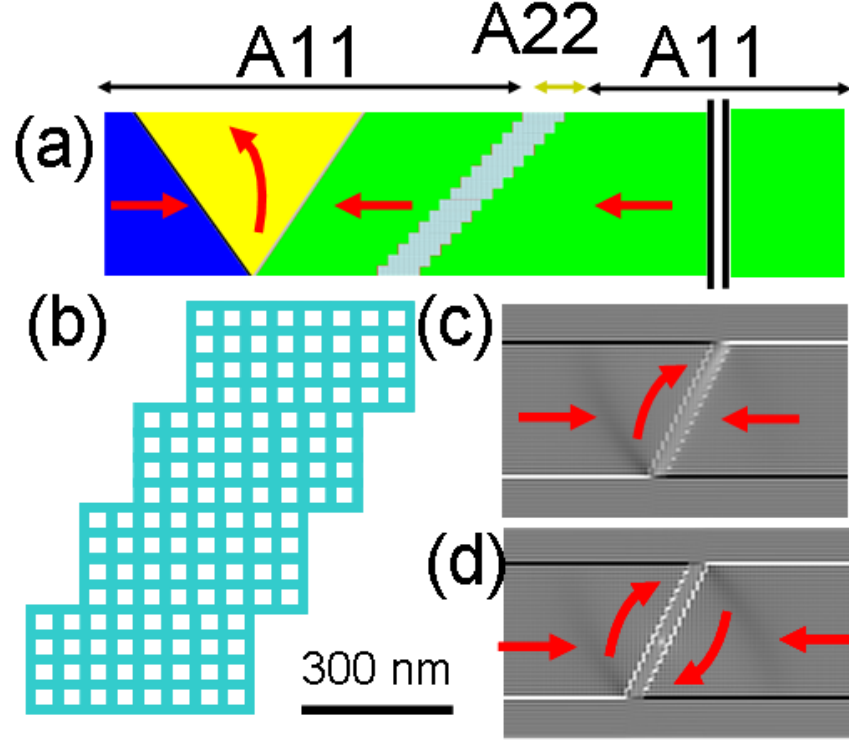


Figure 5.30: (a) Schematic of initial configuration before relaxation. This is an asymmetric TDW along with the modelled pinning site in a 300 nm wide and 10 nm thick nanowire. The length of the wire axis has been reduced for this schematic indicated by vertical bars. (b) Schematically part of the 8 (horizontal) x 4 (vertical) cells modelled pinning site. (c) Calculated Fresnel image shows pinning of an asymmetric TDW at the pinning site in which  $M_s$  is 70% of its original value and exchange constant was changed accordingly. (d) Calculated Fresnel image demonstrates the transformation of initial asymmetric TDW into a VDW at the pinning site in which  $M_s$  is 30% of its original value and the exchange constant was changed accordingly.

Inside the pinning site,  $M_s$  was set to 70% and then alternatively 30% to the original value. For the unmodified region of the Py nanowire an exchange stiffness constant  $A_{11} = 13 \times 10^{-12} \text{ J/m}$  was used. The exchange stiffness constant  $A_{22}$  of the pinning site with reduced  $M_s$  and the exchange coupling stiffness constant between the unmodified and modified region  $A_{12}$  were calculated with the relations  $A_{22} = A_{11}(\frac{M_{s,modified}}{M_{s,unmodified}})^2 \text{ J/m}$  and  $A_{12} = A_{21} = 0.5(A_{11} + A_{22})$ , respectively. For the determination of  $A_{22}$  we used the relation between the exchange constant  $A$  and the spin  $s$ ,  $A = 4Js^2/a$  (this relationship was described in **chapter 1** section 1.3.1), as well as the connection between the expectation values of the spin operator  $S_z$  and saturation magnetization  $M_s$ ,  $\langle M_s \rangle^2 \propto \langle S_z \rangle^2$ . There  $a$  is the lattice constant.

For 70%  $M_s$ ,  $A_{22} = 6.37 \times 10^{-12} \text{ J/m}$  and  $A_{12} = 9.685 \times 10^{-12} \text{ J/m}$  whereas for 30%  $M_s$ ,  $A_{22} = 1.17 \times 10^{-12} \text{ J/m}$  and  $A_{12} = 7.085 \times 10^{-12} \text{ J/m}$ .

Figure 5.30(c) shows under the application of 30 Oe magnetic field the pinning of DW at the pinning site in which  $M_s$  is 70% of its original value along with the corresponding exchange constant values. The wall structure is an asymmetric TDW with magnetisation points up in the rightward direction. If  $M_s$  of the pinning site is 30% and exchange values are changed accordingly, then under the application of the same amount of field, as soon as a DW is pinned at the pinning site, the wall structure transforms into a cw VDW which is in good qualitative agreement with the experimental results. The total energy  $E_{tot.} = E_{demag.} + E_{exchan.}$  associated with the cw VDW is  $3.3897 \times 10^{-17} \text{ J} = 3.1814 \times 10^{-17} \text{ J} + 0.2083 \times 10^{-17} \text{ J}$  which is 8.5% less than that of the asymmetric TDW for the same Zeeman field. The demagnetisation (exchange) energy associated with the TDW is 91 % (9 %) whereas with the VDW is 94 % (6 %). We expected that as soon as DWs come into the pinning potential, the DW energy changes at the pinning site. It was observed from low angle electron diffraction experiments described in section 5.6 that magnetisation of the irradiated region changes as a function of irradiation doses. Results from micromagnetic simulations provided an indication about the wall energy at the pinning site in which magnetisation was changed upon ion irradiation. Given the simplistic nature of the simulation here we get an insight that changing the magnetic properties results in a change in the wall type as seen in the experiment, of course it has been assumed that an abrupt change occurs in the model whereas a real system is likely to have a smoother profile. However the initial results suggests that further work in this area would be useful e.g. simulation using Nmag [40] may be carried out. Like OOMMF simulation the LLG equation is used in the Nmag for the magnetisation evolution. However, OOMMF is based on discretising space into small cells. One disadvantage is that this method works less accurately if the geometry shape does not align with a cartesian grid as the boundary then is represented as a staircase pattern. The advantage of Nmag over oommf simulation is that geometries can be spatially resolved much more accurately. Therefore, a pinning site oriented approximately at  $45^\circ$  from the wire axis may be modelled much accurately and strength of these pinning potentials can be calculated by calculating the depinning fields.

## 5.10 Summary

We demonstrate that for multilayered magnetic nanowires, where the thickness and composition of the individual layers has been carefully chosen, domain walls can be pinned at non-topographic sites created purely by ion irradiation in a focused ion beam system. A tri-layer thin film of Cr(3 nm)/Py(10 nm)/Cr(5 nm) was purposely created to optimise sensitivity to ion irradiation through localised beam induced alloying of the Py and Cr in a FIB microscope. The thickness of each layer of the tri-layer system was optimized by studying results from the dynamic ion irradiation simulation package TRIDYN. These simulations showed that an asymmetric thickness of the top and bottom Cr layer yielded the most uniform Cr concentration, resulting directly from the distribution of energy lost with depth of the implanted ions. Experiments to investigate micro alloying due to interfacial atomic mixing were performed using FIB irradiation. Low angle electron diffraction experiments using Lorentz TEM demonstrate that micro-alloying due to a combined effect of ion irradiation and interfacial Cr mixing modified the ferromagnetic properties of this alloy system. Nanowires were written on this continuous film using FIB milling and ion irradiation pinning features were created at predefined locations. The pinning results from irradiation induced alloying leading to magnetic property modification only in the affected regions.

Using Lorentz TEM, we have studied the pinning behavior of domain walls at the irradiation sites. We observed that the inclusion of the non topographic pinning features along the length of the patterned nanowires allow a degree of reproducible control of pinning and depinning of DWs at predefined locations. Although quite a range of behavior was observed some clear patterns of dependency was deduced. Irrespective of the direction of the central magnetization (up/down) of the initial wall at nucleation, at the pinning site the asymmetric TDW with downwards pointing magnetisation was most often observed up to a dose of  $8 \times 10^{15} \text{ ions/cm}^2$ . Furthermore, the de-pinning field of this wall was seen always to be higher than that of the asymmetric TDW with the upwards magnetised central domain. These observations, and the measured de-pinning field strengths, show that the lines irradiated with the two lowest doses act as effective pinning sites for asymmetric TDWs of both upwards and downwards central magnetisation but that the latter are pinned more strongly. Owing to the quasi-static

manner of applying the propagating field and its low value, we believe that the asymmetric TDW up/down transformations are mediated by the pinning site itself rather than occurring during propagation. Thus due to their greater energetic stability, downwards magnetized asymmetric TDWs are observed more frequently. At higher doses,  $12 \times 10^{15} \text{ ions/cm}^2$  and greater, the VDW became the dominant structure observed at the pinning site. These pinning features behave like potential wells and the strength of the wells is seen to increase with increasing ion dose until the VDW is observed at the higher doses. Wall transformations are observed with a tendency of one type of asymmetric TDW wall favoured at lower doses and only VDWs at the highest doses. In this sense the pinning site can be seen as setting the DW type for the higher doses whilst increasing the probability of one type of asymmetric TDW at the lower doses. Additionally the depinning field for the VDW appeared to be fairly independent of the ion dose of the pinning site. Clearly the irradiated line (width in the range 30-60 nm), which is very much narrower than the effective width of either of the asymmetric TDW or VDW types, exerts a significant influence over which type is most energetically favourable, for irradiation doses  $> 12 \times 10^{15} \text{ ions/cm}^2$ . We propose that this effect arises at these doses because the magnetic moment strength along the irradiated line is reduced. This likely allows the asymmetric TDW, when arriving at the pinning site, to convert to a lower energy VDW type. Initial micromagnetic simulations indicate that the irradiated lines result in a reduction of the demagnetising of the DWs when they are located at these positions.

Notably, in a previous investigation [12], a relationship between the orientation of the irradiated line and the chirality of the domain wall that pinned at the site was observed very clearly. However, in that investigation, the strength of the pinning potential on ion irradiation doses as well as any clear pattern of the DW depinning fields as a function of irradiation doses was not reported. The strength of the pinning potential that can be tuned by the ion implantation doses was reported recently [13,14]. In these investigations, implantation of chromium ions was used to induce pinning sites (referred as magnetic soft spots) via a local reduction in the saturation magnetisation. The size of the chromium implanted square-shaped magnetic soft spot in permalloy nanowires was around 300 nm. However, our investigation demonstrates the novelty of using a single irradiated line feature by varying the ion irradiation doses. The pinning sites



results from irradiation induced alloying leading to magnetic property modification only in the affected regions. We observed that depending on the irradiation dose, a single line feature not only pinned the domain walls but also acted to control their structure and the strength of their pinning. Therefore, the originality of this finding compared to the other published work [13, 14] is that the pinning site can control the location of DW as well as can set the DW type for the higher doses whilst increases the probability of one type of asymmetric TDW at the lower doses. Therefore, we can conclude that in addition to the control of the DWs, our findings indicate potential for engineering and filtering DWs of certain types as they pass irradiated features at predefined locations in nanowires, dependent on the dose associated with these features in magnetic nanowires sandwiched between metallic layers.

# Bibliography

- [1] D. A. Allwood, G. Xiong, M. D. Cooke, C. C. Faulkner, D. Atkinson, N. Vernier, and R. P. Cowburn, *Science* **296** 2003 (2002).
- [2] S.S.P. Parkin, M. Hayashi, L. Thomas, *Science* **320** 5873 (2008).
- [3] C. H. Marrows, *Adv. Phys.* **54** 585 (2005).
- [4] A. O. Adeyeye and R. L. White, *J. Appl. Phys.* **95** 2025 (2004).
- [5] K. He, D. J. Smith and M. R. McCartney, *Appl. Phys. Lett.* **95** 182507 (2009).
- [6] D. Petit, A. V. Jausovec, D. Read, and R. P. Cowburn, *J. Appl. Phys.* **103** 114307 (2008).
- [7] K. J. O'Shea, S. McVitie, J. N. Chapman, and J. M. R. Weaver, *Appl. Phys. Lett.* **93** 202505 (2008).
- [8] M. Kläui, C. A. F. Vaz, J. A. C. Bland, W. Wernsdorfer, G. Faini, E. Cambril, L. J. Heyderman, F. Nolting, U. Rüdiger, *Phys. Rev. Lett.* **94** 106601 (2005).
- [9] M. Kläui, H. Ehrke, U. Rüdiger, T. Kasama, R. E. Dunin-Borkowski, D. Backes, L. J. Heyderman, C. A. F. Vaz, J. A. C. Bland, G. Faini, E. Cambril, and W. Wernsdorfer, *Appl. Phys. Lett.* **87** 102509 (2005).
- [10] M. Herrmann, S. McVitie and J. N. Chapman, *J. Appl. Phys.* **87** 2994 (2000).
- [11] M. A. Basith, S. McVitie, D. McGrouther, J. N. Chapman, and J. M. R. Weaver, *J. Appl. Phys.* **110** 083904 (2011).
- [12] S. Turnbull, *Characterisation of focused ion beam nanostructures by transmission electron microscopy*, PhD thesis, University of Glasgow, 2008.

- [13] A. Vogel, S. Wintz, J. Kimling, M. Bolte, T. Strache, M. Fritzsche, M. Y. Im, P. Fischer, G. Meier, and J. Fassbender, IEEE Trans. Magn. **46** 1708 (2010).
- [14] A. Vogel, S. Wintz, T. Gerhardt, L. Bocklage, T. Strache, M. Y. Im, P. Fischer, J. Fassbender, J. McCord and G. Meier, Appl. Phys. Lett, **98**, 202501, (2011).
- [15] J.W. Mayer, L. Eriksson, J.A. Davies, Ion Implantation of Semiconductors, Academic Press, New York, 1970.
- [16] J.S. Williams, J.M. Poate (Eds.), Ion Implantation and Beam Processing, Academic Press, Sydney, 1984.
- [17] M. I. Guseva, G. V. Goedeveeva, physica status solidi (a), **95** 385 (1986).
- [18] C. Chappert, H. Bernas, J. Ferre, V. Kottler, J. Jamet, Y. Chen, E. Cambril, T. Devolder, F. Rousseaux, V. Mathet, and H. Launois, Science **280** 1919 (1998).
- [19] B. D. Terris, L. Folks, D. Weller, J. E. E. Baglin, A. J. Kellock, H. Rothuizen, P. Vettiger, Appl. Phys. Lett. **75** 40 (1999)
- [20] W. M. Kaminsky, G. A. C. Jones, N. K. Patel, W. E. Booij, M. G. Blamire, S. M. Gardiner, Y. B. Xu, and J. A. C. Bland, Appl. Phys. Lett. **78** 1589 (2001).
- [21] D. Ozkaya, R. M. Langford, W. L. Chan, A. K. Petford-Long, J. Appl. Phys. **91** 9937 (2002).
- [22] S. I. Woods, S. Ingvarsson, J. R. Kirtley, H. F. Hamann, R. H. Koch, Appl. Phys. Lett. **81** 1267 (2002).
- [23] J. Fassbender and J. McCord, Appl. Phys. Lett. **88** 252501 (2006).
- [24] J. Fassbender, J. von Borany, A. Mcklich, K. Potzger, W. Mller, J. McCord, L. Schultz and R. Mattheis, Phys. Rev. B **73** 184410 (2006).
- [25] L. Folks, R. E. Fontana, B. A. Gurney, J. R. Childress, S. Maat, J. A. Katine, J. E. E. Baglin, and A. J. Kellock, J. Phys. D App. Phys. **36** 2601 (2003).
- [26] J. Fassbender *et al.*, J. Magn. Magn. Mater. **320** 579 (2008).
- [27] D. McGrouther *et al.*, J. Appl. Phys. **95** 7772 (2004).

- [28] D. McGrouther *et al.*, J. Phys. D App. Phys. **38** 3348 (2005).
- [29] D. McGrouther *et al.*, Appl. Phys. Lett. **87** 022507 (2005).
- [30] C.C. Faulkner, D. Atkinson, D.A. Allwood, R.P. Cowburn, J. Magn. Magn. Mater. **319** 9 (2007).
- [31] R M Bozorth, Ferromagnetism (Piscataway: IEEE) 1993.
- [32] W. Möller and W. Eckstein, Comput. Phys. Commun. **51** 355 (1988).
- [33] Autoscript language: Autoscript Technical Note, FEI Company, Hillsboro, Oregon, USA, <http://www.feic.com>.
- [34] N. Owen, H.-Y. Yuen, and A. Petford-Long, IEEE Transactions on Magnetics **38**, 2553 (2002).
- [35] J. N. Chapman, J. Phys. D: Appl. Phys. **17** 623 (1984).
- [36] C. Brownlie, S. McVitie, J. N. Chapman, and C. D. W. Wilkinson, J. Appl. Phys. **100** 033902 (2006).
- [37] Y. Nakatani, Y. A. Thiaville, J. Miltat, J. Magn. Magn. Mater. **290** 750 (2005).
- [38] R. D. McMichael and M. J. Donahue, IEEE Trans. Magn. **33** 4167 (1997).
- [39] M. J. Donahue and D. G. Porter, Report No. NISTIR 6376 (National Institute of Standards and Technology, Gaithersburg, MD, 1999).
- [40] T. Fischbacher and H. Fangohr, arXiv:0907.1587.

# Chapter 6

## Magnetisation reversal processes in ion irradiated magnetic stripes

### 6.1 Objective and motivation

The previous chapter (**chapter 5**) dealt with the local modification of the magnetic properties in a Py nanowire structure by irradiation with *Ga* ions in a focused ion beam microscope. Furthermore, recent work on magnetic patterning has been studied by local modification of the magnetic properties of thin continuous films by means of ion irradiation [1–5]. It has been observed that by lateral magnetic patterning of ferromagnetic thin films the magnetic properties, like saturation magnetisation  $M_s$  [6,10,11] and induced anisotropy [7–9] can be changed on a local scale. If the patterning size is chosen below certain intrinsic magnetic length scales the patterned medium may show novel magnetic behaviour with a hybrid structure being created. The easiest experimentally accessible intrinsic magnetic length scale is the domain wall width, especially the width associated with the tails of the Néel wall, which can extend over several  $\mu m$  in soft magnetic Py thin films. Saturation magnetisation patterning in a stripe like manner has proven already the influence of the (dimension of the) lateral patterning on the micromagnetic behaviour of the hybrid material [10,11]. During external field reversal along the stripe axis densely packed  $180^\circ$  inter-stripe domain walls are created for stripe width equal and above  $1 \mu m$ . Upon scaling the patterning size down into the *nm* regime, a transition from the tendency of a discrete switching to a collective switching of the stripe patterns may be observed due to the overlapping of the Néel wall tails of neighboring inter-stripe domain walls. Associated with the overlapping of

Néel walls is also the constriction of domain walls by the patterning size. The Néel wall width does not depend only on the material properties but also on the geometry and the lateral dimensions [12,13] of the microstructure where it is located. In this project, in a continuous  $16.9 \pm 0.8$  nm thick Py film, magnetically softer (irradiated) and harder (unirradiated) regions, which are in direct lateral contact by means of exchange coupling, were fabricated in the Institute of Ion Beam Physics and Materials Research, Helmholtz-Zentrum Dresden - Rossendorf, Dresden, Germany using 30 keV focused  $Ga^+$  beam irradiation. The investigations were performed in a joint collaboration with Dresden colleagues using the high resolution Lorentz TEM imaging facilities of Glasgow to observe the influence of the downscaling of the patterning size on the domain wall formation and the magnetisation reversal in the equivalent stripe structures.

### 6.2 Material deposition and sample preparation

For the experiments nanocrystalline permalloy ( $Ni_{81}Fe_{19}$ ) films of  $16.9 \pm 0.8$  nm thickness have been deposited by magnetron sputtering on top of  $Si_3N_4$  window membranes [14], suitable for transmission electron microscopy (TEM). During the deposition of the magnetic material an external magnetic field was applied to produce a saturation magnetisation induced magnetic anisotropy. The magnetic properties of the thin film have been determined by means of magnetooptic Kerr effect magnetometry. In-plane magnetic field reversal shows a well defined uniaxial anisotropy. The anisotropy field  $H_K$  for the hard axis direction and the coercivity  $H_C$  for the easy axis direction are measured to be  $5.1 \pm 0.2$  Oe and 1 Oe, respectively. The  $H_K$  and  $H_C$  were determined from hard and easy axis loop, respectively. Magnetic hybrid structures consisting of arrays of periodic stripes structures on continuous film, as shown in the schematic 6.1 (a), were produced by magnetic patterning. The long axis of the stripes was aligned parallel to the anisotropy axis of the  $Ni_{81}Fe_{19}$  film. The patterning was realised by  $Ga^+$  focused ion beam (FIB) irradiation based lithography, performed on a *Zeiss NVision 40* dual beam system using a *Raith Elphy Plus*. Structure sizes and ion irradiation parameters are stated in table 6.1.

An ion dose of  $1000 \mu C/cm^2$  ( $6.24 \times 10^{15}$  ions/ $cm^2$ ) was applied on the irradiated stripes. The plan-view TEM image in Fig. 6.1 (b) shows both irradiated and non-

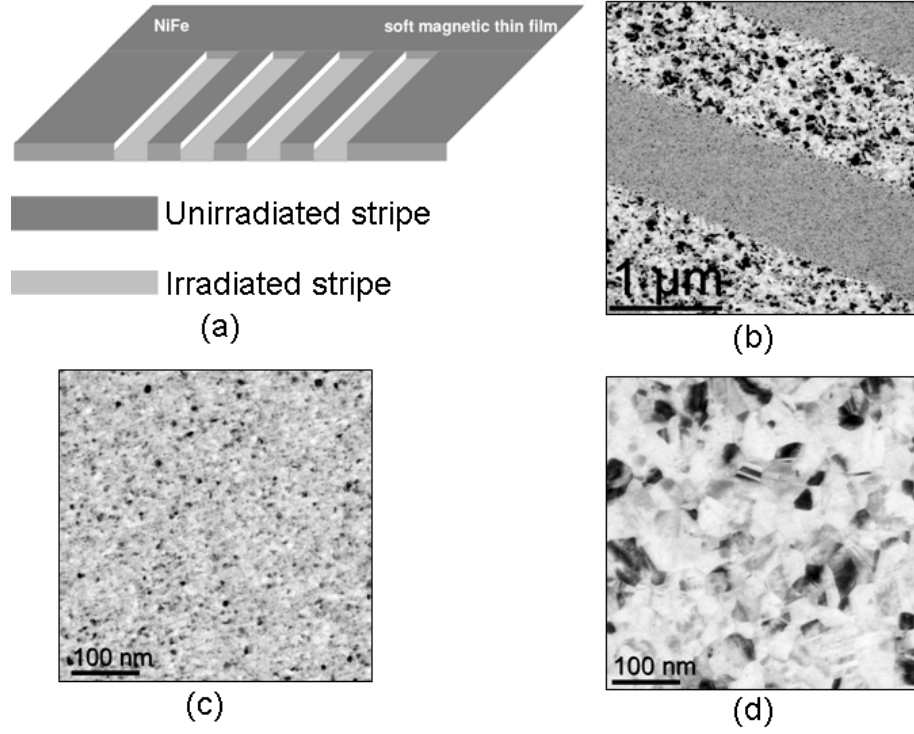


Figure 6.1: (a) Schematic diagram of unirradiated and irradiated stripe patterns in a thin continuous Py film. (b) Plan-view TEM bright field (BF) image demonstrates irradiated stripes by the increased grain size surrounded by the unirradiated stripe. Higher magnification TEM BF images show (c) the grain size distribution in the unirradiated stripe and (d) the grain growth inside the irradiated stripe due to the effects of irradiation .

Table 6.1: Structures and ion irradiation parameters.

structures		ion irradiation parameters	
stripe width	array size	<i>Ga</i> ion fluence	$1000 \mu\text{C}/\text{cm}^2$ $6.24 \cdot 10^{15} \text{ ions}/\text{cm}^2$
1000 nm	20 $\mu\text{m}$	<i>Ga</i> ion energy	30 keV
750 nm	20 $\mu\text{m}$	beam current	10 pA
500 nm	20 $\mu\text{m}$	step size	6 nm
400 nm	16 $\mu\text{m}$	dwel time	0.036 ms
300 nm	12 $\mu\text{m}$	beam speed	0.167 mm/s
200 nm	8 $\mu\text{m}$	repetitions / point	0

irradiated stripes with a width of 1000 nm. The irradiated material can be well distinguished from the initial film by the increase in grain size from 5-10 nm, Fig. 6.1(c), to 30-40 nm, Fig. 6.1(d) due to the effects of irradiation. This effect of  $Ga^+$  focused ion beam irradiation of  $Ni_{81}Fe_{19}/Si_3N_4$  has been observed before by several authors [15, 17] and we have also observed in **chapters 4 and 5**.

### 6.3 Characterisation technique

Both the Fresnel and differential phase contrast (DPC) modes of Lorentz TEM (LTEM) were used to investigate the magnetisation structures during external field reversal inside the stripe patterns. LTEM imaging was performed in a Philips CM20 field emission gun TEM equipped with Lorentz lenses and suitable for performing *in situ* magnetising experiments [18]. In Fresnel mode of Lorentz TEM, electrons passing through a magnetic region experience a Lorentz deflection due to the Lorentz force, whereas those passing through a non-magnetic region are not deflected. As was described in **chapter 3**, for a parallel beam, which is incident perpendicular to the plane of the specimen, the deflection angle due to Lorentz force is given by

$$\beta_L = \frac{e\lambda B_s t}{h} \quad (6.1)$$

with  $B_s = \mu_0 M_s$  being the saturation magnetic induction and  $t$  the film thickness. Previously Fresnel images were described for DWs and at edges in free space. However, the deflection angle also changes where the  $B_s t$  value changes either side of a boundary, which is what occurs here and results in contrast similar but weaker than that due to domain walls. In this particular mode of LTEM contrast arises in the defocused image for magnetic materials due to changes in the direction or magnitude of the magnetic induction, or more precisely the integrated induction. Therefore this mode reveals domain wall as black and white lines. In addition, edges where the integrated induction changes will also be revealed as having black and white contrast as was also described in **chapters 3 and 4**.

The microscope used for the Fresnel imaging has a scanning capability and is used also for the DPC mode of Lorentz microscopy. This particular mode of Lorentz microscopy was used to investigate the details of the switching behavior in the stripe patterns and also to map domain walls profiles, due to its much better spatial resolution ( $< 10$  nm) [18,19] than Fresnel imaging. In this imaging mode, the microscope is operated using a scanning transmission electron microscope (STEM) technique in which the electron beam is focused to a probe and scanned across the sample. By measuring the difference signals from opposite sides of the detector, pairs of images of integrated orthogonal magnetic induction perpendicular to the electron trajectory are obtained



as was described in details in **chapter 3**. These images were used to gain quantitative insight during the reversal of the stripe pattern under the application of magnetic fields. Furthermore, using Lorentz microscopy, low angle electron diffraction [19, 20] experiments were carried out to measure integrated magnetic induction  $B_s t$  of the unexposed and exposed areas of the films. The magnification of the intermediate and projector lenses of the Philips CM 20 electron microscope used for this investigation was sufficient to provide visible the small Lorentz deflections which is typically of the order of  $12 \mu rad$  for 20 nm thick Py film.

### 6.4 Reduction of integrated magnetic induction due to irradiation

In order to quantify the reduction of integrated magnetic induction due to *Ga* ion irradiation, low angle electron diffraction experiments were carried out using Lorentz microscopy. This technique was described in **chapter 3**, section 3.10. To conduct low angle diffraction experiments, using Fresnel mode of Lorentz TEM, an  $180^\circ$  domain wall was formed along the stripe pattern during reversal so that oppositely magnetised domains in both regions were present, Fig. 6.2(a). Therefore, pairs of diffraction spots were formed by illuminating the area, marked by red circle, of the anti-parallel alignment of magnetisation, Fig. 6.2(a). The Lorentz deflection angle present in the region of the film under investigation is proportional to  $B_s t$  as was shown in *equation 6.1*. Therefore, the separation between two diffraction spots of a pair is higher if the deflection takes place from a region containing two uniformly magnetised and anti-parallel aligned domains. In Fig. 6.2(b) four diffraction spots are observed for the stripe pattern, two from oppositely magnetised non-irradiated regions (green marked) and the other two from the oppositely magnetised regions with reduced saturation magnetisation value (blue marked). Notably, low angle diffraction experiments were also carried out in **chapter 5** by illuminating an area of anti-parallel alignment of magnetisation of the unirradiated and irradiated film (results described in section 5.6). In that case, we were able to form a state with a  $180^\circ$  degree wall perpendicular to the stripes. But in the present investigation, there was a field induced anisotropy along the stripe axis and an  $180^\circ$  domain wall was formed along the stripe pattern

during reversal so that oppositely magnetised domains in both regions were present. Therefore, stray field was generated from the far end of the stripes and the influence of stray magnetic field was negligible. Therefore, we have observed four diffraction spots, two from oppositely magnetised non-irradiated regions and the other two from the oppositely magnetised regions with reduced saturation magnetisation. In the absence of stray magnetic field, saturation magnetic induction  $B_s = \mu_0 M_s$ , where,  $M_s$  is the saturation magnetisation.

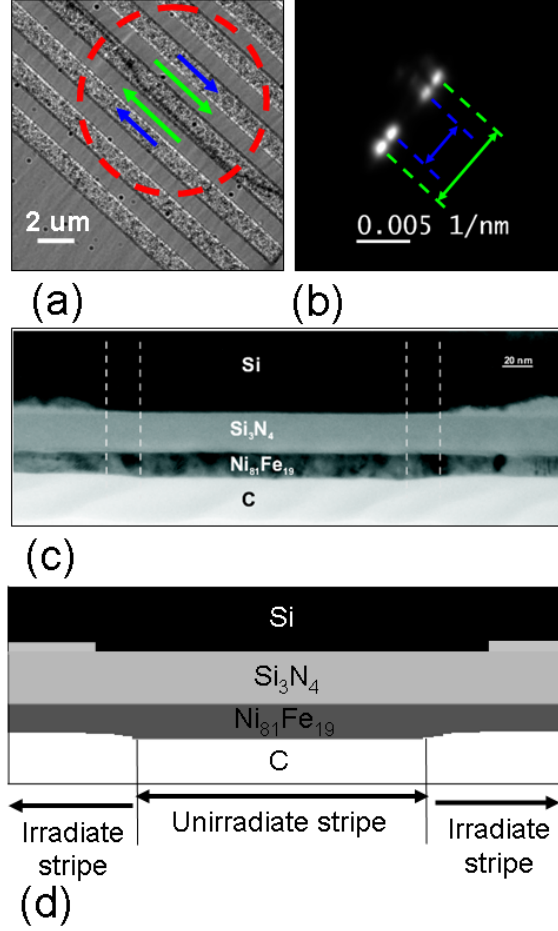


Figure 6.2: (a) Fresnel image showing the oppositely magnetised magnetic region of the unirradiated and irradiated stripes by forming a  $180^\circ$  domain wall along the stripe pattern. (b) Electron diffracted spots were obtained by illuminating the area, marked by red circle in image (a), from low angle diffraction experiments using Lorentz TEM. The two outer spots (green mark) arise from the unirradiated regions whereas two inner spots (blue mark) are from the irradiated regions. (c) cross-sectional TEM image of a non changed area between two FIB irradiated stripes (this cross-section was prepared in Dresden). (d) A schematic of the TEM cross-section (c).

By measuring the distance between the two outer spots (green marked),  $B_s t$  of the unirradiated stripes is calculated. The separation between the two inner spots (blue marked) is the  $B_s t$  of the irradiated stripes. The measured  $B_s t$  of the irradiated stripes

is 60% of the unirradiated stripes. As both saturation magnetisation (induction) and (effective magnetic) film thickness are reduced for the irradiated stripes, the change in saturation magnetic induction can be determined if the change in thickness is known. The thickness change was measured by preparing a TEM cross-section described next. A cross-sectional transmission electron microscopy image of a stripe pattern of 200 nm stripe width, located on a frame of a silicon-nitride membrane, is shown in Fig. 6.2(c). A schematic of this TEM cross-section is shown in Fig. 6.2(d). To avoid any morphological change of the stripe pattern during TEM lamella preparation by FIB, a protection layer of carbon was deposited on the sample. The irradiated layer stack can be recognised by both the reduced thickness due to irradiation induced sputtering, as well as by the changed contrast of the silicon wafer beneath the silicon-nitride layer. The latter one results from the amorphisation of silicon induced by the atomic displacements of the collision cascades. The thickness of the unirradiated and irradiated  $Ni_{81}Fe_{19}$  layer has been determined from the TEM cross-section to be  $16.9 \pm 0.8$  nm and  $14.0 \pm 0.6$  nm, respectively. For a decrease in film thickness of  $2.9 \pm 0.7$  nm as obtained from cross-sectional TEM measurements, the magnetic induction is reduced to  $72.0 \pm 0.7\%$ . The thickness differences between the unirradiated and irradiated stripe patterns is clearly seen in TEM cross-section Fig. 6.2(c) and in the schematic diagram Fig. 6.2(d). The changes in the magnetic properties due to  $Ga^+$  and other ion species e.g.  $Cr^+$  implantation have been observed previously but not as quantitatively as here [15,16]. In the next stage of this investigation, Fresnel imaging was performed to investigate the details of the magnetisation reversal processes in the stripe patterns of varying width.

## 6.5 Magnetic characterisation

### 6.5.1 Fresnel imaging

Magnetisation reversal inside the stripes with a width of 1000 nm was studied by Fresnel imaging. The in-plane component of the applied external field is parallel to the stripe axis. Prior to describe the Fresnel imaging it may be mentioned here again using equation 6.1 that electrons passing through the non-irradiated regions are more deflected compared to the electrons passing through the irradiated regions as shown

in the schematic Fig. 6.3(a). Therefore alternate dark and bright contrast appears at the interfaces of the stripes due to the variation of both magnetic induction and film thickness as is seen in the schematic intensity profile Fig. 6.3 (b). Figure 6.4(a-d) show a Fresnel image sequences of a typical magnetisation reversal process of 1000 nm wide stripe pattern. Starting from saturation, Fig. 6.4(a), the stripe pattern and the surrounding film are nearly uniformly magnetised parallel to the applied field direction. From the visible magnetisation ripple the net magnetisation direction can be deduced, as it is always orientated perpendicular to the ripple. At the interfaces between the unirradiated and irradiated stripes alternating dark and bright Fresnel contrast is apparent, Fig. 6.4(a).

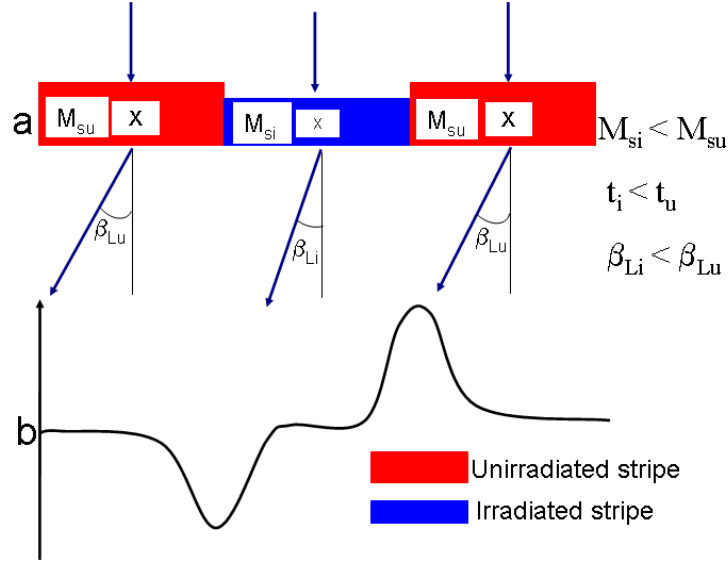


Figure 6.3: (a) Schematic diagram illustrates that saturation magnetisation of the unirradiated stripe ( $M_{su}$ ) is higher than that of the irradiated stripe ( $M_{si}$ ). Film thickness  $t_i$  of the irradiated stripe is lower than that of the unirradiated stripe  $t_u$ . Electron deflection from the unirradiated stripe is larger compared to that of the irradiated stripe, and (b) Resulting intensity distribution due to the deflections of the electron beams.

Upon reversing the external field, Fig. 6.4 (b), high angle domain walls in the film are initially pinned at the outer irradiated stripes. Clearly it is energetically more favourable to locate these walls in the irradiated material due to lower saturation magnetisation and film thickness meaning the walls have less energy in this region. It should be noted that the walls are seen only in the irradiated stripes, but not in the unirradiated stripes. On application of an increased negative field, Fig. 6.4(c), a two step reversal process of the stripe pattern is observed. Upon further increase of the negative external field, the magnetisation inside the non-irradiated stripes starts re-

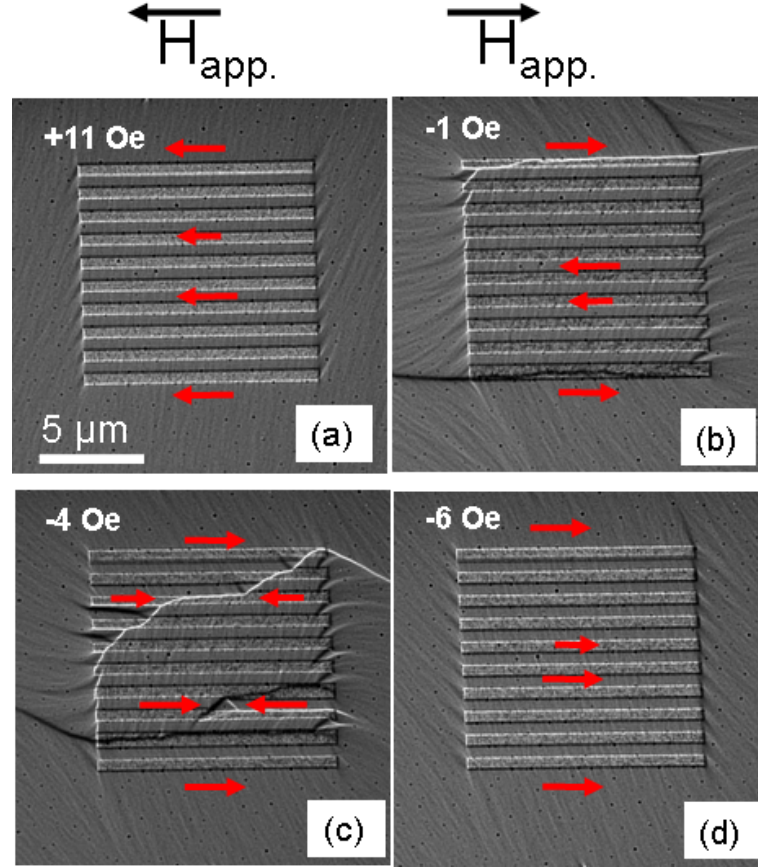


Figure 6.4: Fresnel image sequences (a-d) for magnetisation reversal of the 1000 nm wide stripe patterns. Magnetisation reversal inside the stripe panel is driven by domain walls in the surrounding film. Reversal completed with an intermediate anti-parallel orientation of magnetisation in neighboring stripes.

versing before the irradiated stripes have completed their reversal, Fig. 6.4(c). Domain walls propagating now along the non-irradiated stripes are pinned at the places where the quasi-domain walls are located (Fig. 6.4(c), upper right corner). There transverse domain walls are formed, which are only present inside the non-irradiated stripes. The reversal of the hybrid structure is influenced by the high angle domain walls in the surrounding film, which were initially pinned at the outer structure regions. These domain walls move when the external field exceeds the appropriate depinning fields. In Fig. 6.4(d) the hybrid structure has finally completed the magnetisation reversal. Looking at the two step reversal process of the stripes, it can be determined whether the unirradiated or irradiated stripes with high or low saturation magnetisation value, respectively start the magnetisation reversal. Both the Zeeman energy and the increased coercivity in the irradiated stripes with low saturation magnetisation value support a switching of the unirradiated stripes with high saturation magnetisation value. Notably, changes of the magnetisation reversal along the initial easy axis were measured

## Chapter 6: Magnetisation reversal processes in ion irradiated magnetic stripes

for  $70\text{ }\mu\text{m} \times 70\text{ }\mu\text{m}$  squares of a  $\text{Ni}_{81}\text{Fe}_{19}(20\text{nm})/\text{Si}_3\text{N}_4$  reference sample irradiated with focused ion beam with the same parameters. The coercivity  $H_C$  increased to at least 6 Oe due to an increase in pinning of the domain walls. However, by considering the difference in energy between the two regions, it would be expected that the energy associated with the irradiated region is lower due to lower moment and possibly exchange. Therefore, a switching of these irradiated stripes first is expected. Obviously this seems to be the dominant part and the fact that the DWs reside in the irradiated stripe is an indication of this. The details of this two-step process will be described again in section 6.5.2 using high resolution DPC images.

The magnetisation directions in the Fresnel images described in this chapter were

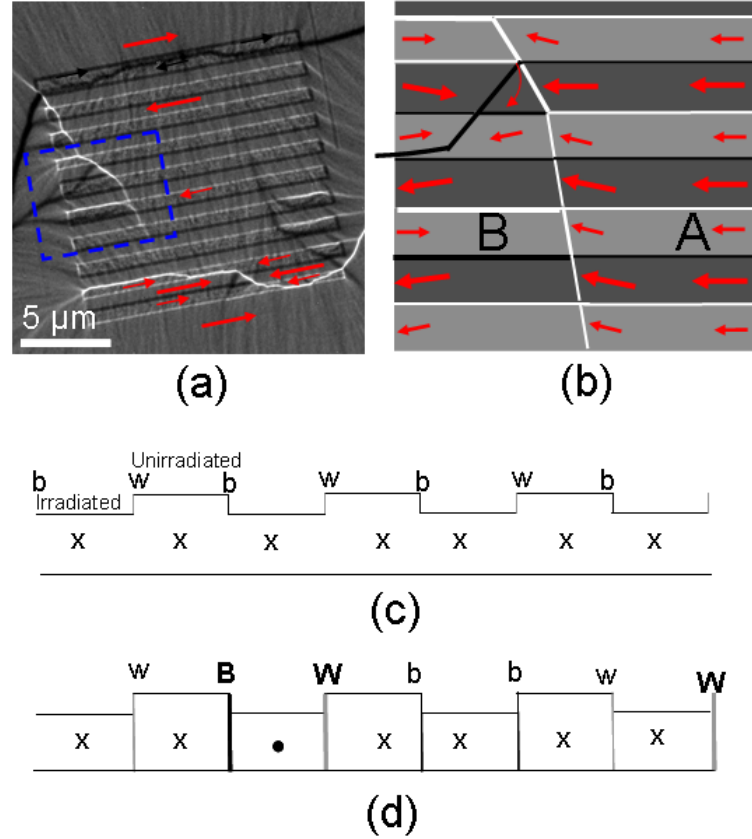


Figure 6.5: (a) Fresnel image showing strong black and white wall contrast as an example within the blue marked region. (b) Schematically magnetisation directions in the unirradiated and irradiated stripes followed by blue rectangular region of Fresnel image (a). Cross-section of the stripe patterns showing schematically (c) magnetisation directions of the unirradiated and irradiated stripes in the region 'A' of schematic (b), where w and b indicate white and black contrast, respectively; (d) reversal of the irradiated stripes take place in region 'B' and white and black contrast became stronger as indicated by **W** and **B**, respectively.

assigned by looking at the edge contrast and with the aid of the intensity profiles taken from a line trace perpendicular to the stripes. Notably, the light/strong black and

## Chapter 6: Magnetisation reversal processes in ion irradiated magnetic stripes

---

white contrast observed in the Fresnel image 6.4(c) may be explained with the aid of Fresnel image 6.5 (a) which shows a similar wall contrast marked by the blue rectangle. Figure 6.5(b) shows schematically the magnetisation direction of the unirradiated (indicated by large size arrow) and irradiated stripes (indicated by small size arrow) within the blue marked region. Figure 6.5(c) is the cross-section of the nanostripes showing schematically the magnetisation distribution of the unirradiated and irradiated stripes of the schematic 6.5(b), where w and b indicate white and black contrast, respectively. Cross section 6.5(c) is the situation observed in the region 'A' of the schematic 6.5(b) and Fresnel image 6.4(a) where magnetisation of the unirradiated and irradiated stripe patterns are aligned in the same direction. Upon the reversal of some of the irradiated stripes in region 'B' of schematic 6.5(b), the magnetisation of the unirradiated and irradiated stripes is oriented in opposite direction which results a stronger black and white contrast as shown in cross section 6.5(d), where **W** and **B** indicates strong black and white contrast, respectively. This is the situation observed in the region 'B' of the schematic 6.5(b) and Fresnel image 6.4(c) where stronger black and white wall contrast were observed.

Figures 6.6(a-c,e,f) show magnetisation reversal sequences for 500 nm wide stripe patterns where in-plane component of the applied external field is parallel to the stripe axis. At an applied magnetic field +11 Oe, the stripe pattern and the surrounding film are nearly uniformly magnetised parallel to the applied field direction. Like the Fresnel image 6.4(a), alternating dark and bright contrast is apparent at the interfaces between the unirradiated and irradiated stripes, Fig. 6.6(a). By applying a magnetic field in the opposite direction, Fig. 6.6(b), 180° black and white contrast associated with DWs was visible in the outer stripes. Similar to 1000 nm irradiated stripes, these 180° walls are initially pinned at outer irradiated stripes and existed only in the irradiated stripes but not in the unirradiated stripes. If the field strength is increased further in the negative direction, strong black and white wall contrast appear at the left side of the image 6.6(c) along with the formation of lower angle domain walls. Figure 6.6(d) is the schematic of Fresnel image 6.6(c) (blue marked region) and showing the magnetisation direction including low angle DWs. This again may be attributed to the reversal of the irradiated stripes but not the unirradiated stripes. Formation of the stronger black and white contrast can be described similarly using schematic diagrams 6.5(a-d). Unlike



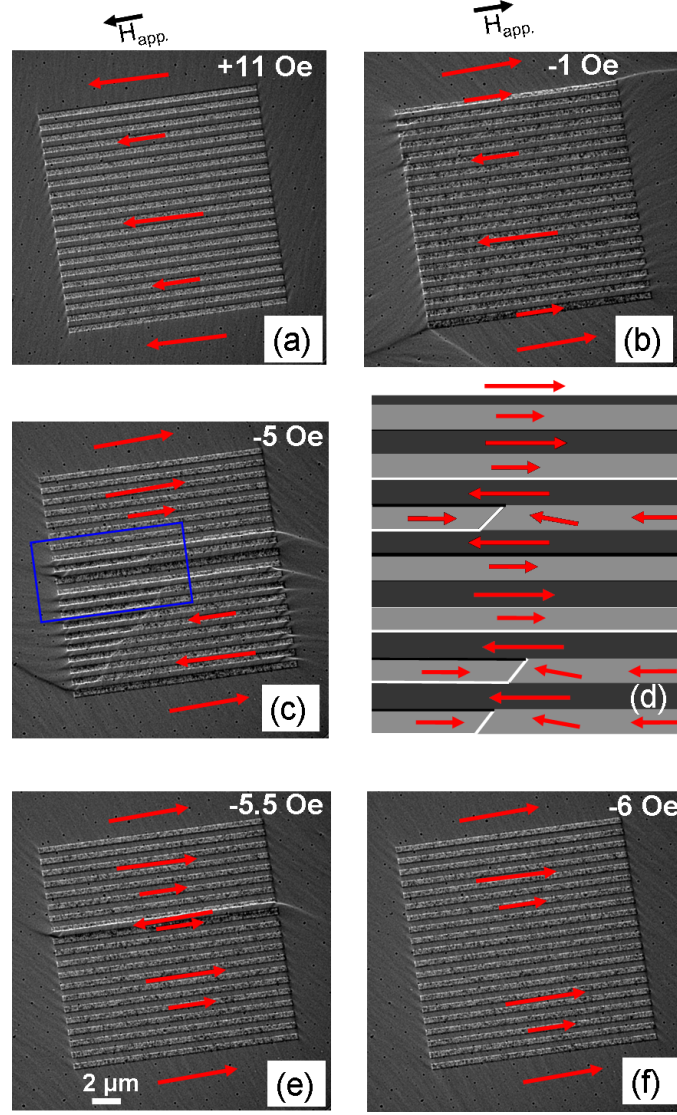


Figure 6.6: Fresnel image sequences (a-c,e,f) for magnetisation reversal of the 500 nm wide stripe patterns. Magnetisation reversal inside the stripe panel is driven by domain walls in the surrounding film. (d) is a schematic of blue marked region of Fresnel image (c).

1000 nm wide stripe patterns, high angle head to head transverse DWs are not formed between the unirradiated regions of the 500 nm wide stripe patterns. A further field increase to 5.5 Oe, Fig. 6.6(e) causes step like reversal of the stripes and the movement of  $180^\circ$  DWs. By increasing the field strength,  $180^\circ$  DWs were annihilated and reversal of the stripe patterns were completed. This is observed in Fresnel image 6.6(f) where alternating black and white contrast now appear in the opposite sense compared to image Fig. 6.6(a).

Figures 6.7(a-d, f) shows the Fresnel image sequence for the magnetisation reversal of 200 nm wide narrower stripe patterns. By applying an in-plane external field parallel to the stripe axis, the stripe pattern and the surrounding film were nearly uniformly



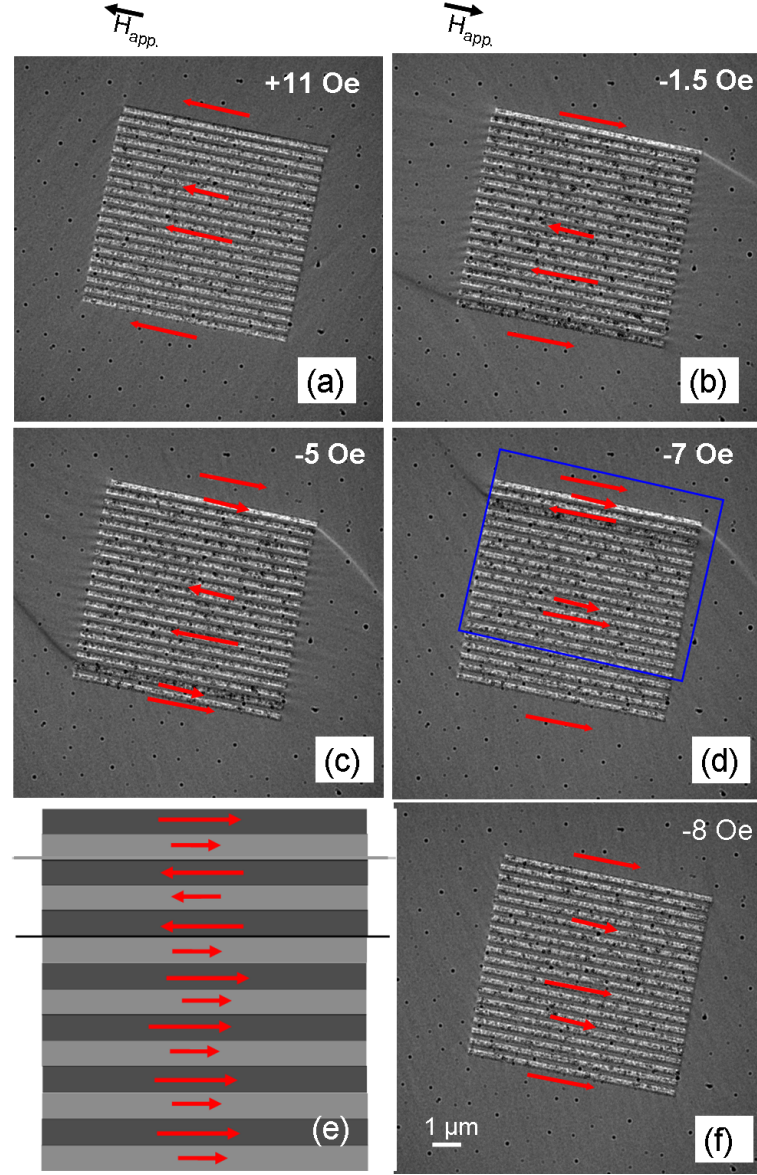


Figure 6.7: Fresnel image sequences (a-d, f) for magnetisation reversal of the 200 nm wide stripe patterns. (e) is the schematic within the blue marked region of Fresnel image (d) and showing the magnetisation directions.

magnetised, Fig. 6.7(a), parallel to the field direction. Upon the application of magnetic field in the opposite direction, similar to 1000 and 500 nm wide stripe patterns,  $180^\circ$  DWs of white and black contrast were initially formed and pinned only in the outer irradiated stripes, Fig. 6.7(b). By further field increase to 5 Oe and 7 Oe, Figs. 6.6(c,d), again causes step like reversal of the stripe patterns as was also observed as for 500 nm wide stripes. However, in the 500 nm stripes there is the stable state where partial reversal of stripes is seen, which is not visible here. The magnetisation directions within the blue marked region of Fresnel image Fig. 6.7(d) is shown schematically in Fig. 6.7(e). Magnetisation reversal process was completed at an applied magnetic

field of 8 Oe, Fig. 6.7(f). The initial formation and then pinning of  $180^\circ$  DWs only in the irradiated stripes is again notable. Formation and pinning of the  $180^\circ$  DWs in the irradiated region of both wider and narrower stripe patterns will be further realised by micromagnetic simulation in section 6.5.3. In contrast to this similar micromagnetic behaviour between wider or narrower stripes, the notable difference was the tendency of a collective switching of the stripe patterns upon downscaling the patterning size from 1000 nm to 200 nm. For the intermediate stripe width (500 nm) the reversal process was mostly similar to the nanostripe of width 1000 nm. Therefore, in the next stage of this investigation, high resolution DPC images were taken for a representative domain state during external magnetic field reversal of 1000 nm and 500 nm stripe patterns.

### 6.5.2 DPC imaging

The aim of acquiring high resolution DPC images is to extract quantitative information during magnetisation reversal. Using DPC images the aim is to provide detailed vector maps of the magnetic induction to assist in the understanding of the two-step process in 1000 nm wide nanostripe described in the previous section. The two-step reversal process is visible in the domain state shown in Fig. 6.8, recorded in another reversal experiment using the DPC mode of Lorentz microscopy. This typical structure represents a stable state during reversal. Figure 6.8(a) represents the magnetic induction component parallel to the stripes; Fig. 6.8(b) represents the component perpendicular to the stripes. Magnetisation components in Figs. 6.8 (a) and (b) are shown schematically in Fig. 6.8(c) along with the rotation angles measured from these DPC images. The calculation was based on consistency between the signal levels on the two components, the wall angles and the assumption of no net charge on the walls and interfaces. As shown in Fresnel image 6.4(c), the reversal started in the irradiated stripes. This happens by nucleation of domain walls at the stripe ends and their propagation along the stripes, Fig. 6.8(a). What happens in the application of a reverse field is that there is a rotation of the magnetisation in the stripes. At low fields this is fairly small in the non-irradiated stripes. If there is to be no charge at the interface then there is a much larger rotation in the irradiated stripes and we get a larger angle DW there. This is in fact what we see from the schematic shown in Fig. 6.8(c). If we consider the

unirradiated and irradiated stripes 1 and 2 in the schematic Fig. 6.8(c), it is clear that this state is consistent with no net charge being present at the interfaces and walls. Therefore, a larger rotation of magnetisation in the irradiated stripe is expected by forming high angle DWs.

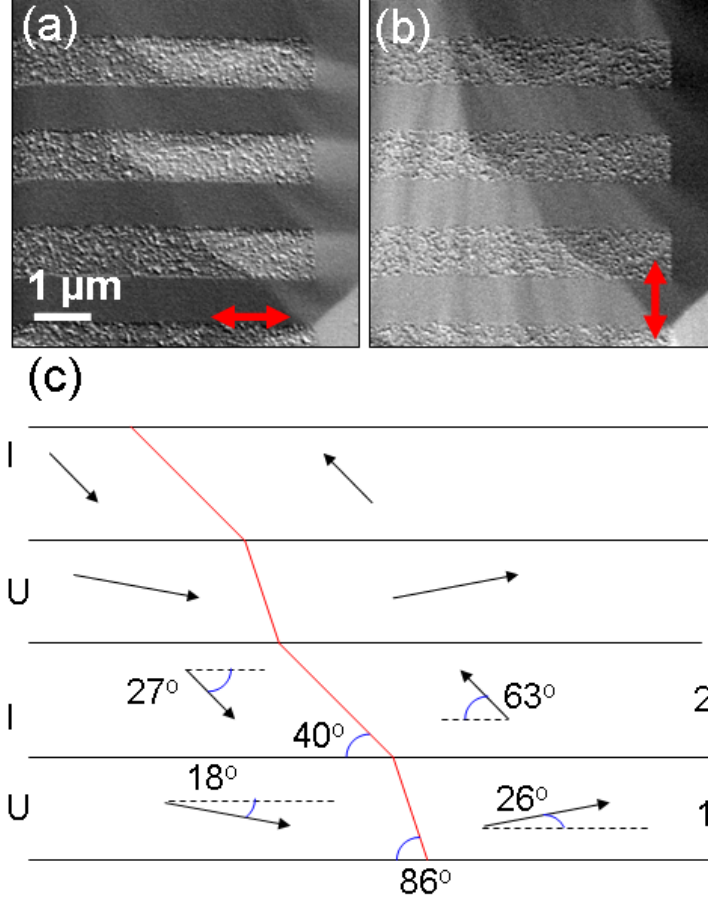


Figure 6.8: Domain state of a separate reversal experiment in 1000 nm wide stripe pattern. The induction component parallel and perpendicular to the stripes are shown in (a) and (b). Induction components in (a) and (b) are shown schematically in (c).

It is notable that similar to extended hybrid stripe patterns [10], the irradiated stripes can reverse in a collective way. This happens by the movement of domain walls [10] across the stripe pattern. These domain walls separate areas of nearly opposite magnetisation orientations inside the irradiated stripes, being high angle walls. On the left side the longitudinal component is parallel in all stripes, whereas on the right side the longitudinal component is anti parallel between the irradiated and nonirradiated stripes. However, in either side of the "walls" the transverse component is down on the left and up on the right, Fig. 6.8(b). There they separate areas with magnetisation orientations slightly tilted in respect to each other, being low angle walls. Notably,

the high angle domain walls between the stripes are densely packed Néel walls. Both the angle of the low angle domain wall with respect to the stripe axis, as well as the mapped magnetic induction component perpendicular to the stripe axis Fig. 6.8(b) show a strong transverse magnetisation component in both kind of stripes. Despite this transverse magnetisation component periodic anti-parallel magnetisation components along the stripe axis are observed, Fig. 6.8(a), in wider stripes.

Figures 6.9(a-f) show differential phase contrast images for a representative domain state during external magnetic field reversal of 200 nm wide stripe patterns. The mapped magnetic induction components in the images are indicated with the double headed arrows. The *subset (a,e)* show the magnetic induction distribution for the whole hybrid structure. The upper situated stripes as indicated by the red arrows, Fig. 6.9(a), show the left hand part of the structure has already completed reversal and the stripes are magnetised along the external field direction. In *subset (b,f)* a magnified region of the left lower part of the structure is shown. Comparing the longitudinal and transverse magnetisation component, it is evident that the quasi-domain wall is a low angle wall. It separates areas with slightly different magnetisation orientations. Not only the magnetisation inside the stripes with low saturation magnetisation value is rotating away from the stripe axis, but also the magnetisation in the stripes with high value follow this rotation for reason of flux continuity. Also from the angle of the quasi-domain wall in respect to the stripe axis it could be deduced that the magnetisation at the stripes ends have a transverse component. Apparently no discrete pattern with anti-parallel alignments of the magnetisation of neighboring stripes is found which was observed for wider stripes. In *subset (c,g)* a magnification into the right lower part of the structure is shown. Compared to the left structure side, the quasi-domain wall is a high angle wall for two irradiated stripes as shown in the schematic diagram, Fig. 6.9(d). Inside them the magnetisation has opposite longitudinal components on both sides of the wall. Therefore a high angle domain wall is formed at the interfaces of the reversed irradiated stripe parts and the neighboring unirradiated stripes. But periodic neighboring high angle domain walls between adjacent stripes which were observed for wider stripes (1000 nm) are not found in these narrower stripes. Instead of this the stripes tend to reverse together. The formation of densely packed high angle Néel walls between the stripes is suppressed for this structure size. In the next stage of this

investigation, micromagnetic simulations were carried out for a further understanding of how the walls change in these structures.

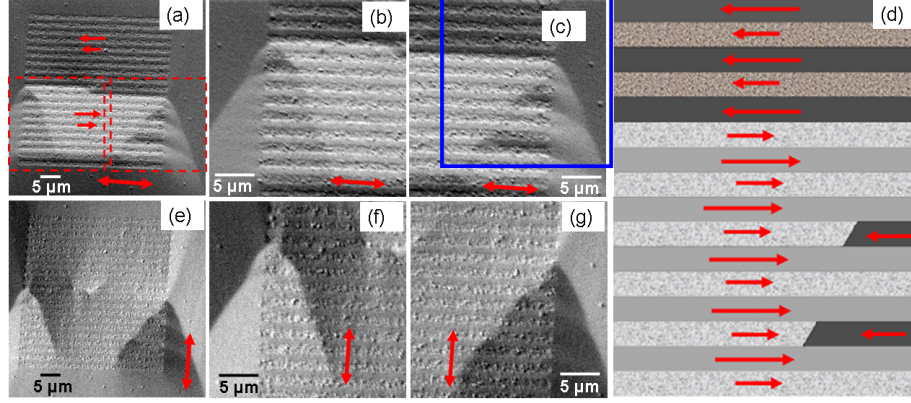


Figure 6.9: DPC images of stripe array with stripe width of 200 nm. The two sensitivities are shown in the upper and lower row. Images b and c (f and g) are showing the magnification of the square marked regions of image a (e). (d) is the schematic of the marked region in Fresnel image (c).

### 6.5.3 Micromagnetic simulation on stripe patterns

The simulations were carried out using object oriented micromagnetic framework (OOMMF) [21] by varying magnetisation parameters between two neighboring stripes. Schematically cross-sections of these stripes are illustrated in Fig. 6.10(a), where  $M_s$  is 100% of the moments of Py for one stripe (referred as unirradiated stripe) and 60% of total for the other (referred as irradiated stripe). The initial states with anti-parallel orientation of magnetisation of these two stripes are shown in Fig. 6.10(b) where upper and lower stripes are considered as unirradiated and irradiated stripes, respectively. The simulations were relaxed from this state, i.e. it is a starting state. The parameters used for simulation are standard for Py: saturation magnetisation  $M_s = 8.6 \times 10^6$  A/m, exchange stiffness constant  $A = 1.3 \times 10^{-11}$  J/m, magnetocrystalline anisotropy  $K = 0$  and damping coefficient  $\alpha = 0.5$ . The dimensions of each of these structures are  $4 \mu\text{m} \times 400 \text{ nm} \times 20 \text{ nm}$  and a cell size of  $5 \times 5 \times 5 \text{ nm}^3$  was used. In addition to the magnetisation values, the other parameter that was varied between these two stripe is the exchange stiffness constant 'A'. It was seen from low angle electron diffraction experiments, Fig. 6.2 that  $B_s t$  of the irradiated stripes is 60% of the unirradiated stripes. For a decrease in film thickness of  $2.9 \pm 0.7 \text{ nm}$  as obtained from cross-sectional TEM measurements, magnetisation (actually magnetic induction)

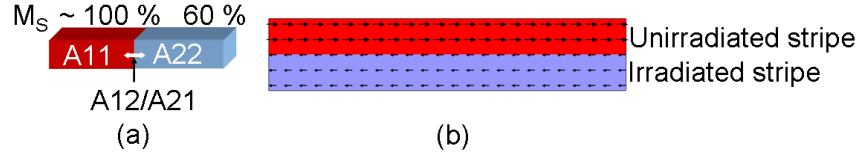


Figure 6.10: (a) Schematic cross-section of the initial magnetisation configuration of the stripe patterns where  $M_s$  is 100% for one stripe and 60% for the other. The exchange stiffness constants of the unirradiated and irradiated regions are indicated as  $A_{11}$  and  $A_{22}$ , respectively. The coupling term between these two regions are indicated as  $A_{12}$ . (b) Initial magnetisation states with anti-parallel orientation of magnetisation of the unirradiated and irradiated stripes.

was decreased to  $72.0 \pm 0.7\%$  due to ion irradiation as was described in section 6.4. Due to the changes of magnetisation, the exchange will also be changed. For the determination of exchange constant in the irradiated region, we have used the relation (as was addressed in **chapter 5**) between the exchange constant  $A$  and the spin  $s$ ,  $A = 4Js^2/a$ , as well as the connection between the expectation values of the spin operator  $S_z$  and saturation magnetisation  $M_s$ ,  $\langle M_s \rangle^2 \propto \langle S_z \rangle^2$ . There  $a$  is the lattice constant.

The exchange constant for the unirradiated region is indicated as  $A_{11}$ . The standard value for Py  $13 \times 10^{-12} \text{ J/m}$  was considered for  $A_{11}$ . The exchange constant for the irradiated region and the coupling term between these two different regions are marked as  $A_{22}$  and  $A_{12}$ , respectively. The exchange constant for these two terms are defined by equations 6.2 and 6.3 for  $M_s$  values of 100% and 60% for the unirradiated and irradiated stripes, respectively:

$$A_{22} = A_{11} \left( \frac{M_{s,irradiated}}{M_{s,unirradiated}} \right)^2 = 4.68 \times 10^{-12} \text{ J/m} \quad (6.2)$$

$$A_{12} = A_{21} = 0.5(A_{11} + A_{22}) = 8.84 \times 10^{-12} \text{ J/m} \quad (6.3)$$

The initial states with anti-parallel orientation of magnetisation of these two stripes are shown in Fig. 6.10(b). The DW was formed near to the interface of the two stripes at zero applied magnetic field. Then DW was moved either towards or away from the interface based on applied field direction. Figures 6.11(a-d) show the magnetisation reversal process as a function of an applied field where field direction is away from the interface. Figure 6.11(a) is the relaxed state of the initial magnetisation configuration



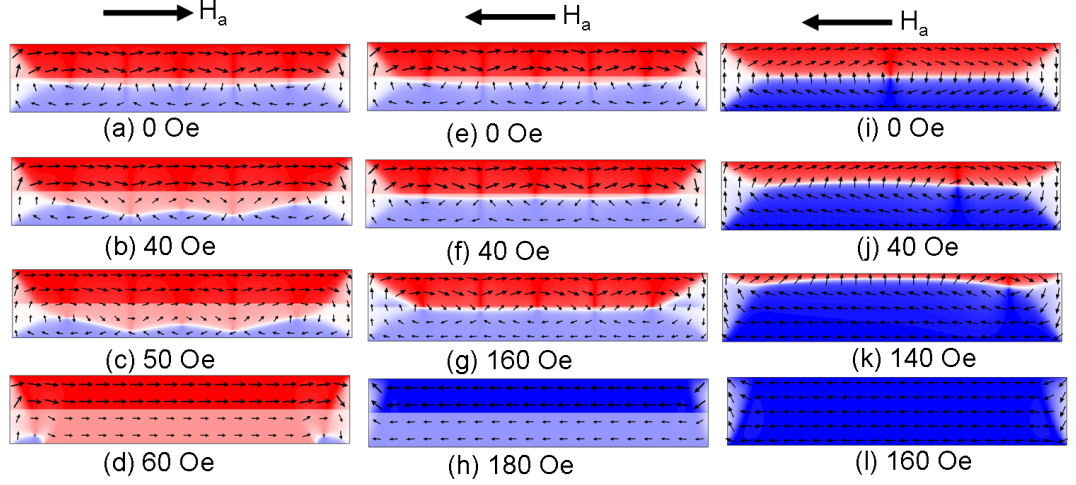


Figure 6.11: Magnetisation reversal process as a function of applied field from an initial anti-parallel orientation of magnetisation states of the stripe patterns. Magnetisation of the unirradiated and irradiated stripes are 100% and 60%, respectively in (a-h). Magnetisation is 100% in the two stripes in (i-l). Magnetic field was applied away from the interface at (a-d) and towards the interface at (e-l).

of Fig. 6.10(b) in which the magnetisation of the unirradiated (upper) and irradiated (lower) stripe is 100% and 60%, respectively. It is obvious that in the relaxed state the DW is pinned at the interface and exists in the irradiated stripe due to the lower wall energy of the reduced magnetisation stripe. Then by applying the magnetic field in a direction away from the interface, the domain wall moves significantly into the irradiated stripe 6.11(b) and then finally reversal completed at 60 Oe, Fig. 6.11(d).

Figures 6.11(e-h) show the magnetisation reversal process for a magnetic field applied towards the interface of the stripe patterns. In the relaxed state, Fig. 6.11(e), the DW is formed again in the irradiated stripe. It is the same relaxed state of Fig. 6.11(a). An applied magnetic field 40 Oe does not cause any significant movement of the DW, Fig. 6.11(f), towards the interface of the unirradiated and irradiated stripes. By a further application of the magnetic field up to 160 Oe, Fig. 6.11(g), the DW is pinned close to the interface of the unirradiated and irradiated stripes but still stays at the irradiated stripe region. Finally, reversal is completed at an applied magnetic field of 180 Oe, Fig. 6.11(h). The pinning of the DW in the irradiated stripe region was further clarified by applying magnetic field towards the interface of the stripe patterns for the initial anti-parallel orientation of magnetisation and with uniform  $M_s$  in each stripes. Figures 6.11(i-l) is the reversal sequences as a function of applied field. In the relaxed state, Fig. 6.11(i), the DW is formed at the interface of stripe

patterns and an applied magnetic field of 40 Oe moves the domain wall significantly. Finally, magnetisation reversal is completed at an applied magnetic field of 160 Oe, Fig. 6.11(l). By comparing the reversal sequences Figs. 6.11(e-h) and Figs. 6.11(i-l), it is clear that the reduced  $M_s$  in the irradiated stripe lowers the domain wall energy and favours the formation of the DW in the lower energy region. The reversal of the magnetisation in the stripe with uniform saturation magnetisation value is completed by rotation of the moments inside the stripe instead of moving the high angle domain wall across the energy barrier, Figs. 6.11 (e-h). Therefore, the different field direction dependent behaviour confirms the impact of the reduction in wall energy due to the reduction of the saturation magnetisation value on the reversal mechanisms. This ultimately supports the argument that irradiated stripe start reversal process during the experiments.

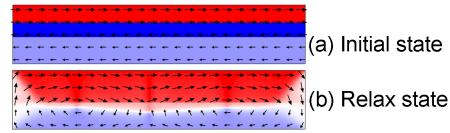


Figure 6.12: (a) Initial state of the magnetisation configurations in which an anti-parallel orientation of the magnetisation was settled in the unirradiated stripe. (b) The relax state of the initial configuration, DW is formed in the region of the irradiated stripe where  $M_s$  is 60%.

The preference for the formation of the DW in the irradiated stripe pattern was further verified by changing the initial magnetisation configuration of the stripe patterns, Fig. 6.10(b) in another simulation. Figure 6.12(a) show that an anti-parallel orientation of magnetisation resided in the unirradiated stripe where  $M_s$  is 100%. In the irradiated stripe the magnetisation value and orientation of the magnetisation was unchanged. Figure 6.12(b) is the relaxed state of this initial configuration that confirms the existence of the DW in the irradiated region. In the next section, DWs were characterised by calculating the wall widths as a function of wall angle using the DPC mode of Lorentz microscopy.



## 6.6 Domain wall width in the unconstrained and constrained film

Domain walls in  $16.9 \pm 0.8$  nm thin Py film are expected from theory [22] to be one dimensional symmetric Néel walls. These Néel walls are composed of a rather small core, having the exchange energy balanced by the stray field energy [22] due to the dipolar charges associated with the divergence of the magnetisation, and a tail which can extend over several  $\mu m$  beyond the core [13] in soft magnetic Py thin continuous films. In the constrained region, the extended tail is restricted by the edge of the element. During the course of this investigation, domain wall widths were calculated from fitted induction profiles across the walls [23,24] for wall structures formed in the unconstrained continuous Py film and also in the restricted region of the unirradiated stripe of the hybrid structures. Therefore, in order to approximate an induction/magnetisation profile across the wall, an arctangent function for the unconstrained region and a hyperbolic tangent function for the constrained region is a convenient and reasonable approximation. Figure 6.13 shows an example of an arctangent and hyperbolic tangent functions. If we denote  $x$  as the coordinate normal to the wall and  $y$  as the coordinate

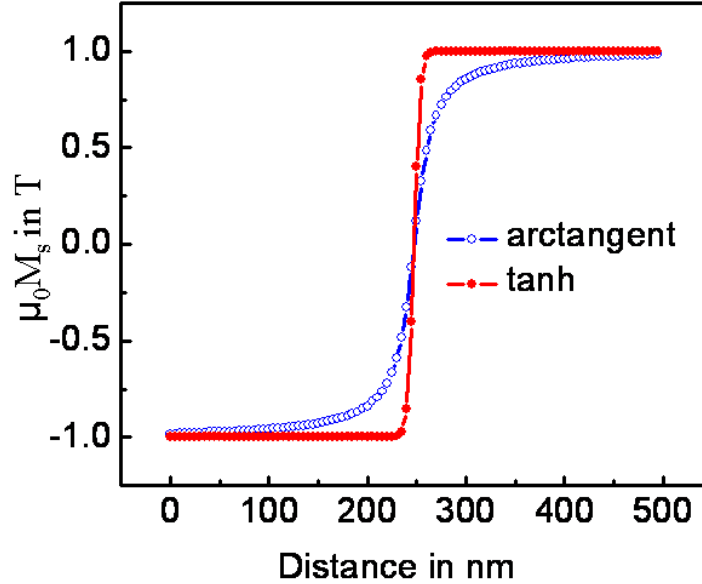


Figure 6.13: Example of an arctangent and hyperbolic tangent functions.

parallel to the wall, the induction and magnetisation profiles of the unconstrained and

constrained walls are given by the following equations, respectively, [22–26]:

$$B_y(x) = \frac{\pi}{2} \times B_s \arctan\left(\frac{x}{A}\right) \quad (6.4)$$

$$B_y(x) = B_s \tanh\left(\frac{x}{A}\right) \quad (6.5)$$

$$M_y(x) = \frac{\pi}{2} \times M_s \arctan\left(\frac{x}{A}\right) \quad (6.6)$$

$$M_y(x) = M_s \tanh\left(\frac{x}{A}\right) \quad (6.7)$$

where,  $B_s$  is the saturation magnetic induction,  $M_s$  is the saturation magnetisation and 'A' is the wall width fitting parameter which has dimensions of length. The width of the domain wall is determined as the full width at half maximum (FWHM) of the first-order derivative of the fitted induction/magnetisation profile functions above [23, 24] which gives a width of  $2A$  for arctan function and  $1.76A$  for tanh function.

In the present stage of this investigation, our interest is to calculate wall widths of two different wall structures, one formed in the unconstrained continuous Py film, marked by red rectangle in Fig. 6.14(a), and the other one formed in the unirradiated stripe of the hybrid structures, marked by green rectangle in Fig. 6.15(a). The unconstrained wall in the continuous Py film is a  $125^\circ$  wall and the constrained wall considered for wall width measurement inside the hybrid structure is a transverse type of wall where wall angles are nearly  $90^\circ$ . The wall angle of  $125^\circ$  DW was calculated using the ripple contrast of Fresnel image Fig. 6.14(a) in which the ripple lines run perpendicular to the average direction of the magnetisation. Confirmation of the wall angles were measured using the difference and sum signals of DPC images Fig. 6.14(b) and Fig. 6.15(b).

Figures 6.14(b) and 6.14(c) are the longitudinal and transverse induction components (in respect to the wall) of the DPC images of the unconstrained domain wall shown in Fig. 6.14(a). Red color arrows indicate the direction of magnetic induction each image is sensitive to. In order to measure the wall width, the induction map of the longitudinal component normal to the DW was modelled by an arctangent function.

Figure 6.14(d) shows the experimental profile averaged over 40 lines normal to the longitudinal component of the DPC image containing the  $125^\circ$  unconstrained wall. Figure 6.14(d) also shows the arctangent fitting of the induction profile and the first order derivative of the fitted induction profile. The width of this wall is  $(90 \pm 10)$  nm

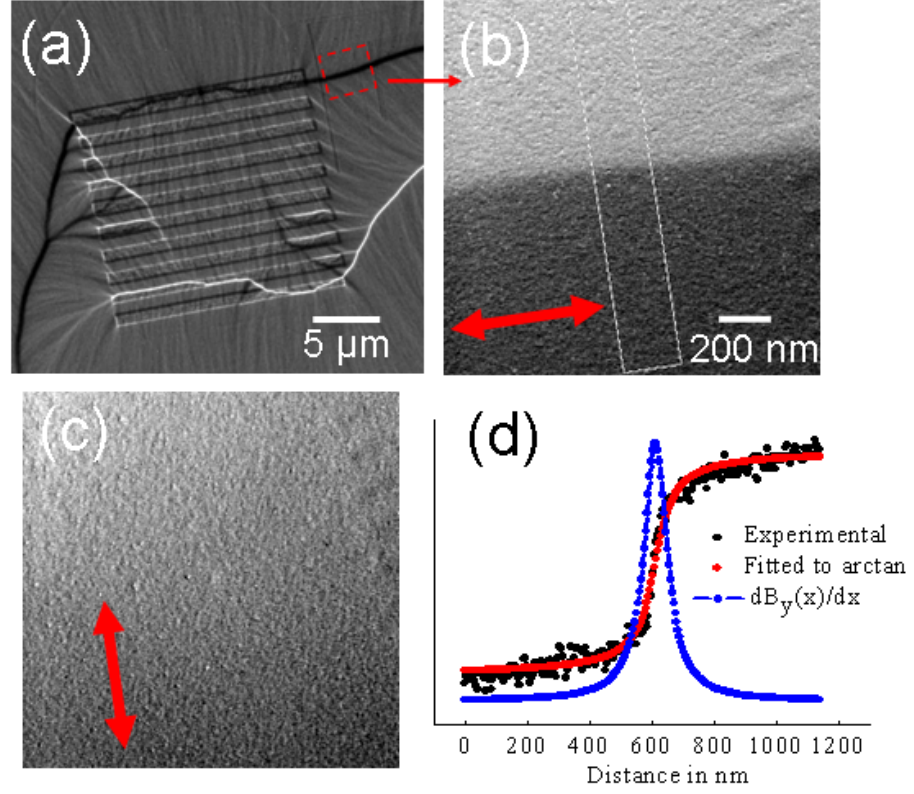


Figure 6.14: (a) Fresnel image showing a 125° DW in the continuous film, marked by red rectangle. DPC images of (b) longitudinal and (c) transverse induction component (in respect to wall) of the unconstrained wall in the continuous film as shown in Fresnel image (a). (d) Experimental induction profile, fitted profile and derivative of the fitted profile marked by black, red and blue circles, respectively. In Figs. (b,c) red arrows indicate the direction of the integrated induction components.

Table 6.2: Domain wall widths for two different wall angles. Experimental wall widths were compared to theory [23] for 20 nm thick continuous film.

Wall angle in degrees	Domain wall width in nm	
	Experimental	Theory
125	$90 \pm 10$	93
90	$70 \pm 7$	137

determined from the FWHM of the first order derivative of the fitted induction profile. Figures 6.15(b and c) are the longitudinal and transverse induction components, respectively, of the DPC images of the constrained domain wall shown in Fig. 6.15(a), indicated by the green rectangle and green arrow in the unirradiated stripe. Red arrows indicate the direction of the integrated induction components mapped. The longitudinal component of the induction profile of the 90° wall was fitted to the hyperbolic tangent function and DW width was measured again from the full width at half max-

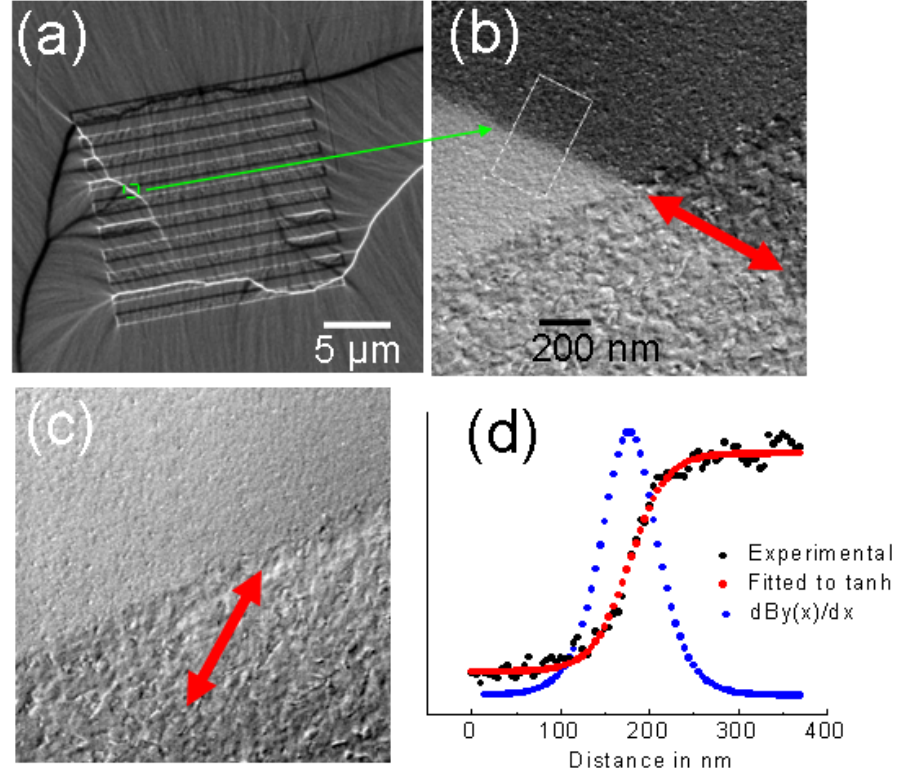


Figure 6.15: (a) Fresnel image showing a 90° DW in the constrained unirradiated stripe, marked by green rectangle and green arrow. Longitudinal (b) and transverse (c) induction components (in respect to wall) of the magnetisation in the constrained wall. (d) Experimental induction profile, tanh fitted profile and derivative of the fitted profile marked by black, red and blue circles, respectively. In Figs.(b,c) red arrows indicate the direction of the integrated induction components.

imum (FWHM) of the first-order derivative of the induction profile function fitted to the tanh function. Figure 6.15(d) shows the experimental profile average over 40 lines normal to the longitudinal induction component of the DPC image containing a 90° wall in the constrained region of the unirradiated stripe. The *tanh* fitting along with the first order derivative of the fitted induction profile is also included in this figure. The results are included in table 6.2 along with the theoretical wall widths for a 20 nm thick continuous Py film [22] for these two different wall angles. The results in table 6.2 confirm that the walls in the continuous film region are Néel type with a width consistent with predictions whilst in the constrained region the wall width appears to be compressed significantly compared to the equivalent wall in a continuous film. This is consistent with the theoretical calculation of wall width in references [13,27]. It was observed that [13] because of the extended tails in the Néel walls, the wall width in micron sized Py elements was reduced when the lateral size of the magnetic element is decreased. Previously a reduction of Bloch wall width has been predicted [27] theo-

retically in a geometrically constrained magnetic wall in a constriction separating two wider regions.

In order to gain a clear insight into the wall width effects for constrained structures initially we simulate a rectangular element of dimension  $2\ \mu\text{m} \times 500\text{nm} \times 20\text{nm}$  using simulation package oommf. The parameters used for simulation were standard for Py as was described in section 6.5.3. Figure 6.16 is the minimised energy state which arises from this well known flux closure configuration. The three components of magnetisation  $M_x$ ,  $M_y$  and  $M_z$  are shown in the gray scale images 6.16(a-c) respectively as calculated using the OOMMF simulation package. Figure 6.16(d) is a overall schematic of the domain structure which comprises four domains separated by  $90^\circ$  and  $180^\circ$  Néel walls. At the centre of the element magnetisation points out of the plane as shown in Fig. 6.16(c). The image calculations were performed using the Fast Fourier Transforms (FFTs) available on the software package Digital Micrograph (Gatan incorporated) as was described in **chapter 3**.

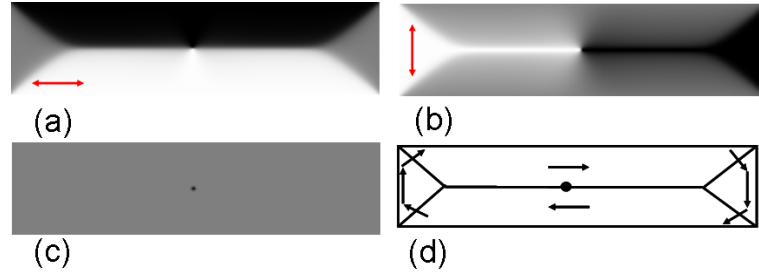


Figure 6.16: Gray scale images of the magnetisation components of a 20 nm thick Py element with in-plane dimensions  $2\ \mu\text{m} \times 500\text{nm}$  as calculated from OOMMF simulation package. The three components of magnetisation are (a)  $M_x$ , (b)  $M_y$  and (c)  $M_z$ . Double headed red arrows indicate the direction of sensitivity of magnetisation components.(d) Schematically the four domain structure.

The magnetisation profiles across the walls from different position as marked in Figs. 6.17(i-l) of the 500 nm wide element were fitted both to the arctangent and tanh functions, respectively and are shown in Figs. 6.17 (a-d). It is apparent from Figs. 6.17(a-d) that for 500 nm wide elements the magnetisation profiles are fitted well to the arctangent function compared to that of the tanh function. Therefore, even at this width the extended tails of the Néel walls were well approximated by an arctan function. The magnetisation profiles were considered from four different positions so that we can obtain an idea about the influence of magnetisation variations from the left end of the element and also from the central vortex core.

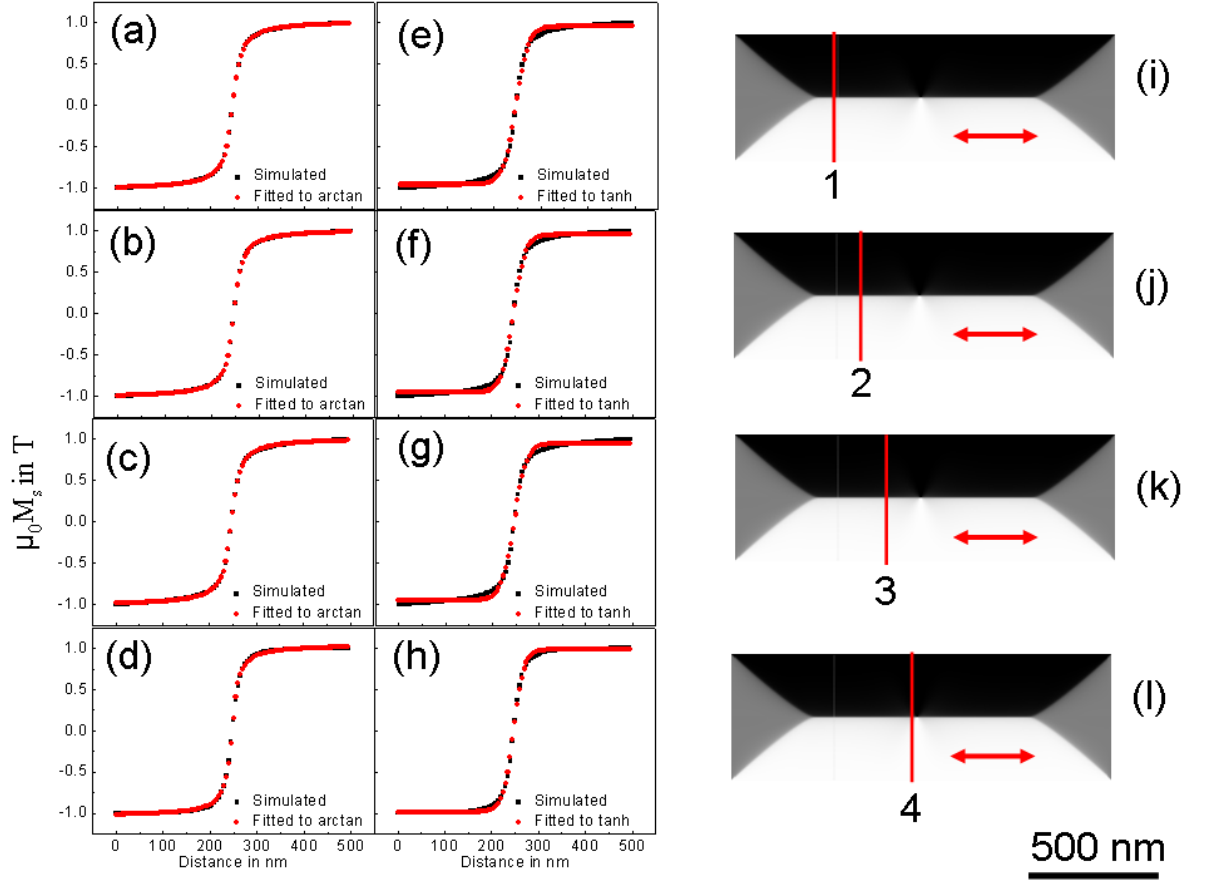


Figure 6.17: Magnetisation components parallel to the wall were fitted to (a-d) arctan function and (e-h) tanh function. The corresponding positions of the line traces were shown in (i-l). Red arrows in simulated images (i-l) indicate the sensitivity direction of the magnetisation components.

In order to observe the influence of constricted geometry on the DW width, the dimension of this element was changed to  $15 \mu m \times 5 \mu m \times 20 nm$  which we refer as a large element compare to 500 nm wide element. A cell size of  $5 \times 5 \times 10 nm^3$  was used in this case to speed up the simulation time. The dimension was further changed to  $2 \mu m \times 200 nm \times 20 nm$  and simulations were run with a cell size of  $5 \times 5 \times 5 nm^3$ . This element is considered as a constricted element compare to the two other elements of widths  $5 \mu m$  and 500 nm.

From the four domain structure the width of such an  $180^\circ$  wall was calculated from the magnetisation components parallel to the wall formed in the elements of widths  $5 \mu m$  and 200 nm. It was found that similar to the 500 nm wide element the magnetisation profiles for these two elements of widths  $5 \mu m$  and 200 nm were also fitted well to the arctan function compare to that of the tanh function. Table 6.3 shows domain wall widths of an  $180^\circ$  wall measured from magnetisation components in these three

Table 6.3: Domain wall width of an  $180^\circ$  domain wall measured from magnetisation components in different elements of varying width. In each element the position of the profiles were kept same.

Position of of the line trace	Domain wall width in nm		
	Elements width		
	$5\ \mu m$	500 nm	200 nm
1	$60 \pm 2$	$26 \pm 0.5$	$18.5 \pm 0.5$
2	$60 \pm 2$	$26 \pm 0.5$	$18.5 \pm 0.5$
3	$69 \pm 3$	$27 \pm 0.5$	$19 \pm 0.5$
4	$67 \pm 2$	$23 \pm 0.5$	$16.5 \pm 0.5$

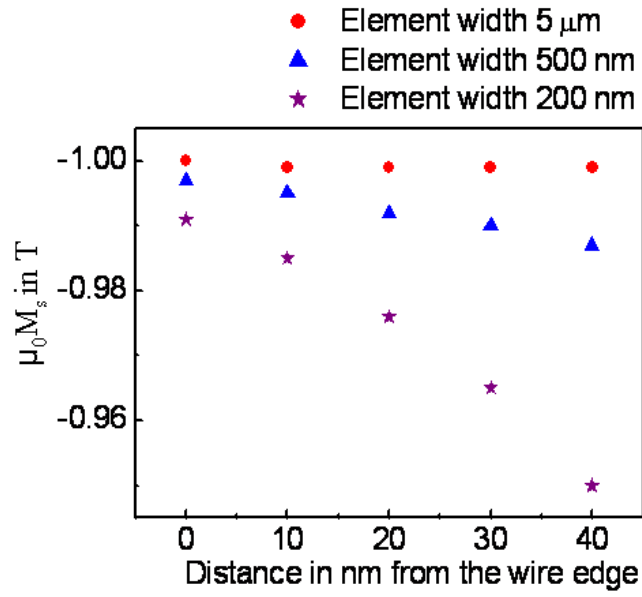


Figure 6.18: The parallel component of magnetisation values around the edges of the different elements.

elements of varying width. In each element the position of the profiles were kept the same. The wall width is much smaller for 500 nm and 200 nm elements compared to that of the  $5\ \mu m$  wide element. This is probably due to the edge of the elements which ultimately restrict the extended tail of the Néel walls. Figure 6.18 shows for example the magnetisation distribution up to 40 nm from the element edges of these three elements. It is seen that the magnetisation distribution is significantly different around the edges of these elements. Due to the edge effect of the magnetisation distribution of the profiles, the wall width reduces with reduced element width. Results from simulations clearly indicate that wider element supports a larger wall width. For the narrower elements the wall width is decreased significantly. This is consistent with

experimentally measured wall widths that demonstrate that the wall width in a restricted region is much less than that of the unconstrained continuous film (refer to table 6.2).

### 6.7 Summary

Saturation magnetisation modulated stripes embedded in a  $Ni_{81}Fe_{19}$  matrix were investigated regarding the occurrence of anti-parallel magnetisation components for adjacent stripes. Starting from a stripe width of 1000 nm a pronounced two step reversal with nearly anti-parallel orientated magnetisation in neighboring stripes is observed. The spacing between the neighboring nearly  $180^\circ$  domain walls still allows for discrete stripe domain patterns. The constriction of the Néel walls, formed at the interfaces between the stripes, by the structure size leads to an overlapping of neighboring tails. This is connected with a magnetisation component perpendicular to the stripes. The constriction of these domain walls goes together with the constriction of domain walls separating regions of different magnetisation orientations within the stripes. There the domain wall size is set by the geometrical size of the stripes. Due to strong domain wall tail interactions in adjacent stripes the formation of neighboring high angle domain walls at the interfaces of the stripes is suppressed. Therefore a tendency of collective reversal of the stripe pattern is observed. Domain walls constricted inside the stripes are characterized concerning the connection between domain wall width and domain wall angle. For a particular wall angle the wall width in the constricted region is smaller than that of the unconstrained wall. The wall widths determined using micromagnetic simulation demonstrate the edge effect of the elements of varying width which ultimately restrict the tail of the wall and decrease the wall widths.



# Bibliography

- [1] C. Chappert, H. Bernas, J. Ferreacut, V. Kottler, J. Jamet, Y. Chen, E. Cambril, T. Devolder, F. Rousseaux, V. Mathet, and H. Launois, *Science* **280** 1919 (1998).
- [2] W. M. Kaminsky, G. A. C. Jones, N. K. Patel, W. E. Booij, M. G. Blamire, S. M. Gardiner, Y. B. Xu, and J. A. C. Bland, *Appl. Phys. Lett.* **78** 1589 (2001).
- [3] J. Fassbender, D. Ravelosona, Y. Samson, *J. Phys. D: Appl. Phys.* **37** R179 (2004).
- [4] J. Fassbender and J. McCord, *J. Magn. Magn. Mater.* **320** 579 (2008).
- [5] S. Turnbull, *Characterisation of focused ion beam nanostructures by transmission electron microscopy*, PhD thesis, University of Glasgow, 2008.
- [6] L. Folks, R. E. Fontana, B. A. Gurney, J. R. Childress, S. Maat, J. A. Katine, J. E. E. Baglin, and A. J. Kellock, *J. Phys. D: Appl. Phys.* **36**, 2601 (2003).
- [7] S. I. Woods, S. Ingvarsson, J. R. Kirtley, H. F. Hamann, and R. H. Koch, *Appl. Phys. Lett.* **81**, 1267 (2002).
- [8] J. McCord, T. Gemming, L. Schultz, J. Fassbender, M. O. Liedke, M. Frommberger, and E. Quandt, *Appl. Phys. Lett.* **86**, 162502 (2005).
- [9] J. McCord, I. Moench, J. Fassbender, A. Gerber, and E. Quandt, *J. Phys. D: Appl. Phys.* **42**, 055006 (2009).
- [10] J. McCord, L. Schultz, and J. Fassbender, *Advanced Materials* **20**, 2090 (2008).
- [11] J. Fassbender, T. Strache, M. O. Liedke, D. Marko, S. Wintz, K. Lenz, A. Keller, S. Facsko, I. Moench, and J. McCord, *New J. Phys.* **11**, 125002 (2009).
- [12] T. Haug, C. H. Back, J. Raabe, S. Heun, and A. Locatelli, *Appl. Phys. Lett.* **86** 152503 (2005).

- [13] P.-O. Jubert, R. Allenspach, and A. Bischof, Phys. Rev. B **69** 220410 (2004).
- [14] M. Ruehrig, B. Khamsehpour, K. Kirk, J. Chapman, P. Aitchison, S. McVitie, and C. Wilkinson, IEEE Trans. Magn. **32**, 4452 (1996).
- [15] D. Ozkaya, R. M. Langford, W. L. Chan, and A. K. Petford-Long, J. Appl. Phys. **91** 9937 (2002).
- [16] J. Fassbender, J. von Borany, A. Mcklich, K. Potzger, W. Mller, J. McCord, L. Schultz and R. Mattheis, Phys. Rev. B **73** 184410 (2006).
- [17] C.-M. Park and J.A. Bain, J. Appl. Phys. **91** 6830 (2002).
- [18] J. N. Chapman, A. B. Johnston, L. J. Heyderman, S. McVitie, W. A. P. Nicholson, and B. Bormans, IEEE Trans. Magn. **30**, 4479 (1994).
- [19] J. N. Chapman, J. Phys. D: Appl. Phys. **17** (1984) 623.
- [20] J. N. Chapman and M. R. Scheinfein, J. Magn. Magn. Mater. **200** 729 (1999).
- [21] M. J. Donahue and D. G. Porter, Report No. NISTIR 6376 (National Institute of Standards and Technology, Gaithersburg, MD, 1999).
- [22] A. Hubert and R. Schaefer, Magnetic Domains (Springer, 1998).
- [23] A. Hubert, phys. stat. sol. (b) **38** 699 (1970).
- [24] S. McVitie and J. Chapman, J. Magn. Magn. Mater. **83**, 97 (1990).
- [25] S. McVitie, G.S. White, J. Scott, P. Warin and J.N. Chapman, J. Appl. Phys. **90** 5220 (2001).
- [26] S. McVitie, M. Cushley, *Ultramicroscopy* **106** 423 (2006).
- [27] P. Bruno, Phys. Rev. Lett. **83** 2425 (1999).

# Chapter 7

## Conclusions and Future Work

### 7.1 Introduction

The investigation of magnetic nanostructures is one of the major current subjects in magnetism due to the recent advancement in nanofabrication techniques and magnetic characterisation methods. This interest is stimulated by the unexplored fascinating fundamental physics at the nanoscale as well as by the perspective of future technological applications such as magnetic logic and memory devices [1, 2]. In such devices, bits of information are encoded in the magnetic domain walls (DWs). The access and manipulation of the stored information is realised by the controlled movement of DWs along the patterned nanowires. The technique promises lower- powered, higher speed and non-volatile devices and allows the architecture of the computing system to be greatly simplified. However, one of the major challenges associated with the realisation of these devices is that any physical defects within the patterned wires or material can perturb the propagation of information and thus the performance of the device is also determined by the fabrication quality. Therefore, during the course of this PhD project, investigations were carried out to observe the differences in behaviour of magnetic domain walls in nominally identical permalloy nanowires patterned by alternative fabrication techniques, namely, electron beam lithography and focused ion beam milling. The results were described in **chapter 4**. Applications of such devices rely on the ability to control domain wall motion along the patterned nanowires in a highly predictable way. Deliberately fabricated trapping sites such as a notch/anti-notch [3–5] of different geometries allow control of the position of DWs in ferromagnetic nanowires. A possible alternative approach to this is to use pinning sites by effectively

locally modifying the properties of the magnetic material [6, 7] without changing the shape of the wire structure. In order to explore the strong potential of this approach, investigations were performed to reproducibly pin and depin domain walls from non topographic pinning sites in a permalloy nanowire structure without using any geometrical features. The outcomes were presented in **chapter 5**. Previous investigations demonstrated that by lateral magnetic patterning of ferromagnetic thin films the magnetic properties, like saturation magnetisation  $M_s$  [8, 9] and induced anisotropy [10–12] can be changed on a local scale. In the present investigation, magnetic patterning in a stripe like manner has been performed on thin continuous  $16.9 \pm 0.8$  nm Py film using focused ion beam irradiation. Afterwards investigations were carried out using the high resolution Lorentz TEM imaging to observe the influence of the downscaling of the patterning size on the magnetisation reversal mechanism and domain wall formation in the equivalent stripe structures. The results of this investigation were presented in **chapter 6**.

The noteworthy outcomes of **chapters 4, 5 and 6** are discussed in this chapter. At the end of this chapter, some avenues to explore in the future are also described.

## 7.2 Conclusions

In **chapter 4** by fabricating Permalloy (Py) nanowires by electron beam and focused ion beam lithography a comparative study has been made in which key differences in the magnetic behaviour have been identified using Lorentz TEM. Nominally identical permalloy nanowires, with widths down to 150 nm, were fabricated onto a single electron transparent  $\text{Si}_3\text{N}_4$  membrane. Transmission electron microscopy (TEM) experiments were performed to compare the nanostructures produced by these two techniques. Both EBL and FIB methods produced high quality structures with edge roughness being of the order of the mean grain size, 5 -10 nm, observed in the continuous films. However, significant grain growth was observed along the edges of the FIB patterned nanowires. Therefore, the differences between the physical nanostructure of the patterned nanowires are clearly associated with the regions close to the edge of the wires. It is well known that the profile of the beam has a long exponential tail and therefore, during the sputtering process, the  $\text{Ga}^+$  implantation from the extended

tail of the ion beam may affect the ferromagnetic properties of the Py particularly along the edges of the FIB patterned nanowires. However, TEM x-sectional images have confirmed that well defined edge profile result for nanowires patterned using both EBL and FIB techniques. *In situ* magnetising experiments were carried out using the Fresnel mode of Lorentz TEM to compare the magnetic behavior of the domain walls in the patterned nanowires with anti-notches present to pin domain walls. The overall process of domain wall pinning and depinning at the anti-notches showed consistent behaviour between nanowires fabricated by the two methods with the FIB structures having slightly lower characteristic fields compared to the EBL wires. This is probably due to the differences in edges crystallites seen in TEM images as a consequence of  $Ga^+$  implantation from the extended tail of the ion beam along the FIB patterned wire edges. The effect of  $Ga^+$  implantation was simulated using OOMMF simulation by varying  $M_s$  along nanowire edges. Evidence from micromagnetic simulations suggest that this different reversal process between the nanowires fabricated by the FIB techniques may be associated with the reduction of  $M_s$  along the wire edges. Such a reduction of  $M_s$  along the wire edges reduces the DW depinning fields and is consistent with the experimentally observed magnetisation behavior of the FIB milled nanowires. Indeed, this point is consistent with a study of nanoelements with dimensions  $< 100$  nm in which the residual irradiation from the FIB seriously affected the magnetic structure of the whole element [13]. In that case the entire magnetic structure appeared to be modified by residual irradiation from the FIB, whereas in this study there is a clearly defined affected edge and non affected internal regions. The difference in the reversal process between EBL and FIB patterned nanowires are also demonstrated by the formation of a ccw vortex structure inside the anti-notches of the EBL nanowires after the depinning of DWs. The presence of these vortices appears irrespective of the chirality of the depinned DWs. No vortex structure was seen inside the anti-notches of the FIB patterned nanowires. The presence of these vortices could potentially be very problematic for nanowire applications where a series of domain walls pass through wires in proposed memory and logic applications [1, 2]. Therefore for the wire dimensions considered here FIB may actually be beneficial as a fabrication method. However, it must be noted that the edge modification induced by the FIB method does have implications, particularly if smaller dimensions are to be fabricated, and this certainly

needs to be carefully considered when using this method.

In **chapter 5** ion induced intermixing in a multilayer thin film system of Cr(3 nm)/Py(10 nm)/Cr(5 nm) was optimised using dynamic simulation package TRIDYN so that the Cr concentration can be well controlled. Simulations also gave an indication of the Cr concentration in the Py film as a function of irradiation dose. The asymmetry of the top and bottom Cr layer greatly enhanced the uniformity of Cr concentration in the Py film. Alloying Py with Cr is known to significantly change its magnetic properties. In order to investigate the effective local modification of the multi-layer thin film system due to radiation induced interfacial mixing, alternate unirradiated and irradiated stripe patterns were written on continuous thin film of Cr(3 nm)/Py(10 nm)/Cr(5 nm). Low angle electron diffraction experiments performed on stripe like patterns demonstrated that micro-alloying due to a combined effect of ion irradiation and modest elemental mixing across interfaces modified the ferromagnetic properties of this alloy system. From large area irradiation experiments, magnetisation was found to reduce as a function of irradiation doses and for higher doses the region rendered non-ferromagnetic. Therefore, isolated nanowires were patterned using FIB milling on a thin continuous film and a single irradiation line was exposed to create a pinning site at an angle of 45 degrees to the wire length by locally modifying the magnetic properties of the nanowire. Observation of the magnetic state of the nanowires was made using Lorentz microscopy. A transverse DW was created at the end of a 500 nm wide nanowire and then a field applied to move it towards the pinning site. Initial investigation demonstrated that nanowires and irradiation lines written on an isotropic magnetic thin film system did not result in pinning of DWs reproducibly at these pinning sites. In this film system, beside DW contrast significant ripple contrast along the wire axis was also visible in the Fresnel images. The ripple suggests considerable deviation of the magnetisation from the nanowire axis and was problematic for reproducible DW behaviour. Materials of nominally the same thicknesses were deposited using magnetron sputter deposition and field induced anisotropy was created during deposition. Nanowires were written using the FIB milling technique with their length being oriented along the anisotropy direction. Thereafter, *in situ* magnetising experiments were performed using Fresnel mode of Lorentz TEM. In this case we were able to pin reproducibly transverse wall

at the irradiated line for low doses. This indicates that creation of the field induced anisotropy during the material deposition and thereby fabrication of the nanowires along this anisotropy direction played a vital role to establish the reproducibility of these experiments. By irradiating a line across the width of the nanowire, magnetic properties of the wire were modified locally. A local modification of magnetic properties creates a potential well which is a local minimum in potential energy. The depth of the well is increased dramatically with increasing ion doses and finally almost leveled off at higher doses.

We observe that the inclusion of the non topographic pinning features along the length of the patterned nanowires allow a degree of control of pinning and depinning of DWs at predefined locations. These pinning features behave like potential wells and the strength of the wells is seen to increase up to the formation of the VDWs at which point it appears to plateau. Wall transformations are observed with a tendency of one type of asymmetric TDW wall favoured at lower doses and only VDWs at the highest doses. In this sense the pinning site can be seen as setting the DW type for the higher doses whilst increasing the probability of one type of asymmetric TDW at the lower doses. Initial micromagnetic simulations indicate that the irradiated lines result in a reduction of the demagnetising of the DWs when they are located at these positions. In addition to the control of the DWs, our findings indicate potential for engineering and filtering DWs of certain types as they pass irradiated features at predefined locations in nanowires, dependent on the dose associated with these features in magnetic nanowires sandwiched between metallic layers.

In **chapter 6** on a continuous  $16.9 \pm 0.8$  nm thick Py film, magnetically softer and harder stripes, which are in direct lateral contact by means of exchange coupling, were fabricated by focused  $Ga^+$  irradiation. The irradiation dose was  $6.24 \times 10^{15}$  ions/cm<sup>2</sup> and the width of the alternate exposed and unexposed stripes were varied from 1000 nm to 200 nm. Low angle electron diffraction experiments confirmed that due to this ion dose, saturation magnetic induction of the irradiated stripe is reduced to  $72.0 \pm 0.7\%$  of the unirradiated stripe, assuming a thickness reduction of  $2.9 \pm 0.7$  nm determined from TEM cross-sectional image. Magnetisation reversal experiments were carried out using high resolution Lorentz microscopy. Saturation magnetisation modulated stripes

embedded in a  $Ni_{81}Fe_{19}$  matrix were investigated regarding the occurrence of anti-parallel magnetisation components for adjacent stripes. Starting from a stripe width of 1000 nm a pronounced two step reversal with nearly anti-parallel orientated magnetisation in neighboring stripes is observed. High angle ( $180^\circ$ ) domain walls in the film are initially pinned at the outer irradiated stripes and existed only in the irradiated stripes but not in the unirradiated stripes. The energy associated with the irradiated region is lower due to lower moment and possibly exchange and therefore the switching of these irradiated stripes were observed first. The application of a magnetic field along the stripe axis causes a rotation of the magnetisation in the stripes. At low fields this is fairly small in the non-irradiated stripes. However, due to the opposite direction of induction components and differences in the rotation angles, no net charge in the walls and interfaces results. Therefore, a larger rotation of magnetisation in the irradiated stripe is expected by forming high angles DWs. The spacing between the neighboring nearly  $180^\circ$  domain walls still allows for discrete strip domain patterns. The constriction of the Néel walls, formed at the interfaces between the stripes, by the structure size leads to an overlapping of neighboring tails. This is connected with a magnetisation component perpendicular to the stripes. The constriction of these domain walls goes together with the constriction of domain walls separating regions of different magnetisation orientations within the stripes. There the domain wall width is influenced by the geometrical size of the stripes. Due to strong domain wall tail interactions in adjacent stripes the formation of neighboring high angle domain walls at the interfaces of the stripes is suppressed. Therefore a tendency of collective reversal of the stripe pattern is observed. Domain walls constricted inside the stripes are characterized concerning the connection between domain wall width and domain wall angle. For a particular wall angle the wall width in the constricted region is smaller than that of the unconstrained wall. Using micromagnetic simulations we have investigated the configuration of  $180^\circ$  Néel wall by varying the width of a rectangular element. Evidence from micromagnetic simulation demonstrated that DW width is dependent on the dimensions of the element. The extended tail of the Néel type of DW is strongly confined by the elemental edge and therefore the wall width in these elements is reduced when the size of the magnetic element is decreased.

Based on the insights gained in this thesis, several further experiments promise inter-



esting results. Some ideas are briefly outlined in the following sections.

### 7.3 Future work

In **chapter 4**, nominally identical Py nanowires, with widths down to 150 nm, were fabricated onto a single electron transparent  $\text{Si}_3\text{N}_4$  membrane by EBL and FIB milling techniques. A recent investigation demonstrated that nanoelements created by FIB with widths less than 100 nm were not able to be determined as magnetic using LTEM [13]. In that case the entire magnetic structure appeared to be modified by residual irradiation from the FIB. Nevertheless, it may be interesting to fabricate nominally identical Py nanowires with widths about 100 nm using these two alternative techniques. The outcome of this investigation may allows further insight on the edge modification induced by the FIB method particularly for smaller dimensions and may provide an indication about the limiting widths of FIB milling wire structure to extract magnetic information. Furthermore, in order to accumulate quantitative information about  $\text{Ga}^+$  implantation from the extended tail of the ion beam along the FIB patterned wire edges, analytical microscopy like energy dispersive X-ray (EDX) analysis may be performed to some extent. A comparative EDX analysis of the EBL and FIB milled wire structure may also give an indication regarding  $\text{Ga}^+$  implantation during the preparation of the TEM x-section using FIB milling technique.

In **chapter 5**, using low angle electron diffraction experiments integrated magnetic induction ( $B_{st}$ ) was calculated both in the unirradiated and irradiated regions. Due to the ion irradiation the film thickness may change due to sputter effects. It may be interesting as well as challenging to prepare a TEM x-section, in order to measure the exact thickness of the film before and after ion irradiation. By knowing the film thickness the magnetic induction will be calculated as a function of irradiation dose. In this chapter, a single irradiation line was exposed to create pinning site at an angle of 45 degrees to the wire length by locally modifying the magnetic properties of the nanowire. The orientation of these pinning sites is shown in the schematic Fig. 7.1(a). It may be worthwhile to know the influence of pinning sites orientation on pinning and depinning mechanism of DWs. Samples were already prepared by changing the orientation of these pinning sites as shown in the schematic Fig. 7.1(b). In situ magnetising

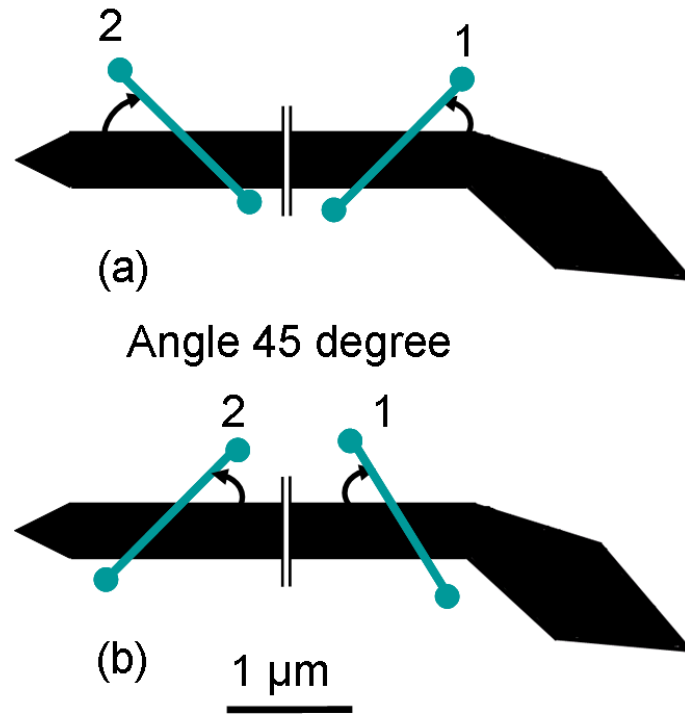


Figure 7.1: (a) Schematic of the nanowires geometry. The length of the wire axis has been reduced for this schematic indicated by vertical bars. Ion irradiated pinning sites were indicated by the two lines oriented at  $\pm 45^\circ$  and marked as pinning sites 1 and 2 in each nanowire. This structure was used in **chapter 5** for magnetising experiments. (b) The orientation of the pinning sites has been changed.

experiments of the samples will be carried out using the Fresnel mode of Lorentz TEM. Furthermore, investigations may be carried out by varying the dose of each line. For example, irradiation line 1 may be written by lower dose compared to that of line 2. Therefore, we may expect to pin a transverse type of domain wall at site 1 and a vortex type of domain wall at site 2 which was irradiated with higher dose. In order to figure out the strength of these non topographic pinning features in the patterned nanowires of reduced dimensions a further investigation may be promising. Therefore, nanowires of width about 100-200 nm may be fabricated and this might have a great impact on high density storage device fabrication. Beside, a multilayer thin film system of Cr(3 nm)/Py(7 nm)/Cr(5 nm) was deposited by magnetron sputter deposition with field induced anisotropy. Similar investigation may be performed for a 7 nm thickness Py film. It is expecting that due to the reduced thickness of the Py film, modest elemental mixing across interfaces may be more uniform and modifications of the ferromagnetic properties of the Py film will be comprehend at lower doses. Realistic simulation e.g. Nmag (as was introduced in **chapter 5**, section 5.9) may carry out to aid interpretation

of experimental images as well as to understand magnetic behaviour of the modified Py at higher doses where a change in miromagnetic wall structure was observed.

In **chapter 6**, magnetically softer and harder stripes, which are in direct lateral contact by means of exchange coupling, were fabricated on thin continuous Py film using focused  $Ga^+$  irradiation. It was intended to study a field dependent alignment of magnetisation, termed as lateral exchange spring structures behaviour. In the lateral exchange spring system, upon application of an external field, a magnetic interface domain wall forms which disappears upon removal of the field as the soft layer magnetisation rotates back in alignment with the hard magnetic layer [8]. However, during the course of this investigation, changes of the magnetisation reversal along the initial easy axis were measured for  $70\ \mu m \times 70\ \mu m$  squares of a  $Ni_{81}Fe_{19}(20nm)/Si_3N_4$  reference sample irradiated with focused ion beam with the same parameters described in **chapter 6**, section 6.2. The coercivity  $H_C$  increased to at least 6 Oe due to an increase in pinning of the domain walls. Large  $H_C$  for irradiated stripes works against lateral exchange spring effect. Therefore, in order to observe lateral exchange spring effect, a new set of samples were prepared by depositing Ta (6 nm) as a buffer layer on top of  $Si_3N_4$ . Irradiation experiments were already performed using the same parameters described in **chapter 6**, section 6.2 on thin continuous film of  $Ni_{81}Fe_{19}(20nm)/Ta(6nm)/Si_3N_4$ . At present, *in-situ* magnetisation reversal experiments are being performed using high resolution Lorentz TEM imaging.

# Bibliography

- [1] D. A. Allwood, Gang Xiong, M. D. Cooke, C. C. Faulkner, D. Atkinson, N. Vernier, and R. P. Cowburn, *Science* **296** 2003 (2002).
- [2] S.S.P. Parkin, M. Hayashi, L. Thomas, *Science* **320** 5873 (2008).
- [3] D. Petit, A. V. Jausovec, D. Read, and R. P. Cowburn, *J. Appl. Phys.* **103** 114307 (2008).
- [4] K. J. O'Shea, S. McVitie, J. N. Chapman, and J. M. R. Weaver, *Appl. Phys. Lett.* **93** 202505 (2008).
- [5] M. Kläui, H. Ehrke, U. Rdiger, T. Kasama, R. E. Dunin-Borkowski, D. Backes, L. J. Heyderman, C. A. F. Vaz, J. A. C. Bland, G. Faini, E. Cambril, and W. Wernsdorfer, *Appl. Phys. Lett.* **87** 102509 (2005).
- [6] A. Vogel, S. Wintz, J. Kimling, M. Bolte, T. Strache, M. Fritzsche, M. Y. Im, P. Fischer, G. Meier, and J. Fassbender, *IEEE Trans. Magn.* **46** 1708 (2010).
- [7] A. Vogel, S. Wintz, T. Gerhardt, L. Bocklage, T. Strache, M. Y. Im, P. Fischer, J. Fassbender, J. McCord and G. Meier, *Appl. Phys. Lett.*, **98**, 202501, (2011).
- [8] J. McCord, L. Schultz, and J. Fassbender, *Advanced Materials* **20**, 2090 (2008).
- [9] J. Fassbender, T. Strache, M. O. Liedke, D. Marko, S. Wintz, K. Lenz, A. Keller, S. Facsko, I. Moench, and J. McCord, *New Journal of Physics* **11**, 125002 (2009).
- [10] D. Ozkaya, R. M. Langford, W. L. Chan, A. K. Petford-Long, *J. Appl. Phys.* **91**, 9937 (2002).
- [11] S. I. Woods, S. Ingvarsson, J. R. Kirtley, H. F. Hamann, R. H. Koch, *Appl. Phys. Lett.* **81**, 1267 (2002).

- [12] J. Fassbender and J. McCord, Appl. Phys.Lett. **88** 252501 (2006).
- [13] X. Kong, S McVitie, J. N. Chapman, J. M. W. Weaver and C. D. W. Wilkinson,  
J Vac. Sci Tech., submitted for publication.